Unsteady Aerodynamics of Wing-Gust Encounters

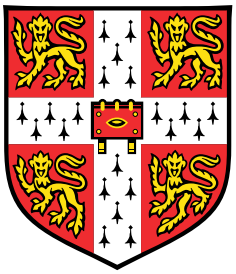

Simon James Corkery

Department of Engineering
University of Cambridge

This dissertation is submitted for the degree of
Doctor of Philosophy

Churchill College

December 2018

I would like to dedicate this thesis to my loving family.

Declaration

I hereby declare that this dissertation is the result of my own work and includes nothing which is the outcome of work done in collaboration except as declared in the Preface and specified in the text. It is not substantially the same as any that I have submitted, or, is being concurrently submitted for a degree or diploma or other qualification at the University of Cambridge or any other University or similar institution except as declared in the Preface and specified in the text. I further state that no substantial part of my dissertation has already been submitted, or, is being concurrently submitted for any such degree, diploma or other qualification at the University of Cambridge or any other University or similar institution except as declared in the Preface and specified in the text. This dissertation contains 59,600 words, and has 109 figures.

Simon James Corkery
December 2018

Acknowledgements

The author would like to acknowledge Professor Holger Babinsky for his significant advice, encouragement, opportunities presented, and impressive willingness to tolerate me for 3 years. This work reflects your efforts as much as mine. To Professor John Harvey, thank you for your gentle guidance and the time spent chatting about all things aero- and un-aerodynamics related. I have learnt so much. Dr Will Graham, you inspired many of the fundamental ideas that define this work. To my lab mates, past and present, thank you for making each day enjoyable and for the snacks, refreshments and jokes you've shared. Many thanks to the Aerodynamics and Fluid Mechanics Laboratory technicians for assisting with the continual stream of odd-jobs. Thank you to my family for your unconditional support. I don't want to hear about any mistakes you may find! Finally, thank you to my dearest Tahmina. I am forever indebted to you.

This work was generously supported by Schlumberger Limited, the Cambridge Trusts and Churchill College.

Abstract

Unsteady Aerodynamics of Wing-Gust Encounters

Simon James Corkery

Wind gusts can be highly detrimental to the performance of fixed wing aircraft. At low flight speeds, gusts transverse to the lifting surfaces can cause massive changes to the angle of incidence, fluctuations in lift and drag, and result in flight instability. This may be catastrophic for small drones, and hazardous for larger aircraft during take-off and landing. Onboard gust sensing and counter-control is a promising solution, but requires a model of the wing-gust interaction. The problem is that only simple linear models such as Küssner's theory exist, and the physics of large amplitude wing-gust encounters is unknown. This work is a fundamental study into the physics of such interaction. The aims are to uncover the phenomenon which contribute toward the force response of the wing. In particular, the role of free vortices and added mass are investigated and compared with the conditions modelled within Küssner's transverse gust theory.

Two sets of experiments were conducted using flat plate wing models in a water towing tank. Data was acquired using a combination of Particle Image Velocimetry (PIV), dye flow visualisation, and force measurements. A novel methodology was also developed to isolate added mass effects from standard resolution PIV. The first experiment involved accelerating the plate in translation and angular directions to validate the added mass extraction methodology, and investigate viscous effects on added mass. The experiments successfully demonstrated both the technique, and that the potential flow added mass solution is valid even for viscous and separated flows.

For the second experiment, equipment was constructed to facilitate the generation of a 'sharp edged' top-hat shaped gust velocity profile in the towing tank. The wing models were towed through this, thereby replicating a wing-gust encounter. Test cases with gust ratios of 0.2, 0.5 and 1.0, as well as Reynolds numbers from 5,000 to 40,000 were conducted. The results showed that Küssner's model predicted the force response for each encounter surprisingly well, albeit discrepancies emerged at the higher gust ratios. This was attributed to significant leading edge separation as well as deflection and subsequent roll-up of the gust shear layers. For wing-gust encounters it was shown that the force component attributed to added mass in Küssner's model is not equivalent to that of an accelerating body, rather it can be attributed to the relative advection of gust shear layer vortices. We call this a 'non-circulatory vortex force'. A second non-circulatory vortex force was additionally proposed, attributed to the generation of free vortices. This was shown to be responsible for the buoyancy and added mass like force, for cases where a flow field is accelerated past a stationary body.

Table of contents

List of Publications **xiii**

Nomenclature **xv**

1 Introduction **1**
1.1 Motivations for the present research 3

2 Literature Review **5**
2.1 Definition of a ‘gust’, and gust interaction 5
2.2 Origin and impact of different gust types 5
2.2.1 Gust types 5
2.2.2 Transverse gust models for aircraft design 6
2.3 Classical aerodynamics 8
2.3.1 Fundamental concepts 8
2.3.1.1 Continuity and the momentum equations 8
2.3.1.2 Vorticity and the vorticity transport equation 9
2.3.1.3 Potential flow 9
2.3.1.4 The steady and unsteady Bernoulli equations 10
2.3.1.5 Circulation and the Kutta-Joukowski theorem 11
2.3.1.6 Vortex force 13
2.3.1.7 General impulse methods 14
2.3.2 Steady thin airfoil theory 15
2.3.3 Quasi-steady thin airfoil theory 17
2.3.4 Unsteady models 17
2.3.4.1 Added mass (a non-circulatory force) 18
2.3.4.2 Wagner’s model 22
2.3.4.3 Küssner’s model 24
2.4 Transverse wing-gust interaction studies 27
2.4.1 Experimental studies 27
2.4.2 Computational studies 28

2.5 Surging, pitching and plunging wings . . . 30
2.5.1 Lift production mechanisms . . . 30
2.5.2 Low-order modelling . . . 32
2.6 Literature summary . . . 37
2.7 Approach and aims . . . 38

3 Added Mass Revisited **41**
3.1 Cylinder flows . . . 42
3.1.1 Accelerating cylinder case . . . 42
3.1.2 Accelerating flow field case . . . 44
3.2 Translating and rotating flat plate . . . 45
3.2.1 Problem geometry . . . 45
3.2.2 Complex potential and velocity . . . 47
3.2.3 Surface velocity and bound vortex sheet . . . 47
3.2.4 Linear impulse and force . . . 50
3.2.5 First moment of impulse and mid-chord moment . . . 50
3.2.6 Point vortex approximation . . . 51
3.3 Added mass in Küssner's sharp edged gust . . . 52
3.3.1 Geometry . . . 52
3.3.2 Non-circulatory vortex sheet . . . 52
3.3.3 Impulse and force . . . 53
3.4 Added mass in viscous separated flows . . . 55
3.4.1 Further objectives . . . 56
3.5 Summary . . . 57

4 Experimental Methodology **59**
4.1 Towing tank . . . 59
4.2 Wing models . . . 61
4.3 Force balance . . . 62
4.3.1 Calibration . . . 63
4.3.2 Error . . . 63
4.4 Inertial force decomposition . . . 64
4.4.1 General equations of motion . . . 65
4.4.2 Modal vibration . . . 67
4.4.3 Combined force . . . 68
4.4.4 Calibration . . . 69
4.4.5 Note on wing vibration . . . 71
4.5 Dye flow visualisation . . . 72
4.6 Particle Image Velocimetry . . . 72

4.6.1 Implementation . . . 73
4.6.2 Measurement error estimation . . . 75
4.7 Gust rig . . . 77
4.7.1 Review of gust generators . . . 77
4.7.2 Design of the towing tank gust generator . . . 81
4.7.3 Streamwise velocity profile . . . 84
4.7.4 Flow unsteadiness . . . 85
4.7.5 Theoretical response between the real and ideal velocity profiles . . . 87
4.7.6 Spanwise velocity profile . . . 87
4.7.7 Pump operating range . . . 89
4.7.8 Assumption of two-dimensional flow . . . 90
4.8 Summary . . . 91

5 Isolating Added Mass with 2D PIV 93
5.1 Inviscid flow field model . . . 94
5.1.1 Vortex sheet components . . . 94
5.1.1.1 Circulatory 'shed vorticity' vortex sheet . . . 95
5.1.1.2 Systematic error compensation (lost circulation) . . . 96
5.1.2 Potential flow model summary . . . 98
5.2 Quantification of γ^b from PIV measurements . . . 98
5.3 Error . . . 101
5.4 Summary . . . 101

6 Translating and Rotating Plate Experiments 103
6.1 Kinematics . . . 104
6.2 Flow topology . . . 104
6.3 Flow field circulation . . . 109
6.4 Non-circulatory vortex sheets . . . 110
6.5 Instantaneous non-circulatory vortex sheet . . . 114
6.6 Impulse and forces from PIV . . . 116
6.7 Summary of findings . . . 120

7 Gust-Encounter Results 123
7.1 Gust kinematics and configurations . . . 123
7.2 Gust off . . . 124
7.3 Gust ratio 0.2 . . . 124
7.4 Gust ratio 0.5 . . . 129
7.5 Gust ratio 1.0 . . . 132
7.6 Influence of the gust outlet position on the unsteady response . . . 139
7.7 Reynolds number effects . . . 141

7.8 Isolating the boundary-layer vorticity components . . . 141
7.8.1 Approach . . . 142
7.8.2 Vortex sheets: $GR = 1.0$ . . . 143
7.9 Summary . . . 144

8 Added Mass and Wing-Gust Encounters 147
8.1 General non-circulatory vortex flows . . . 147
8.1.1 Force . . . 149
8.2 On the role of gust shear layer vorticity for a wing-gust encounter . . . 150
8.2.1 Küssner's model . . . 150
8.2.1.1 Isolation of $\gamma^{nc}_{ext.}$ . . . 151
8.2.2 Experimental wing-gust encounter . . . 153
8.2.2.1 Extracting $\gamma^{nc}_{ext.}$ using a finite measurement window . . . 154
8.2.2.2 Measurements of $\gamma^{nc}_{ext.}$: $GR = 1.0$ . . . 155
8.2.2.3 Force breakdown: $GR = 1.0$ . . . 157
8.2.3 The non-circulatory vortex growth force . . . 159
8.2.4 Application to unsteady wind and water tunnels . . . 163
8.3 Summary . . . 164

9 Conclusions and Future Work 167
9.1 General comments . . . 167
9.2 Isolating added mass effects with PIV . . . 167
9.3 Gust encounters . . . 168
9.4 Subsequent discussion on added mass and wing-gust encounters . . . 169
9.5 Recommendations and future work . . . 170

Appendix A Duhamel's Integral 173

Appendix B Extracting added mass with PIV - validation with an artificial flow field 175

References 179

List of Publications

Much of the contents of this thesis has been published in the following Journal or Conference articles.

1. Corkery, S. J., Babinsky, H., Graham, W. R. (2019). Quantification of added mass using PIV measurements for a translating and rotating flat plate (in press). *Journal of Fluid Mechanics*.

2. Corkery, S. J., Babinsky, H., Harvey, J. K. (2018). On the development and early observations from a towing tank-based transverse wing-gust encounter test rig. *Experiments in Fluids*, 59:16. doi: 10.1007/s00348-018-2586-0.

3. Simpson, C. E., Babinsky, H., Harvey, J. K., Corkery, S. (2018). Detecting vortices within unsteady flows when using single-shot PIV. *Experiments in Fluids*, 59:125. doi: 10.1007/s00348-018-2575-3.

4. Corkery, S. J., Babinsky, H. (2019). An investigation into gust shear layer vorticity and the added mass force for a transverse wing-gust encounter. *AIAA SciTech Forum*. pp 1-18.

5. Corkery, S. J., Babinsky, H. (2018). Force production mechanisms for a flat plate wing at low Reynolds numbers. *AIAA SciTech Forum*. pp 1-13.

6. Corkery, S., Babinsky, H., Harvey, J. (2018). Response of a flat plate wing to a transverse gust at low Reynolds numbers. *AIAA SciTech Forum*. pp 1-15.

7. Corkery S. J., Stevens, P. R. R. J., Babinsky, H. (2017). Low Reynolds number surge response of a flat plate wing at 90 degrees incidence. *AIAA SciTech Forum*. pp 1-16.

Nomenclature

Roman Symbols

$\mathbf{F}$	Complex, 2-dimensional force vector $\mathbf{F} = F_x + iF_y$ (N/m)
$\mathbf{r}$	Position vector (m)
$\mathbf{U}$	Complex velocity of a geometric body in the global coordinate frame($\mathbf{U} = U_X + iU_Y$) (m/s)
$\mathbf{u}$	Velocity vector (u,v,w) (m/s)
A	Area (m^2)
a	Cylinder radius (m)
a_w	Acceleration of wing (m/s^2)
$a_{v,w}$	Acceleration of wing due to vibration (m/s^2)
$b(s)$	Principle response function to a unit step input
$b_e(s)$	Effective response function
C	Constant
C_l	Lift force coefficient, 2-dimensional: $C_l = l/(\frac{1}{2}\rho U^2 c)$
C_L	3-dimensional lift force coefficient, defined for an aircraft at altitude: $C_L = L/(\frac{1}{2}\rho_0 U_e^2 S)$
d	Distance between a vortex pair (m)
$e(s)$	Forcing function
e_r	Error
f	An arbitrary function
f_{Hz}	Frequency (Hz)
$F_{x,y}$	Force components, 2-dimensional (N/m)

G	An arbitrary or unknown function
$G(s/c)$	Küssner's response function
GR	Gust Ratio: $GR = V/U$
H	Gust width (m)
i	Imaginary unit $i = \sqrt{-1}$
$I_{x,y}$	Components of impulse, or first moment of vorticity (m^3/s)
j,k	index numbers
$J_{x,y}$	Momentum per unit length (kg/s)
K	Pressure drop coefficient
k^*	Reduced frequency ($k^* = \pi fc/U$)
K_g	Gust alleviation factor
L	3-dimensional lift force (N)
l	Lift force per unit length (N/m)
L_{max}, l_{max}	Maximum lift force (N or N/m for three- and two-dimensional quantities)
m_v	Modal mass of wing (kg)
m_w	Mass of wing (kg)
m_{vt}	Virtual mass (kg)
N	An arbitrary quantity
p	Pressure (N/m^2)
Re	Reynolds Number (based on free stream velocity and chord): $Re = \rho Uc/\mu$
S	Wing planform area (m^2)
s	Convective time ($s = Ut$), where $t = 0$ is the start of motion for surging cases, or entry into the gust flow for gust cases (m)
t	Time (s)
U	Magnitude of the body or free stream velocity (m/s)
u_θ	Circumferential velocity (m/s)

U_e Equivalent air speed (m/s)

V Gust velocity (m/s)

V^{dc} Direct current voltage

V_p Peak gust velocity (m/s)

Z Complex position ($Z = X + iY$) in the global coordinate frame (m)

z Complex position ($z = x + iy$) in the local coordinate frame (m)

Greek Symbols

α Angle of incidence (radians)

β Angle (in the z-direction) between the local plate reference frame, and global reference frame (radians, unless otherwise indicated)

Ω Angular velocity vector (1/s)

ω Vorticity vector (1/s)

$\chi(s/c)$ The Wagner function

Γ Circulation (m^2/s)

γ Vortex sheet (m/s)

Γ^* Non-dimensional circulation ($\Gamma^* = \Gamma/(Uc)$)

$\Gamma^b, \Gamma^b_\infty$ Bound circulation (m^2/s), where the Γ^b_∞ represents $\Gamma^b\big|_{s/c=\infty}$

κ Doublet strength (m^3/s)

μ Dynamic viscosity (kg/(ms))

∇ Vector differential operator

ν Kinematic viscosity (m^2/s)

ϕ Velocity potential (m^2/s)

ρ Density (kg/m^3)

ρ_0 Density of air at sea level (kg/m^3)

τ Polar coordinate of the gust location in the local coordinate frame (radians)

θ Polar coordinate (radians)

υ_z Second moment of vorticity (m^4/s)

ζ Complex position ($z = \varepsilon + i\eta$) in the circle frame

c Chord length (m)

M_z Net moment per unit length of a group of fluid immersed bodies (Nm/m)

Superscripts

b Bound

$buoy.$ Buoyancy

c Circulatory

$cyl.$ Cylinder

$ext.$ External, not generated by the wing

nc Non-circulatory

w Wake

$wing$ Generated by the wing

Subscripts

in Inside the measurable field of view

mc Mid-chord

mir Mirror

n Normal

nl No load

out Outside the measurable field of view

r Rotation

t Translation

tn Tangential

x, y, z Component in the x, y, or z-direction

Acronyms / Abbreviations

AR Aspect Ratio

CUED Cambridge University Engineering Department

FFT Fast Fourier Transform

LE Leading Edge

LEV Leading Edge Vortex

MAV Micro Air Vehicle

MEMS Micro Electro-Mechanical Sensor

TE Trailing Edge

TEV Trailing Edge Vortex

UAV Unmanned Aerial Vehicle

Chapter 1

Introduction

Over a century ago the Wright brothers made history, when for 12 seconds, the *Flyer* lifted from the ground in mankind's first controlled powered flight. From these humble beginnings, aviation has since become essential for transport, geographical surveying, surveillance, search and rescue operations and for military purposes. Historically, the majority of aerodynamic research was directed toward pushing the boundaries of manned flight. The aim was to fly faster, higher, with increased payload, reliability, safety, as well as at a lower cost. Steady, high Reynolds number (*Re*) aerodynamics was key to flight, and consequently was extensively studied.

Now, attention is shifting to very small and low speed aircraft. The rapid technological development of Micro Electro-Mechanical Sensor (MEMS), and actuator systems, has enabled the development of autonomous aircraft at similar sizes to biological fliers (Petricca et al., 2011). Vehicles such as those shown in figure 1.1 may be categorised as Micro Air Vehicles (MAV), Unmanned Aerial Vehicles (UAVs), or drones. Micro air vehicles have a wing span of order 15 cm and weigh less than 200 grams (Davis et al., 1996; Grasmeyer and Keennon, 2001).

(a) Flapping wing

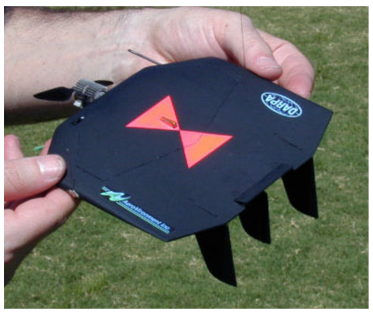

(b) Fixed wing

Fig. 1.1 Examples of flapping and fixed wing Micro Air Vehicles. After Keennon et al. (2012) and Grasmeyer and Keennon (2001).

As shown in figure 1.2, with reducing vehicle mass the optimal flight speed is also reduced. MAVs operate within the range of 10-20 m/s. The small size, portability, manoeuvrability and potentially low cost mean the devices would find significant application complementing, or even replacing, some of the services currently provided by manned aircraft. However, with reducing size comes increasing aerodynamic problems. According to Lissaman (1983), below a Reynolds number of 70,000, conventional aerofoils see a marked drop in performance due to an increasing prevalence of viscous effects. Drag is increased, the peak lift coefficient drops, and importantly, the flow is prone to separation because the boundary-layer over the suction side of the aerofoil remains laminar beyond the point at which pressure recovery commences. MAVs operate at a Reynolds number in the range of 10^4 (Petricca et al., 2011), and as a consequence, suffer from comparatively poor aerodynamic performance even in ideal or low atmospheric turbulence conditions.

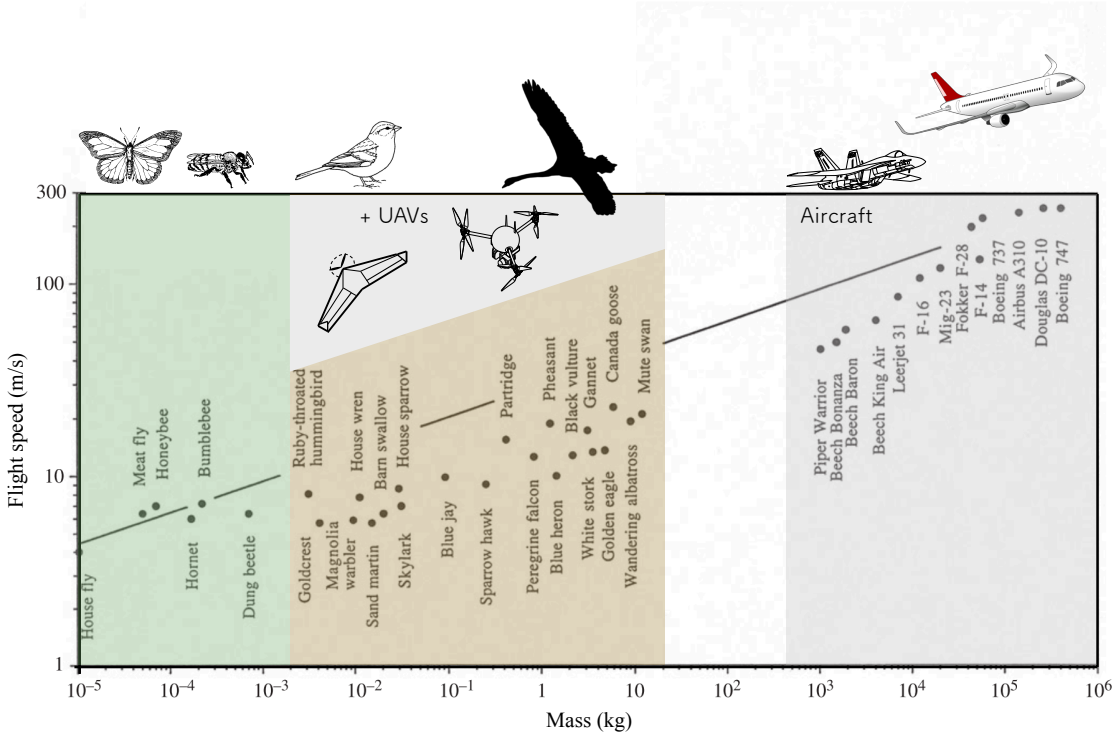

Fig. 1.2 Maximum flight speeds with mass for biological fliers, UAVs and aircraft (Bejan (2005) and references therein).

While aerofoil performance is relatively poor in ideal, steady conditions, most flight conditions are not ideal. MAVs are expected to operate at altitudes well within the atmospheric boundary-layer and fly across high shear and wake regions behind local obstructions (Watkins et al., 2006). Normal flight is anything but steady. As shown in figure 1.3, in this domain the wind turbulence intensity can exceed 50% (Mohamed et al., 2015; Walshe, 1972). Watkins et al. (2006) showed that for a typical radio aircraft sized fixed wing UAV there can be rapid changes in angle of incidence in excess of 25°, as well as spanwise variations in incidence of up to 15°. Given both poor resistance to separation,

and wild fluctuations in angle of incidence, the authors showed that MAVs are plagued by problems with attitude control. The devices consequently have poor ability to maintain a desired flight path and may experience complete loss of control (Mohamed et al., 2015, 2014; Ol et al., 2008). Reducing the MAV mass and flight speed increases the susceptibility to atmospheric disturbances (Mohamed et al., 2015; Spedding and Lissaman, 1998; Watkins et al., 2006, 2010; White et al., 2012). We will characterise the relative flow unsteadiness by the Gust Ratio (GR) parameter, defined as

$$GR = V/U, \tag{1.1}$$

which is proportional to V, the gust velocity, and inversely proportional to U, the free stream velocity or flight speed.

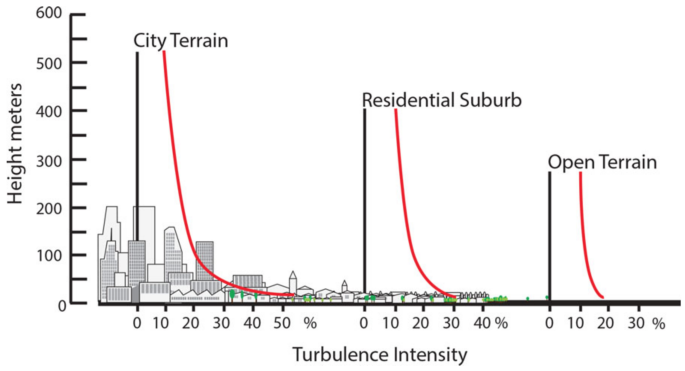

Fig. 1.3 Typical turbulence intensity of city, residential, and open terrain environments. After (Mohamed et al., 2015; Walshe, 1972).

One potential means to improve the gust performance of MAVs, is through onboard wind sensors and 'counter control' actuation. A low-order model of the fluid-dynamic response of the lifting surfaces would be invaluable, as it enables the correct control authority of actuators to be determined within millisecond timescales. The onboard sensor systems could then be utilised for gust disturbance rejection using closed loop control, and the operating wind envelope of MAVs may therefore be extended. The development of such a model requires a sound understanding of the dynamics of a wing-gust encounter.

1.1 Motivations for the present research

The motivations for this thesis, as preluded in the introductory section, stems from our desire to improve the performance of MAVs. This directs our attention to 'gusts' and the low Reynolds number regime. The aims of this work, as described later in section 2.7, are not to directly design a single model for the MAV application. Rather, we seek to learn from existing theories, modelling methods, as well as experiments, to broaden our understanding, and abilities to experimentally characterise

the flows typical of the MAV scenario. The findings described within this thesis, may therefore find application to any situation where MAV-like physics apply, namely those with strong 'added mass' and vortex dynamics effects. This incorporates the majority of unsteady aerodynamic situations, including high performance yachts, and submarines within the marine industry. The findings are relevant to the energy sector, in the design of wind and water turbines, which are subjected to turbulent flows. The general aviation industry may be a further application, particularly during take-off and landing scenarios, where low flight speeds and highly transient loads are common.

Chapter 2

Literature Review

2.1 Definition of a ‘gust’, and gust interaction

In the context of this thesis, a ‘gust’ is defined as a flow velocity perturbation, relative to a quiescent fluid, which is caused by some mechanism external to a body of interest. A gust interaction, is simply an interaction between a body with the velocity perturbation.

2.2 Origin and impact of different gust types

In this section the literature on common gust encounters is reviewed to ascertain the type, source, impact and modelling methods used to quantify the response to such interaction.

2.2.1 Gust types

Depending on the local geographical topology, time and date, the atmospheric boundary layer extends up to an altitude ranging from approximately 500 to 2,000 metres above ground level (Davies et al., 2007). Above this, there are two main gust types (or ‘atmospheric turbulence’) which aircraft experience in flight. ‘Convective’ turbulence is attributed to disturbances around thunderstorms and clouds, while ‘clear air’ turbulence is attributed to buoyant convection from localised heating, or gradients in wind velocity with altitude (Turner, 1977). General atmospheric turbulence is often described by the von Karman spectrum (Leahy, 2008; Turner, 1977) and velocity perturbations occur in directions both tangential to the aircraft path, normal to the wing planform (transverse), or spanwise (see figure 2.1). For manned fixed wing aircraft, Rhode and Lundquist (1931) argued that velocity perturbations in the direction tangential to the flight path have only a small effect on wing loading. Leishman (1996) explained that tangential velocity perturbations can usually be ignored as they produce mostly quasi-steady loading effects, and attributes the majority of the unsteady disturbances to vertical

(transverse) velocity perturbations. Spanwise velocity variations are relatively insignificant as they do not invoke a change to the aerofoil section lift (perhaps with the exception of aircraft with significantly swept wings). At the lower levels of the atmosphere, well within the atmospheric boundary-layer we find flows typical of urban and city environments. These are characterised by low mean wind speeds, but high turbulent fluctuations (Watkins et al., 2006). The flow can experience sudden changes in wind speed and direction due to high surface roughness, instabilities and interactions with local obstructions (Evans et al., 2017). A static measurement probe situated somewhere in this environment will record significant random fluctuations in velocity, but there can additionally be coherent structures shed from an object within the flow field. It is in this region which biological fliers and MAVs reside. Many authors have attributed the transverse gust component, acting asymmetrically across the wing span, to the roll instability of MAVs (Mohamed et al., 2015, 2014; Ol et al., 2008; Watkins et al., 2006).

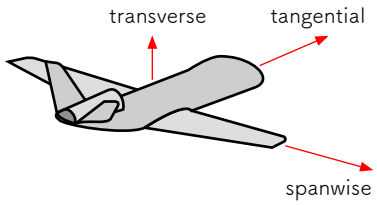

Fig. 2.1 Schematic showing the potential directions of a gust velocity perturbation relative to an aircraft.

A wind gust need not be the result of atmospheric turbulence at all. An aircraft flying through a second aircraft's wake, can also experience changes in velocity due to trailing vortices. During forward flight of helicopters or tilt-rotor aircraft, the tip vortices from the upstream blades are advected downstream and can interact with the following blades (Leishman, 2000). A military aircraft landing on an aircraft carrier can experience large-scale vortical structures shed from the ship body and superstructure. It is apparent that there is no one gust type or shape applicable to all situations. Little emphasis is therefore placed on the source of the wind gust. Transverse gusts, however, appear to be the most problematic from the perspective of flight stability, given they induce a change to the angle of incidence, and may incite separation. They will therefore be the focus of this work. Note, however, that it is later argued in section 8.1, that a 'gust' is must always be accompanied by a free vorticity field. The analytical treatment of a body, in response to this vorticity field, is identical regardless of whether the gust flow velocities acts in the 'longitudinal' or 'transverse' directions relative to the body.

2.2.2 Transverse gust models for aircraft design

The response of aircraft to transverse wind gusts have been studied since the 1930s, with the objective of determining peak structural loads for design purposes. While gusts attributed to atmospheric

turbulence have a random structure, early models used simple geometrically shaped 'discrete' gust velocity profiles. Each discrete model requires knowledge of the gust magnitude, shape, period and frequency of occurrence (Donely, 1950; Frost and Turner, 1982). One of the first adopted by Rhode and Lundquist (1931) was 'sharp edged'. The profile was decided upon because *"abrupt bumps are frequently encountered wherever bumps are found"*, thereby indicating that the true velocity gradient was somewhat steep. At the time little was known about the structure of the atmosphere. Later a linear ramp gust velocity profile was defined, while from the 1950s to today a 1-minus-cosine gust shape is used (Flomenhoft, 1994). From Noback (1986), the velocity (V) of the 1-minus-cosine gust shape is defined by

$$V(t) = \frac{V_p}{2}\left(1 - \cos\frac{2\pi U t}{H}\right). \tag{2.1}$$

The term, H, is equal to the distance of 25 geometric wing chords*, V_p is a prescribed, altitude dependent gust magnitude, U is the (true) flight speed, and t is the time since entry into the gust disturbance. It should be noted that the intent of the 1-minus-cosine gust profile is not to provide a 'true' description of gust velocities, rather, the profile serves as an idealised description of a gust for which the gust design loads on aircraft may be approximated based on acceleration measurements from existing aircraft. New aircraft are designed to withstand the peak loads experienced during entry into this 1-minus-cosine gust. From Pratt (1953) and Noback (1986), the peak lift force on an aircraft constrained to motion only in the vertical direction, is

$$\overbrace{\Delta L_{max}}^{\text{peak lift increment}} = \overbrace{\Delta C_L \frac{1}{2}\rho_0 U_e^2 S K_g}^{\text{reference lift}}. \tag{2.2}$$

The ρ_0 term is the air density at sea level, S is the wing planform area, and U_e is the equivalent aircraft velocity†. The three-dimensional lift coefficient is defined as, $C_L = L/(\frac{1}{2}\rho_0 U_e^2 S)$. Assuming small gust ratios, the change in this lift coefficient is $\Delta C_L = \frac{dC_L}{d\alpha}\frac{V_p}{U_e}$, where α is the angle of incidence.
Of primary interest is K_g, the gust alleviation factor. This variable scales the reference lift term to account for both the geometry of the gust profile, aircraft mass and wing section characteristics. Most importantly, it additionally accounts for the delay in the lift response of the aircraft due to unsteady aerodynamic effects. These unsteady effects are based on the solution for a wing of infinite aspect ratio encountering a 'sharp edged' gust of infinite extent (Pratt, 1953). This is Küssner's model, a classical theory described further in section 2.3.4.3.

Since the mid 1950s, a second method for determining gust loading was developed using power spectra techniques. For the implementation described by Noback (1986), atmospheric turbulence is modelled as a quasi-stationary Gaussian process, while the aircraft is modelled as a linear spring

*According to Noback (1986), this gust length was set arbitrarily.

†The aircraft velocity at sea level for which the aircraft will experience the same dynamic pressure as the actual aircraft velocity at altitude (Anderson, 2011).

mass system. Force and structural loads on the aircraft are calculated by superimposing aerodynamic forces with those attributed to structural vibration. Aerodynamic loads are often calculated using panel code implementations (Turner, 1977). The loading on each panel is regulated by the classical Wagner, Küssner or Theodorsen unsteady aerodynamic functions. Today both the 1-minus-cosine and power spectra methods are used for aircraft certification (Federal Aviation Administration, 2014). The classical unsteady theories are therefore still highly relevant for modern aircraft design.

2.3 Classical aerodynamics

The previous section highlighted the use of classical unsteady aerodynamic models for the design of modern aircraft. Next, in section 2.3.1 fundamental fluid-mechanic concepts are outlined to ease the reader into some of the more difficult problems. These are referred to heavily throughout this thesis. Afterward, classical steady and later unsteady models are reviewed to highlight key lift production mechanisms, simplifying assumptions, as well as the more general 'mathematical tools' used to acquire a solution to each kinematic problem. This knowledge is essential to understand the flow physics of the relatively complicated high amplitude wing-gust encounters.

2.3.1 Fundamental concepts

2.3.1.1 Continuity and the momentum equations

Given the intended applications for this work (MAVs and landing aircraft), only low speed flows are considered. Below a Mach number of 0.30 in air, variations in density are less than 5% and may be considered as incompressible Lighthill (1986). Pressure waves travel at sufficient speed that they can be considered to propagate instantaneously relative to the velocities of the fluid. For such a case, the continuity equation is

$$\nabla \cdot \mathbf{u} = 0, \tag{2.3}$$

where $\mathbf{u}$ is the velocity vector field. For an infinitesimally small element of an incompressible Newtonian fluid, the equations of motion are given by the momentum or Navier-Stokes equations (Anderson, 2011). In vector form and ignoring body forces, the momentum equation may be written as

$$\rho \frac{D\mathbf{u}}{Dt} = \overbrace{-\nabla p}^{\text{pressure}} + \overbrace{\mu \nabla^2 \mathbf{u}}^{\text{shear stress}}, \tag{2.4}$$

where p is the scalar pressure field and μ is the dynamic viscosity. The term on the left-hand side is the product of the fluid density and the material derivative of velocity, or acceleration of a fluid 'particle' moving with the flow field (mass per unit volume $\times$ acceleration). The terms on the right

hand side make up the net force on the fluid element due to pressure and shear stresses. For an inviscid fluid $\mu = 0$, and the momentum equation is known as the Euler equation,

$$\rho\left(\frac{\partial \mathbf{u}}{\partial t} + \mathbf{u}\cdot\nabla\mathbf{u}\right) = -\nabla p. \tag{2.5}$$

2.3.1.2 Vorticity and the vorticity transport equation

While the Navier-Stokes equations define the dynamics of a fluid element in a linear sense, the vorticity transport equation defines the angular motion. Vorticity, defined as $\omega = \nabla \times \mathbf{u}$ is a measure of the rotation of a fluid element. If a spherical element of fluid is rotating with angular velocity Ω in a rigid body manner, then the vorticity is defined as twice the angular velocity $\omega = 2\Omega$ (Lighthill, 1986).

From Wu (1981), the vorticity transport equation may be found by taking the curl of each term in the Navier-Stokes equation

$$\frac{D\omega}{Dt} = (\omega\cdot\nabla)\mathbf{u} + \nu\nabla^2\omega, \tag{2.6}$$

where $\nu = \mu/\rho$, the kinematic viscosity. The first term on the right hand side describes the effect of the vortex stretching and tilting. The second term describes diffusion of vorticity because of viscosity. For an inviscid fluid, the diffusion term vanishes, and vorticity may only be transported by advection (it is 'carried' with the flow). Importantly there is no vorticity 'source' term in the transport equation (Wu, 1981). Vorticity may only enter the flow field through diffusion at a boundary (as there may be no advective transport through a surface). Saffman (1992) also describes a process whereby a topological change is imposed to a region of an inviscid flow field, resulting in the creation of distributions of sheets of vorticity. This mechanism is described for an inviscid fluid, but it is presumably equally valid for a viscous fluid, albeit the vorticity is free to diffuse into the surrounding flow. Durand (1935) describes a similar mechanism whereby impulsive, and continuous pressures are applied to a circular region of flow. This results in the formation of a singular, or series of ring vortices away from physical boundaries.

2.3.1.3 Potential flow

From Anderson (2011), a potential flow is one that is defined as inviscid, incompressible and irrotational. For an irrotational flow the vorticity is

$$\omega = \nabla\times\mathbf{u} = 0. \tag{2.7}$$

The velocity field is often expressed as the gradient of the potential function Φ

$$\mathbf{u} = \nabla\Phi, \tag{2.8}$$

which substitued into the continuity equation, (2.3), yields

$$\nabla^2\Phi = 0. \tag{2.9}$$

The stream function, ψ, is orthogonal to the potential function. It is constant along a streamline, and is defined such that the difference between the stream function at any two given points $\Delta\psi = \psi_2 - \psi_1$ is equal to the volume flow rate passing across a line drawn between each point. If this line is given by the elemental, two-dimensional vector **dl**, the incremental change to the stream function is

$$\begin{aligned} d\psi &= \mathbf{u} \times \mathbf{dl} \\ &= udy - vdx. \end{aligned} \tag{2.10}$$

Since the total derivative is $d\psi = \frac{\partial\psi}{\partial x}dx + \frac{\partial\psi}{\partial y}dy$, we have

$$\frac{\partial\psi}{\partial y} = u, \qquad \frac{\partial\psi}{\partial x} = -v. \tag{2.11}$$

Substituting equations (2.11) into (2.7) gives

$$\nabla^2\psi = 0. \tag{2.12}$$

Both equations (2.9) and (2.12) are in the form of Laplace's equation, a second order, linear, partial differential equation. The solutions to Laplace's equation may be linearly superimposed as a result. This point will be utilised to construct (and deconstruct) complex flow fields.

2.3.1.4 The steady and unsteady Bernoulli equations

In potential theory the unsteady Bernoulli equation relates a distribution of 'excess' pressure in terms of a dynamic and transient contribution (Lighthill, 1986). Starting with the Euler equation

$$\rho\left(\frac{\partial\mathbf{u}}{\partial t} + \mathbf{u}\cdot\nabla\mathbf{u}\right) = -\nabla p,$$

for an irrotational flow, $\mathbf{u}\cdot\nabla\mathbf{u} = \frac{1}{2}\nabla|\mathbf{u}|^2$ (Lighthill (1986)). With the definition for the potential function, equation (2.8), the Euler equation can be written in the form

$$\nabla\left(\rho\frac{\partial\Phi}{\partial t} + \frac{1}{2}\rho|\mathbf{u}|^2 + p\right) = 0. \tag{2.13}$$

Since the spatial gradients of the term within the brackets is zero, everywhere through the flow field

$$\overbrace{\rho\frac{\partial\Phi}{\partial t}}^{\text{transient}}+\overbrace{\frac{1}{2}\rho|\mathbf{u}|^2}^{\text{dynamic}}+\overbrace{p}^{\text{static}}=f(t), \tag{2.14}$$

where $f(t)$ is an arbitrary function of time. For flow fields that are time independent, i.e. steady, the transient potential term is zero. The steady Bernoulli equation is

$$\frac{1}{2}\rho|\mathbf{u}|^2+p=f. \tag{2.15}$$

This shows that an increase in the flow velocity will result in a corresponding decrease in the static pressure. For symmetric flows about, say, a circular cylinder, the flow velocities either side are equal. On the upstream and downstream surfaces the static pressures balance, therefore there will be zero drag. The equivalent flow about a cylinder in a real (viscous) fluid will, however, have a drag force. This is famously known as d'Alembert's paradox, which illustrates that viscous stresses are responsible for steady state drag (Anderson, 2011). We note that in unsteady cases the transient term of the unsteady Bernoulli equation adds an additional pressure contribution. This means the net pressure drag on a body in unsteady inviscid fluid may not necessarily be zero. This gives rise to a phenomenon known as added mass, which will be discussed further in section 2.3.4.1.

2.3.1.5 Circulation and the Kutta-Joukowski theorem

Kelvin (1869) showed that if a closed curve is taken around a region of an inviscid fluid, and constrained to move with the same fluid particles such that the geometry of the curve may change with time, a quantity called circulation (Γ), is conserved. Circulation is defined by

$$\Gamma=\oint\mathbf{u}\cdot\mathbf{dl}, \tag{2.16}$$

where **dl** is a vector segment of the curve. Physically the circulation is a measure of the sum of vortex strengths on and within the closed curve (Anderson, 2011). For viscous fluids, circulation is approximately conserved if the closed curve avoids crossing over regions where shear stresses are important (Lighthill, 1986). Wu (2018) explains that the circulation may only change due to vorticity transport through diffusion between fluid inside, and outside the curve. This is simply because there may be no advective vorticity transport across the dividing curve, as it moves with the fluid. Furthermore, if the curve is drawn large enough, circulation will always be conserved after a finite time as vorticity may advect and diffuse only a finite distance in the flow field. The closed curve may therefore be taken around this rotational region, through fluid that is entirely irrotational. Circulation is therefore conserved even in a viscous fluid.

The circulation about a body within a steady flow field is famously related to the lift force acting on the body. This is known as the Kutta-Joukowski theorem (Anderson, 2011; Durand, 1935),

$$l = -\rho U \Gamma \tag{2.17}$$

where l is the lift per unit length. Given that this work is directed at investigating the gust response of an aerofoil, as an example we will next consider the relationship between circulation and the lift force for the aerofoil geometry in a viscous fluid.

In steady state conditions the aerofoil must travel at a constant velocity. Furthermore, for reasons discussed later in section 2.3.4.2, at a very large distance behind the wing there must be a starting vortex. This is illustrated in figure 2.2. On the surface of the aerofoil the no-slip condition means there is a shear stress acting on the fluid adjacent to the aerofoil surfaces (aside from at the stagnation points, and assuming no flow separation). The shear stress 'rotates' the fluid, thereby generating vorticity on the surface. This vorticity diffuses into the surrounding flow at such a rate that it balances that advected from the surface. This results in a finite thickness, time invariant vorticity layer 'bound' to the surface (Lighthill, 1986). The net circulation of the aerofoil is the result of an imbalance of positive and negative vorticity contained within this boundary-layer. This is referred to as 'bound circulation' (Durand, 1935). While usually used to describe only steady flows, in the context of this thesis the term bound vorticity and circulation will be used even in unsteady cases.

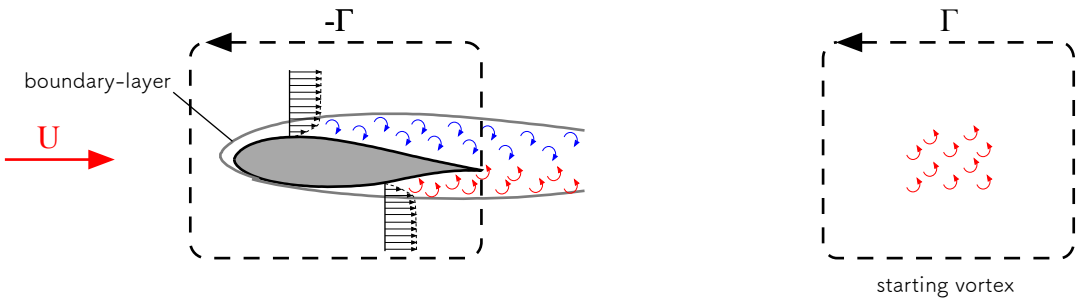

Fig. 2.2 Schematic of the starting vortex formed behind a lifting aerofoil section, at an angle of incidence.

The lift force may be calculated from the bound circulation and equation (2.17). This is equivalent to the force that would be obtained from the surface pressure and shear stress. For high Reynolds number flows, the pressure may be approximated as that from potential flow theory, determined from the steady Bernoulli equation [‡].

[‡]For a viscous fluid, the Bernoulli equation applies exactly in the irrotational flow outside the viscous boundary-layer. If the Reynolds number is high, the thickness of the boundary-layer is small, has little effect on the curvature of the inviscid outer flow, and the pressure outside the boundary-layer is close to that on the surface of the aerofoil.

2.3.1.6 Vortex force

The aerofoil example demonstrates a link between a force on the flow field and circulation. As was shown by the Navier-Stokes equations, a force can only be applied to an element of fluid by a pressure or shear stress[§]. The circulation provides a convenient 'shortcut' to enable the net force on the fluid to be determined. For an inviscid fluid the Biot-Savart law provides a link between circulation and flow velocity (Saffman, 1992). This is defined as

$$\mathbf{du} = \frac{\Gamma}{4\pi}\frac{\mathbf{dl}\times\mathbf{r}}{|\mathbf{r}|^3}, \tag{2.18}$$

where **du** is a vector increment in velocity at some point (say j) in the flow field, **dl** is an element of a vortex filament, while **r** is a vector from the vortex element to j. In two dimensions, the Biot-Savart law reduces to $u_\theta = \Gamma/(2\pi|\mathbf{r}|)$, where u_θ is orthogonal to the vector **r**. With the velocity, the momentum and kinetic energy of the flow is known, therefore force and work may be calculated. Lamb (1895) derived the net momentum (J) for a flow field with two equal and opposite point vortices, separated by the distance d, as illustrated in figure 2.3. Per unit length,

$$J = \rho\Gamma d. \tag{2.19}$$

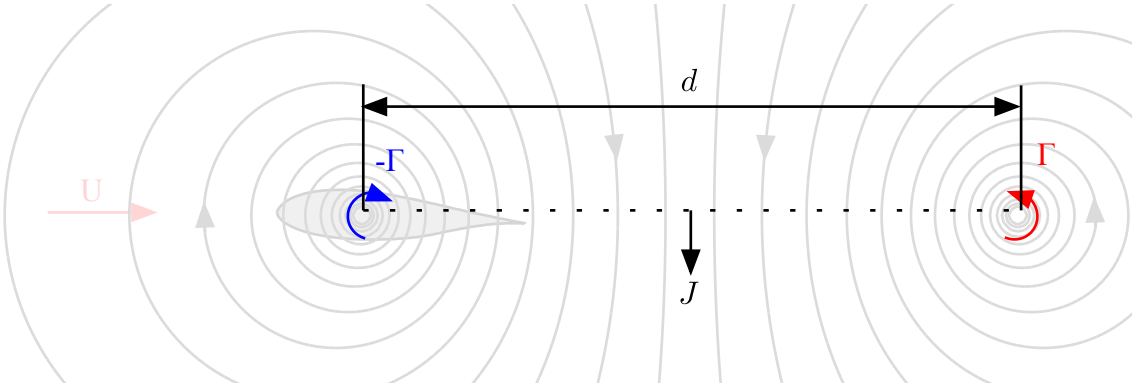

Fig. 2.3 Streamlines between a pair of complementary point vortices. At steady state a wing may be approximated by a point vortex.

This acts vertically downward. Since a force is equal to the time rate of change of momentum $F = dJ/dt$, the net force on a flow field with two equal and opposite point vortices is

$$F = \rho(\dot{\Gamma}d + \Gamma\dot{d}), \tag{2.20}$$

where $\dot{()} \equiv d/dt$, as per Newton's notation. From equation (2.20) it can be seen that a force must be applied to the flow field if the pair of vortices are to either grow in strength ($\dot{\Gamma} \neq 0$), or have finite circulation and advect away from one another $\dot{d} \neq 0$. This is referred to as a 'vortex force' (Li and Wu,

[§]Ignoring body forces.

2016). Now if the aerofoil example is reconsidered. At steady state, the aerofoil and starting vortices may be approximated by the point vortices illustrated in figure 2.3. The lift force experienced by the wing must be equal and opposite to the vortex force. Since the rate of change of distance between each vortex is the velocity of the wing ($\dot{d} = U$)[¶], and circulation is time invariant ($\dot{\Gamma} = 0$), the lift force on the aerofoil may be calculated from equation (2.20). This gives

$$l = -F = -\rho U \Gamma. \tag{2.21}$$

The Kutta-Joukowski result is therefore recovered. This is referred to as the 'vortex lift' (Stevens, 2013) or 'circulatory lift' (Pitt Ford, 2013).

2.3.1.7 General impulse methods

Lamb's result is but one specific case of a general vortical flow. Wu (1981) showed that a solution for any general incompressible flow problem may be found entirely from the circulatory flow region. He subsequently derived a general theory that relates forces, whether that be lift, drag or moments on an arbitrary number of bodies within a viscous, or inviscid, flow field to the rate of change of vorticity moments. Here we briefly review some of the key concepts of his theorem.

Wu considers the problem of an infinite flow field in two-dimensions[‖], with an arbitrary number (N) of bodies (each indexed j), of cross sectional area A_j, at finite locations. Initially the flow field and bodies are at rest. In his theorem, each body is treated as a continuum with the surrounding fluid. Translation of a body creates a distribution of vorticity, initially confined to a boundary-layer on the surface of the body; rotation results in the interior acquiring a vorticity with magnitude equal to twice the rigid-body angular velocity, as well as boundary-layer vorticity. Since each body is represented by a region of fluid with externally prescribed rigid-body kinematics, they do not follow Helmholtz's second law of motion, which requires vortex lines to move with the fluid (Saffman, 1992). Wu showed that with increasing distance from each body, the strength of any vorticity in the flow field decays toward zero. The vorticity must therefore be confined to a finite spatial region after a finite time period.

For such a flow field the impulse in the x and y directions is defined as the first moment of vorticity

$$I_x = \int_A y\omega_z dA, \qquad I_y = -\int_A x\omega_z dA. \tag{2.22}$$

The net aerodynamic force on the bodies is related to the impulse by

$$F_x = -\rho \frac{dI_x}{dt} + \rho \sum_{j=1}^{N} \frac{d}{dt} \int_{A_j} u_j dA, \qquad F_y = -\rho \frac{dI_y}{dt} + \rho \sum_{j=1}^{N} \frac{d}{dt} \int_{A_j} v_j dA, \tag{2.23}$$

[¶]After a long time period, flows induced by the wing onto the starting vortex will diminish to zero. It will therefore advect relative to the wing at the free stream velocity.

[‖]Expressions for three-dimensional flows are also derived, but are not considered here.

where u_j and v_j are the x and y rigid-body components of velocity[**]. The integral term in equations (2.23) represent an inertial 'correction' force. This is equal to the mass of the volume of fluid displaced by the body, accelerating at a rate equal to the body. The term arises because the fluid and each body were considered a continuum, with constant density. To accelerate the fluid represented within each body, a force must be applied, which is included in the $-\rho dI/dt$ terms. The integrals therefore correct for this fictitious force.

A similar expression was derived for the net moment acting on the bodies. The second moment of vorticity, υ_z, for a continuous vorticity field is

$$\upsilon_z = \int_A (x^2 + y^2)\omega_z dA. \tag{2.24}$$

This is related to the first moment of impulse (J_z) by

$$J_z = -\frac{1}{2}\upsilon_z. \tag{2.25}$$

The net moment, per unit length, on the bodies is

$$M_z = -\rho\frac{dJ_z}{dt} + \rho\sum_{j=1}^{N}\frac{d}{dt}\int_{A_j}(xv_j - u_j y)dA. \tag{2.26}$$

Once again the second term accounts for the fluid displaced by the body. Equations (2.23) and (2.26) are useful as, provided that the vorticity field and body kinematics are quantifiable, the net aerodynamic force and moment can be determined for any unsteady, two-dimensional flow. The formulation incorporates forces attributed to both surface shear stresses and pressure. The equations do not, however, indicate where this vorticity should be generated, or at what rate (except for the rigid body vorticity). To predict the forces on a flow field, the dynamics of vorticity must therefore be determined, such that Wu's impulse relations can be applied.

2.3.2 Steady thin airfoil theory

In the 1920s, Munk, Birnbaum and Glauert derived the thin airfoil theory to predict the performance of aerofoils in steady flow (Anderson, 1997, 2011). Here the fundamental principles of the theory are briefly reviewed, before approaching the more complex unsteady problems. In thin airfoil theory it is assumed that an aerofoil of finite thickness, in a viscous fluid, may be replaced with a single distribution of vorticity at the camber line. Physically this vortex sheet is a representation of vorticity that would be contained within the boundary-layers either side of the aerofoil (Durand, 1935), as illustrated in figure 2.4a. This bound vorticity (γ^b, with the superscript b reading 'bound'), is equal to

[**]In the original paper the fluid density ρ before the $dI_{x,y}/dt$ term appears to be absent. Dimensional checks indicate this to be in error.

the difference in the velocity either side of the plate

$$\gamma^b = u_2 - u_1. \tag{2.27}$$

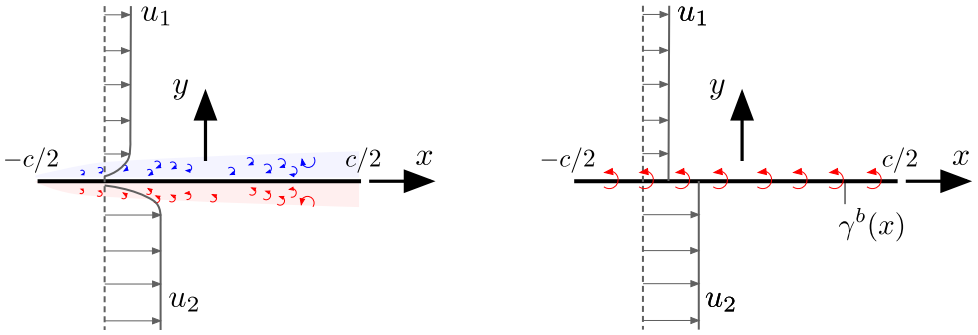

(a) Boundary layers **(b)** Vortex sheet

Fig. 2.4 Representation of boundary-layers as a vortex sheet.

Two boundary conditions determine the strength of this bound vortex sheet. The first condition: flow induced by the vortex sheet, as given by the Biot-Savart law, must be such that there is no-net flow through the vortex sheet. This is the no-penetration condition, which requires the camber line of the thin airfoil, or in this thesis a flat plate wing, to be a streamline of the flow. The second condition: at the sharp (or cusped) trailing edge, the steady Kutta condition requires flow to leave tangential to the edge (Xia and Mohseni, 2016). In a viscous fluid, the flow is unable to travel around a sharp corner as doing so would require the boundary-layer to withstand an infinitely strong adverse pressure gradient. Instead the flow separates. In the inviscid representation of the flow, the velocities (and pressure) either side of the sharp edge are finite and equal, and the strength of the vortex sheet (γ^b) is zero. There is therefore no shedding of vorticity into the wake (Poling and Telionis, 1986).

From Anderson (2011), for an un-cambered flat plate wing at a small angle of incidence, the bound vortex sheet is

$$\gamma^b(x) = -2\alpha U \frac{\sqrt{\frac{c}{2}-x}}{\sqrt{\frac{c}{2}+x}} \qquad \text{for } -\frac{c}{2} \leq x \leq \frac{c}{2}, \tag{2.28}$$

where c is the chord length, and x is the distance from the mid-chord ($x = -c/2$ at the leading edge and $x = c/2$ at the trailing edge). The bound circulation is

$$\begin{aligned} \Gamma^b &= \int_{-c/2}^{c/2} \gamma^b dx \\ &= -\pi\alpha c U. \end{aligned} \tag{2.29}$$

From the Kutta-Joukowski theorem (equation 2.17), the lift force and coefficient are

$$l = \pi\rho\alpha c U^2, \tag{2.30}$$

$$\begin{aligned} C_l &= \frac{l}{\frac{1}{2}\rho U^2 c} \\ &= 2\pi\alpha. \end{aligned} \tag{2.31}$$

From equation (2.30), it can be seen that in steady flow conditions, lift is dependent only on the angle of incidence and the free stream velocity. This result is only because of the steady flow assumption inherent in the Kutta-Joukowski theorem; the wing (or free stream) velocity U and angle of incidence are constant, and the wing is a large distance from the starting vortex.

2.3.3 Quasi-steady thin airfoil theory

In 'quasi-steady' thin airfoil theory, the 'steady' assumptions are partially relaxed. Pitt Ford (2013) describes the forces derived from quasi-steady thin airfoil theory as those equivalent to steady motion adjusted to the same instantaneous velocity and angle of incidence. When the wing changes circulation, vorticity must be shed into the flow field to conserve circulation. It is assumed that downwash induced onto the wing from vorticity in the wake is negligible compared to the flow component resulting from the free stream and kinematic motion. It is additionally assumed that added mass effects are insignificant. In the formulation described by Leishman (2000), the motion of the airfoil is decomposed into two contributions. For the first kinematic motion, the airfoil is 'plunged' in the negative y-direction with a velocity V, thereby changing the angle of incidence uniformly across the chord. For the second motion, the airfoil is pitched about an arbitrary pivot point, resulting in a non-uniform change in the angle of incidence across the wing. This is often called 'virtual camber', as the change in incidence is equivalent to that of a cambered aerofoil travelling at constant velocity. The lift coefficient is

$$C_l = 2\pi\Big[\alpha + \overbrace{\frac{V}{U}}^{\text{plunge}} + \overbrace{\frac{c}{2}\Big(\frac{1}{2} - \frac{2x_m}{c}\Big)\frac{\dot{\alpha}}{U}}^{\text{pitch}}\Big], \tag{2.32}$$

where x_m is the distance to the pitch axis from the mid-chord, and V, in this context is the plunge velocity.

2.3.4 Unsteady models

The classical unsteady models incorporate the velocities induced onto the aerofoil by vorticity in the wake, as well as added mass effects. From Leishman (2000), closed form solutions were derived by:

- **Wagner:** Impulsively accelerated wing at small incidence;
- **Theodorsen:** Harmonically pitching and plunging wing with steady free steam;

- **Küssner:** Wing at zero incidence entering a sharp edged transverse gust of infinite extent;
- **Sears:** Wing at zero angle of incidence moving through a sinusoidal transverse gust field.

Küssner's sharp edged gust model is most representative of the large amplitude wing-gust encounters considered in this work, however, the wake effects of Küssner's model originate from Wagner's theory. Both theories include added mass effects. First the literature on added mass will be reviewed, followed by the Wagner and Küssner models.

2.3.4.1 Added mass (a non-circulatory force)

Added or virtual mass is an unsteady fluid dynamic effect that has been discussed in the literature for over a century (see Benjamin (1986); Brennen (1982); Darwin (1953); Lamb (1895); Saffman (1992)). It describes an increase in the force required to accelerate a body at a given rate when immersed in a fluid compared to the equivalent kinematics in a vacuum. While the mass of the body is unchanged whether surrounded by fluid (or not), Darwin (1953) showed that a physical volume of fluid is 'carried' by a body during its motion in potential flow. This is called the 'drift volume', the mass of which corresponds to the added mass.

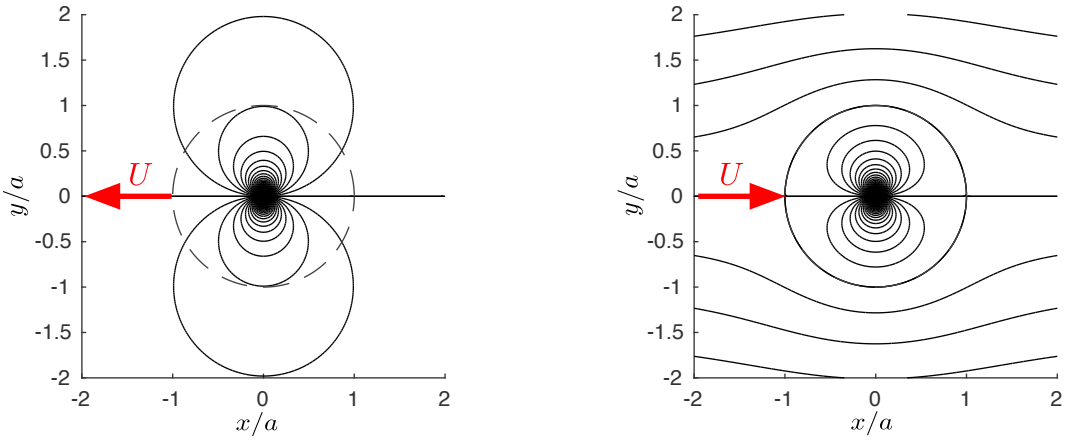

(a) Moving cylinder frame

(b) Fixed cylinder frame

Fig. 2.5 Comparison of the potential flow stream function for flows past a circular cylinder in the cylinder fixed, and moving reference frames.

The flow about a circular cylinder is the canonical added mass case. For a cylinder of radius a, moving from right to left with a velocity of magnitude U, the potential function is equal to that of a source-sink doublet with a strength $\kappa = 2\pi U a^2$. This case is illustrated in figure 2.5a. The potential

function and its time derivative on the surface of the cylinder are

$$\Phi|_{r=a} = Ua\cos\theta \tag{2.33}$$

$$\left.\frac{\partial\Phi}{\partial t}\right|_{r=a} = \frac{dU}{dt}a\cos\theta, \tag{2.34}$$

respectively, where θ is measured anticlockwise from the positive x-axis. Taking the unsteady Bernoulli equation, (2.14), and rearranging for the static pressure gives

$$p = -\rho\frac{\partial\Phi}{\partial t} - \frac{1}{2}\rho|\mathbf{u}|^2 + f(t). \tag{2.35}$$

The net force on a body may be found from the surface pressures,

$$\mathbf{F} = -\oint_a p\mathbf{n}dl, \tag{2.36}$$

where $\mathbf{F}$ is the pressure force vector, $\mathbf{n}$ is a complex, surface normal unit vector ($\mathbf{n} = \cos\theta + i\sin\theta$ for a cylinder). The force is therefore,

$$\mathbf{F} = \rho\oint_a\left(\frac{\partial\Phi}{\partial t} + \frac{1}{2}|\mathbf{u}|^2 - \frac{1}{\rho}f(t)\right)\mathbf{n}dl. \tag{2.37}$$

Note that an elemental length about the circumference is $dl = ad\theta$, and due to symmetry the $|\mathbf{u}|$ and $f(t)$ terms, as well as all forces in the y-direction integrate to zero. The net force in the x-direction is

$$F_x = \rho a\int_0^{2\pi}\frac{\partial\Phi}{\partial t}\cos\theta d\theta. \tag{2.38}$$

Substituting equation (2.34) into (2.38), and evaluating the integral gives

$$F_x = \rho\pi a^2\frac{dU}{dt}. \tag{2.39}$$

A force is therefore applied to the cylinder that is proportional to the acceleration[††]. The terms preceding dU/dt are the fluid 'added' or 'virtual' mass. The phenomenon may be explained as follows. If the fluid and cylinder are both initially at rest, and the cylinder is accelerated, then the surrounding fluid must also accelerate to accomodate the changing velocity of the cylinder. This gives rise to the flow fields shown in figure 2.5a. The acceleration is actioned by pressure waves that propagate from the cylinder surface, at infinite speed for an incompressible fluid. A difference in surface pressures across the upstream and downstream sides of the cylinder generates a net force. The flow field experiences a net change in momentum to match the impulse (in the classical mechanics sense) applied to the cylinder; equivalently the kinetic energy of the flow is changed to match the

[††]Here it is a 'coincidence' that the added mass term is equal to the displaced volume of the cylinder. For other geometries this will not necessarily be the case.

work done. This change only occurs when the velocity of the body is altered.

Equation (2.39) was derived for a cylinder accelerating in an otherwise quiescent fluid. In figure 2.5b the cylinder is at rest, and the flow field is accelerated from left to right. Here the forces on the flow field are not equivalent to the accelerating cylinder case. The potential function is equal to the sum of a doublet, again with strength $\kappa = 2\pi U a^2$, plus an additional uniform free stream term (Anderson, 2011). On the surface of the cylinder,

$$\Phi|_{r=a} = 2Ua\cos\theta, \tag{2.40}$$

which is twice the magnitude for the accelerating cylinder case. The force is therefore

$$F_x = 2\rho\pi a^2 \frac{dU}{dt}. \tag{2.41}$$

Brennen (1982) and Granlund et al. (2014) explain that the difference is attributed to a buoyancy force. Taking the x-component of the Euler equation (2.5),

$$\rho\frac{\partial U}{\partial t} = -\frac{\partial p}{\partial x}, \tag{2.42}$$

there must be a pressure gradient through the flow field in order to accelerate the free stream. Integrating (2.42) with respect to x gives

$$p = -\rho\frac{\partial U}{\partial t}x + C, \tag{2.43}$$

where C is the constant of integration. Substituting (2.43) into (2.36), noting that along the surface of the cylinder $x = a\cos\theta$, and evaluating the integral gives

$$F_x^{\text{buoy.}} = \rho\pi a^2 \frac{dU}{dt}. \tag{2.44}$$

This is of course equal to the mass of the volume (per unit length) of the fluid displaced by the cylinder, scaled by the acceleration of the flow field. The origin of the force is analogous to buoyancy in hydrostatics. In addition, the term is coincidently equal in magnitude to the added mass force, thereby accounting for the doubling of the force between the accelerating cylinder and accelerating flow field cases.

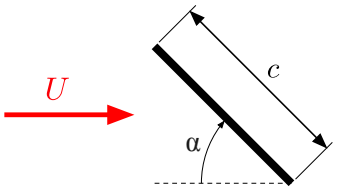

Fig. 2.6 Flow streaming past a flat plate wing at an angle of incidence of α.

Added mass effects can arise for a body with any (and variable) geometry. Within the Wagner and Küssner models, the added mass component is calculated for a flat plate. Using the unsteady surface pressures, Pitt Ford (2013) derived the added mass component of the lift and drag forces for flow streaming past a plate at a fixed angle of incidence. This is illustrated in figure 2.6. The result is

$$F_x = \rho\pi\frac{c^2}{8}\frac{dU}{dt}(1-\cos 2\alpha) \tag{2.45}$$

$$F_y = \rho\pi\frac{c^2}{8}\frac{dU}{dt}\sin(2\alpha). \tag{2.46}$$

Since the plate has zero thickness, the net force must act perpendicular to the chord and have a magnitude proportional to the relative acceleration of the fluid in the plate normal direction. Resolving F_x, F_y and the velocity U, into the plate normal direction (U_n) gives

$$F_n = \overbrace{\rho\frac{\pi c^2}{4}}^{\text{added mass}}\frac{dU_n}{dt}. \tag{2.47}$$

The corresponding flow topology is shown in figure 2.7a. The added mass is equal to the mass per unit length of a cylindrical volume of fluid with a diameter equal to the chord. Pitt Ford (2013) further explains that, unlike the cylinder flows, the forces on the plate are equivalent for the accelerating flow field and accelerating body cases. This is because the volume displaced by a plate of infinitesimal thickness is zero, therefore there is no buoyancy force. The argument further suggests that the added mass force on a stationary body in an accelerating flow is indeed the same as that of a body accelerating. If the body has volume one simply needs to add the buoyancy term. We will challenge this later in Chapter 8. In figure 2.7b, the streamlines about a flat plate wing rotating about the mid-chord are shown. This illustrates that the fluid must further be accelerated when a body undergoes rotational motion, therefore added mass effects can be expected here also. This is discussed in more detail in Chapter 3.

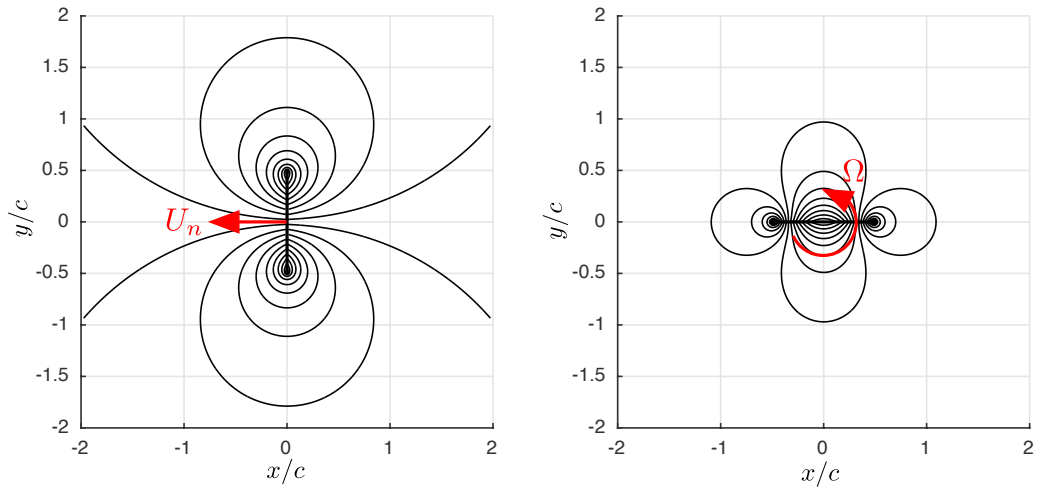

(a) Translation **(b)** Rotation

Fig. 2.7 Streamlines for a flat plate in potential flow undergoing translation and rotation about the mid-chord. Streamlines are shown for the moving body reference frame.

2.3.4.2 Wagner's model

In steady thin airfoil theory (section 2.3.2) it was shown that the bound circulation of an aerofoil changes if either the angle of incidence, or the free stream velocity, is modified (see equation 2.29). This, however, does not occur instantaneously. Because circulation is conserved in the flow field, a change in bound circulation requires vorticity with equal and opposite sign to be shed at the trailing edge. This is the mechanism responsible for the formation of the starting vortex shown in section 2.3.1.6. When in close proximity to the wing, this vorticity can induce downwash which reduces the effective angle of incidence, and delays the growth rate of both lift and circulation. Wagner (1925) modelled the effect the shed vorticity has on the transient response of a flat plate wing, impulsively started from rest to a finite velocity at low incidence. A schematic of this model is shown in figure 2.8. At the trailing edge the steady Kutta condition is applied, and vorticity is shed at such a rate that the strength of the bound vortex sheet at the trailing edge is zero. Despite the plate having an angle of incidence α, the small angle assumption is applied and all vorticity is assumed to be confined to the horizontal axis.

For Wagner's impulsively started wing, the lift coefficient may be written as

$$C_l(s/c) = \overbrace{\frac{\pi c}{2U^2}\delta(s/c)\alpha}^{\text{added mass}} + \overbrace{2\pi\alpha\chi(s/c)}^{\text{bound circ.}}, \tag{2.48}$$

where $s = Ut$, the distance the wing has travelled since the start of motion. The first term on the right hand side of equation (2.48) describes the added mass lift due to the impulsive acceleration (the Dirac delta function $\delta(s/c)$). The second term is lift due to bound circulation, delayed by $\chi(s/c)$, the

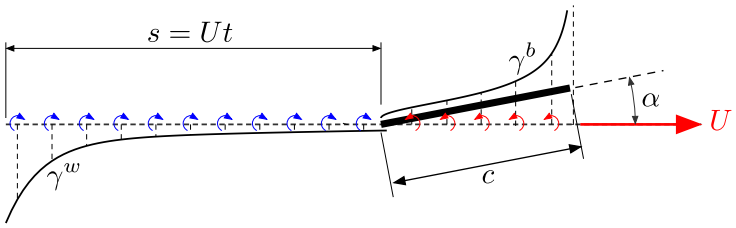

Fig. 2.8 Schematic of Wagner's model. The plate is moving with a velocity U, and angle of incidence α, through an initially quiescent fluid. The vorticity shed into the wake is represented by the vortex sheet γ^w, while γ^b represents bound vorticity.

Wagner lift response function (Leishman, 2000). While no exact analytical function for $\chi(s/c)$ exists, an approximate fit to the numerically acquired lift delay solution are given by von Karman and Sears (1938), and Garrick (1938). The function given by Garrick (1938) is within approximately 2% of the exact Wagner solution for $0 < s/c < \infty$. Garrick's function is

$$\chi(s/c) = 1 - \frac{1}{2 + s/c}, \tag{2.49}$$

which is plotted in figure 2.9a. At $s/c = 0$ the circulatory lift coefficient is 50% of the steady state, while the function asymptotes toward 1 as $s/c \to \infty$. The asymptotic behaviour arises because as the distance (Δs) between each elemental length of the shed vortex sheet and the aerofoil increases, the downwash induced by the elements scales with $1/\Delta s$. Bound circulation, as shown in figure 2.9b, is zero at the start of motion. Thereafter it rapidly increases, and after long time periods the circulation eventually asymptotes to the steady state value ($|\Gamma^b_\infty| = \pi\alpha c U$) (Durand, 1935; Saffman, 1992). Babinsky et al. (2016) explains that despite circulation starting from zero, giving zero lift from the Kutta-Joukowski theorem ($L = \rho U \Gamma$), the finite lift at the start of motion is a result of the initial finite growth rate of bound and shed vorticity (see the vortex growth term in equation 2.20). Pitt Ford and Babinsky (2013) additionally provide an approximate function for bound circulation with position. This is given by equation (2.50), which is plotted in figure 2.9b. The function provides a good approximation of the exact solution, but is valid for only relatively short time periods as it does not asymptote to the steady state circulation.

$$\frac{\Gamma^b}{\Gamma^b_\infty} = 0.9140 - 0.3151 e^{\frac{-s/c}{0.1824}} - 0.5986 e^{\left(\frac{-s/c}{2.0282}\right)} \tag{2.50}$$

A few years following Wagner publishing his theorem, Walker (1931, 1932) and Francis and Cohen (1933), developed an early towing tank apparatus, and measured the circulation of an R.A.F. 30 aerofoil section during starting motion. For the experiment, an early form of Particle Image Velocimetry was developed to acquire quantitative flow field measurements. Walker (1932) concluded that Wagner's theory can be used to predict the unsteady flow about a symmetrical aerofoil (at moderate

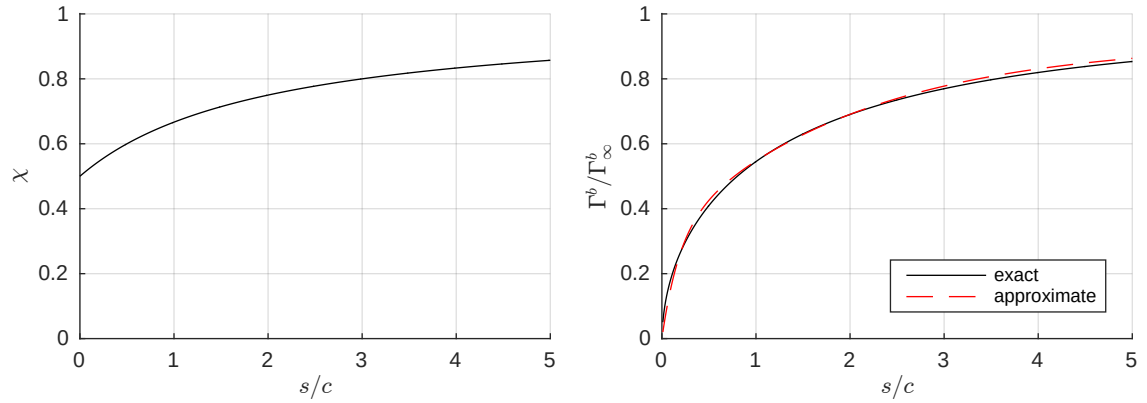

(a) Garrick's (Garrick, 1938) approximation for the Wagner lift response

(b) Comparison of the approximate circulation delay function, given by equation (2.50), with the numerically obtained (exact) response

Fig. 2.9 Lift and circulation delay functions, describing the unsteady response of a flat plate wing subjected to an instantaneous change in velocity.

Reynolds numbers and low angle of incidence) with a *"fair degree of accuracy"*. Interestingly, the author further reasoned that the apparatus used *"may become a standard instrument for certain classes of work, which cannot be done in the wind tunnel. In particular, it appears to provide the most suitable means of investigating the flow around a wing (or cylinder), before the motion has reached steady state"*. The prediction has since been proven to be remarkably accurate. Walker's result was more recently confirmed by Beckwith and Babinsky (2009) for aerofoils at low angles of incidence below stall, again with a towing tank and Particle Image Velocimetry (PIV) system.

2.3.4.3 Küssner's model

It was shown in section 2.2.2 that Küssner's model finds application in the design of modern aircraft. Provided that principles of linear superposition hold, the response to gusts of arbitrary 'shape' may be found from Duhamel's integral (see Appendix A for details) and the Küssner function. Küssner (Küssner, 1930; Kussner, 1932) modelled the response of a flat plate wing encountering a sharp edged transverse gust of infinite extent. This is illustrated in figure 2.10a. Inherent in Küssner's model are a number of simplifying assumptions. The wing has zero initial angle of incidence, therefore only perturbations due to the gust velocity are considered. The gust is assumed to have very low amplitude such that linearised thin airfoil theory applies. The advancing gust edge, or shear layer is assumed to be 'rigid'. This means that the strength and position of the gust is unchanged by the wing on entry; it will always have a velocity V, and advect relative to the wing with a velocity U. Finally, vorticity shed into the wake is assumed to be planar, and also advect relative to the wing at the free stream velocity.

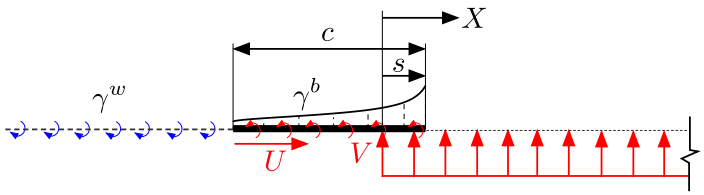

(a) Physical configuration

(b) Broken line aerofoil

Fig. 2.10 Schematic of Küssner's sharp edged gust model. The gust extends from $0 \leq X \leq \infty$, and all vorticity is assumed to be confined to the horizontal axis. The strength of the bound vortex sheet is zero at the trailing edge to satisfy the steady Kutta condition. It is assumed that the change in angle of incidence due to the gust is small, such that $\delta\alpha = V/U$.

The position of the wing, relative to the gust is defined as $s = Ut$, being zero when the leading edge first reaches the gust step change in velocity at $X = 0$. The response of the wing may be characterised by two main zones. In the entry zone, defined as $0 \leq s/c \leq 1$, there is a progressive change in the angle of incidence that moves from the leading to trailing edges. Von Karman and Sears (von Karman and Sears, 1938) and Jones (1940) equate the change in incidence to a broken line aerofoil with a dynamically moving camber point at the gust front. This broken line aerofoil moves with constant velocity in an otherwise irrotational flow, as shown schematically in figure 2.10b. With both a change in camber, and angle of incidence, the circulation of the wing will change. In a manner similar to Wagner's problem, vorticity must be shed into the flow field to conserve circulation, which again induces downwash back onto the wing and reduces the growth rate of both bound circulation and the lift force. In the derivation by von Karman and Sears (1938), the authors indeed use Wagner's function directly to calculate the effects of the wake. The corresponding force breakdown for a unit gust is shown in figure 2.11. The quasi-steady term is the change in lift attributed to bound circulation, assuming wake vorticity has no effect on the wing; it may be calculated directly from steady thin-airfoil theory using the broken line representation of the wing. In the range $0 \leq s/c \leq 1$, this is highly non-linear due to the varying angle of incidence and camber. The wake term represents a lift 'deficit' due to downwash induced by shed vorticity. This has no known analytical solution, and was calculated using a convolution of Wagner's model. Within the entry region a significant portion of the force response is attributed to added mass (called 'apparent mass' by von Karman and Sears (1938)). In the range $s/c \geq 1$ the only forces on the wing are attributed to bound circulation, the growth rate of which is still delayed by wake vorticity.

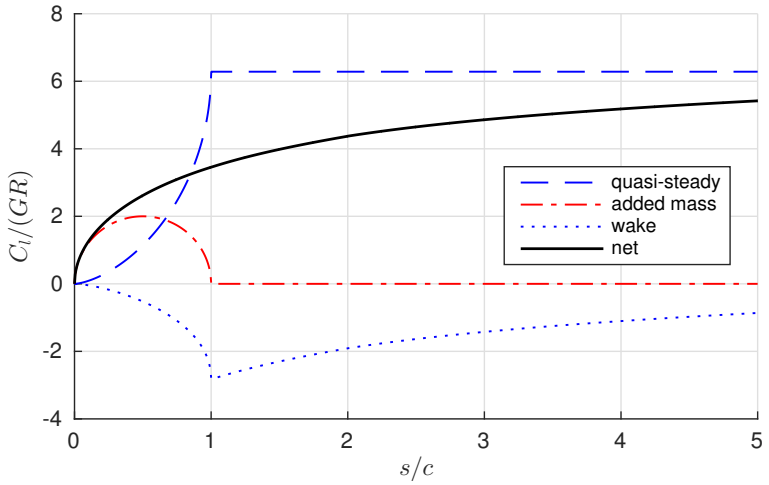

Fig. 2.11 Deconstruction of the lift force coefficient, according to von Karman and Sears (1938).

If the quasi-steady, wake, and added mass force contributions are summed, one reaches the net lift force on the wing. From Leishman (2000), the net force is

$$C_l = 2\pi \frac{V}{U} G(s/c), \tag{2.51}$$

where $G(s/c)$ is Küssner's response function. Bisplinghoff et al. (1955) gives the following approximation for the Kussner response function,

$$G(s/c) = \frac{4(s/c)^2 + 2(s/c)}{4(s/c)^2 + 5.64(s/c) + 0.80}. \tag{2.52}$$

Unlike the Wagner function, the lift force starts from zero because the growth rate of bound circulation at gust entry is zero. At long time periods, however, the response is similar to the Wagner function as lift asymptotes to the steady state.

Since its inception, Küssner's model has been extended to include a travelling gust component (Miles, 1956), account for finite aspect ratio wings (Jones, 1940), and subsonic compressible flows (Drischler and Diederich, 1957). It has been extensively validated by Leishman (1996, 1997); Parameswaran (1995); Parameswaran and Baeder (1997); Zaide and Raveh (2006), who demonstrated excellent agreement between Küssner's model and CFD calculations for wings entering gusts at small angles of incidence. It is apparent that the theory correctly captures the net force of a wing entering a low amplitude sharp edged gust. Despite this, the presence of an added mass force constituent is conceptually problematic because the wing and flow field are both at constant velocities. In section 2.3.4.1 it was discussed that added mass describes an increase in the force required to **accelerate** a body at a given rate when immersed in a fluid compared to the equivalent kinematics in a vacuum. The effect is even described by von Karman and Sears (1938) as *"the force and moment which the*

airfoil would encounter in a flow without circulation, due to the reaction of the accelerated fluid masses". Given that the wing and flow field do not accelerate, the force von Karman and Sears (1938) describe as added mass within Küssner's model appears to conflict with the more generally accepted consensus of the added mass phenomenon. The cause of this force is therefore not conceptually clear.

2.4 Transverse wing-gust interaction studies

The classical unsteady aerodynamic theories can provide significant insight into the mechanics of a wing-gust encounter. The problem is that the models are inherently limited to simple geometries and kinematic cases. In Küssner's case the model is limited to gusts of small amplitude, the flow field is assumed to be irrotational and the velocity perturbation due to the gust is rigidly advected past the wing. For real wing-gust encounters, the flow field will not (necessarily) be irrotational, there could be coupling between the wing and gust velocities, and for large gust ratios, there may be leading edge flow separation. In this section, experimental and computational studies on the response to large amplitude transverse gusts are described.

2.4.1 Experimental studies

There are many experimental wing-gust interaction studies for manned rotorcraft applications. During the forward flight of a rotorcraft, each aerofoil experiences a periodic velocity perturbation in the streamwise and transverse direction. This arises from an interaction with a tip vortex shed previously in the rotor's cycle. The resulting wing vortex interaction may be considered as one example of a general wing-gust encounter. The experimental studies conducted by Homer et al. (1993); Leishman (1996); Mai et al. (2011); Peng and Gregory (2015); Rival et al. (2010) are but a small sample of the literature on this type of interaction. The main parameters, for each study, are summarised in table 2.1. The strength of the 'gust' is characterised by the non-dimensional circulation of the incident vortex, $\Gamma^* = \Gamma_{vortex}/Uc$. The non-dimensional circulation may, in theory, be related to the gust ratio, however, this requires exact knowledge of the vorticity distribution relative to the wing. If an inviscid point vortex is assumed to directly advected toward the leading edge of an aerofoil, the gust ratio may be approximated as $GR = \Gamma^* c/(2\pi s)$, where s, in this case, is the distance between the vortex and leading edge. For $s/c = 1$, $\Gamma^* = 1$ would correspond to a gust ratio of $GR = 1/2\pi \approx 0.159$. We note that in the instance of Leishman (1996) and Peng and Gregory (2015), the gust ratio is relatively small, and the aerofoils would generally operate within the attached flow regime. These studies are likely not applicable to the MAV gust interaction problem. For MAVs, gust velocities are of the same order of magnitude as the free stream, the Reynolds number is of order 10^4, and separated flow conditions are expected. The study by Rival et al. (2010) is more representative of our problem. The authors showed, that at a Reynolds number of 30,000, and $\Gamma^* \approx 3$, the flows induced are sufficient to induce dynamic-stall like separation on a SD7003 aerofoil at an angle of incidence of 8° (pre vortex

interaction).

While the majority of the literature appears to be directed toward rotorcraft applications, only one experimental study was found which directly investigates large amplitude transverse wing-gust encounters. Perrotta and Jones (2017), conducted a series of towing tank experiments where a flat plate wing was towed through a free jet described by a *"sine-squared"* velocity profile. Force and PIV measurements were taken at angles of incidence ranging from -4° to 45°. The gust ratios, based on the peak gust velocity, were 0.42, 0.84 and 1.68. The PIV measurements showed significant flow separation and the authors argued that both steady thin airfoil theory and Küssner's response are likely inapplicable due to the deviation from the modelled flow conditions, albeit a direct comparison of force or circulation histories with Küssner's model were not provided.

2.4.2 Computational studies

From the search of the literature, few directly applicable computational studies were found. Many authors, including Leishman (1996, 1997); Parameswaran and Baeder (1997) and Raveh (2007) investigated gusts of low amplitude in compressible flow. The aims, generally speaking, were to determine the linear step response functions for a unit gust in transonic flows. This cannot readily be obtained experimentally or analytically. The acquired response functions could then be applied to a general gust using Duhamel's integral, allowing the calculation of unsteady loads at little computational cost (Parameswaran and Baeder, 1997).

For the computational simulations, a commonly utilised gust modelling technique is the 'grid velocity' method. At each time step, the travelling gust velocity field is superimposed onto each grid element, thereby fixing the gust edges, as was assumed within the Küssner model. For an incompressible flow, the results are, perhaps, unsurprisingly consistent with Küssner's theory, provided the gust amplitude is small. The grid velocity method may however, suffer significant problems for large amplitude gusts, if there is coupling between the gust velocity and wing, i.e. movement of the gust shear layers. Simple prescription of the gust velocity would not capture this. Perhaps, as a result, this is why there were no identified computational studies which test how well Küssner's model predicts the response of a large amplitude wing gust encounter.

Table 2.1 Summary of experimental and computational gust studies from the literature.

Authors	**Study Type**	**Encounter type**	**Re**	**Strength**
Homer et al. (1993)	Experimental	Discrete vortex	600,000	$0.132 \leq \Gamma^* \leq 3.29$
Leishman (1996)	Exp. + Computational	Discrete vortex	∞	$\Gamma^* = -0.15$
Rival et al. (2010)	Experimental	Discrete vortex	30,000	$-1 \leq \Gamma^* \leq 3$
Peng and Gregory (2015)	Experimental	Discrete vortex	80,000-110,000	$0.3 < \Gamma^* < 0.55$
Perrotta and Jones (2017)	Experimental	Free jet (sine-squared)	10,000-40,000	$0.42 \leq GR \leq 1.68$
Parameswaran and Baeder (1997)	Computational	Sharp edged jet	∞	$GR = 0.08$
Leishman (1997)	Computational	Discrete vortex + sharp edged gust	∞	$GR = 0.0349$
Raveh (2007)	Computational	Discrete + random	∞	$GR \leq 0.0875$

2.5 Surging, pitching and plunging wings

The work by Perrotta and Jones (2017) indicated that the dynamics of vortices shed into the flow may play a significant role toward the force produced through a large amplitude wing-gust encounter. We found, however, little further literature which described the physics of this process in detail. In this section we investigate the literature within a more developed field, that of rapidly accelerating 'surging', 'pitching' and 'plunging' aerofoils at low Reynolds numbers, as similar separated flow physics to those found by Perrotta and Jones (2017) are commonplace.

The NATO Applied Vehicle Technology (AVT-202) report (Ol and Babinsky, 2016) collates much of the research in the area. It was recognised by the authors that during the manoeuvring of MAVs, the lifting surfaces may experience high frequency and amplitude changes to the angle of incidence that far exceed that for transport aircraft, missiles and fighter aircraft. The aim of the AVT-202 task group, in a similar fashion to this study, was to develop understanding of the physics of this highly unsteady problem, which led to the development of a simple low-order model that would be useful for engineers. The approach taken was to conduct a series of simple abstract kinematic problems, from which flow field phenomena could be linked to the unsteady force history. Generally, the experiments or simulations were conducted using simple flat plate wing geometries (Granlund et al., 2013; Hartloper et al., 2013; Manar et al., 2016; Ol and Babinsky, 2016; Ol, 2009; Stevens, 2013). Despite being a *"gross simplification"* of a real wing (Stevens, 2013), the flow topology and force histories were shown to be similar, regardless of wing geometry (Ol and Babinsky, 2016; Ol, 2009). Given the low Reynolds number, and exceeding high angles of incidence, the flow will almost certainly separate, and wing leading edge geometry has only minor effect on the resulting flow. Furthermore, at angles of incidence post stall, Reynolds number effects in the range 10,000 to 60,000 have been demonstrated to have little influence on resulting flow topology and force histories (Ol and Babinsky, 2016; Ol et al., 2010; Pitt Ford, 2013; Stevens, 2013).

2.5.1 Lift production mechanisms

For high angle of incidence surging wing motions, such as that shown for the sharp edged plate at 45° incidence in figure 2.12, it is common for the flow to separate at the leading edge of an aerofoil, roll up, and form a coherent vortex that forms a low pressure zone on the suction surface (Beem et al., 2012; Chen et al., 2010; Ellington et al., 1996; Jones and Babinsky, 2011; Lentink and Dickinson, 2009; Maxworthy, 2007). Except in some particular combinations of kinematics and geometry, the vortex grows quickly and is generally shed into the flow field (Beem et al., 2012; Jones and Babinsky, 2011).

For short time periods, however, it can be seen that the leading and trailing edge vortices dominate the flow topology. Both the vortices appear approximately equal and opposite in strength. To conserve

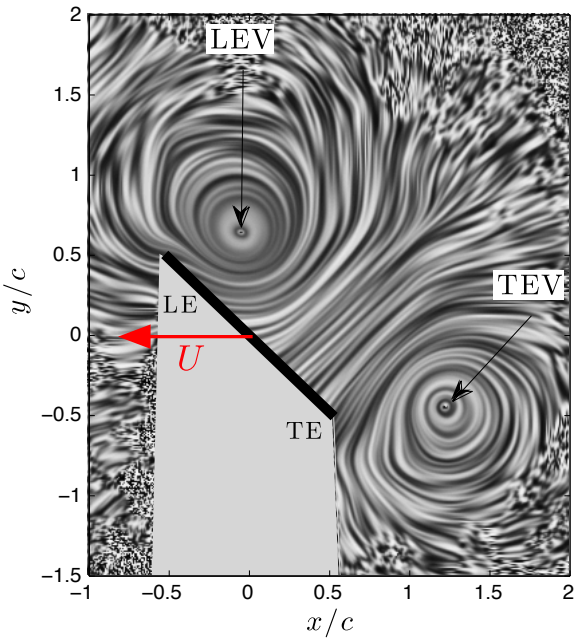

Fig. 2.12 Flow topology about a flat plate wing, surging from rest (in the negative x-direction) at 45° incidence. The wing has travelled 1 chord length, and shows Leading and Trailing Edge Vortices. These are fed by vorticity shed at the Leading Edge (LE) and Trailing Edge (TE) of the plate. Figure adapted from Pitt Ford (2013).

circulation, this indicates that bound circulation is small. Pitt Ford and Babinsky (2013) confirmed this using a combination of experimental data and a potential flow model. In section 2.3.4.2 it was discussed that for an impulsively started wing at low incidence, the Wagner model describes the growth in bound circulation and lift force due to the regulating effect of vorticity shed at the trailing edge. At high angles of incidence the shedding of vorticity at the leading edge disrupts this process by preventing the growth of bound circulation. By application of impulse methods, lift may be explained by a combination of vortex growth and advection of the leading and trailing shed vorticity (see section 2.3.1.5), as well as added mass effects (Babinsky et al., 2016; Eldredge and Wang, 2010; Ol and Babinsky, 2016; Pitt Ford, 2013; Stevens, 2013; Stevens and Babinsky, 2017).

In the case of aerofoils undergoing periodic surging oscillations, Granlund et al. (2014) and Choi et al. (2015) showed that the strength of the shed leading and trailing edge vortices are dependent on the reduced frequency, defined as

$$k^* = \pi f_{Hz} c/U, \tag{2.53}$$

where f_{Hz} is the oscillation frequency. According to Choi et al. (2015), at angles of incidence above stall, there exists a critical Reynolds number at which laminar vortex shedding naturally commences, with its own natural frequency. When the reduced and natural frequencies are close, a lock-in phenomenon occurs, where the growth and detachment of the leading edge vortex synchronises with

the plate oscillation. Here there is an enhancement of the average force normal to the plate. Further increase in the reduced frequency beyond the natural frequency, results in the strength of the shed vortices to diminish, as well as a delay in the phase of LEV detachment. Similar behaviour has been shown for harmonic plunging kinematics Gursul and Cleaver (2018), albeit with additional lift amplification zones at harmonics of the shedding frequency. On the applicability of the classical models for such flows, McGowan et al. (2011) showed that the prediction by Theodorsen's method is resilient to conditions which its mathematical assumptions are violated (post stall conditions), provided that the pitch and plunge perturbations are small. Similar resilience was not found for harmonically surging flows, where the lift amplitude and phase experienced strong reduced frequency dependence (Granlund et al., 2014).

2.5.2 Low-order modelling

To understand why the classical models, may, or may not, be applicable to large amplitude kinematic, and post stall cases, we must understand the role of both vortex dynamics, and added mass effects on force production. To study force production roles, numerous techniques including CFD (Minotti, 2011; Nakata and Liu, 2012; Ramesh et al., 2018), high fidelity discrete point and vortex sheet methods (Eldredge and Wang, 2010; Jones, 2003; Pullin, 1978; Shukla and Eldredge, 2007; Xia and Mohseni, 2013), as well as low-order models (Babinsky et al., 2016; Eldredge and Wang, 2010; Pitt Ford, 2013; Stevens, 2013; Stevens and Babinsky, 2017) have been employed. Here we review on the latter, in particular the model developed by Babinsky et al. (2016), and Stevens and Babinsky (2017), as the fundamental lift production mechanisms are presented in a forthright manner.

The author's model assumes that bound circulation and the Leading Edge Vortex (LEV) can be approximated as a single vortex, located at the effective 'centre of mass' point. This point is free to move from the wing surface due to the advective motion of the leading edge vortex. The shed shear layer at the trailing edge is assumed to be in the form of a single Trailing Edge Vortex (TEV). For a pitching or surging wing, the total lift coefficient, per unit length is

$$C_l = \sum_{i=1}^{m} C_{l,i}^{nc} + \sum_{j=1}^{n} C_{l,j}^{c}, \tag{2.54}$$

where m and n are the number of constituent non-circulatory and circulatory terms. The non-circulatory terms may be identified by the superscript $(.)^{nc}$, while the circulatory terms may be identified by the superscript $(.)^{c}$. For the case of a surging wing, the non-circulatory lift comprises a single added mass component ($C_{l,1}^{nc}$). This is calculated from the velocity normal to the wing, at the mid-chord location. The circulatory lift ($C_{l,1}^{c}$), is calculated from the rate of change of momentum caused by the growth

and advection of the vortex pair. These are

$$C_{l,1}^{nc} = \frac{\pi c \dot{U}}{4U_\infty^2} \sin 2\alpha \tag{2.55}$$

$$C_{l,1}^{c} = -\frac{2}{U_\infty^2 c}\Big((u_{LEV} - u_{TEV})\Gamma + (x_{LEV} - x_{TEV})\dot{\Gamma}\Big), \tag{2.56}$$

where U_∞ is the steady state velocity of the wing. The terms $u_{TEV,LEV}$ and $x_{LEV,TEV}$ are the horizontal velocities and positions of the LEV and TEV. Each have a time dependent circulation of magnitude Γ. Babinsky et al. (2016) suggested that the circulation may be approximated by the Wagner function, scaled by the instantaneous velocity of the wing to correct for acceleration over a finite period. For a flat plate wing at 45° incidence, undergoing constant acceleration over a distance of 1 chord length, this corrected Wagner function is shown in figure 2.13. The function is compared with experimental measurements of the circulation of the leading edge vortex, which clearly agree.

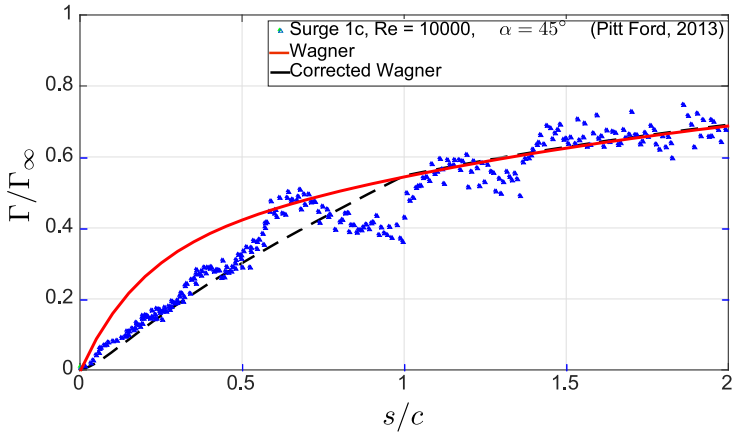

Fig. 2.13 Wagner and corrected Wagner functions for a surging flat plate at 45° incidence. $Re = 10,000$. Figure adapted from Stevens (2013) and Pitt Ford (2013). According to Pitt Ford (2013), the oscillations in the measured circulation are not the result of experimental apparatus vibration, and is instead likely the result of intermittent, non-vibration induced shedding of leading edge vorticity.

While the modified Wagner function fits the measurement data relatively well, there is a discontinuity in the growth rate of circulation at both the start and end of the acceleration region ($s/c = 0$ and $s/c = 1$). The circulatory force predicted by the model, with a component proportional $\dot{\Gamma}$ will therefore experience a discontinuous change. Manar and Jones (2017) found that the rate vorticity is shed at the leading and trailing edges is directly correlated with the edge velocity, which suggest that the discontinuities imposed by scaling the Wagner function are unphysical. The uncorrected Wagner function, used with Duhamel's integral may therefore be a better method for correcting for finite acceleration effects. For a continuous velocity profile the gradients in circulation will also be continuous. We also note that at long time periods, the circulation predicted by the Wagner function

will asymptote to a constant value, which will not capture the continual shedding of vorticity if the plate is at an angle of incidence of 45°. The use of the modified Wagner function, is thus a simple approximation. The relative advection rate of the LEV and TEV was found to be approximately half the steady state free stream velocity, ($u_{LEV} - u_{TEV} = 0.5U_\infty$). New vorticity was assumed to be shed at the leading and trailing wing edges, so $x_{LEV} - x_{TEV} = c\cos\alpha$.

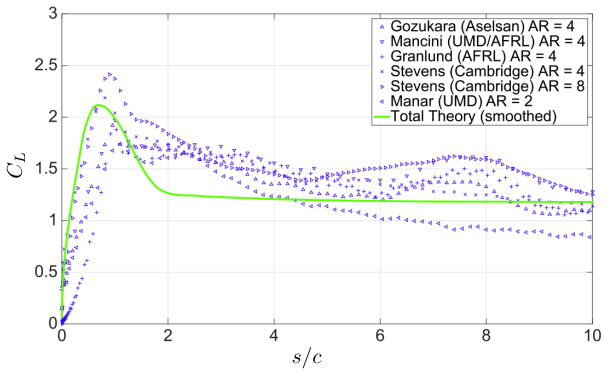

Fig. 2.14 Comparison of the lift force coefficient predicted using the low-order model, described by equation (2.54), with experimental measurement. The tested wings were all rectangular flat plates, with Aspect Ratios (AR) ranging from 2 to 8. Each plate underwent a surging kinematic motion, with a constant acceleration over 1 chord length. The an angle of incidence was $\alpha = 45°$, and Reynolds Number was $Re = 10,000$. After Babinsky et al. (2016).

For the flat plate at an angle of incidence of $\alpha = 45°$, the lift force coefficient when accelerating over a distance of one chord length is shown in figure 2.14. The steady state lift force is attributed to the relative advection of the vortices, as well as initial vortex growth. The large rise and drop in lift coefficient, at the start and end of the acceleration regions ($s/c = 0$ and 1), is attributed to added mass. Note that the magnitude of the drop in force at $s/c = 1$, is greater than the initial rise in force at $s/c = 0$. This is the result of the discontinuous gradient of the corrected Wagner function. Overall, however, the low-order model captures the dynamics, and underlying flows for a surging wing well. This suggests that the low-order approach has significant merit.

For the pitching case, the authors suggest three additional force components. The first component is non-circulatory

$$C_{l,2}^{nc} = \cos\alpha \frac{\pi c^2}{4U^2}\left(1 - 2\frac{x_{le}}{c}\right)\ddot{\alpha}. \tag{2.57}$$

This term is caused by a linear acceleration at the wing mid-chord, that arises when the pitch axis is offset from this point (note, x_{LE} is defined as the distance between the leading edge and pivot point, as illustrated in figure 2.15).

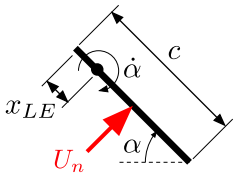

Fig. 2.15 Schematic showing the position of the pitch axis relative to the leading edge of the wing.

The other two force components are circulatory. $C^c_{l,2}$, given by equation (2.58), is caused by an effective change in incidence at mid-chord, due to pitch axis offset. The final contribution, $C^c_{l,3}$, is attributed to the Magnus effect, or virtual camber. This is caused by a non-uniform change in the local angle of incidence across the wing chord, due to the rotation. The sum of the additional circulatory components is equivalent to the rotation term given in quasi-steady thin airfoil theory (equation 2.32). The circulatory terms are

$$C^c_{l,2} = \frac{2\pi}{U_\infty}\left(\frac{c}{2} - x_{le}\right)\dot{\alpha}, \tag{2.58}$$

$$C^c_{l,3} = \frac{\pi c}{2U_\infty}\dot{\alpha}. \tag{2.59}$$

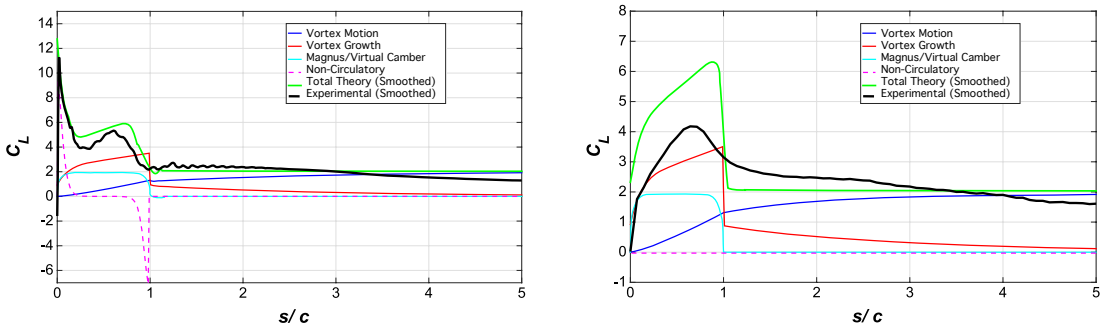

(a) Pitch about the leading edge

(b) Pitch about the mid-chord

Fig. 2.16 Comparison of the low-order model with experiment. The pitch motion occurs over 1 chord length between $s/c = 0$ to $s/c = 1$. After Stevens and Babinsky (2017).

The deconstruction of the lift force coefficient for a flat plate wing, pitching about the leading edge and mid-chord is shown in figure 2.16[‡‡]. There is relatively good agreement between the experimental measurements and the low-order model after the wing has stopped rotation for both cases. During rotation the low-order model over-predicts the force, almost consistently by an amount equal to the Magnus term. It is interesting to note that the circulatory components of the low-order model for the pitch case, less the vortex lift term (equation 2.56), are equivalent to the circulatory terms in the

[‡‡]The $C^c_{l,2}$ term is assumed to be incorporated with the vortex growth term.

classical Theodorsen function for a harmonically oscillating aerofoil (for Theodorsen's function see Leishman (2000)). The non-circulatory terms, however, are not equivalent. Theodorsen includes an additional non-circulatory term caused by relative acceleration of the flow in the plate normal direction, due to a change in incidence.

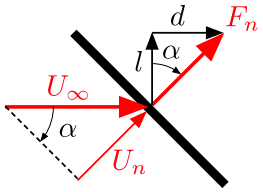

Fig. 2.17 Schematic of the un-accounted for non-circulatory force.

As illustrated in figure 2.17, the plate normal velocity U_n and acceleration $\dot{U}_n$ are

$$U_n = U_\infty \sin(\alpha) \tag{2.60}$$

$$\dot{U}_n = U_\infty \cos(\alpha)\dot{\alpha}. \tag{2.61}$$

Substituting equation (2.61) into equation (2.47) and resolving into the lift direction

$$l = \frac{\rho\pi c^2}{4} U_\infty \cos^2(\alpha)\dot{\alpha}. \tag{2.62}$$

This may be given in the non-dimensional form

$$C_{l,3}^{nc} = \frac{l}{\frac{1}{2}\rho U^2 c} = \frac{\pi c}{2U_\infty}\cos^2(\alpha)\dot{\alpha}, \tag{2.63}$$

which linearised gives Theodorsen's additional term

$$C_{l,3}^{nc} = \frac{\pi c}{2U_\infty}\dot{\alpha}. \tag{2.64}$$

This additional non-circulatory term will increase the discrepancies between the low-order model and experiment, as it introduces yet a further lift component during the pitching motion period. The work on surging and pitching wings provides an insight into the sort of flows that might be expected for a large amplitude wing-gust encounter. Separation at the leading edge is the norm, bound circulation appears to be small, and added mass effects feature prominently. However, we have encountered some problems with the phenomenological modelling of such flows, in particular, during rotation where substantial error arises. It is this author's belief that the pitch error arises because the quasi-steady terms $C_{l,2}^c$ and $C_{l,3}^c$ are incorrectly added. For there to be bound circulation, vorticity must be shed into the flow field to conserve circulation. This circulation will be accounted for by the measurement of the leading and trailing edge vortices. The terms $C_{l,2}^c$ and $C_{l,3}^c$ would therefore already be accounted for by the vortex growth term in $C_{l,1}^c$. While this model will

not be pursued further in this work, it is noted that there is a need to develop a means to directly check, measure, or isolate the effect of each of the modelled lift production mechanisms independently.

The review of the low-order modelling methods has demonstrated that relatively complex flows may be represented in a simple, phenomenological based manner. The models provide a unique perspective on the force contributions for the physical problem, often hidden by more complex models or simulations. Despite the simplicity, the methods may demonstrate remarkable accuracy at little computational cost, which is critical for mobile and time precious applications. Based on the present model for surging and pitching plates, the added mass component, despite being derived for an inviscid fluid, appears representative of the sharp force transients present at the start and end of acceleration motions in a real viscous flow. Furthermore, the classical analytical models, such as the Wagner function, appear to reasonably capture growth rates of vorticity, despite many of the underlying mathematical assumptions not holding. It has further been shown by Ol et al. (2010) and McGowan et al. (2011) that in some high acceleration pitching and plunging plate cases, forces predicted using the Theodorsen function are surprisingly consistent with measurement, even in cases with significant leading edge separation. Despite the difference in problem kinematics, each of these lessons finds relevance for approaching the wing-gust interaction model desired in this work.

2.6 Literature summary

The review of the literature showed that at present, gust loading for aircraft is determined directly, or from a variation of the Küssner theory. This linear model describes the response of a flat plate wing to a sharp edged gust. Convolution methods are generally applied to determine aerodynamic loads for arbitrary gust profiles, including the 1-minus-cosine gust. Küssner's model has been extensively validated for gusts of low amplitude. Little, however, is known about the flow physics of high amplitude wing-gust encounters experienced by MAVs. It is currently unknown whether Küssner's model is representative of such interactions.

Because of the absence of directly relevant gust literature, the physics of surging and pitching flat plate aerofoils at high angles of incidence was investigated. The literature indicated that separation at the leading edge of the aerofoil is the norm, bound circulation is small (if not negligible), and the flow field is dominated by vortices. An existing low-order model, as well as experimental measurements indicated that added or virtual mass plays a significant role toward the unsteady aerodynamic response. Circulatory forces were attributed to the growth and relative advection of vortices in the bulk flow field.

Our brief exposition of Küssner's model also revealed that added mass contributes significantly toward the unsteady response of wing-gust interactions. It is therefore likely that similar effects will be prominent for a large amplitude gust, so the origins of the force were investigated in detail. Added mass describes the increase in force required to accelerate a body when immersed in an ideal fluid. It

originates from an asymmetric change to the body surrounding pressure field to satisfy the no through flow condition. It is perhaps surprising that the added mass effect features in Küssner's model, given that both the wing and gust are at a constant velocity. At present we have no explanation for this discrepancy. From the review of the literature there are clearly a number of fundamental problems that require further investigation.

2.7 Approach and aims

It is recognised that for a wing-gust encounter there are a number of variables including aerofoil profile, gust ratio, gust distribution, Reynolds number, wing aspect ratio, angle of incidence, sweep and so on, which will ultimately influence the force response and flow field. No attempt will be made to characterise all of these. Instead, the effort will be directed toward developing a deep understanding of the flow physics of a select few cases.

For large amplitude wing-gust encounters we have the following unanswered questions:

1. What is the role of vorticity shed into the flow field on force production, and how does it differ with Küssner's model?
2. What is the role of added mass or the non-circulatory forces for a wing-gust encounter, and why are they at odds with the general consensus on the effect?
3. Are the assumptions inherent in Küssner's model sufficiently limiting that it is an unreasonable approximation of a large amplitude wing-gust encounter?

The aim of this thesis is to understand the role of the circulatory and non-circulatory force production mechanisms for a large amplitude wing-gust encounter. Such understanding will enable the limitations of Küssner's model for such flows to be assessed, and may form an integral part of future low-order modelling endeavours.

An experimental approach was taken to circumvent the difficulties of simulating gust encounters with CFD. This also enables general flow features of real wing-gust encounters to be characterised. The test cases were conducted in a similar manner to the studies on surging and pitching wings. Only a simple flat plate wing model geometry was considered, as the flow field will likely be similar regardless of model geometry. The many analytical models for flat plate flows may also be utilised. Furthermore, the experiments conducted will additionally be a 'gross simplification' of a real gust encounter. For a wing-gust encounter, the simplest interaction is that of a wing encountering a gust with a sharp edge. We therefore seek to replicate Küssner's problem as close as experimentally possible, so that deviations from the modelled conditions may be identified, and not obscured by differences such as gust profile. The hardware, and techniques, that were developed to experimentally

replicate Küssner's gust are described in Chapter 4.

In the following Chapter, however, we revisit the fundamentals of the added mass phenomenon. The purpose of this revisit, is to challenge a common misconception about the effect, and present an alternative view on how it may be represented in inviscid and viscous flows. This is necessary to understand the role of the non-circulatory force in Kussner's model, and ultimately spurs insight into how it may be quantified experimentally. In Chapter 5, a potential flow model and techniques used to isolate added mass effects from experimental PIV measurements are described. In Chapter 6 the methods are applied to the cases of a flat plate undergoing acceleration in a translation and rotational sense. The experiments are used to validate the added mass isolation technique, and determine whether the potential flow added mass solution is valid for cases with significant flow separation. Finally, wing-gust encounters with gust ratios of 0.2, 0.5 and 1.0 are presented in Chapter 7. These cases are used to both characterise the flow for a high amplitude wing-gust encounter, and isolate and understand role of the circulatory and non-circulatory force components.

Chapter 3

Added Mass Revisited

In the review of the literature, it was discussed that added mass is a constituent force production term within the Wagner and Küssner theories. The effect is also prominent for rapidly accelerating aerofoils at high incidence. The origin of this force, as discussed in section 2.3.4.1, is an asymmetric change to the body surface pressure, as required to accelerate the surrounding flow field. For the cylinder and flat plate geometries the pressure change, and thus force was calculated using the unsteady Bernoulli equation. There is an alternative, but lesser known and accepted interpretation for the added mass effect. Despite being derived for a potential flow, the force can be explained entirely (and perhaps surprisingly) from the production of vorticity. Recall Wu's impulse equations from section 2.3.1.7, where it was argued that any force on a flow may be determined from the change to the vorticity field. This includes added mass in a potential flow, as will be shown in this Chapter.

While seemingly illogical, the connection between added mass, and vorticity, arises because any body immersed in a flow may be represented by a vortex sheet on its surface, with a magnitude equal to the surface tangent slip in velocity (Lighthill, 1986; Saffman, 1992) (see section 2.3.2). The vortex sheet attributed to added mass, however, must have zero net circulation to satisfy Kelvin's theorem. The idea that added mass forces are linked to a vortex sheet is not new. Von Karman and Sears (von Karman and Sears, 1938) used such an interpretation for their derivation of the Theodorsen and Küssner functions. Eldredge (2010), Leonard and Roshko (2001) and Graham et al. (2017) have all utilised a similar interpretation for their respective calculations of added mass quantities.

In this Chapter, we seek to derive the distributions of this 'added mass vortex sheet'. This will prove to be a critical step toward developing a means for isolating the circulatory and non-circulatory force contributing effects from gust measurements, and identify why the added mass in Küssner's model is at odds with the general theory on the effect. It is at this point where we divide our efforts into two parallel paths. Along the first path we will investigate the 'baseline' added mass effect, that is investigate in detail how the phenomenon behaves for accelerating bodies (and flow fields). Along

the second path we investigate gust flows.

In the following section, we first derive the added mass vortex sheets and force for a simple cylinder flow, given that the geometry is the typical canonical case. In section 3.2 the parameters are derived for general translating and rotating flat plate flows, and Küssner's gust in section 3.3. Finally, we acknowledge that real flows are not inviscid or generally irrotational, so the effects of viscosity on our interpretation of added mass are addressed in section 3.4.

3.1 Cylinder flows

3.1.1 Accelerating cylinder case

To calculate the added mass force using impulse methods, we require the vortex sheet distribution about the body. Physically the flow field only incorporates fluid elements exterior to the body surface. However, in potential flow theory we generally assume that the interior of a body is also contained by fluid, with a somewhat arbitrary velocity that depends on the mathematical construction of the problem. Here we approach the problem differently. We assume the potential flow solution is valid only for the body exterior flow. For the body interior flow the velocity is prescribed a magnitude and direction equal to the rigid body kinematics. The slip between the interior (rigid body) and exterior flows can then be calculated, giving the desired added mass vortex sheets.

For a cylinder the surface exterior flow can be calculated from the potential function, given in section 2.3.4.1. The cylinder, with radius a, moving in the direction from right to left with a velocity of magnitude U, has the surface potential function

$$\Phi|_{r=a} = Ua\cos\theta,$$

with $x = a\cos\theta$ (see figure 3.1a). The circumferential component of the flow velocity, u_θ, is given by the gradient of the potential function in the surface circumferential direction, $u_\theta = \frac{1}{a}\frac{d\Phi}{d\theta}$. The circumferential flow velocity is therefore

$$u_\theta|_{r=a} = -U\sin\theta. \tag{3.1}$$

Since the cylinder has a velocity with magnitude U, the interior velocity at the cylinder surface, in the circumferential direction is $u_\theta^{cyl.} = U\sin\theta$. The strength of the vortex sheet, given the superscript nc for 'non-circulatory', is equal to the slip in velocity between the cylinder surface and flow,

$$\begin{aligned}\gamma^{nc} &= u_\theta - u_\theta^{cyl.} \\ &= -2U\sin\theta.\end{aligned} \tag{3.2}$$

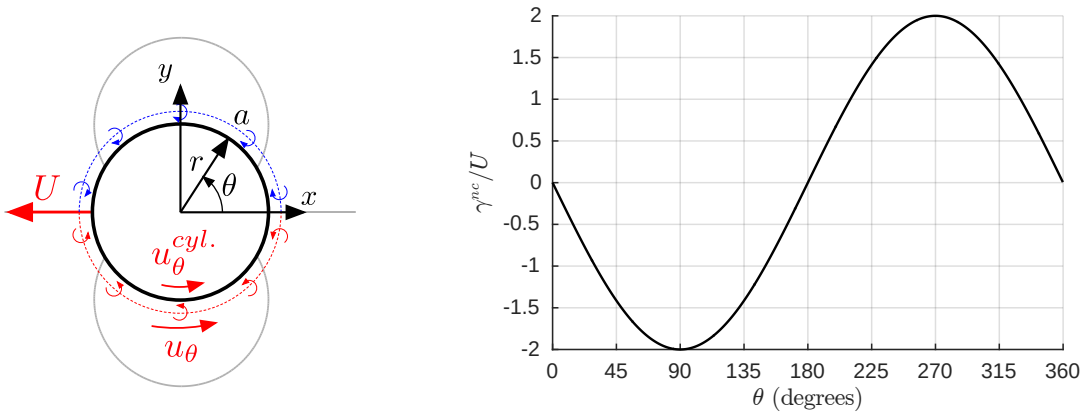

(a) Vortex sheet schematic

(b) Vortex sheet distribution

Fig. 3.1 Vortex sheet about a translating cylinder.

Equation (3.2) is plotted in figure 3.1b. The positive and negative vorticity is spatially separated, thus the flow field can have net momentum and require a force if the vortex sheet changes strength. The x-component of the flow field impulse, equation (2.22), may be written as the line integral

$$I_x = \oint y\gamma(x,y)dl, \tag{3.3}$$

where dl is an elemental length of the vortex sheet. On the cylinder surface, $y = a\sin\theta$ and $dl = ad\theta$, this becomes

$$I_x = a^2 \int_0^{2\pi} \sin\theta\gamma d\theta. \tag{3.4}$$

Substituting equation (3.2), for γ in equation (3.4), and evaluating the integral gives

$$I_x = -2\pi U a^2. \tag{3.5}$$

The force on the cylinder, given by equation (2.23) is

$$\begin{aligned} F_x &= -\rho\frac{dI_x}{dt} + \rho\frac{d}{dt}\int_A -U dA \\ &= \rho\pi a^2\frac{dU}{dt}, \end{aligned} \tag{3.6}$$

which is equal to the added mass force calculated using the surface pressure (see equation (2.39))*.

*The integral term in equation (3.6) corrects for the inertia of cylinder encapsulated fluid.

3.1.2 Accelerating flow field case

For the case where the cylinder is at rest, and flow field is accelerated (see figure 3.2a), the surface potential function was given by equation (2.40),

$$\Phi = 2Ua\cos\theta.$$

The flow velocity is therefore twice that for the accelerating cylinder case, given by equation (3.1),

$$u_\theta = -2U\sin\theta. \tag{3.7}$$

Since the cylinder is at rest,

$$\begin{aligned}\gamma^{nc} &= u_\theta \\ &= -2U\sin\theta,\end{aligned} \tag{3.8}$$

which is plotted in figure 3.2b. The vortex sheet is equal to that for the accelerating cylinder case because the flow velocity, relative to the cylinder is equivalent. The impulse is therefore,

$$I_x = -2\pi U a^2. \tag{3.9}$$

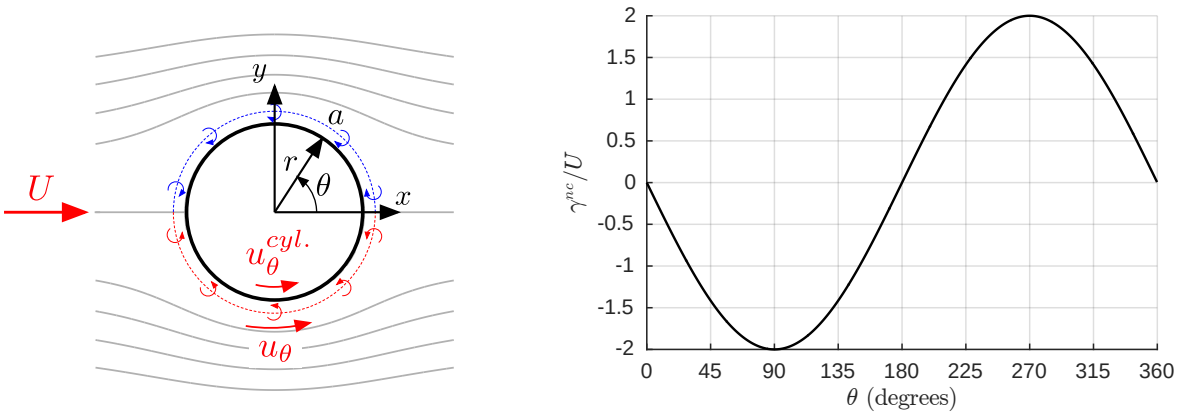

(a) Vortex sheet schematic

(b) Vortex sheet distribution

Fig. 3.2 Vortex sheet about a fixed cylinder and moving flow field.

The force on the cylinder, given by equation (2.23) is

$$\begin{aligned}F_x &= -\rho\frac{dI_x}{dt} \\ &= 2\rho\pi a^2\frac{dU}{dt},\end{aligned} \tag{3.10}$$

which is twice that for the accelerating cylinder case due to the buoyancy-like force.

For both the accelerating cylinder, and accelerating flow field cases we see that a vortex sheet is created on the surface of the body, at a rate proportional to the relative acceleration of the free stream. This is the same regardless of the frame of reference. The vortex sheet that forms, will persist with constant strength and distribution for any given relative velocity. This sheet can be interpreted as a physical manifestation of the change in momentum of the flow (assuming the body is also constructed of fluid). A change in strength of this sheet, must result in a change in momentum of the flow, requiring a force proportional to the magnitude of acceleration.

3.2 Translating and rotating flat plate

To derive the added mass vortex sheet distributions, impulse and forces on a flat plate that is undergoing translation and rotation motions, we utilise the potential flow about an ellipse. This is given in various forms by Milne-Thomson (1986) and Lamb (1895). The flow about a flat plate is equivalent to that of an ellipse, by taking the limit case where the thickness of the ellipse about the minor axis is zero. The derivation utilises the complex potential, and conformal mapping methods. Stream and potential functions are derived about a circle geometry (in the 'circle plane'), which is then mapped using a coordinate transformation to the 'plate frame', giving the ellipse (or plate) geometry and flow field.

3.2.1 Problem geometry

The physical geometry, in the plate frame, is shown in figure 3.3. The flow field is assumed to be unbounded and at rest at an infinite distance from the globally 'fixed' XY coordinate system origin. The global coordinate frame will herein be identified by capital lettering. Positions in the flow field are given in complex vector notation, $Z = X + iY$. The plate, with chord length c, has the position $Z_{mc} = X_{mc} + iY_{mc}$, defined at the mid-chord. It has a complex velocity $\mathbf{U} = dZ_{mc}/dt$. For many calculations it is simpler to work in a plate reference frame xy. As shown in figure 3.3b, this is centred at the mid-chord with x in the plate tangential direction and y in the plate normal direction, oriented at an angle β to the XY coordinate frame. Herein coordinates in the plate reference plane can be identified by the lower case lettering. In complex notation, positions in the plate frame are given by $z = x + iy$, related to the global frame by,

$$z = e^{i\beta}(Z - Z_{mc}). \tag{3.11}$$

The plate velocity vector $\mathbf{U}$ can be resolved into a component normal to the plate U_n (y-direction) and a tangential component U_{tn} (x-direction). Only the plate normal velocity U_n is of importance, as the tangential component does not contribute to the velocity difference across the plate. The angular velocity of the plate is $\Omega = -d\beta/dt$.

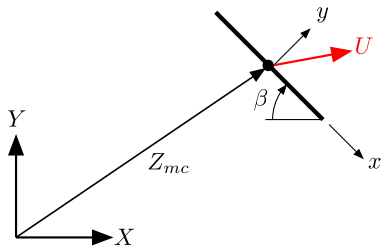

(a) Position of the plate in the global 'fixed' coordinate frame. A position in the global coordinate frame is given by $Z = X + iY$

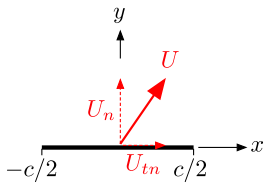

(b) Plate coordinate frame. A position in the plate frame is given by $z = x + iy$

Fig. 3.3 Problem geometry and coordinates frames.

Positions in the circle plane are assigned the complex position $\zeta = \varepsilon + i\eta$. As illustrated in figure 3.4, the transform

$$z = \frac{c}{4}\left(\zeta + 1/\zeta\right), \tag{3.12}$$

maps a circle with unit radius to the flat plate with chord c.

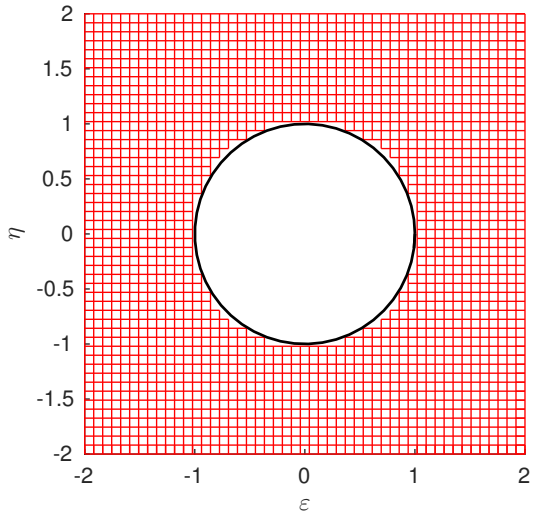

(a) Circle frame

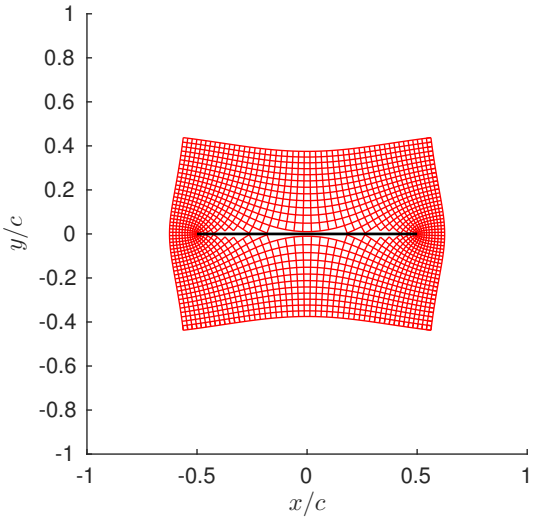

(b) Plate frame

Fig. 3.4 Transform from the circle to plate frames.

3.2.2 Complex potential and velocity

The complex potential is defined as $F(\zeta) = \Phi + i\Psi$, where Φ and Ψ are the potential- and stream-functions. For the flat plate geometry, this is

$$F(\zeta) = -A\zeta^{-1} - B\zeta^{-2}, \tag{3.13}$$

with

$$A = iU_n\frac{c}{2}, \qquad B = \frac{\Omega}{4}\left(\frac{c}{2}\right)^2. \tag{3.14}$$

Iso-contours of the stream-functions for each of the constituent terms are given in figure 2.7. The flow velocities are given by the spatial derivative of the complex potential $u - iv = dF/dz$. Using the chain rule,

$$\frac{dF}{dz} = \frac{dF}{d\zeta}\left(\frac{dz}{d\zeta}\right)^{-1}. \tag{3.15}$$

Taking the derivative of equation (3.13) yields,

$$\frac{dF}{d\zeta} = A\zeta^{-2} + 2B\zeta^{-3}. \tag{3.16}$$

Differentiating equation (3.12) with respect to ζ gives,

$$\frac{dz}{d\zeta} = \frac{c}{4}(1 - \frac{1}{\zeta^2}). \tag{3.17}$$

Substituting equations (3.16) and (3.17) into (3.15) results in the complex velocity

$$\frac{dF}{dz} = \frac{A\zeta + 2B}{\frac{c}{4}\zeta(\zeta^2 - 1)}. \tag{3.18}$$

3.2.3 Surface velocity and bound vortex sheet

The surface of the plate corresponds with the circumference of the circle, defined by

$$\begin{aligned}\zeta &= e^{i\theta} \\ &= \cos\theta + i\sin\theta.\end{aligned} \tag{3.19}$$

Substituting equations (3.19) and (3.14) into (3.18) gives the velocity on the surface of the plate as a function of the angle θ, angular velocity Ω and the plate normal velocity U_n. Separating into real and

imaginary terms and simplifying yields

$$\frac{dF}{dz} = \overbrace{U_n \frac{\cos\theta}{\sin\theta} + \Omega\frac{c}{4}\frac{\cos 2\theta}{\sin\theta}}^{u} - i\overbrace{(U_n + \Omega\frac{c}{2}\cos\theta)}^{v}. \tag{3.20}$$

Since the plate is oriented on the x-axis, the vertical component, v, is equal to the plate velocity, while the horizontal component u is equal to the instantaneous surface 'slip' velocity. The bound vortex sheet, defined in section 2.3.2, is equal to the difference in the horizontal velocity component either side of the plate

$$\begin{aligned}\gamma^{nc}(\theta) &= u(-\theta) - u(\theta) \\ &= \underbrace{-2U_n\frac{\cos\theta}{\sin\theta}}_{\text{translation}} - \underbrace{\Omega\frac{c}{2}\frac{\cos 2\theta}{\sin\theta}}_{\text{rotation}}.\end{aligned} \tag{3.21}$$

This expression is valid for the range $0 \leq \theta \leq \pi$. The $\sin\theta$ terms in the denominator of both the terms indicates that at the plate edges the magnitude of the vortex sheet is infinite.

To relate the polar-coordinates back to cartesian, we will use the mapping relation given by equation (3.12). Substituting $\zeta = e^{i\theta}$ gives,

$$z = x = \frac{c}{2}\cos\theta. \tag{3.22}$$

With application of the identities $\sin^2\theta + \cos^2\theta = 1$ and $\cos(2\theta) = 1 - 2\sin^2\theta$, the vortex sheet may be written with respect to the cartesian coordinate x,

$$\gamma^{nc}(x) = \underbrace{-2U_n\frac{x}{\sqrt{(c/2)^2 - x^2}}}_{\text{translation: } \gamma_t^{nc}} - \underbrace{\Omega\frac{2x^2 - (c/2)^2}{\sqrt{(c/2)^2 - x^2}}}_{\text{rotation: } \gamma_r^{nc}}. \tag{3.23}$$

The sheet comprises a component due to translation in the direction normal to the chord (γ_t^{nc}) and a component due to rotation about the mid-chord point (γ_r^{nc}). As shown in figure 3.5, these scale with the respective kinematic velocities and are independent of the magnitude of the acceleration. For later analysis of experimental data, the vortex sheets are given in non-dimensional form to allow for comparison between data sets with different kinematics. From equation (3.21), we see that the translation term may be given in a non-dimensional form by dividing by U_n, and Ωc for the rotation term. Each of these non-dimensional sheets are plotted in figure 3.6.

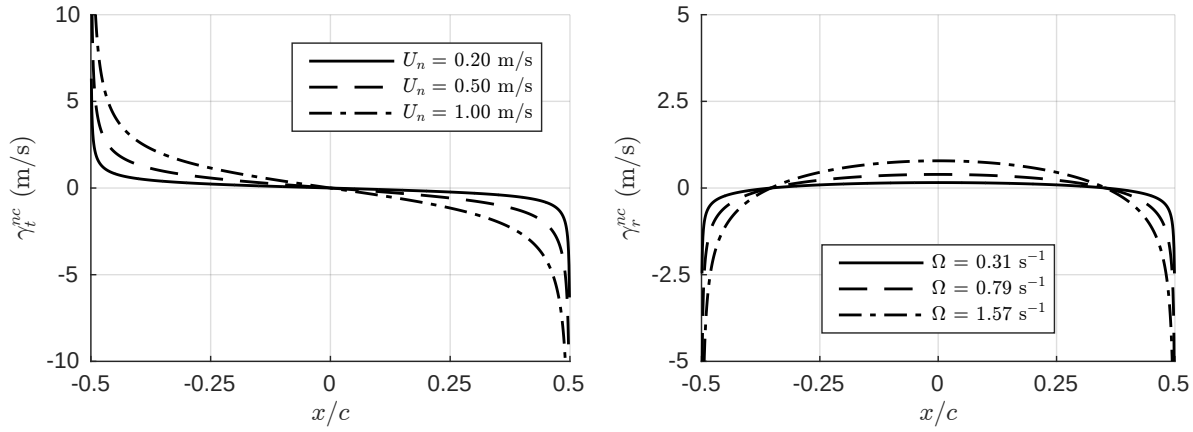

(a) Translation case **(b)** Rotation case

Fig. 3.5 Theoretical added mass vortex sheets at various velocities. $c = 1$ m.

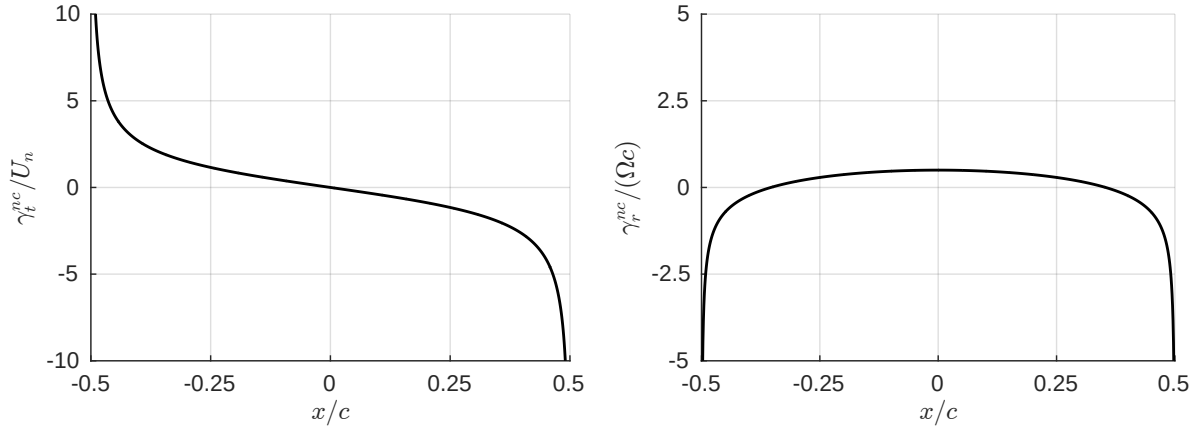

(a) Translation **(b)** Rotation

Fig. 3.6 Non-dimensional, theoretical added mass vortex sheet components for a translating and rotating flat plate.

3.2.4 Linear impulse and force

From the bound vortex sheet the flow field impulse (or 'first moment of vorticity') and force may be found using the relations given in section 2.3.1.7. For a vortex sheet the impulse components become the line integrals

$$I_x = \int y\gamma(x,y)dl, \qquad I_y = -\int x\gamma(x,y)dl, \tag{3.24}$$

where l represents the distance along the sheet. Here the sheet is restricted to the x-axis, $dl = dx$ and $I_x = 0$. The integral I_y may be evaluated in polar form. Differentiating equation (3.22) with respect to θ gives $dx = -\frac{c}{2}\sin\theta d\theta$. Substituting in x and dx, and noting the limits of integration, $-c/2$ corresponds to $\theta = \pi$ and $c/2$ corresponds to $\theta = 0$, equation (3.24) becomes

$$I_y = -(\frac{c}{2})^2 \int_0^\pi \cos\theta \sin\theta \gamma(\theta) d\theta. \tag{3.25}$$

Substituting the polar equation for the bound vortex sheet (equation 3.21) and integrating gives

$$\begin{aligned} I_y &= 2U_n(\frac{c}{2})^2 \int_0^\pi \cos^2\theta d\theta + \omega(\frac{c}{2})^3 \int_0^\pi \cos\theta\cos(2\theta)d\theta \\ &= \pi\frac{c^2}{4}U_n. \end{aligned} \tag{3.26}$$

From equation (3.26) it can be seen that the flow field impulse is both independent of the angular velocity of the plate and is proportional to the plate normal velocity U_n. Since the volume of the plate is zero, the force acting on the plate is

$$\begin{aligned} F_y &= -\rho\frac{dI_y}{dt} \\ &= -\rho\pi\frac{c^2}{4}\frac{dU_n}{dt}. \end{aligned} \tag{3.27}$$

Equation (3.27), is equal to the added mass force as calculated from the pressure field (equation 2.47).

3.2.5 First moment of impulse and mid-chord moment

In a similar manner, the first moment of impulse and mid-chord pitching moment can be found. The second moment of vorticity, defined in section 2.3.1.7, may be written as

$$\begin{aligned} \upsilon_z &= \int_{-c/2}^{c/2} x^2\gamma dl \\ &= (\frac{c}{2})^3 \int_0^\pi \cos^2\theta \sin\theta\gamma d\theta. \end{aligned} \tag{3.28}$$

Substituting equation (3.21) into (3.28), and integrating gives

$$\begin{aligned}\upsilon_z &= -2U_n(\frac{c}{2})^3\int_0^\pi \cos^3\theta d\theta - \Omega(\frac{c}{2})^4\int_0^\pi \cos^2\theta\cos(2\theta)d\theta \\ &= -\frac{\pi}{4}(\frac{c}{2})^4\Omega. \end{aligned} \tag{3.29}$$

The second moment of vorticity, (υ_z), is related to the first moment of impulse (J_z) by

$$\begin{aligned}J_z &= -\frac{1}{2}\upsilon_z \\ &= \frac{\pi}{8}(\frac{c}{2})^4\Omega, \end{aligned} \tag{3.30}$$

and the moment on the plate is

$$\begin{aligned}M_z &= -\rho\frac{dJ_z}{dt} \\ &= -\rho\frac{\pi}{8}(\frac{c}{2})^4\frac{d\Omega}{dt}. \end{aligned} \tag{3.31}$$

3.2.6 Point vortex approximation

For the translation case, illustrated by figure 3.5a, positive and negative vorticity is distributed toward opposite edges of the plate. This could be approximated by a pair of equal and opposite point vortices. The circulation of each point vortex may be approximated by the half-plate circulation

$$\begin{aligned}\Gamma &= \int_{-0.5c}^{0}\gamma_t^{nc}dx \\ &= cU_n. \end{aligned} \tag{3.32}$$

The separation distance of the point vortices may be found by equating the flow field momentum for the vortex pair, with that of the translating plate. Since the linear momentum is related to flow field impulse by $J_y = \rho I_y$, from equation (3.26) the plate flow field momentum is

$$J_y = \rho\pi\frac{c^2}{4}U_n. \tag{3.33}$$

Substituting equation (3.32) into (2.19) gives

$$J_{point} = \rho c U_n d. \tag{3.34}$$

Equating equation (3.33) with (3.34), gives the distance between each point vortex (d)

$$d = \frac{\pi}{4}c. \tag{3.35}$$

3.3 Added mass in Küssner's sharp edged gust

Having derived the added mass vortex sheets for a flat plate in general planar motion, we now proceed to the term in Küssner's gust model. The workings given by von Karman and Sears (1938) is followed, but with minor changes to incorporate a plate of arbitrary chord length, and the gust entry direction is reversed for consistency with the experiments in this thesis.

3.3.1 Geometry

Figure 3.7 illustrates the geometry of the problem. The plate has a velocity U, the gust velocity is V, and the chord length is c. Positions along the plate surface are defined by x. In polar form, the position x is related to the coordinate θ by $x = \frac{c}{2}\cos\theta$. The position of the gust front in polar form is $\tau = \cos^{-1}(1-2s/c)$, where as defined in section 2.3.4.3, $s = Ut$, the distance from the leading edge of the wing to the gust edge. The primary difference between the gust problem, and that modelled for a translating plate in section 3.2, is that the plate does not experience a uniform change to the velocity. Instead, in the range $0 \leq \tau \leq \pi$, the wing gradually progresses into the cross flow, therefore the gust edge moves from the leading to trailing edge of the plate.

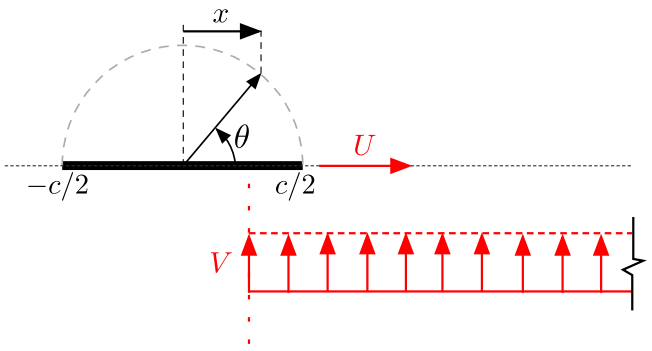

Fig. 3.7 Küssner model schematic.

3.3.2 Non-circulatory vortex sheet

To satisfy the no-penetration condition, a non-circulatory vortex sheet must form. The Kutta condition is not enforced, therefore no vorticity is shed into the flow field. Fluid is free to pass around the sharp leading and trailing edges, and bound circulation is zero. This vortex sheet, given by von Karman and Sears (1938) is

$$\gamma^{nc}(\theta,t) = \sum_{k=1}^{\infty} a_k \frac{\cos(k\theta)}{\sin\theta}, \tag{3.36}$$

with

$$a_k(t) = \frac{4V}{\pi} \int_0^{\tau} \sin\theta \sin(k\theta) d\theta. \tag{3.37}$$

The sheet is found from the results of thin airfoil theory, given by Durand (1935), using the broken line aerofoil gust representation described in section 2.3.4.3. The vortex sheet, equation (3.36), is plotted in figure 3.8 for entry positions from $s/c = 0.25$ to $s/c = 1$.

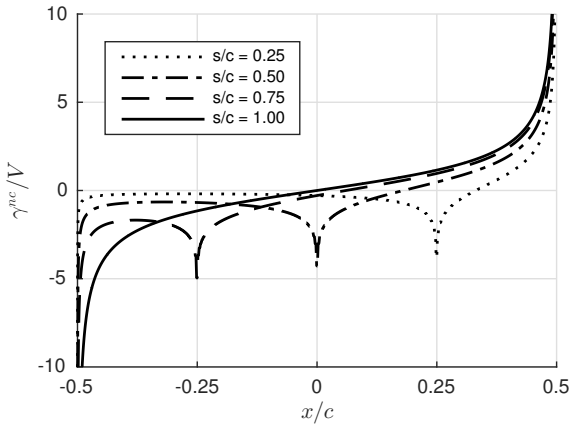

Fig. 3.8 The non-circulatory vortex sheet component of Küssner's model.

During the entry region, we note that the vortex sheet is significantly more complex than that for the translating plate case. The sheet changes magnitude and distribution as the plate enters the gust cross flow. When the plate is fully submerged in the gust ($s/c \geq 1$), the non-circulatory vortex sheet is equivalent to that at $s/c = 1$, because it experiences a uniform, time independent gust velocity across the full chord. It can be noted, that the vortex sheet for $s/c = 1$ is exactly equal to that of a translating plate at 90° incidence, with a velocity equal to that of the gust (it is equal to the translation term of equation 3.23).

3.3.3 Impulse and force

With the non-circulatory vortex sheet, we may now calculate the contribution to the impulse and lift force for the gust entry. Substituting the vortex sheet, equation (3.36), into (3.25), and evaluating the integral gives the flow impulse in the y-direction,

$$I_y = -\frac{\pi}{2}\left(\frac{c}{2}\right)^2 a_1. \tag{3.38}$$

From equation (3.38) it can be seen that only the first term ($k = 1$) of the infinite series given by equation (3.36) contributes toward the net vertical impulse of the flow field (and thus the lift force). Furthermore, von Karman and Sears (1938) show that only the second term ($k = 2$) of the series contributes toward the pitching moment of the plate. Each of these vortex sheet components are shown in figure 3.9. The first mode, or lift contributing vortex sheet has an identical distribution to

that of a plate undergoing translation in the chord normal direction, while the second is equivalent in distribution to that of a plate rotating about the mid-chord, albeit with different scaling (see figure 3.6).

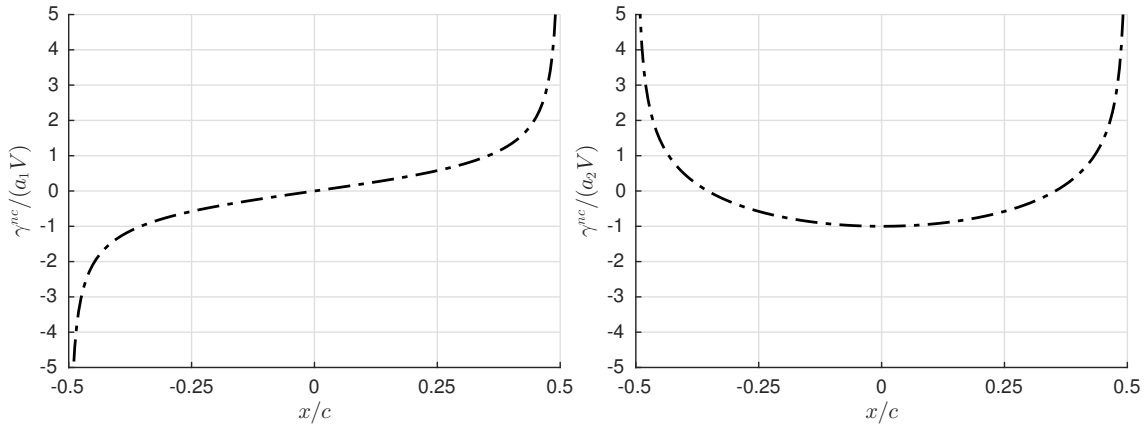

(a) $k = 1$ **(b)** $k = 2$

Fig. 3.9 Components of the non-circulatory vortex sheet that contribute to force generation.

From equation (2.22), the force on the plate can be found from the impulse,

$$\begin{aligned} F_y &= -\rho d I_y/dt \\ &= \frac{\pi}{2}\rho\left(\frac{c}{2}\right)^2 \frac{da_1}{dt}. \end{aligned} \tag{3.39}$$

Evaluating the derivative yields

$$\begin{aligned} F_y &= \rho c U V \sin\tau \\ &= 2\rho U V \sqrt{s(c-s)}, \end{aligned} \tag{3.40}$$

which is plotted in figure 3.10. We have seen that on entry of the plate into the gust cross flow, a non-circulatory vortex sheet forms, resulting in a force contribution that von Karman and Sears (1938) attribute toward added mass. When the plate is fully immersed within the gust the vortex sheet has an identical distribution to that of a translating plate. This suggests that the two components are equivalent. However, given that both the wing and gust are at a constant velocity, while the added mass vortex sheet for a flat plate only arises due to acceleration, we still have no explanation as to why there is a conceptual discrepancy.

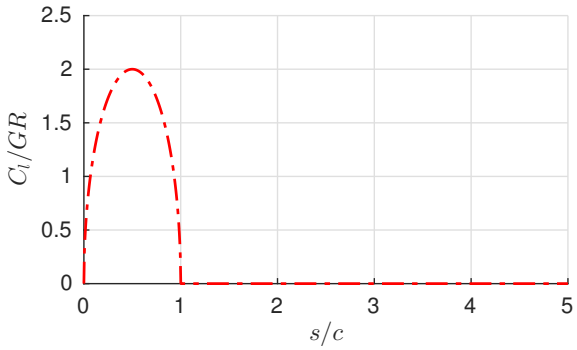

Fig. 3.10 The non-circulatory force component of Küssner's model.

3.4 Added mass in viscous separated flows

In this Chapter, it has been argued that added mass effects in potential flow theory may be explained by a change in impulse due to the formation of a non-circulatory vortex sheet. The force was shown to be equivalent to that calculated with the unsteady Bernoulli equation, an equation that is only valid in irrotational flow (or along a streamline). For applications of practical interest, however, the working fluid is not inviscid and as shown in figure 3.11, the flow field can be significantly different to that of potential flow. The boundary condition between a body and fluid changes from free slip, to no slip, and the aforementioned vortex sheets will no longer persist as they would in an inviscid fluid. Instead, diffusion causes vorticity to be transported from the surface of a body and into the adjacent fluid (forming a boundary-layer). When subjected to a strong adverse pressure gradient, such as that about sharp edges, the resulting boundary-layer can separate. Vorticity is thus shed into the bulk flow, giving a rotational, non-potential, field. We must therefore question whether the potential flow added mass derivations are applicable, or how they may differ in a viscous, separated flow.

(a) Potential flow field, arrows indicate the surface slip velocities

(b) Real, viscous flow field with boundary-layers and flow separation

Fig. 3.11 Schematic comparing the vorticity distributions between a potential and viscous flow.

In the literature, it has been suggested that added mass effects are largely unchanged in a viscous fluid. Leonard and Roshko (2001) and Eldredge (2010) have argued that the added mass force on a body is proportional to the rate new vorticity is generated on the body surface, with an identical singular distribution to that given by inviscid theory. This is regardless of viscous effects and the

consequential changes to the flow topology. Graham et al. (2017) assumed a similar process to identify the added-mass contribution to forces derived from experimental data. This *'added mass vorticity'* diffuses from the surface and into the surrounding flow over time periods of order Reynolds number greater than the advective time scale. Thus, in practice, the vorticity is confined to an intensely spatially concentrated region. If the added mass attributed vorticity is confined to a very thin wall bound layer, that is superimposed onto the existing rotational flow, then it suggests that outside of this newly created layer there will be a potential (inviscid, incompressible, irrotational) change to the existing velocity field (Leonard and Roshko, 2001). This implies that the unsteady Bernoulli equation, given by (2.14), applies exactly in this superimposed potential field. Despite the body being immersed in a viscous and rotational flow, the change in pressures, and thus force, on the body will therefore be equal to that of a potential flow. The same conclusion can be reached by considering the change in impulse of the flow field from the production of the wall bound vorticity, which is superimposed onto the existing vortical field.

While the existence of the added mass vorticity has been theorised, surprisingly there appear to be no experimental flow field measurements confirming its presence and demonstrating its independence of the bulk rotational flow. Nor has it been experimentally demonstrated that a flow field may be deconstructed into the sum of a viscous and potential component. The wealth of measurements taken in the literature utilising PIV to resolve the flow field around an accelerating body, such as that about pitching, plunging, or rotating aerofoils, has spatial resolutions of order of a boundary-layer thickness (see Buchner et al., 2012; Pitt Ford and Babinsky, 2013; Poelma et al., 2006; Polet et al., 2015; Rival et al., 2009). The intention of such experimental setups, is to capture wide regions of the flow field to include starting vortices, which reduces spatial resolution. It is questionable, whether with such measurements, the distribution of added mass attributed vorticity can be resolved, and isolated, from changes made to the flow field resulting from other viscous effects.

3.4.1 Further objectives

Given the aims of this thesis, to understand the role of the circulatory and non-circulatory force production mechanisms for a large amplitude wing-gust encounter, establishing whether added mass effects are influenced by viscosity is a critical step. It is therefore argued that the challenges with measuring added mass experimentally must be overcome. This would enable a measure of added mass attributed vorticity to be compared with the theoretical result, thus allowing the effects of viscosity to be assessed. The non-circulatory force components in a physical gust encounter experiment could be isolated, and questions as to how the effect arises may be addressed.

To meet the wider aims of this study we set the following additional objectives:

- Develop a methodology from which non-circulatory and circulatory effects can be quantified from an experimentally acquired flow field.
- Determine whether added mass vorticity is fully, or partly, included in PIV derived flow field vorticity measurements. This will influence impulse and force quantities subsequently calculated. It will also determine whether the circulation of vortices in close proximity to a body may be 'contaminated' by vorticity attributed to added mass. This may potentially lead to double counting of added mass quantities in models that have some empirically derived components.
- Prove or disprove whether fluid viscosity or flow separation influences the added mass quantities, compared with inviscid theory.

3.5 Summary

Despite added mass having been discussed in the literature for over a century, there is still a surprising amount unknown about the phenomenon. In this Chapter it was shown that added mass can be attributed to the time dependence of a non-circulatory bound vortex sheet in potential flow, and wall bound vorticity in a viscous flow. This idea is not entirely new, having shown roots perhaps preceding von Karman and Sears (1938), but it is not generally known or accepted today. Non-circulatory, added mass attributed vortex sheets and force quantities were derived for a cylinder, a translating and rotating plate, and for Küssner's sharp edged gust. It is still unknown why there appears to be an added mass like force in Küssner's model when the wing and flow field are at constant velocity.

A review of the literature discussing the applicability of the inviscid added mass result for viscous and separated flow was conducted. It has been theorised that the inviscid added mass formulation is valid even for viscous separated flows, however, this has never been experimentally proven. We conclude that in order to understand force production mechanisms for a wing-gust encounter, it is imperative that the many basic questions still surrounding the added mass phenomenon in viscous flows are answered first. We must develop the tools to isolate the added mass phenomenon, address questions as to when the effect will and will not be captured experimentally. Following this we can approach the questions as to the origins of added mass in Küssner's gust problem, and how it, along with the circulatory force contributions change when moving from gusts of low to high amplitude. In the next Chapter the experimental equipment and main data acquisition techniques utilised for this study are described.

Chapter 4

Experimental Methodology

Equipment and techniques were developed specifically for this work to facilitate the generation, and measurement of a sharp edged wing-gust interaction. The main equipment used was the Cambridge University Engineering Department (CUED) towing tank, described in section 4.1. The wing models are described in section 4.2. Force and PIV were the primary quantitative data acquisition methods utilised. To acquire force measurements, a new balance and inertial system were developed to ensure the data was free of inertial contamination. These are described in sections 4.3 and 4.4. For PIV, it was necessary to resolve the full flow field to enable quantities of added mass to be determined (for reasons described in Chapter 5). The configurations, and error sources are described in section 4.6. Finally, the apparatus designed to replicate Küssner's sharp edged gust is described in section 4.7.

4.1 Towing tank

As illustrated in figure 4.1, the CUED towing tank is 9 metres in length, has a width of 1 metre, and the water depth is approximately 0.80 metres. The working premise is simple, a model is mounted to an actuated carriage that traverses the length of the tank, therefore the fluid moves relative to the model. The test section is 2 metres in length and has glass side walls and floor for optical access. The carriage is belt-driven by a single 1.47 kW digital servo motor, and has a maximum velocity of 4.75 m/s (Pitt Ford, 2013).

The towing tank is used for a number of reasons. For unsteady aerodynamic experiments it is easiest to accelerate the model, rather than the fluid. The mass that must be accelerated is lower and there are no buoyancy-like forces on the model, due to the pressure gradient required to accelerate the flow field. The use of water as a working fluid is also beneficial because of Reynolds number scaling effects. It can be shown that by equating the Reynolds number for air as the working fluid, with water,

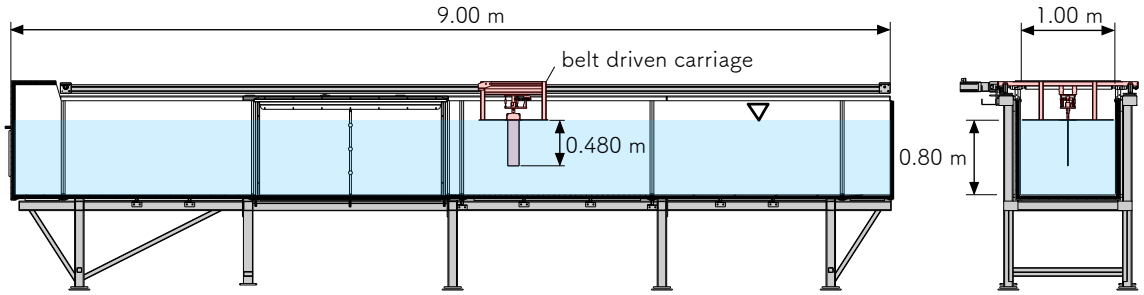

Fig. 4.1 Schematic of the CUED towing tank.

$$
\begin{aligned}
Re_{\text{water}} &= Re_{\text{air}} \\
\frac{U_{\text{water}}}{U_{\text{air}}} &= \frac{\nu_{\text{water}}}{\nu_{\text{air}}} = \frac{1.1386 \times 10^{-6}}{1.4657 \times 10^{-5}} = 0.077,
\end{aligned} \tag{4.1}
$$

we find that for a given model size, flow velocities in water are only approximately 7.7% that of air*. In addition, fluid-dynamic forces on a model are approximately 3.7 times greater in water (Pitt Ford, 2013). The longer timescales, plus ease of suspension of tracer particles makes water an ideal fluid for PIV data acquisition. Turbulence levels within the tank are additionally exceedingly low, pre-acceleration of the test model. After being left to settle for 15 minutes, turbulent velocity perturbations within the tank decay to below the measurement noise of the PIV system (Jones and Babinsky, 2011) (when taken with a large field of view). For the experiments conducted in this work, the generation of gust perturbations is significantly simpler in a towing tank compared to a wind-tunnel based apparatus (see section 4.7).

Carriage kinematics were measured using an on-carriage linear quadrature encoder with 1 mm step resolution, as well as an accelerometer. The velocity and position of the carriage was calculated by numerically integrating the acceleration measured using the carriage mounted accelerometer. Gradual 'drift' in velocity and position due to cumulative sensor error was corrected using the absolute position given by the encoder. Combined position accuracy is estimated to be of order of 0.01 mm, albeit for the experiments in this thesis, position accuracy of this order is not necessary. Analogue signals from all carriage mounted sensors was recorded using LabView and a National Instruments 14 bit data acquisition card at a sampling frequency of 5 kHz.

*Fluid properties taken from Cengel et al. (2008).

4.2 Wing models

Two wing models were manufactured for the experiments. Both models have 120 mm chord, 480 mm span and 4 mm thickness. One model was made from toughened glass and was used for PIV measurements that require the gust rig (described in section 4.7). The gust rig limits laser optical access into the tank. The glass wing allowed for PIV measurements to be acquired in the usual 'shadow' region. The second model, shown in figure 4.2a, was carbon fibre, and had a 3-component MEMS accelerometer embedded within. This wing was used for force measurements. The purpose of the accelerometer will be discussed in section 4.4. The wiring to the accelerometer ran internally through the wing for minimal flow disturbance. The sensor can measure accelerations up to ± 29.43 ms^{-2}, has a nonlinearity of less than $\pm 0.3\%$ and cross-axis sensitivity of $\pm 1\%$. As shown in figure 4.2b, the carbon wing had square cut edges, while the toughened glass was square cut with 1 mm chamfers on each corner. For pitching and surging wing kinematic cases, Ol and Babinsky (2016) showed that edge shape has little effect on the resulting flow topology and force, presumably because the separation point and rate circulation is shed at the edge is unchanged by the geometric shape. Both wings have a tensile modulus of elasticity of approximately 70 GPa in the spanwise direction.

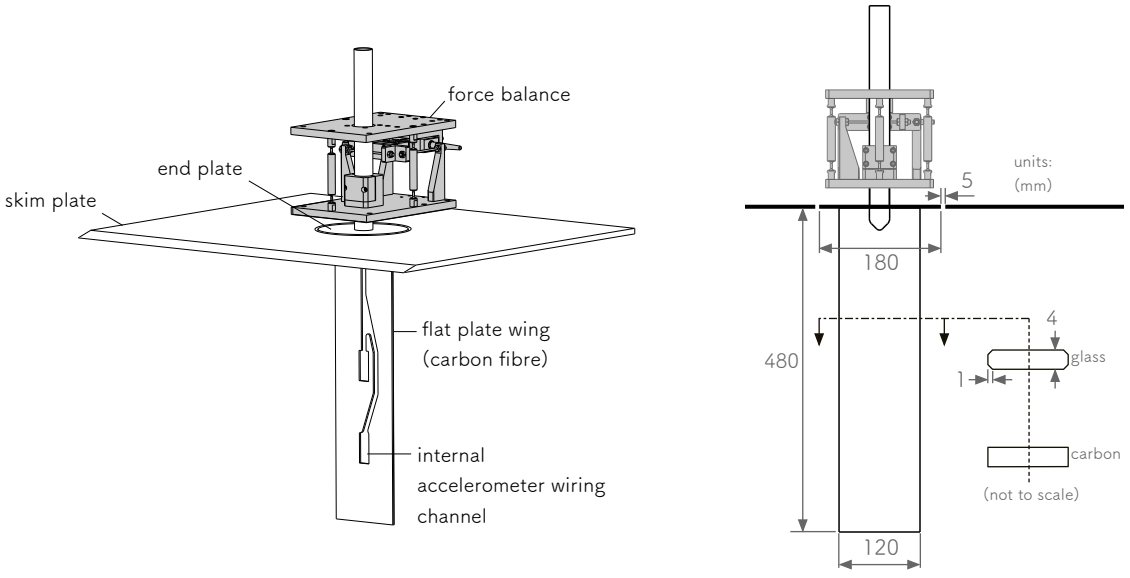

(a) Overview **(b)** Wing detail

Fig. 4.2 Schematic of the wing, force balance and skim plate configuration.

The mounting configurations, shown in figure 4.2b, are identical for each model. A 180 mm diameter end plate was located at the top wing tip, which was set flush into the skim plate spanning the width of the tank. The skim plate was attached rigidly to the carriage just below the water line, and suppresses surface wave effects in the vicinity of the wing. There was a 5 mm radial gap between the end- and skim-plates to circumvent the transmission of forces from the skim plate to the force balance. The arrangement produces a mirror image of the flow and wing, thus giving the wing an

effective aspect ratio of 8. The design additionally avoids the requirement for a tip clearance gap between the wing and skim plate, which has been suspected of introducing three-dimensional effects that are detrimental to spanwise coherence of a leading edge vortex (Ol and Babinsky, 2016; Son et al., 2016). For all experiments the balance was mounted directly to the tank carriage, such that the balance sensors are in fixed alignment with the lift and drag directions. The angle of incidence of the wing was adjusted relative to the balance.

4.3 Force balance

Lift and drag forces on the wing were measured using the two-component 50 N strain-gauge force balance shown in figure 4.2. This balance was designed specially to react lift and drag forces through the sensed balance elements, while bending moment loads due to the cantilever loading of the wing model are reacted by stiff, non-sensed members. This configuration increases stiffness, and reduces vibration that often contaminates towing tank based low Reynolds number force measurements.

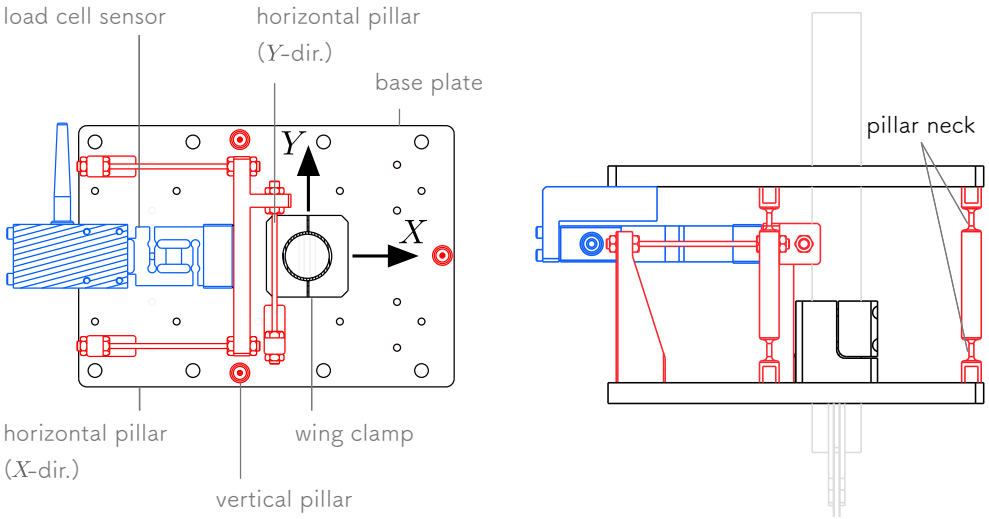

(a) Top view (upper plate removed) **(b)** Side view

Fig. 4.3 Inner workings of the force balance.

The basic balance operation is as follows. Three pillars, visible in figure 4.3, connect the top and bottom plates of the balance. The neck at the end of each pillar was designed such that the pillars have a combined shear stiffness of order 1/1000 times that of the load cell, but have high stiffness in tension and compression. With just the three vertical pillars the plates are constrained to planar motion relative to one another. A pair of horizontal pillars constrains relative motion of the lower plate in the X- and pitching-moment directions, with the net X-direction force routed through a Flow-Dynamics shear web load cell sensor. This pair of flexures additionally have low shear stiffness, therefore the two

parallel plates can still move in the X-direction. A third horizontal pillar constrains this motion, with the forces additionally routed through a sensing element. The top and bottom plates of the balance are now constrained to each other in all 6 degrees of freedom, with only forces in the X- and Y-directions sensed. Each of the load cell sensor elements has a maximum resolution of 0.01 N.

4.3.1 Calibration

Due to the non-zero shear stiffness of each pillar, not all force applied to the balance will be routed through the sensor (the percentage is dependent on the combined stiffness of the pillars relative to the balance). The load cell sensor was therefore calibrated in situ of the balance. Calibration curves are shown in figure 4.4. Each is calculated by incrementally loading the balance in a single channel direction using fixed weights and a pulley system. The linear fit in the X-direction is $F_x = 19.780V_x^{dc}$ and in the Y-direction $F_y = 28.477V_y^{dc}$. The linear fits for both of the calibration data sets have a coefficient of determination (R^2) value greater than 0.999999, therefore indicating excellent agreement.

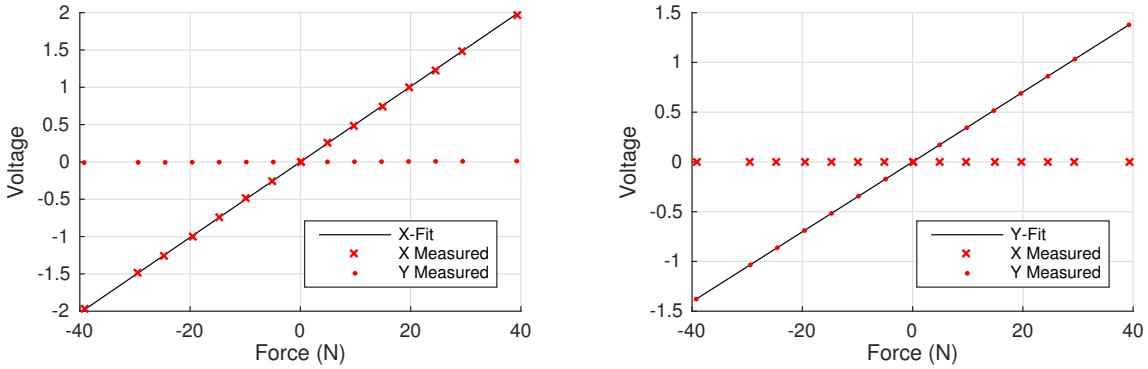

(a) X-direction **(b)** Y-direciton

Fig. 4.4 Calibration of the force balance.

4.3.2 Error

During the calibration, both the voltages in the X- and Y-directions were simultaneously recorded to quantify the cross talk between each channel. Error can arise due to both structural deformation of the balance and misalignment error of the load applied to each channel. The voltages of the unloaded channel are shown in figure 4.4. Some very slight variation from zero is visible. Using the calibration fits for each channel, this cross talk in the X-direction is quantified as a percentage of the load applied to the Y-direction. The same was repeated for the Y-direction cross talk. The error is plotted in figure 4.5a. There is measured cross talk up to a maximum of 0.8% of the applied load.

A second source of error arises due to the offset loading of the wing relative to the balance. Offset loading applies a large bending moment to the bottom and top plates of the balance, resulting in slight

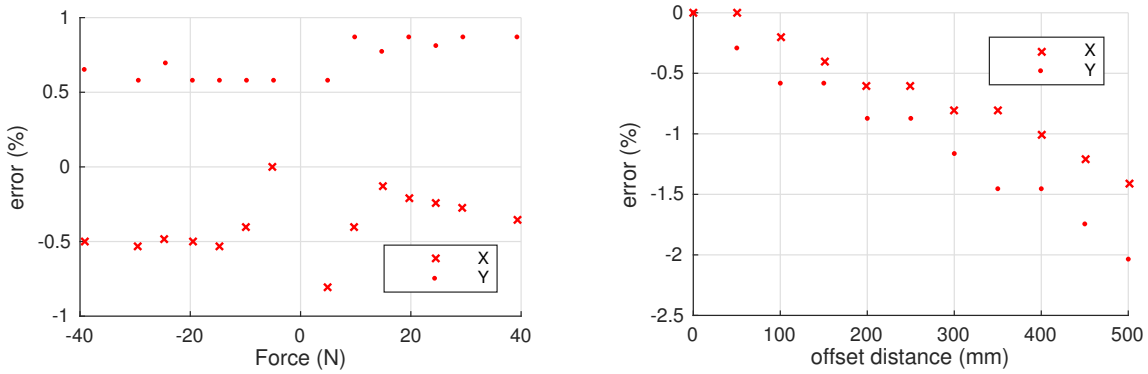

(a) Cross-talk error

(b) Bending moment error

Fig. 4.5 Sources of force balance measurement error.

deflection and loading of the sensor elements. This error source was quantified by applying a 1 kg load separately in the X- and Y-directions at varying offsets (Z) from bottom plate of the balance. If the no-load voltage is V_{nl}^{dc}, and the voltage with the load applied at position Z is V_z^{dc}, then the error (e_r) is

$$e_r = \frac{V_z^{dc} - V_{z=0}^{dc}}{V_{z=0}^{dc} - V_{nl}^{dc}}. \tag{4.2}$$

This is plotted in figure 4.5b. The error increases approximately linearly with load offset position. Since the wing is 0.480 metres in length, and the wing is uniformly loaded, the error is at maximum approximately 1%. For the experiments described in this thesis, an error of order 1% is deemed to be negligible.

4.4 Inertial force decomposition

Section 4.3 described the design and calibration of a force balance capable of accurately measuring lift and drag force components on a wing model, whilst ensuring the model is mounted in a stiff structure. This minimises force balance flexibility as a potential source of vibration contamination. However, other sources of vibration include sting and model flexibility, which can add significant detrimental noise to force measurements taken at low Reynolds numbers. Low pass filtering is often employed reduce vibration effects (Granlund et al., 2011; Jones and Babinsky, 2010, 2011; Pitt Ford, 2013; Stevens, 2013), however, this distorts transient forces by reducing their peak and increasing bandwidth (Pitt Ford, 2013). The necessity for filtering can therefore limit the usable frequency range of force measurements to below the lowest mode of vibration of the system. This is problematic for the relatively sharp edged gust experiment conducted here. It is possible that there will be transient

fluctuations in force at higher than resonant frequencies.

An additional source of measurement error results from the model and force balance self-mass. During carriage acceleration, an inertial force is applied though the load cell to accelerate the wing and balance mass. This force component is often quantified by taking the average of a series of 'tare' results from identical kinematic test runs conducted in air. The tare experiment takes advantage of the approximately 850 times difference in density between air and water, thus isolating the inertial component as fluid dynamic forces are comparatively negligible. This method is not, however, without fault. Direct subtraction of the inertial force from each 'wet' run introduces additional noise due to a mismatch in resonant vibration frequencies between the dry and wet tests. The mismatch is a result of the increase in apparent mass of the model in water and subsequent reduction in natural frequency. For high Reynolds number testing of large models (such as those utilised for the study of vehicle aerodynamics), further error in kinematics can be introduced as the carriage actuator responds differently due to increased model loading when in water. It is therefore desirable to improve the means by which both model vibration and the self mass force are rejected.

In the following sections the equations of motion for the wing are derived. By quantifying kinematics, including vibration, the inertial and non-inertial forces measured by the balance may be isolated with increased accuracy.

4.4.1 General equations of motion

First we will consider the equations of motion for a flat plate wing undergoing arbitrary planar translation. The idea is that through deriving the equations of motion, the components contributing toward the balance measured force can be isolated at any instance. Since the masses of the wing model and balance are easily quantifiable, their inertial contribution to the force may be calculated directly from rates of acceleration (measured through sensors, or the prescribed model kinematics). Added mass is also an inertial force. Assuming that the inviscid derived result is valid in a viscous flow, this force contribution may additionally be calculated. Most importantly, however, is the inertial load attributed to vibration. If rates of acceleration due to vibration are quantified, then vibration loads may be isolated and removed without requiring filtering techniques.

As shown in figure 4.6, a wing coordinate frame is defined xy, set at an angle β to a global XY coordinate. The fluid is assumed to be stationary at infinite distance from the XY coordinate origin. If the wing and balance system have a mass m_w, the forces (F) applied by the balance and onto the wing are

$$F_x = m_w a_{wx} - F_{other,x}, \tag{4.3}$$

$$F_y = (m_w + m_{vt}) a_{wy} - F_{other,y}, \tag{4.4}$$

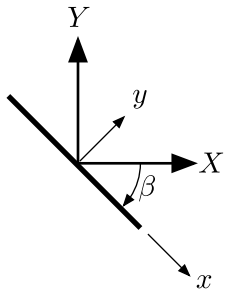

Fig. 4.6 Coordinate systems.

where a_w is an acceleration, and the subscripts x and y, define values in the x and y directions, respectively. The F_{other} terms represent any force that is not attributable to an inertial load. This incorporates all viscous fluid-dynamic effects. The term m_{vt} is the fluid added mass in the plate normal direction. This was given by equation (2.47). Resolving the components of force on the balance in the XY coordinate frame gives equations (4.5) and (4.6). Note that the forces that the wing applies to the balance, act in an equal and opposite direction to the force the balance applies to the wing. The terms $F_{other,X}$ and $F_{other,Y}$ are the transformed equivalent of $F_{other,x}$ and $F_{other,y}$. Thus

$$F_{b,X} = -(m_w + m_{vt})a_{wy}\sin\beta - m_w a_{wx}\cos\beta + F_{other,X} \tag{4.5}$$

$$F_{b,Y} = -(m_w + m_{vt})a_{wy}\cos\beta + m_w a_{wx}\sin\beta + F_{other,Y}. \tag{4.6}$$

For the experiments at hand the wing is constrained in the Y direction by the rails of the tank, therefore the wing can only experience accelerations in the X direction. The X direction acceleration, a_X, is directly measured with a carriage mounted accelerometer. Provided the carriage is stiff, the difference in measured acceleration and that physically experienced by the balance will be negligible regardless of the accelerometer position. Any high frequency vibrations relative to the two can be later filtered. It is best, however, to fix this accelerometer to the non-sensing side of the force balance. The latter was done for the present experiments. Resolving a_X into the wing coordinate system gives

$$a_{wx} = a_X\cos\beta, \tag{4.7}$$

$$a_{wy} = a_X\sin\beta. \tag{4.8}$$

Substituting equations (4.7), (4.8) into (4.5), (4.6), gives the balance applied force in terms of the inertial and non-inertial loads

$$F_{b,X} = -a_X(m_{vt}\sin^2\beta + m_w) + F_{other,X}, \tag{4.9}$$

$$F_{b,Y} = -m_{vt}a_X\sin\beta\cos\beta + F_{other,Y}. \tag{4.10}$$

These are conveniently given with respect to the prescribed carriage acceleration and wing angle of incidence.

4.4.2 Modal vibration

Here we derive the force component due to structural vibration. The strategy is to quantify rates of acceleration relative to the prescribed model kinematics, and use this to determine the force applied to the balance that is responsible for this acceleration. Of course it is desirable to make the model, carriage and balance system as stiff as possible to keep vibration forces to a minimum (this indeed spurred the design of the force balance in section 4.3). The aim of the proposed vibration correction technique is not to be perfect in all scenarios, but simply to make good, or acceptable data better. In the instance of structural vibration, such as that of the relatively thin cantilever design flat plate wing utilised in this study, for any given forcing disturbance applied there are an infinite number of resonant frequencies and vibration mode shapes that may be excited. The first three of which are shown in figure 4.7.

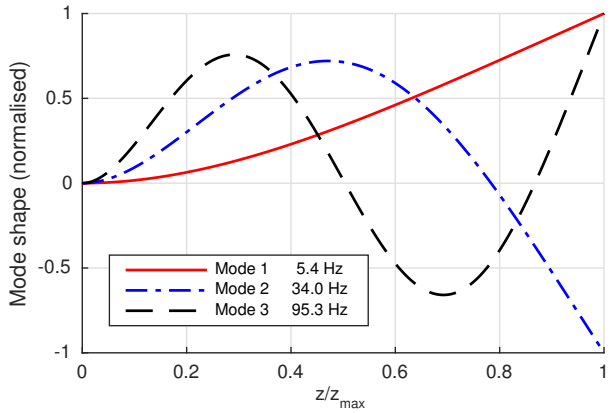

Fig. 4.7 Mode shapes and approximate resonant frequencies for the carbon wing immersed in water. Calculated assuming the wing behaves as a simply supported beam, with an added mass determined from the two-dimensional potential flow solution given by equation (3.27).

Typically low pass filtering is utilised to remove all vibration frequency content. Here it is proposed that the three axis accelerometer shown previously in figure 4.2 may be utilised to quantify forces on the balance associated with the first mode vibration, such that subsequent low pass filtering can be applied at a higher frequency to preserve transient fluid-dynamic forces. For the wing model, submerged in water, the resonant frequencies of the first and second vibration modes are approximately 5 and 34 Hz respectively, thus the frequency response may be significantly improved if forces attributed to the first mode are quantified. Assuming that the body has only one mode of vibration, or all frequency modes higher than the first are filtered, then the acceleration due to vibration (a_v), is the difference between the carriage and wing accelerations

$$a_{v,wx} = a_{wx} - a_X \cos\beta, \tag{4.11}$$

$$a_{v,wy} = a_{wy} - a_X \sin\beta. \tag{4.12}$$

The vibration accelerations $a_{v,wx}$ and $a_{v,wy}$ are dependent on the position of each accelerometer on the body. They must therefore be located such that they are away from the nodal points for the vibration mode to be compensated for. The accelerometer in the wing model shown in figure 4.2 is located toward the wing tip where it will have high acceleration associated with the first mode (at $z/z_{max} = 0.78$ in figure 4.7). Assuming the body is vibrating with simple harmonic motion, the force applied by the balance to the wing in order to accelerate the sensor in the x and y directions is

$$F_{v,wx} = m_{vx} a_{v,wx}, \tag{4.13}$$

$$F_{v,wy} = m_{vy} a_{v,wy}. \tag{4.14}$$

The mass terms (m_{vx} and m_{vy}) are modal or effective masses as the entirety of the model will not experience the same accelerations as that measured with the wing embedded accelerometer. It is important to note that the modal masses are in essence a scaling factor that converts an acceleration measured at a single point on the model, to a force applied to the model by the balance. It need not be equal to the sum of the physical and virtual masses of the body, but will scale proportionally with these terms. The modal masses can be found through an initial calibration as described in section 4.4.4. Resolving the vibration forces into the X- and Y-directions gives

$$F_{v,X} = -m_{vy} \sin\beta (a_{wy} - a_X \sin\beta) - m_{vx} \cos\beta (a_{wx} - a_X \cos\beta), \tag{4.15}$$

$$F_{v,Y} = -m_{vy} \cos\beta (a_{wy} - a_X \sin\beta) + m_{vx} \sin\beta (a_{wx} - a_X \cos\beta). \tag{4.16}$$

4.4.3 Combined force

The total force applied to the load cell is the sum of the mean acceleration and vibration components

$$\begin{aligned} F_X &= F_{b,X} + F_{v,X} \\ &= \underbrace{-a_X m_{vt} \sin^2\beta}_{\text{virtual mass}} \underbrace{- a_X m_w}_{\text{self mass}} + \underbrace{F_{other,X}}_{\text{remainder}} \\ &\quad \underbrace{- m_{vy} \sin\beta (a_{wy} - a_X \sin\beta) - m_{vx} \cos\beta (a_{wx} - a_X \cos\beta)}_{\text{vibration}}, \end{aligned} \tag{4.17}$$

$$\begin{aligned} F_Y &= F_{b,Y} + F_{v,Y} \\ &= \underbrace{-m_{vt} a_X \sin\beta \cos\beta}_{\text{virtual mass}} + \underbrace{F_{other,Y}}_{\text{remainder}} \\ &\quad \underbrace{- m_{vy} \cos\beta (a_{wy} - a_X \sin\beta) + m_{vx} \sin\beta (a_{wx} - a_X \cos\beta)}_{\text{vibration}}. \end{aligned} \tag{4.18}$$

Equations (4.17) and (4.18) show that through application of potential theory and select placement of inertial sensors, the measured force can be deconstructed into virtual mass, self mass and vibration

components. The remaining component encompasses forces arising from vorticity in the flow field. As we are uninterested in force contributions due to the model self mass and vibration, we can simply subtract these components to leave the virtual mass and viscous forces of interest.

4.4.4 Calibration

The mass components m_w, m_{vt}, m_{vx} and m_{vy} can be readily found. Calibration of m_w was performed simply through turning the balance on the side such that the wing and balance self weight force acts in the direction of the balance sensors ($m_w = \Delta F/\Delta a$). The virtual mass m_{vt} is calculated assuming the two-dimensional potential flow solution. The modal masses m_{vx} and m_{vy} may be determined from a vibration calibration experiment. For this the wing is subjected to an impulse load in water, resulting in free vibration. From the resulting acceleration and force measurements the modal masses may be calculated if it is assumed that all viscous forces are negligible in comparison to the inertial loads. Here the wing was set at an angle $\beta = -45°$, and the towing tank carriage displaced 10 mm with high acceleration and deceleration rates. The angle of $-45°$ is similar to the change in incidence for the gust ratio of 1.0 experiment presented in Chapter 7, and will induce vibration in both the x and y directions. The velocity profile is shown in figure 4.8a, and accelerations in figure 4.8b. After the impulse (from 20 seconds and onward) the tank carriage is at rest with negligible acceleration ($a_X = 0$) and the wing freely vibrates ($a_{v,wx} = a_{wx} \neq 0$ and $a_{v,wy} = a_{wy} \neq 0$). The masses m_{vy} and m_{vx} are found by solving equations (4.13) and (4.14). The vibration forces in the wing coordinate frame are $F_{v,wx} = -(F_X \cos\beta - F_Y \sin\beta)$ and $F_{v,wy} = -(F_X \sin\beta + F_Y \cos\beta)$, thus can be determined from the forces F_X and F_Y measured by the balance. These are given by figure 4.8c. Here the modal mass terms were averaged between the time of 20 to 21 seconds (5,000 data points). Given the balance and accelerometer error is of order 1%, post averaging the mass error is a negligible 0.015%. Each mass parameter for the calibration is given in table 4.1.

After calibrating each of the masses, the force across the range of the calibration run (and any other kinematic motion) may be deconstructed. For the calibration run the force deconstruction is shown in figure 4.8d. During the free vibration region the force due to vibration (dashed green line, given by equation 4.15) closely follows the transient force fluctuations measured using the balance (F_x, solid blue line). The virtual and self mass terms attributable to the prescribed carriage motion can be calculated from equation (4.17) using the measure of instantaneous carriage acceleration a_X. Subtraction of the vibration, virtual mass and self mass components from F_x leaves the remainder force contribution (solid black line). There is only minor variation in the remainder force component after the velocity impulse. As we expect inertial force contributions to be dominant during free vibration, this indicates that the decomposition technique was successful. While some low pass filtering was still required to remove high frequency vibration and electrical noise, it was possible to increase the cut-off frequency to approximately 5 times the first mode resonant frequency.

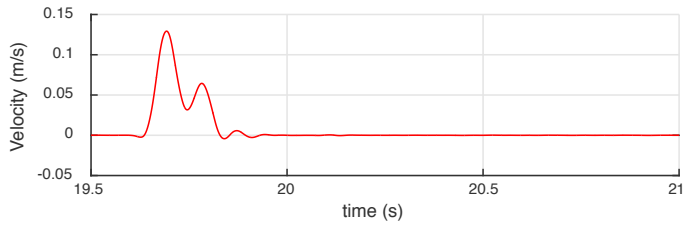

(a) Velocity profile

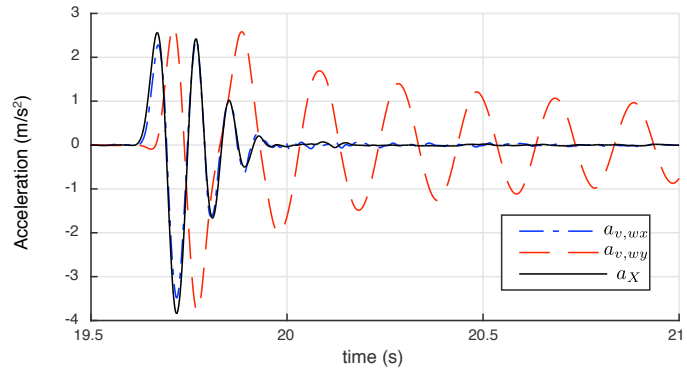

(b) Accelerometer measurements

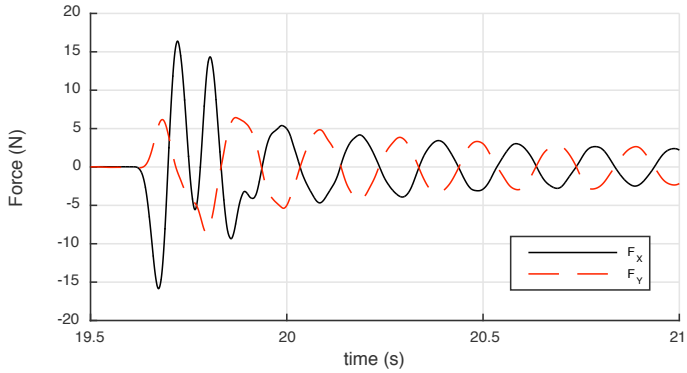

(c) Force balance measurements

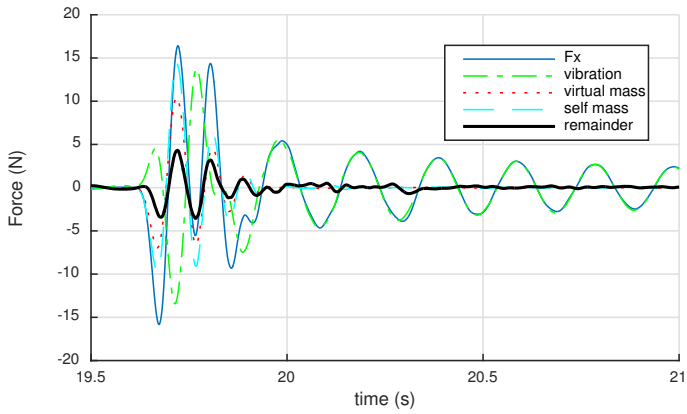

(d) X-direction force decomposition (-drag)

Fig. 4.8 Calibration of inertial force system. A moving average with a period of 0.05 seconds is applied to smooth high frequency noise.

Table 4.1 Mass parameters (kg)

m_w	m_{vx}	m_{vy}	m_{vt}
3.75	1.685	3.85	5.43

4.4.5 Note on wing vibration

If we assume that the wing, after encountering the calibration impulse, vibrates with an acceleration of constant amplitude, we may simply quantify the displacement of vibration. Figure 4.9a shows a Fast Fourier Transform (FFT), of the $a_{v,wy}$ vibration signal shown in figure 4.8b. This was taken over the range $20 \leq t \leq 22$ seconds. The FFT shows that accelerometer embedded within the wing, is recording an average amplitude of 1 m/s^2 at the first mode resonant frequency of 5.0 Hz.

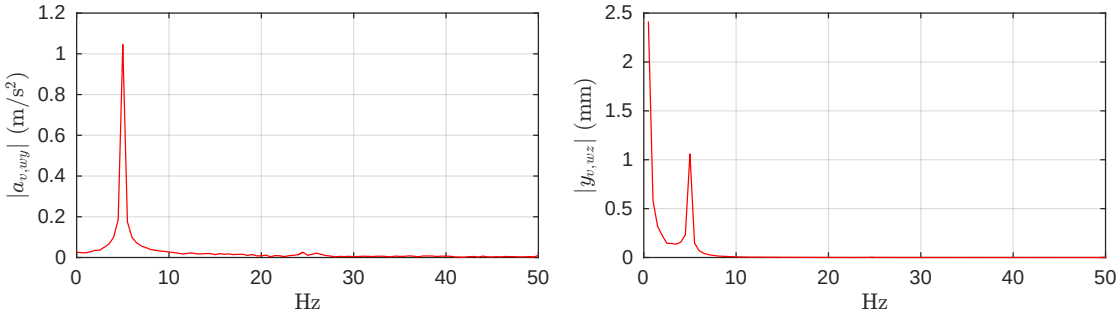

(a) Acceleration amplitude **(b)** Position amplitude

Fig. 4.9 Fast Fourier Transform (FFT) of the $a_{v,wy}$ signal over the range $20 \leq t \leq 22$ seconds.

The position of the wing, $y(t)$, is equal to the sum of each of the frequency modes ($f_{Hz,n}$). If all phase information is omitted,

$$y(t) = \sum_{n=1}^{\infty} |y_n| e^{i2\pi f_{Hz,n} t}. \tag{4.19}$$

The acceleration, equal to the second derivative of the position with respect to time is

$$a_{v,wy}(t) = \sum_{n=1}^{\infty} -(2\pi f_{Hz,n})^2 |y_n| e^{i2\pi f_{Hz,n} t} \tag{4.20}$$

$$= \sum_{n=1}^{\infty} |a_{v,wy,n}| \, e^{i2\pi f_{Hz,n} t}. \tag{4.21}$$

Omitting the negative, we therefore can approximate the displacement amplitude, resulting from the vibration,

$$|y_n| = \frac{|a_{v,wy,n}|}{(2\pi f_{Hz,n})^2}. \tag{4.22}$$

Equation (4.22) is plotted in figure 4.9b. We see that the first mode resonant frequency, at $f_{hz} = 5.0$ Hz, oscillates with an amplitude of approximately 1 mm. Given the impulse applied to the wing is an extreme loading case, we therefore expect wing vibrations for the subsequent surge and gust encounter experiments to be of order 1 mm for the carbon fibre wing. While we have quantified the vibration characteristics for the carbon fibre wing, those of the glass wing are similar. This is because both wings have similar stiffness properties, while the fluid added mass is an order of magnitude greater than the physical mass of each wing model.

4.5 Dye flow visualisation

For each experiment, dye was injected into the flow field to visualise features such as vortices. The dye used was a mixture of soy-milk and methylated spirits. Milk based dye retards diffusion, thereby forming coherent filaments and has good reflective properties (Clayton and Massey, 1967; Stevens, 2013). The soy-variety has the additional benefit of a significantly longer shelf life. Methylated spirits was added to the milk to account for the slight difference in densities between the milk and water (approximately 1030 and 999 kg/m^3 respectively (Wong, 1988)), thereby causing slight spanwise drift. The required mass fraction of methylated spirits (m_e) to milk (m_m) is

$$\begin{aligned} \frac{m_e}{m_m} &= \frac{\rho_e}{\rho_m}\frac{\rho_w - \rho_m}{\rho_e - \rho_c} \\ &= 0.121, \end{aligned} \tag{4.23}$$

where ρ_e is the density of methylated spirits, ρ_m is the density of milk and ρ_w is the desired density (999 kg/m^3). For each test case the dye mixture was injected using a syringe pump at points where flow is entrained into the shear layers leaving the edges of the plate. For the translating wing case, the injection locations were approximately 4 mm from each plate edge, mid span, on the leeward face. For the rotation case dye was injected on the advancing faces at an equivalent location. For the gust cases the dye was injected directly at the leading and trailing wing edges. The flow rate was selected nominally to match the fluid, albeit this was not always possible given the unsteady nature of the experiments. The dye was illuminated using the same laser configuration as for the PIV (described in section 4.6), although the beam was defocussed to a width of approximately 20 mm to illuminate dye that has advected in the spanwise direction. All photographs are taken using Phantom M310 high speed cameras to facilitate synchronisation with the PIV image frames.

4.6 Particle Image Velocimetry

PIV was the primary tool used to obtain quantitative flow field measurements. A schematic of a typical PIV configuration is shown in figure 4.10 and the basic principle of operation is as follows. Small tracer particles are suspended within the working fluid, which closely follow its motion. A plane of

particles is illuminated using a light source, which is photographed using a high speed camera. Each image frame is subdivided into interrogation windows containing a group of particles. For planar PIV, the average particle displacement in pixels within each interrogation area is calculated by means of a two-dimensional cross-correlation between two consecutive image frames, separated by the time period δt. The displacement of particles in pixels is related to a physical distance $\delta \mathbf{x}(x,y,t)$ by an initial calibration to a planar object with markers of known offset at the particle plane. With this information, the velocity is

$$\mathbf{u}(x,y,t) = \frac{\delta \mathbf{x}(x,y,t)}{\delta t}. \tag{4.24}$$

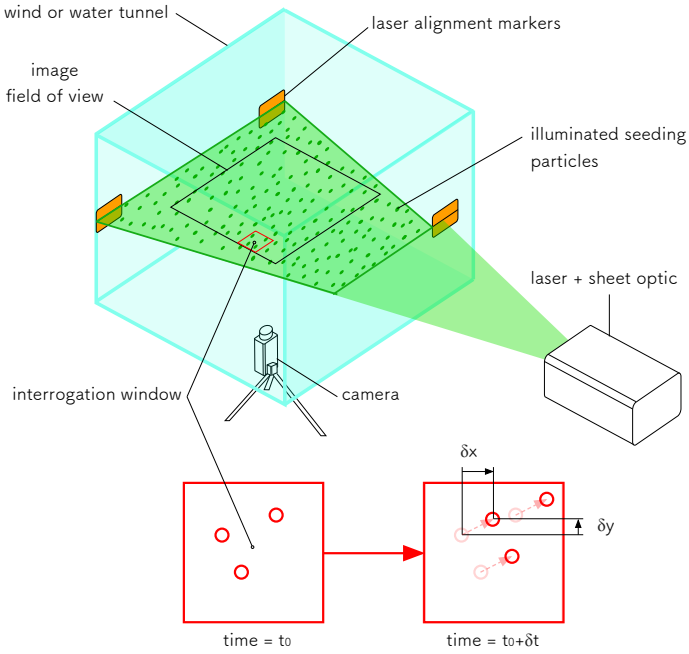

Fig. 4.10 Schematic showing the principles of operation, and alignment, of a basic PIV configuration.

4.6.1 Implementation

A commercial LaVision high speed planar PIV system and the DaVis processing software was used for this study. Within DaVis, velocity vectors are computed in Fourier space for computational efficiency. For each interrogation window a two-dimensional Fast Fourier Transform (FFT) is performed. The Fourier cross-correlation function is the product of the Fourier conjugates of the window at time $t = t_0$, and $t = t_0 + \delta t$, which is then related back to the real frame using an inverse transform. The correlation is performed using an iterative procedure. In this study, first a large interrogation window of 32×32 pixels was used. This gives a high reliability velocity measurement as numerous particles are included within each interrogation window, thereby improving the signal to noise ratio. To improve spatial

resolution this is followed by two passes of a 16×16 pixel window for the surge and gust cases, while 12×12 pixels was used for the rotation case. The final passes have a 50% interrogation window overlap, giving vector densities of approximately 50 vectors per chord for the surge and rotation cases, and 40 for the gust. The time period between consecutive frames was selected such that particles within regions of maximum local velocity, travel up to approximately 3-4 pixels.

The light source is a dual cavity Litron PIV300 series Nd:YLF pulsed laser with a wavelength of 527 nm. The pulse frequency per laser cavity can be varied from 0.2 to 10 kHz, the maximum energy output per pulse is 20 mJ and the pulse width is nominally 150 ns. For seeding, titanium dioxide particles with a maximum diameter of 45 μm are used as the particles have a high reflectivity and low settling rate in water. Since the density of TiO_2 does not match that of water, a fluid tracking error can arise due to each particle having a different acceleration rate to the local fluid when subjected to a pressure gradient. Pitt Ford (2013) showed that the particles are sufficiently small and the flow velocities low such that this following error is negligible.

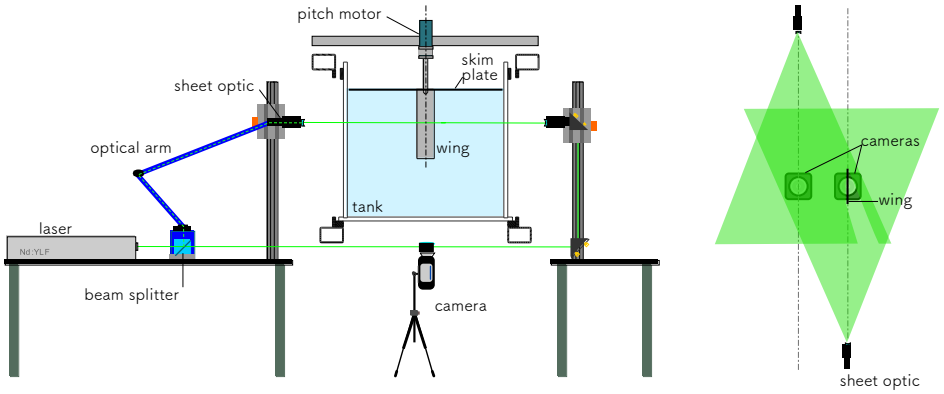

(a) End view **(b)** Top view

Fig. 4.11 Schematic of towing tank, PIV and flow visualisation configurations, showing the laser overlap plane and camera setup. Adapted from Stevens and Babinsky (2017).

The laser configuration used for the surge and rotation test cases is shown in figure 4.11. The dual light sheet method developed by Stevens and Babinsky (2017) is utilised to enable illumination of particles on both sides of the wing model. This setup is essential for the quantification of distributions of boundary-layer vorticity, as described in Chapter 5. Alignment was performed by placing three dual sided photo-luminescent markers on the glass sides of the tank. The markers are illustrated in figure 4.10. Two markers were placed on one side of the tank and the third on the other. The purpose of the markers is to provide three nodal points in space that define the desired laser plane. The initial position of each marker was established by casting a horizontal laser plane at the mid-span height of the wing, using a low-powered auto-levelling laser. Each of the PIV laser beams is subsequently aligned to the markers. The final laser alignment is best performed with the tank filled with water. Air has a refractive index of approximately 1.0, whereas water at 20°C is approximately

1.3 (Fowles, 1989). Filling the tank changes the refractive index of the bulk fluid volume, resulting in the deflection of the laser beams entering the tank if the incident angle is not perpendicular to the glass. The focal point of each laser sheet was for all cases set at the wing centre axis, giving a maximum laser thickness of approximately 1 mm at the edge of each observation window. The dual camera configuration illustrated in figure 4.11b, was used to increase the spatial field of view and resolve optically obstructed regions. These are caused by the section of wing below the particle plane. Obstructed vectors from each camera were first individually masked (set to nan) and subsequently stitched. The stitching was performed by laying a new vector grid across both frames, with vectors determined using two-dimensional linear interpolation. Vectors within the view overlap region were averaged.

4.6.2 Measurement error estimation

A major source of PIV measurement error is attributed to an effect called 'peak-locking'. This arises due to the digitisation of photographic images. If the light from a single particle is only detected with a single image sensor pixel, then the particle position within the pixel is unknown. It is thus desirable to smear light from a single particle over multiple pixels, thereby the sub-pixel position may be resolved by taking the centre of a Gaussian function fit to the light distributed across pixels. Prior to data recording, images were manually checked to ensure the particle size is 2-3 pixels, deemed the optimum by Raffel et al. (2007). For configurations whereby light was notably isolated to a single pixel the cameras were manually defocussed. A typical image frame prior to processing is shown in figure 4.12.

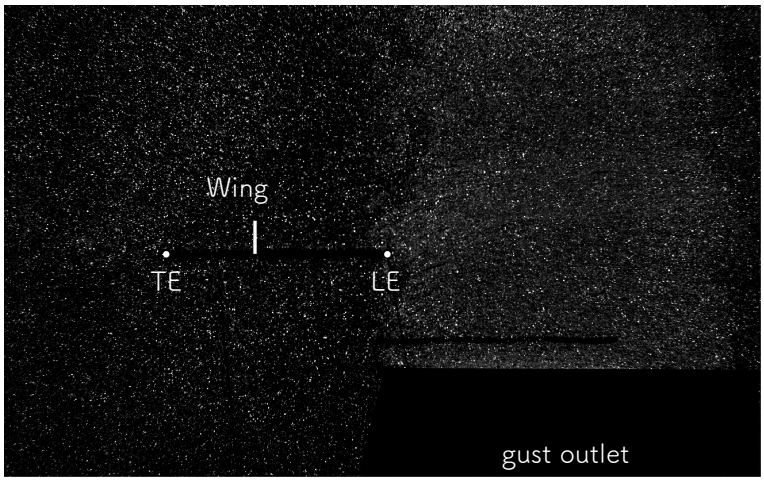

Fig. 4.12 Typical PIV raw image, glass wing for the gust rig configuration. The leading and trailing wing edges are indicated.

Final peak-locking checks were performed after the first test run. Figure 4.13a shows a sample auto-correlation for an interrogation window of 32×32 pixels. The base of the autocorrelation peak is approximately 6 pixels, thus indicating a particle size of 3 pixels. Statistics were additionally gathered

across the whole measurement plane. Figure 4.13b shows the cumulative sum (count) of particle images, binned into displacement ranges in pixels (for example the sum of all particle pairs within the range of 2 to 2.1 pixels). There is little bias of the particle displacements toward integer values. The peak locking effect is therefore small. During the cross-correlation process, particles of higher light intensity bias the measure of particle displacement. To mitigate this effect the light intensities within a moving window of 10×10 pixels were normalised and a background subtraction performed to minimise surface reflections and ambient variations in laser intensity.

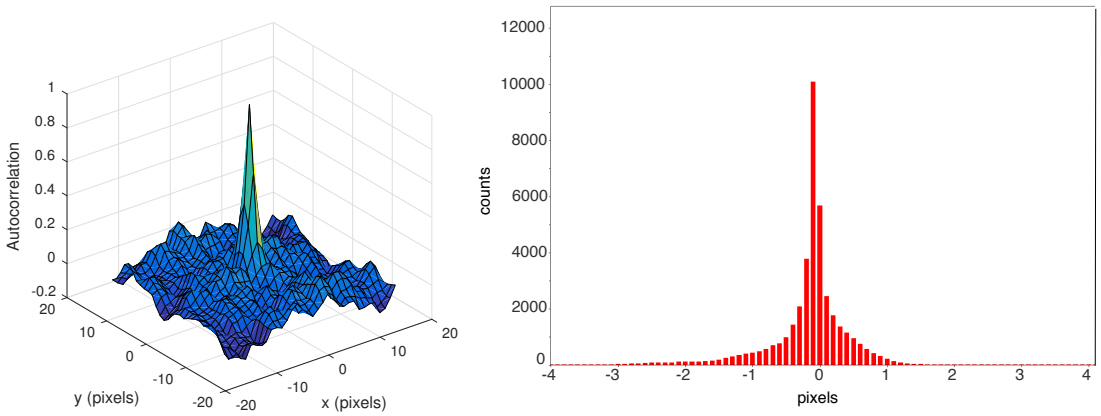

(a) Sample auto-correlation **(b)** Particle displacement histogram

Fig. 4.13 Measures used to check for peak-locking.

Other sources of measurement error were estimated based on the work of Raffel et al. (2007) and Nobach and Bodenschatz (2009), who simulated the PIV technique using synthetically generated particles. The error (in pixels) for each cross-correlated interrogation window may be expressed as,

$$\sum \varepsilon_{\mathrm{PIV}} = \varepsilon_{\mathrm{bias}} + \varepsilon_{\mathrm{rms}_0} + \varepsilon_{\mathrm{rms}_\delta} + \varepsilon_{\mathrm{rms}_\rho} + \varepsilon_{\mathrm{rms}_i}. \tag{4.25}$$

The root mean square (rms) error $\varepsilon_{\mathrm{rms}_0}$ is due to random variation in particle image diameter, $\varepsilon_{\mathrm{rms}_\delta}$ is attributed to image displacement, $\varepsilon_{\mathrm{rms}_\rho}$ results from particle density in each interrogation window and $\varepsilon_{\mathrm{rms}_i}$ from variation in particle intensity due to particle motion in the direction perpendicular to the laser plane. The consistent bias error, $\varepsilon_{\mathrm{bias}}$, is attributed to loss of particle pairs from each cross-correlation window due to the in-plane motion of the fluid. An estimate for each parameter is given in table 4.2. Assuming a particle displacement of approximately 4 pixels, and total random error of 0.145 pixel, the error is 3.6%. To reduce random errors a batch average of 5 test runs was taken for each test case. Following averaging, the sum of random errors reduces to 1.6% since standard error scales with $1/\sqrt{N}$, where N is the number of samples (Adrian and Westerweel, 2011). The bias error is 0.25%, therefore the total error is estimated to be less than 2%.

$\varepsilon_{\text{bias}}$	$\varepsilon_{\text{rms}_0}$	$\varepsilon_{\text{rms}_\delta}$	$\varepsilon_{\text{rms}_\rho}$	$\varepsilon_{\text{rms}_i}$
-0.01	0.01	0.01	0.025	0.10

Table 4.2 Estimation of PIV error from Raffel et al. (2007) and Nobach and Bodenschatz (2009), (pixels).

4.7 Gust rig

The reader is reminded of the main aims of this work; to develop understanding of the mechanisms which contribute toward force generation in a large amplitude transverse wing-gust encounter, and identify how they may differ compared to Küssner's linear theory. To achieve these aims, it is therefore desirable to experimentally replicate Küssner's modelled conditions as closely as possible, such that gust ratio variation effects may be quantified in isolation. This necessitates the experimental reproduction of a 'sharp edged' transverse gust with variable amplitude. Next, in section 4.7.1 the advantages and disadvantages of existing gust generator systems from the literature are reviewed. The objective of the section is to identify features of existing designs that may be adapted to facilitate the practical generation of the desired gust profile. This is followed by a description of the gust generator designed for this work, in section 4.7.2. Here the particular challenges of developing a towing-tank based gust generator, primarily, fitting the system in the confines of a glass walled tank are also described. Finally, an assessment of the performance of the gust rig is given in sections 4.7.3 to 4.7.8.

4.7.1 Review of gust generators

In the literature, gust generator system may be categorised into fixed and moving model designs. The examples of fixed model gust apparatus typically operate by pitching a pair or cascade of actuated aerofoils upstream of the model in a wind tunnel. This method, illustrated in figure 4.14a, has been adopted by Brion et al. (2015); Ham et al. (1974); Patel and Hancock (1977); Saddington et al. (2014); Tang and Dowell (2010); Tang et al. (1996) and Patel (1982). To create a transverse velocity component, the vanes are periodically pitched in phase with each other, thereby shedding an alternating sequence of positive and negative vortices. Each vortex pair induces upwash or downwash as they advect past the test model. Axial velocity perturbations may be generated by pitching the aerofoils out of phase. Gust ratios can, however, be limited to approximately 0.3 due to flow separation on the vanes, coupling of the free stream velocity with vane deflection angle and increased turbulence levels due to the vane wakes.

Another method, proposed by Ryan and Dominy (2000) and adapted by Volpe et al. (2013) for the study of road vehicles in cross wind, utilises two intersecting wind tunnel sections separated by actuated shutter vanes. This design is illustrated in figure 4.14b. The main tunnel is operated in a steady manner, while shutters are sequentially opened at a rate equal to the main tunnel free stream

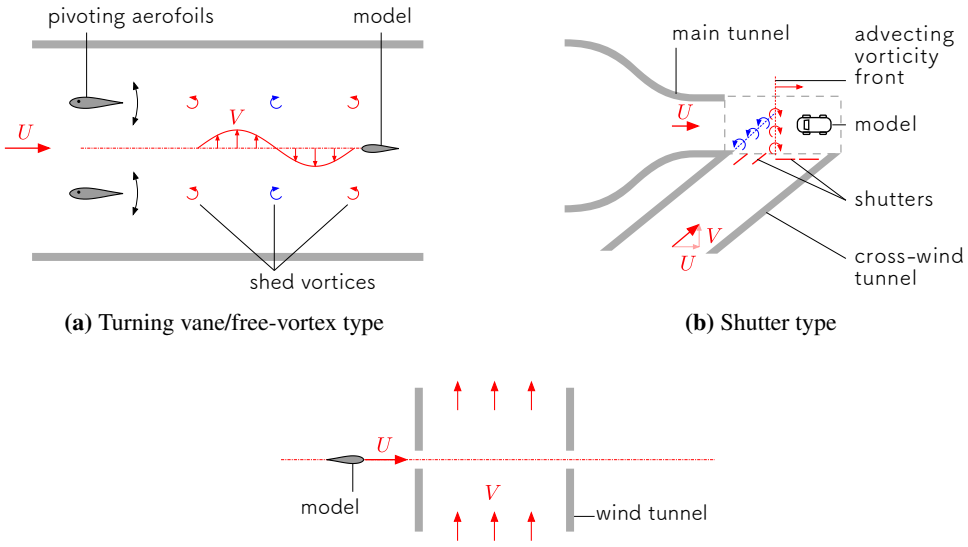

(a) Turning vane/free-vortex type

(b) Shutter type

(c) Towed model type

Fig. 4.14 Comparison of wind tunnel based gust apparatus.

to allow air from the cross flow wind tunnel to enter the working section. The horizontal velocity component of the cross wind tunnel is matched to the streamwise velocity of the main tunnel. The mismatch in vertical components results in the formation of a vorticity front that grows in size and advects over the test model. Following this the model experiences a uniform change in the angle of incidence. In the experiments conducted by Ryan and Dominy (2000), sharp edged gusts were achieved, however, significant velocity under- and over-shoots from the intended top-hat profile were observed. The advantage of this system is that in the model frame of reference a gust of infinite length can be generated. The shutter system is, however, complex. Furthermore, the gust tunnel appears to be optimised for a single gust ratio.[†]

Humphreys (1995) developed a towed model gust facility for the study of railway vehicles, shown schematically in figure 4.14c. A test model is propelled along rails through an opening in the test section of an open return wind tunnel. This system facilitates the use of flow conditioning within the wind tunnel, generating both a sharp edged gust and boundary-layer profiles for their study. By varying the model to wind tunnel velocity, practically any gust ratio may be generated. A water towing tank based gust generator was developed by Perrotta and Jones (2017), which works using a similar principle. The gust outlet comprised of 30 adjacent cylindrical nozzles. The conical jets from each nozzle merge into an approximately planar free jet. This is then passed through a wire mesh flow straightener to remove streamwise 'waving' of the jet. Away from the screen the jet has a 'sine-squared' time averaged velocity profile. It is here that a wing model is towed through. The

[†]It is possible that the system can be run at multiple gust ratios, however, the angle of the vorticity front will not be normal to the free stream of the main tunnel. It is unknown whether this is intended.

advantage of the system is that it is simple and gives full variation in the jet velocity. If the jet outlet manifold has sufficient length, then uniform flow may be induced across the full span of the test model. The disadvantages for our intended application, is that the velocity profile is not 'sharp edged'. The gust shear layers are not clearly defined, and the jetting of high momentum fluid into the tank results in high levels of entrainment and turbulent mixing. This will consequently act to obscure flow features of interest and means that the bulk of the gust flow is rotational.

From the review of the gust apparatus in the literature, summarised in table 4.3, it is apparent that a towed model based design is most suited for the present work. By incorporating the design features of both Humphreys (1995) and Perrotta and Jones (2017), a sharp edged gust profile with variable gust ratios in excess of $GR = 1$ may be generated. In the following section, we outline the apparatus that was developed to achieve the ideal gust profile for our application, and the additional 'pressures' which influenced it.

Table 4.3 Comparison of gust generators from the literature, with the system developed to replicate Küssner's gust (CUED gust generator).

Authors	Fluid	Apparatus Type	Gust profile	Variable GR	GR maximum
Tang and Dowell (2002); Tang et al. (1996)	air	Upstream vanes (circ. control)	sinusoidal	yes	0.035
Saddington et al. (2014)	air	Upstream vanes (pitching)	sinusoidal	yes	0.2
Brion et al. (2015)	air	Upstream vanes (pitching)	sinusoidal	yes	0.005
Patel (1982); Patel and Hancock (1977)	air	Jet shear layer perturbation	sinusoidal	yes	0.043
Ham et al. (1974)	air	Upstream vanes (circ. control)	sinusoidal	yes	0.16
Ryan and Dominy (2000)	air	Shutter cascade	top-hat	-	0.41
Volpe et al. (2013)	air	Shutter cascade	top-hat	no	0.57
Humphreys (1995)	air	Towed model	top-hat	yes	∞
Perrotta and Jones (2017)	water	Towed model	sine-squared	yes	∞
CUED gust generator	water	Towed model	top-hat	yes	∞

4.7.2 Design of the towing tank gust generator

Assuming it is possible to generate a sharp edged velocity profile, the primary design consideration is the gust size. This necessarily impacts the ducting geometry, pump, and power requirements of the system. It is clearly not possible to generate a gust of infinite length. It was further decided that all gust apparatus must reside within the towing tank, as the glass walls of the test section cannot be modified. This further requires the gust apparatus to be modular, such that the equipment may be removed for other test configurations. The necessary gust width may be estimated based on the ideal Küssner response shown in figure 4.15. At $s/c = 2$, the force reaches approximately 70% of the steady state. Thereafter unsteady effects rapidly diminish. For a wing of 120 mm chord length, a gust outlet of 2 chords also approaches the limit of that practical within the confines of the towing tank. A width of 240 mm was therefore selected as the desired gust width[‡]. Thereafter, the challenge is designing the ducting and pump hardware such that a steady 'sharp edged' velocity profile can be achieved practically.

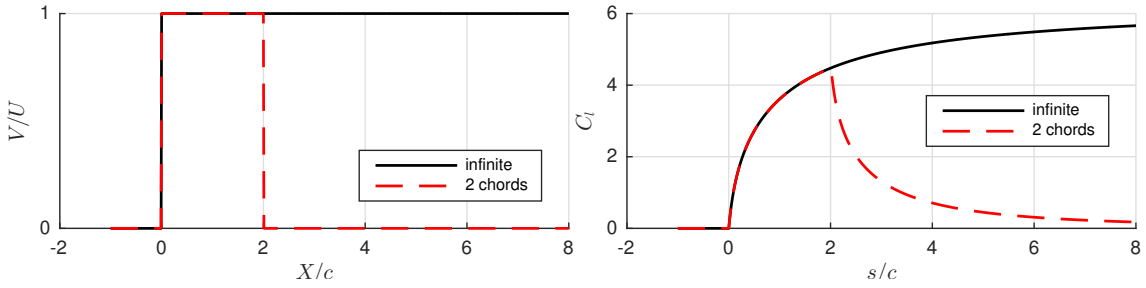

(a) Gust velocity with position **(b)** Lift coefficient with position

Fig. 4.15 Küssner response to a unit gust of infinite extent and a finite width of 2 chord lengths.

The setup constructed for this work is shown in figure 4.16. At the end of the towing tank resides a 2.2 kW 3-phase motor, driving a submerged axial flow pump through a reduction pulley configuration. This has a 2.25:1 gear ratio. The motor is combined with frequency inverter to enable continuous variation of pump speed, and therefore gust cross flow velocity. The pump is connected by flexible hosing to the gust outlet, situated within the glass test section toward the centre of the tank. To create a 'sharp edged' velocity profile, flow conditioning is utilised within the ducting. Details are shown in figure 4.17. Flow from the pump is passed through a series of constant cross-sectional area sections that transition from the circular geometry of the pump hose (250 mm diameter) to a rectangle geometry the height of the gust (600 mm or 1.25 times the wing span, by 80 mm). This height was selected to ensure that the free shear layer at the base of the gust does not intersect the wing tip (at 480 mm). Prior to the geometry transition there is a pair of vanes to remove any swirl from the pump. A fine mesh screen with a pressure drop coefficient of $K = \Delta P / \frac{1}{2}\rho U^2 = 2.0$ (at 0.5 m/s) is located directly following the transition section to reduce axial velocity perturbations. Following the

[‡]larger gust lengths are possible with a smaller chord length wing

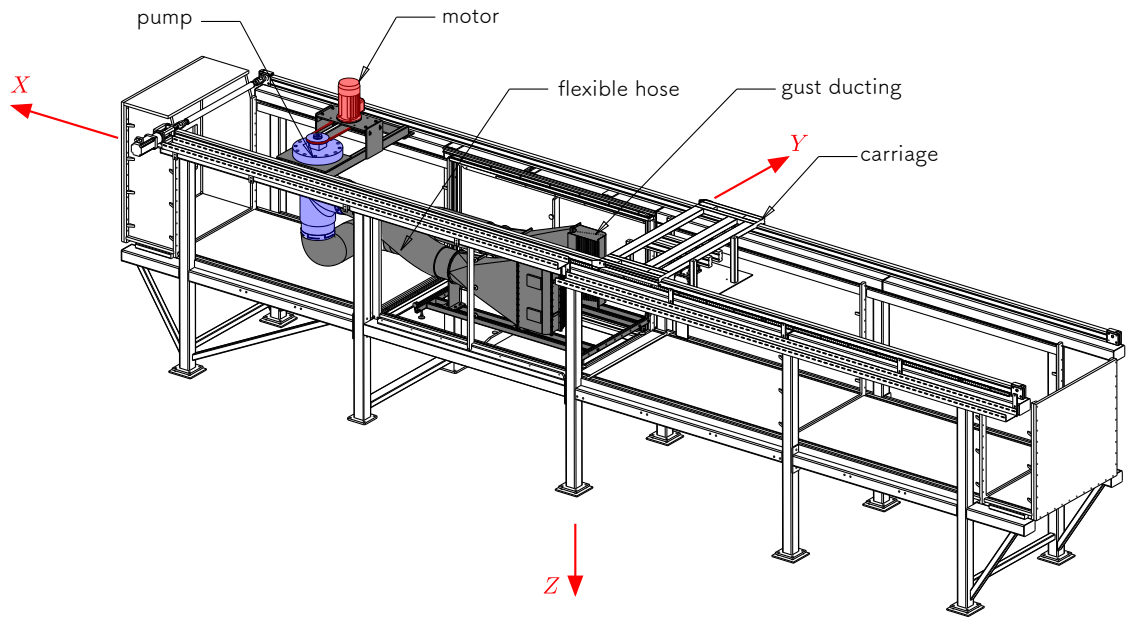

Fig. 4.16 Schematic of the gust rig inside the tank.

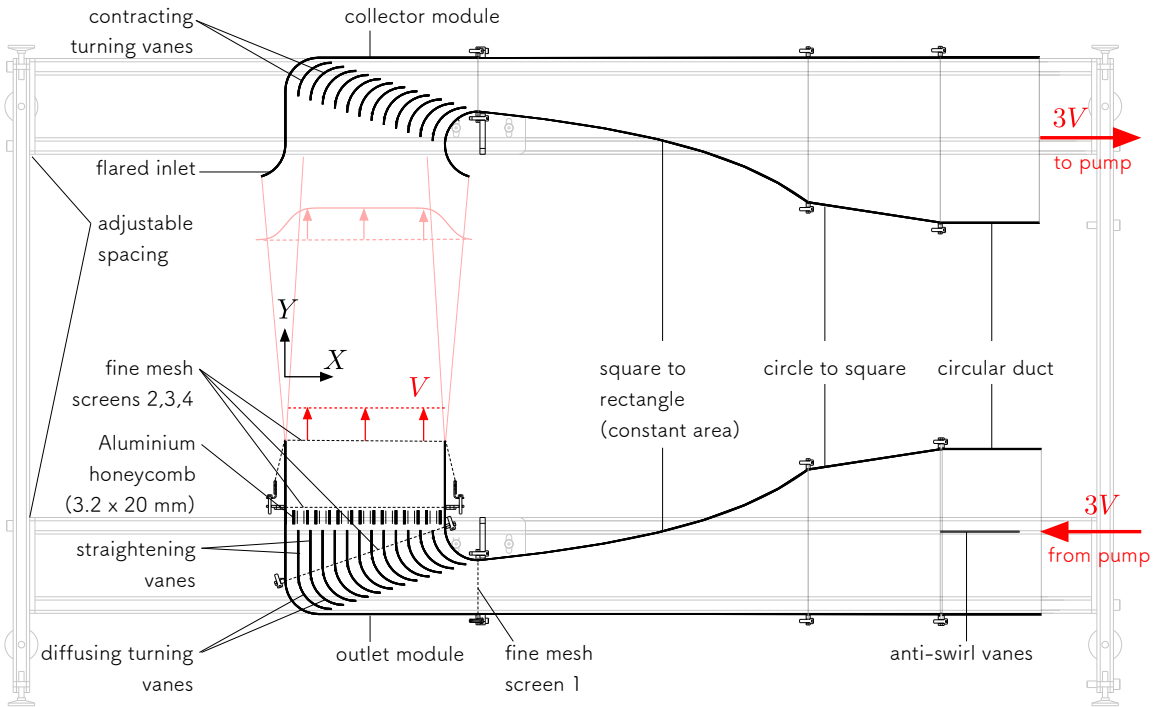

Fig. 4.17 Detail of the gust outlet and collector. View from below the tank.

transition sections the flow must both be turned 90° such that it can exit the outlet ducting in the direction perpendicular to the carriage path, and it must additionally be diffused to the desired gust width.

Within the confines of the tank there is insufficient space to diffuse the flow prior or after the turning vanes. To overcome this constraint diffusing turning vanes are utilised. Without boundary-layer control diffusing turning vanes have been shown to have total pressure losses similar to that of standard turning vanes without diffusion (Friedman and Westphal, 1952), although the maximum expansion ratio tested in the literature is 1.45. The behaviour of a cascade of diffusing turning vanes with area ratio of 3 is unknown, but as shown in figure 4.18a, flow separation leading to non-uniformities and unsteadiness is likely due to the severely adverse pressure gradients imposed on boundary-layer over the vanes.

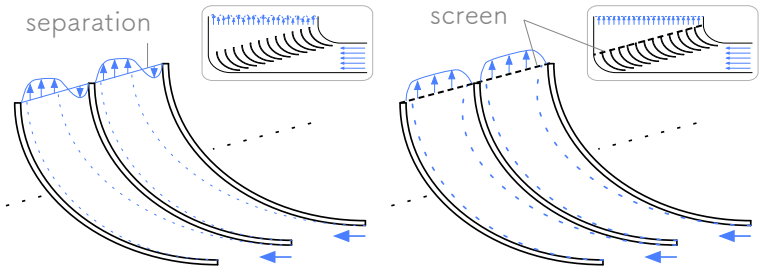

(a) Without screen **(b)** With screen

Fig. 4.18 Hypothesised flow from diffusing turning vanes with and without outlet screen.

To reduce detrimental effects due to separation, flow control similar to that discussed by Mehta and Bradshaw (1979) for wide angle diffusers is utilised. A wire mesh screen is stationed in the diffuser to encourage flow reattachment and uniformity. According to the guidelines by Mehta and Bradshaw (1979), a pressure drop coefficient of $K = 2.0$ will suffice for an expansion ratio of 3. It is desirable to use multiple lower K screens distributed through the diffuser, however, this is impractical given the geometric constraints here. A single high K screen was instead placed at the vane outlet plane (figure 4.18b). According to Mehta (1985), flow passing through wire mesh screens is 'refracted' toward the screen normal direction. Since the screen behind the turning vanes is on an angle relative to the desired flow path, refraction toward one side of the outlet is expected. This may lead to a non-uniform outlet velocity profile. Straightening vanes are therefore placed directly behind the screen. Following the vanes the velocity profile is 'conditioned' using an aluminium honeycomb (3.2 mm cell width) and two high K mesh screens ($K = 8.6$ at 0.5 m/s) to reduce turbulent perturbations and non-uniformities due to vane boundary-layers. On the outlet, spatially variable resistance screens could be installed to generate non top-hat outlet profiles, but these are not used here.

Downstream of the outlet, the return circuit of the pump is used to 'collect' the gust. A set of turning vanes identical to the outlet are utilised. For this section no screens are required as the flow is

entering a gradual contraction. The jet was collected to minimise the turbulence in the 'still' regions of the tank. The collector prevents the majority of the jet from mixing with the still fluid, and prevents the bulk transport of fluid toward the pump inlet which would be located elsewhere in the tank. It is shown later in section 4.7.3 that unsteady shear layers are developed on the edges of the jet, but there is comparatively little disturbance to the ideally quiescent flow regions either side of the gust[§]. The gust outlet and collector are mounted to an adjustable frame that allows the relative spacing to be varied between 240 to 600 mm in 120 mm increments. This is to enable the wing to be moved closer to the outlet to adjust the 'sharpness' of the gust shear layers at the wing entry point, as well as enable the study of blockage effects on the response of the wing.

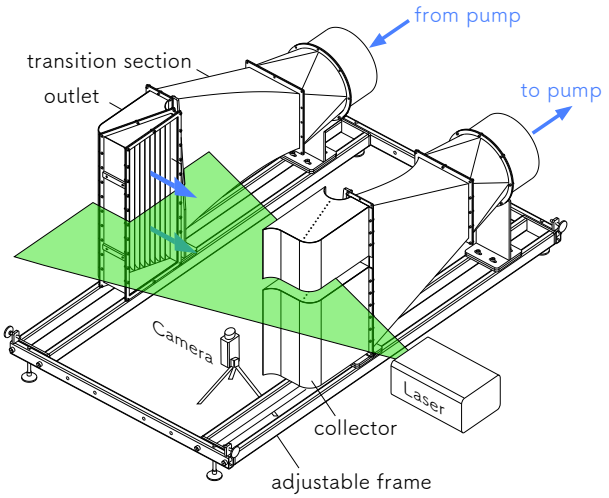

Fig. 4.19 Schematic showing the split collector module for PIV laser access.

Finally, the gust rig system severely reduces optical access from the sides of the towing tank, but laser access is required for PIV. The gust collector module is therefore split into two sections, as shown in figure 4.19. The gap in the collector is at the mid-span height of the wing, enabling a laser sheet to be cast horizontally across the towing tank. The gust outlet was not divided to reduce flow disruption at the measurement plane. This prevents the dual light sheet setup described in section 4.6 from being used. Both sides of the wing must be resolved to employ the methods for extracting added mass effects (described in Chapter 5). The glass wing described in section 4.2 is therefore used for all PIV measurements of wing-gust interactions.

4.7.3 Streamwise velocity profile

A time average of the flow field, taken over a 10 second period is shown in figure 4.20. This is normalised by the mean gust velocity $\overline{V}$, defined as the average gust velocity across the range $0 \leq X/c \leq 2$. Generally, the velocity profile matches the ideal top-hat distribution well, however, the edges of the velocity profile spread due to the growth of the shear layer with increasing distance

[§]This was measured over time periods typical to that of test run, approximately 30 seconds from startup.

from the gust outlet (Y/c)[¶]. Diffusion of vorticity in the shear layers either side of the gust is visible in figure 4.20a. The streaks of vorticity and corresponding fluctuations in the mean velocity profile inside the gust (from $0 < X/c < 2$) are due to the wakes of the turning vanes upstream of the gust rig outlet (see figure 4.17). This suggests that the flow through some of the diffusing turning vanes may have separated, or it may be attributed to thickening of the boundary-layers as a consequence of the adverse pressure gradient.

4.7.4 Flow unsteadiness

The unsteadiness of the cross flow region is quantified by the parameters $I_u = \frac{\sqrt{\overline{(u')^2}}}{\overline{V}}$ and $I_v = \frac{\sqrt{\overline{(v')^2}}}{\overline{V}}$, which is the ratio of the average u- and v-component perturbation velocities (u' and v' respectively) relative to the average gust velocity $\left(\overline{V}\right)$. In figure 4.21, I_u and I_v shown are calculated from 1000 consecutive PIV frames (10 seconds) taken once the gust flow has reached steady state. This parameter is analogous to a turbulence intensity, however, represents a spatial average due to the size of each PIV interrogation window (Westerweel, 1999). For the present setup the side length of each processing interrogation window is 5.6 mm (4.6 % chord), thus turbulent eddies with smaller length scales are not resolved. The error associated with this discretisation of the flow field is considered in section 5.3.

Perturbations in the u and v velocities have a standard deviation of approximately 15 to 20 % of the mean gust velocity within the gust shear layers. The unsteadiness peaks reduce in magnitude and width closer toward the gust outlet. At the centreline of the gust the perturbations are typically between 2 and 3 %, which is similar to the 'undisturbed' regions outside the gust.

[¶]An analytical expression of the gust shear layer velocity profile may be found in the text by Pope (2000), the plane mixing layer in Chapter 5.

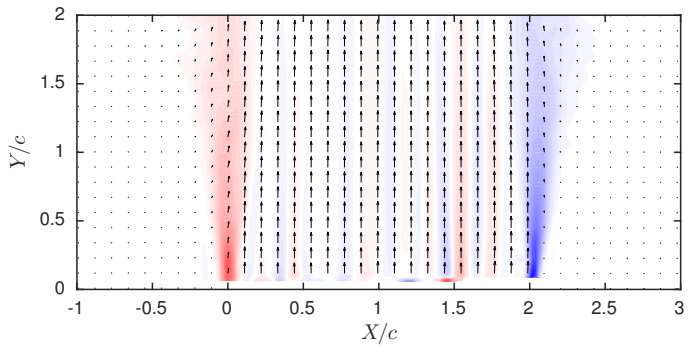

(a) Mean vorticity field

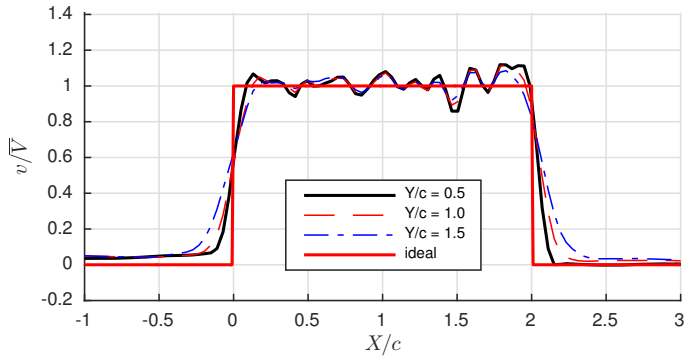

(b) Mean velocity profile

Fig. 4.20 Mean flow and vorticity with position. Motor speed: 700 Revolutions Per Minute (RPM).

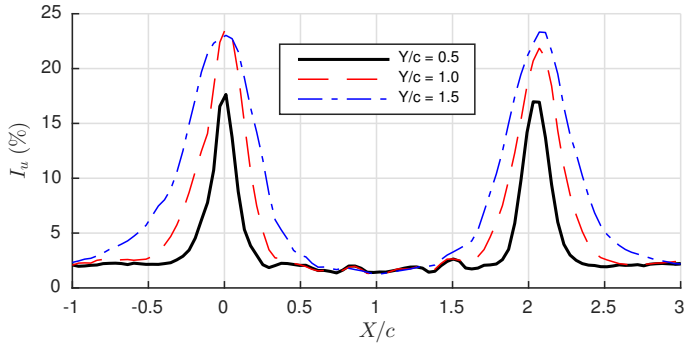

(a) u-component

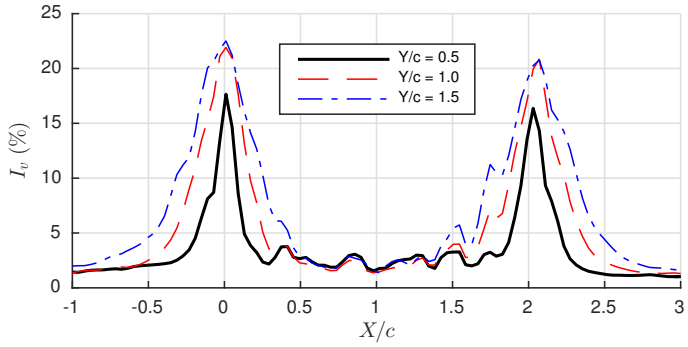

(b) v-component

Fig. 4.21 Flow unsteadiness with position. Motor speed: 700 RPM.

4.7.5 Theoretical response between the real and ideal velocity profiles

With the current configuration, the gust rig generated a velocity profile that deviates from the ideal top-hat, particularly at the shear layers. Here the importance of the variations to the response of the wing are estimated. First, it is assumed that the Küssner function is valid. Keeping in mind that this is likely only correct for gusts of low amplitude, the lift response to each velocity profile shown prior in figure 4.20b was calculated by a convolution of the Küssner function. The change in lift coefficient, normalised by the gust ratio, is shown in figure 4.22. With the small gust ratio assumption, the velocity deviations from the ideal top-hat shaped profile have only a minor effect on the predicted force history. The agreement is deemed to be satisfactory at all y/c locations. Other variations between the experimental and modelled configuration, such as three-dimensionality of the velocity profile, may play a more significant role toward the force response.

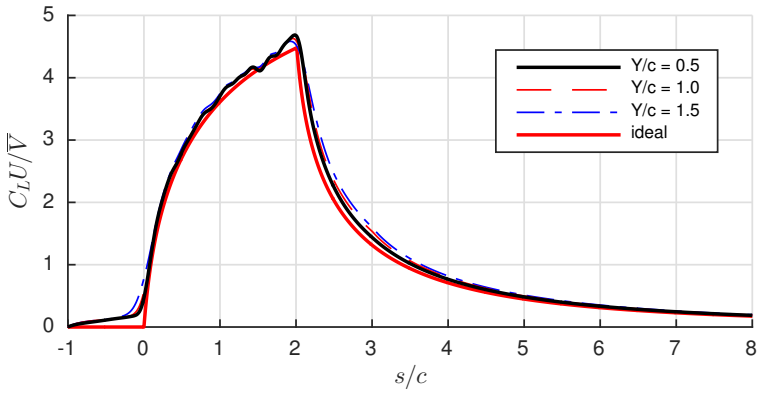

Fig. 4.22 Küssner response for each velocity profile given in figure 4.20b.

4.7.6 Spanwise velocity profile

So far, no consideration has been paid to the three-dimensionality of the gust velocity profile. The spanwise setup of the gust rig and skim plate are shown in figure 4.23. For clearance there is a 25 mm (5% span) gap between the upper edge of the gust outlet and the underside of the skim plate. As the skim plate passes over the gust rig, the boundary condition at the top of the gust will transition from approximately free-slip, due to the water-air interface, to no-slip. At the bottom of the gust rig there is no boundary, instead a free-shear layer will develop.

To quantify the three-dimensionality of the velocity profile, PIV measurements of the gust were taken using a vertical laser sheet at the mid-plane ($X/c = 1$), and Y offset locations from $Y/c = 0.5$ to $Y/c = 1.5$. The velocity profiles, and vorticity distributions are shown in figure 4.24. Aside from at the shear layers, the variation in the spanwise velocity profile is minor. There is a slight reduction in velocity for $Z/c \geq 4$, however, this is similar to the streamwise velocity perturbations which are of order $\pm 15\%$. This reduction may be caused by the difference in the top and bottom shear layer

boundary conditions. The addition of a bottom plate between the outlet and collector may therefore improve the velocity profile, but would impede PIV optical access. This has not been pursued here, but given that the wing tip is located at $Z/c = 4$, it is unlikely to have any significant effect on the present results.

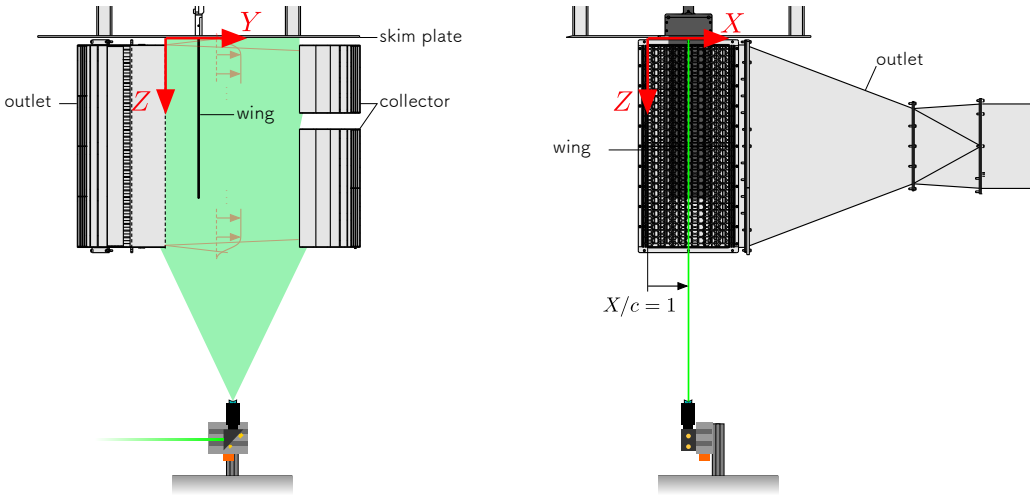

(a) Front **(b)** Side

Fig. 4.23 Schematic of the PIV laser configuration for measuring the spanwise velocity profile. For scale the wing is shown in the schematic, but this was not present in the physical setup.

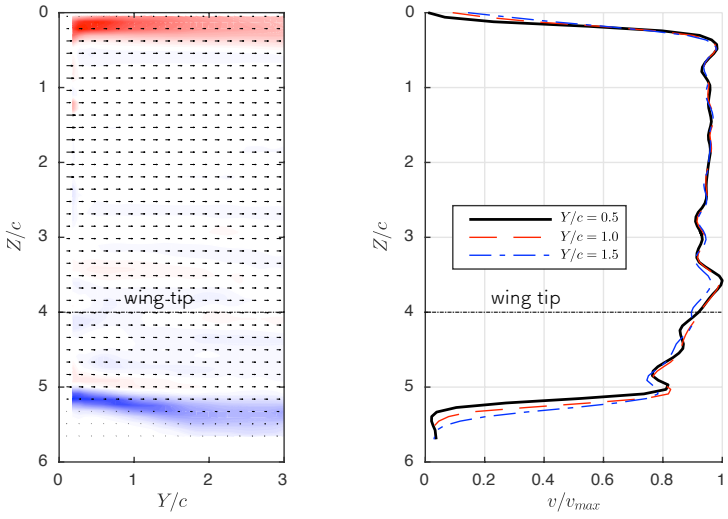

(a) Mean vorticity field **(b)** Mean velocity profile

Fig. 4.24 Average flow velocity in the spanwise direction. Taken with the skim plate above the outlet.

4.7.7 Pump operating range

To assess the operating range of the gust rig, the mean gust velocity $\overline{V}$ was measured using PIV across a range of pump speeds. This is shown in figure 4.25.

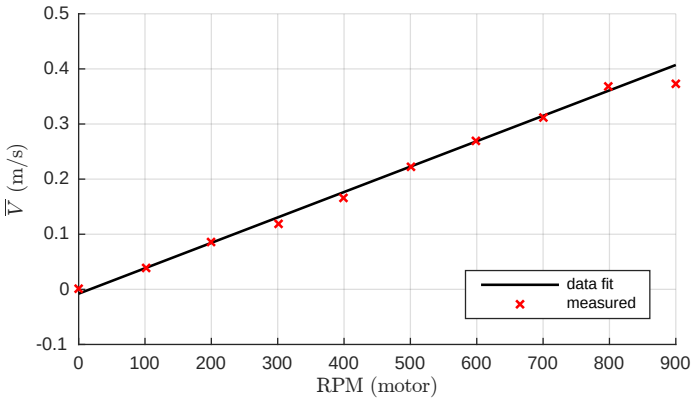

Fig. 4.25 Gust velocity with motor RPM.

The gust velocity increases linearly with RPM, up until 800 RPM where there is a sharp variation from the linear gradient. A linear velocity profile with RPM is expected if the pump is operating within its design pressure and volume flow rate range. Here the lift and drag forces on the pump blades, therefore pressure rise p_{rise} across the pump scales with RPM^2. The scaling for the pressure drop within the ducting, attributed to the wire mesh screens and turning vanes is, $p_{drop} \sim V^2$. Since the pressure rise from the pump equals the pressure drop within the gust rig, $V \sim$ RPM. The outlier at 900 RPM corresponds to a sharp degradation in the velocity profile, and corresponding increase in unsteadiness. This is shown in figure 4.26. It is likely that the pump stalls between 800-900 RPM. The maximum velocity of approximately 0.40 m/s corresponds with a Reynolds number of approximately 40,000, based on wing chord. It is possible that higher velocities can be reached by re-pitching the pump blades, but this was not necessary for the present study. A linear fit through the pre-stalled points is given by $V = 4.611 \times 10^{-4}\text{RPM} - 7.831 \times 10^{-3}$.

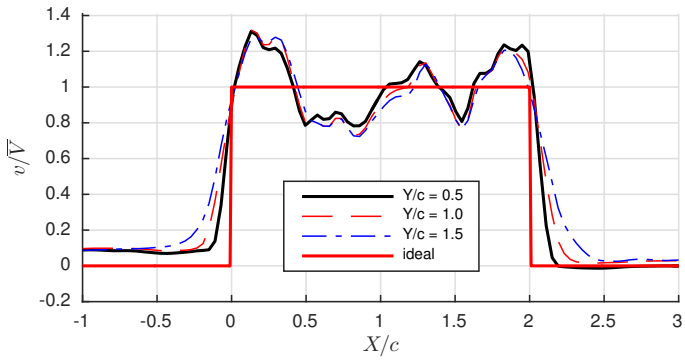

(a) Velocity

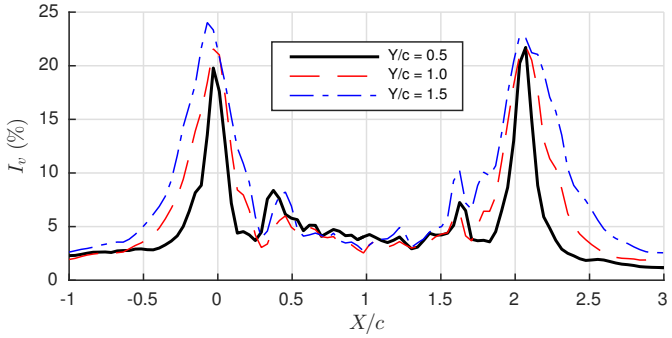

(b) v-component unsteadiness

Fig. 4.26 Flow velocity and unsteadiness at 900 RPM. Calculated from 2000 samples over 10 seconds.

4.7.8 Assumption of two-dimensional flow

For the presentation of all PIV and force measurement data herein, it is assumed that the flow field is two-dimensional. PIV data was, as described in section 4.6.1, taken at the mid-span of the wing (measured from the skim plate to wing tip), which has an effective aspect ratio of 8. Meanwhile, physical force measurements are an integral quantity across the full three-dimensional model. There is therefore a potential source of discrepancy between force balance, PIV, and theoretically calculated quantities. Stevens (2013) showed that for short pitching motions with an identical wing model, up to $X_c/c = 2$, measures of vortex dynamics are similar, whether taken at the midspan or three quarter span locations. This indicates that, provided PIV measurements are taken at less than the (physical) three quarter span location, the data will be independent of measurement location and may be assumed to be two-dimensional. This assumption is further supported by Pitt Ford (2013), who demonstrated that for an impulsively started flat plate wing, at an angle of incidence of $\alpha = 25°$, the shed leading edge vortex remains parallel to the leading edge well beyond the $7/8$ span, and also concludes that the flow is highly two-dimensional. The influence of aspect ratio on the transient forces may be quantified from the experiments conducted by Ringuette et al. (2007). The authors measured the force on an aspect ratio 6 wing, undergoing acceleration over a distance of 0.25 chords. The wing was set at a constant angle of incidence of $\alpha = 90°$, and the force was compared with and without end-plating.

The difference in force between each configuration after two chords travel was approximately 5%. We therefore estimate, that for the highly transient test cases considered in our work, the error attributed to three-dimensional effects present in direct force measurement, and PIV derived quantities, will have an error of order 5-10%, compared to the true two-dimensional quantity.

4.8 Summary

This Chapter describes the equipment and measurement techniques utilised in this study. Experiments were performed in a towing tank to take advantage of favourable Reynolds number scaling effects. Forces were acquired using a custom designed wing balance rig, with inertial compensation to minimise contamination due to vibration. The flow field was characterised using both dye-flow visualisation and PIV, for which a simple dual light sheet alignment procedure was developed. A gust apparatus was constructed for the towing tank, that facilitates the generation of sharp edged transverse gusts. This has demonstrated relatively uniform and steady flow. Each experiment has been designed such that the entirety of the immediate flow field about the wing may be resolved, without camera field of view obstruction or laser light sheet shadow. A complete field of view was essential to identify the added mass phenomenon using PIV. This process is described in the following Chapter.

Chapter 5

Isolating Added Mass with 2D PIV

To experimentally demonstrate that the inviscid added mass solution is applicable to a viscous separated flow field, both the inviscid analytical added mass prediction, and an experimental measure of the quantity is required. Given that added mass is an effect that ultimately gives rise to a force on a body, force is generally the quantity used for such comparison. It is both simple to calculate analytically, and straightforward to measure. The problem is that force alone provides no information on the underlying cause. In this Chapter we develop methods to isolate the added mass mechanism directly from PIV measurements, by determining the trace that the phenomenon leaves in the vorticity field.

In section 5.1 an unsteady potential flow model is described that deconstructs the boundary-layer vorticity on a flat plate into two components, a non-circulatory vortex sheet attributed to added mass, and another circulatory sheet due to velocities induced by free vorticity in the flow field. This potential flow model will be utilised to quantify the circulatory component of an experimentally measured boundary-layer distribution. The approach is based on the work of Graham et al. (2017), who derived quantities for an unsteady flat plate wing translating with constant angle of incidence. Here the methods are extended to compensate for 'missing' circulation, and also incorporate rotation effects.

In section 5.2 a technique is described that enables the quantification of distributions of boundary-layer vorticity using PIV measurements of limited resolution. It will be shown that when coupled with measurements of free vorticity, and the potential flow model, vorticity attributable to added mass may be directly isolated. The errors attributed to the implementation of the technique are summarised in section 5.3, while a more extensive description of the methods used to quantify the errors are given in Appendix B.

5.1 Inviscid flow field model

5.1.1 Vortex sheet components

In Chapter 3 it was argued that a body in a potential flow field may be represented by a vortex sheet on the surface. This sheet has zero circulation, and is attributed to the added mass effect. The problem we now face is that real flows are generally rotational. As a consequence, the vortex sheet representation of a body will not necessarily always have zero net circulation (see the vortex sheet representation of a plate in the thin airfoil theory, section 2.3.2). Eldredge (2010) and Graham et al. (2017) argued that the vortex sheet has two constituent parts, as given by equation (5.1)

$$\begin{aligned} \gamma^b(x) &= u_2(x) - u_1(x) \\ &= \gamma^{nc} + \gamma^c. \end{aligned} \tag{5.1}$$

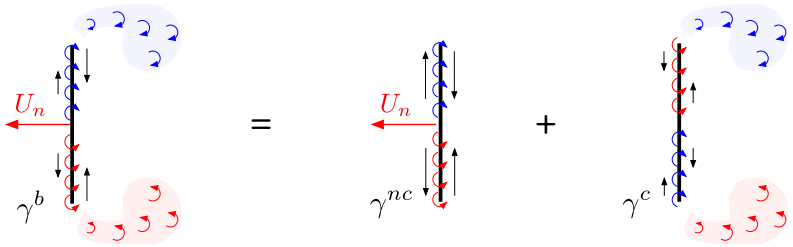

Fig. 5.1 Deconstruction of boundary-layer vorticity into non-circulatory and circulatory components for a translating flat plate. Arrows on the surface of the plate represent flow velocities above the boundary-layer. Shaded regions indicate diffuse vorticity residing in the bulk flow field, while the red and blue colouring represents positive and negative vorticity, respectively.

As illustrated in figure 5.1, the first component, γ^{nc}, is attributed to body motion in an otherwise irrotational flow. This is the vortex sheet associated with added mass, as described in Chapter 3. It will always have the defining characteristic of zero net circulation, and has the superscript *nc* for '*non-circulatory*'. The second constituent part, γ^c, is attributed to vorticity located away from the body, and residing in the 'bulk' flow field. Here the term bulk flow is defined as flow outside the boundary-layer on the body. For this component it is assumed that γ^c is of such strength that self induced velocities (in the body surface normal direction) are equal and opposite to those induced by the free vorticity, so that the no-penetration condition is satisfied. For the calculation it is assumed that the body is at rest, as the body kinematic motion is accounted for by the non-circulatory sheet. The vortex sheet attributed to the free vorticity is allocated the superscript *c* for '*circulatory*' as it may often (but not necessarily) have net circulation. Given that we have calculated theoretically the non-circulatory component in Chapter 3, we only need to find the circulatory part, γ^c, to completely determine the bound vortex sheet γ^b.

5.1.1.1 Circulatory 'shed vorticity' vortex sheet

The circulatory vortex sheet constituent, γ^c, is found from the bulk flow vorticity using the potential flow model described by Graham et al. (2017). This model is 'data-driven', as the position and circulation of each external vortex will be determined using PIV measurements of a physical flow field. For complex geometries, a panel code may be used to find the equivalent γ^c for a body subject to flow induced by external vortices Graham et al. (2017), however, for a simple flat plate the mapping method allows an exact analytical expression to be derived.

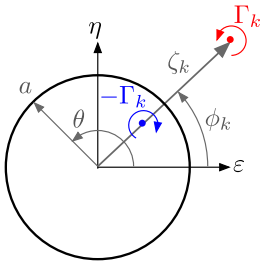

Fig. 5.2 Mapped circle frame.

The plate is mapped to a circle with radius $a = c/4$ using the relation,

$$z = \zeta + \frac{(c/4)^2}{\zeta}, \tag{5.2}$$

where $\zeta = \varepsilon + i\eta$ is a position vector in the mapped frame. The mapped frame is illustrated in figure 5.2. In the mapped frame the circle is subject to the same condition as the plate (flow cannot pass through its surface and circulation is unchanged). As illustrated, a single vortex with circulation Γ_k is located in the flow field at the position ζ_k. This represents a single element from a field of vorticity. To satisfy the no-penetration condition, 'mirror' vortices must be placed inside the circle. This ensures that the circle perimeter is a streamline of the flow by balancing the radial velocity component that the free vortex induces on the circle boundary. According to Saffman (1992) there are an infinite number of mirror vortex combinations which satisfy this condition. The solution given by Graham et al. (2017) satisfies conservation of global circulation and the circle boundary condition with just a single mirror vortex of circulation $-\Gamma_k$ at a location $\zeta_{k,mir} = \frac{a^2}{|\zeta_k|} e^{i\phi_k}$, where ϕ_k is the angle between the ε axis and the free vortex element k. The free vortex and mirror may be used to find γ^c by calculating the surface slip velocities in the plate frame. These are obtained here using the complex potential method. The complex potential ($F_k(\zeta) = \Phi_k + i\Psi_k$, where Φ_k and Ψ_k are the potential and streamfunctions for the vortex pair) is

$$F_k(\zeta) = -i\frac{\Gamma_k}{2\pi} \ln\left(\frac{\zeta - \zeta_k}{\zeta - \zeta_{k,mir}}\right). \tag{5.3}$$

The flow velocity (u_k, v_k) in the plate frame is given by

$$u_k - iv_k = \frac{dF_k}{dz} = \frac{dF_k}{d\zeta}\left(\frac{dz}{d\zeta}\right)^{-1}. \tag{5.4}$$

Evaluating the derivatives yields

$$u_k - iv_k = \frac{i\Gamma_k}{2\pi}\frac{\zeta^2(\zeta_{k,mir} - \zeta_k)}{(\zeta^2 - (c/4)^2)(\zeta - \zeta_{k,mir})(\zeta - \zeta_k)}. \tag{5.5}$$

To calculate the strength of the vortex sheet, the velocity tangential to the surface of the plate (u_k) is required. The plate surface corresponds to the cylinder surface in the complex frame, given by $\zeta = ae^{i\theta}$. Therefore, at the plate surface, equation (5.5) gives:

$$u_k(\theta) = \frac{-\Gamma_k}{\pi c \sin\theta}\frac{(c/4)^2 - |\zeta_k|^2}{|\zeta_k|^2 - \frac{1}{2}|\zeta_k| c\cos(\theta - \phi_k) + (c/4)^2}. \tag{5.6}$$

Here θ, the angle from the ε axis to a position on the cylinder surface (anticlockwise positive), is related to the plate frame by $x = (c/2)\cos\theta$. The vortex sheet attributable to the vortex pair is equal to the velocity difference either side of the plate,

$$\gamma_k^c(\theta) = u_k(-\theta) - u_k(\theta), \tag{5.7}$$

with $0 \leq \theta \leq \pi$. Finally, an unknown a-priori number of vortices (n) will be measured in the flow field. The total circulatory vortex sheet is, however, simply found by linear superposition of the contributions from each measured vortex,

$$\gamma^c = \sum_{k=1}^{n} \gamma_k^c. \tag{5.8}$$

The location of each vortex is to come from PIV measurements in the plate frame, a conversion from the real to mapped frame is needed. Solving for the roots of equation (5.2) gives the inverse mapping,

$$\zeta = \frac{z \pm \sqrt{z^2 - 4(c/4)^2}}{2}. \tag{5.9}$$

As there are two solutions to equation (5.9), one inside the mapped circle and the other outside, only the outer solution $(|\zeta| \geq a)$ is used.

5.1.1.2 Systematic error compensation (lost circulation)

The methodology for determining γ^c described in section 5.1.1.1, is based on the premise that the position and circulation of each bulk flow vortex element can be measured. The circulatory vortex

sheet γ^c has a net circulation equal and opposite to that of all the bulk flow vorticity. Error arises when a vortex element leaves the measurable field of view, which causes the circulation of γ^b to change by the circulation 'lost'. Fortunately it is possible to partially compensate for this effect. Consider a flow field comprising of just the plate and a free vortex of circulation Γ_k, both within an area A that represents a measurable field of view. This is illustrated in figure 5.3a. The plate must have a circulation of $-\Gamma_k$. If the total circulation within A (Γ_{in}) is found using a closed contour of integration

$$\Gamma_{in} = \oint_A \mathbf{u} \cdot \mathbf{dl}, \tag{5.10}$$

then Γ_{in} will be zero.

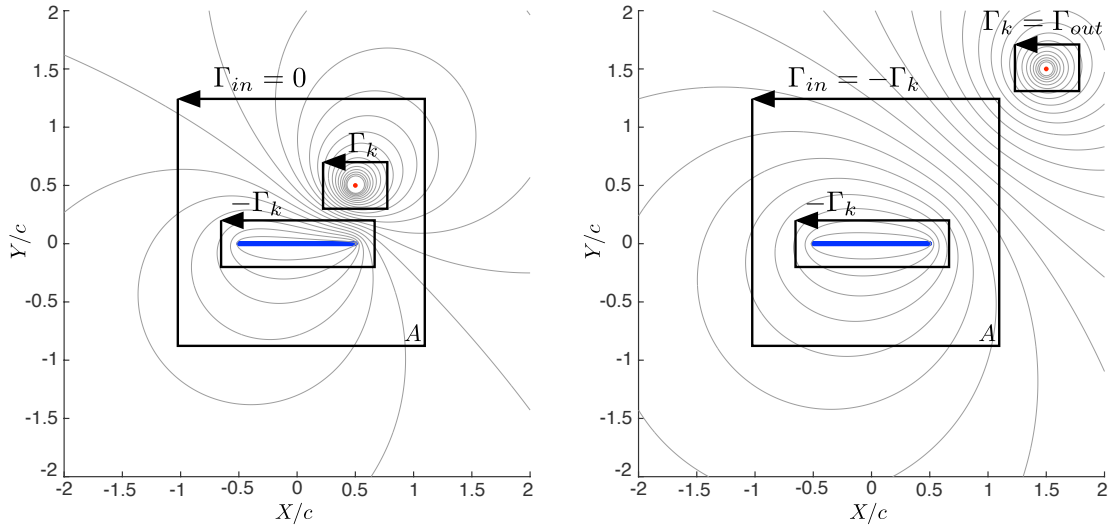

(a) All circulation in the measurement window **(b)** Net circulation outside the measurement window

Fig. 5.3 Example flow field for correcting for the circulation lost from the PIV measurement field of view.

Now if the free vortex moves outside of A, calculation of Γ_{in} will return a non-zero result (the circulation of the plate). This is illustrated in figure 5.3b. The net circulation outside of the observable area A (Γ_{out}), must be equal and opposite to that measured within A to conserve circulation across the whole flow field:

$$\Gamma_{out} = -\Gamma_{in} \tag{5.11}$$

$$= -\oint_A \mathbf{u} \cdot \mathbf{dl}. \tag{5.12}$$

The circulation lost outside the measurement window is therefore determinable, however, its location is unknown*. As described in section 5.1.1.1, the position of each external vortex and the mirror vortices within the mapped circle must be known to calculate the distribution of γ^c. However, it could

*The lost circulation could be in the form of a single point vortex outside the observation window, or arbitrarily distributed vorticity throughout the surrounding flow field.

be *assumed* that the vorticity outside the measurement window is sufficiently far from the plate that it is effectively at infinity. A single mirror vortex of circulation $-\Gamma_{out}$ would therefore be placed at the circle origin. This may not be unreasonable if there is a relatively large measurement field of view either side of the plate. The vortex sheet, γ^c_{out}, that arises due to the missing circulation can be found from equation (5.7) with the condition that the position of the external vortex $\zeta_k \to \infty$ and replacing Γ_k with Γ_{out}. Equation (5.7) becomes

$$\gamma^c_{out} = \frac{-\Gamma_{out}}{\pi\sqrt{(\frac{c}{2})^2 - x^2}}. \tag{5.13}$$

The contribution to the circulatory vortex sheet due to vortices outside the measurement window, can therefore be approximated. More sophisticated corrections might also be possible in specific cases, if the location of the lost vorticity is approximately known. We note that this analysis strictly assumes that the flow is two-dimensional. Further error could be introduced if this assumption is incorrect. Simpson et al. (2018), however, showed that the measure of circulation for a vortex tilted at 40° from a PIV laser plane, has an almost negligible effect on the measured circulation. Meanwhile, flow induced by a vortex ring, not intersection the measurement plane, cannot introduce net circulation to the measured flow field. Three-dimensional effects are therefore likely to have negligible effect on the analysis of the circulatory vortex sheet.

5.1.2 Potential flow model summary

A potential model has been derived to obtain the distribution of boundary-layer vorticity for a flat plate wing undergoing arbitrary translation and rotation kinematic motions through a viscous and separated flow. The boundary-layer is represented by a vortex sheet of strength $\gamma^b = \gamma^{nc} + \gamma^c$. The non-circulatory term, γ^{nc}, comprises a component attributed to translation, γ^{nc}_t, and a component due to rotation, γ^{nc}_r. The circulatory term, γ^c, is due to vorticity in the bulk flow field. Using PIV data, it is possible to determine γ^c experimentally. It is apparent that, if the vortex sheet γ^b can also be quantified experimentally, then the component directly attributable to added mass (γ^{nc}) may be isolated from flow field measurements. Further limiting the kinematic motion to just translation or rotation enables independent measurements of γ^{nc}_t and γ^{nc}_r to be obtained. These may then be compared to the theoretical distributions given in Chapter 3, (see equation (3.23) for a translating and rotating flat plate, and equation (3.36) for a sharp edged gust), thereby testing the validity of the potential flow solution for added mass in separated viscous flows.

5.2 Quantification of γ^b from PIV measurements

In the review of the literature on the added mass effect in section 3.4, it was discussed that the difficulty with directly resolving the vorticity in the boundary-layer using PIV (to obtain a measure of γ^b), stems from the requirement that typically large regions of the flow field must be captured to include starting

vortices. There is a compromise between field of view and spatial resolution, the former often taking priority. Furthermore, the added mass attributed vorticity is generated in an 'intensely concentrated' region of the boundary-layer adjacent to the wall. In this region the scattering of laser light from the surface results in a loss of measurements due to saturation of the camera sensor. With such an experimental setup it is unlikely that velocity gradients within the boundary-layer, and the added mass attributed vorticity in particular can be resolved directly. It is, however, possible to infer the boundary-layer vorticity by application of Stokes' theorem (equation 5.14). The surface integral of vorticity over an area A (circulation) is equal to the closed line integral of the velocities about the circumference. Even for a near-singular and unmeasurable distribution of vorticity, the circulation can be determined by the entirely measurable flow field velocities nearby

$$\Gamma = \int_A \omega_z dA = \oint \mathbf{u} \cdot \mathbf{dl}. \tag{5.14}$$

With the present problem the 'singularity' is not a point vortex free in the flow field, but rather is in the form of a boundary-layer over the surface of a plate. The question is, what happens to the integration contour that crosses over the plate's perimeter? In this case, a body of finite cross-sectional area can be treated as an area of fluid with equivalent kinematic and geometric properties. Thus, in pure translation the 'body fluid' is irrotational, and when in pure rotation it has uniform vorticity with magnitude twice the rate of angular rotation (Wu, 1981). Applying this condition allows an integration contour to cross over the body surface as if the flow field and body geometry were a continuum. The circulation of a segment of the boundary-layer can therefore be measured. For the plate geometry, elements of circulation ($\delta\Gamma_n$) are calculated using the contours of integration shown in figure 5.4a. It is assumed here that the plate used for experiments is infinitely thin and no correction for finite thickness has been made[†]. The circulation of vorticity contained in the boundary-layer may then be equated to that of the vortex sheet, $\int_A \omega_z dA = \int \gamma dx$, and thus a local estimate of a boundary-layer equivalent vortex sheet can be found by dividing the circulation of each element by the element width,

$$\gamma_n^b \approx \delta\Gamma_n / \delta x_n. \tag{5.15}$$

For the boundary-layers shown in figure 5.4b, application of this method returns a vortex sheet of strength $\gamma_n^b = u_2 - u_1$. A measure of the integral boundary-layer vorticity can therefore be acquired without needing measurements of velocity gradients within the boundary-layer. The spatial resolution (in the plate direction, x) is, however, limited by the underlying PIV grid resolution. For the current experiment the plate was discretised into 50 area elements, over a distance of $1.0c$ in the x-direction ($\delta x = 0.02c$). This was similar to the PIV resolution. Unless otherwise specified, each element had a height of $\delta y = 0.20c$. This was selected as it is sufficiently large to include the boundary-layer, while largely avoiding 'free' vorticity in the bulk flow field (shown later in figures 6.3 and 6.5). If the free vorticity is encompassed by the contours of integration, it will be excluded from the circulatory

[†]The mechanical vorticity of the plate, which is 4 mm thickness, was calculated and is comparatively negligible.

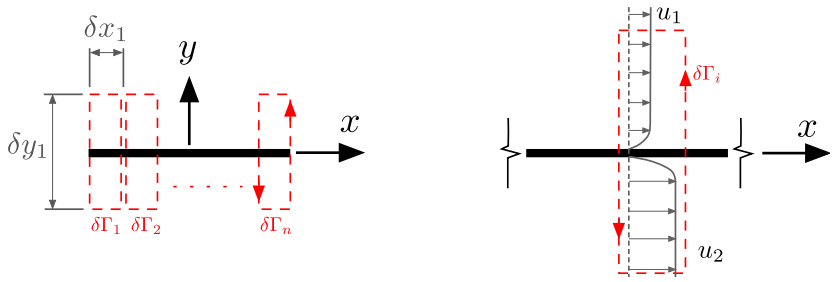

(a) Overview of elements spanning the wing chord

(b) Schematic of the boundary-layers encompassed within a single integration contour

Fig. 5.4 Elements (red rectangles) used for the calculation of the boundary-layer distribution of circulation.

vortex sheet calculation γ^c, and is instead assigned as local boundary-layer vorticity. This is to be avoided where possible. It is reiterated that, while the measurement window is of a finite height (δy), provided that the measurement area incorporates the boundary-layer vorticity over a body, there is no introduced error compared to the comparable result if $\delta y = \infty$. For each test case, the selection of δy, and its position relative to the boundary-layer, and similarly, vorticity which is allocated as 'free' in the flow field is identified by a boundary box. The value of $\delta y = 0.20c$, is approximately the smallest this dimension may be, whilst still encompassing the boundary-layers. This is consistent with our current theoretical understanding of the location of the vorticity attributed to the added mass phenomenon, which is intensely concentrated in the lower portion of the boundary-layer. Since we are attempting to isolate the added mass vorticity, and validate our theoretical understanding of added mass, we refrain from 'tuning' δy until our measure of the vorticity matches, as closely as possible, the theoretical result that we seek.

We now have a method for quantifying the distribution of boundary-layer vorticity. Also available from the PIV measurements, is a means for determining the circulation of all free vortices within the bulk flow field. With this, the component of boundary-layer vorticity required to react the velocities induced by the free vortices, may be determined using the potential flow model described in section 5.1.1.1. This has two primary uses. Firstly, with the impulse relations given in section 2.3.1.7, and the measure of free vortices, the circulatory forces attributable to the creation and advection of such vortices may be calculated entirely from PIV measurements. Secondly, we know that any boundary-layer vorticity not attributable to the free vortices must instead result from the added mass effect. We can therefore isolate the added mass effect from the trace it leaves within the vorticity field, and therefore have a means for directly comparing the strength and distribution of vorticity with potential flow theory (the theoretical added mass vortex sheet). Such a comparison will allow us to prove whether the added mass effect is dependent, or independent of the fluid viscosity. Furthermore, we may go as far as directly calculating the added mass force from the rate, and distribution of created

vorticity directly from PIV. These techniques will be applied to wing-gust encounters to investigate the role of circulatory and non-circulatory force components.

5.3 Error

The discretisation of a continuous flow field into measurement points, inherent with the PIV method, can be a source of error when it comes to extracting distributions of boundary-layer vorticity, impulse and force quantities. This error was quantified by generating an artificial flow field, from which the non-circulatory vortex sheet γ^{nc} was 'measured' using the prior described methodology. Here only the results of the analysis are given, but full details are provided in Appendix B. For a flat plate wing in a discretised flow field with 50 vectors per chord, and equivalent resolution vortex sheet discretisation, the analysis yields the following errors:

- Each measure of the flow field impulse, first moment of impulse and subsequent forces as calculated from vorticity in the entire flow field (that is the sum of the vorticity in the boundary-layer and that shed into the bulk flow field), are shown to have an error due to discretisation of less than 1%.
- Measures of the impulse, first moment of impulse and forces attributed to added mass (from the non-circulatory vortex sheet γ^{nc}), have an error of approximately 5%.

Our selection of the vortex sheet discretisation resolution of 50 elements per chord is the maximum our measurements allow, as a higher resolution will simply result in measures which are a linear interpolation between adjacent PIV vector elements. No additional information is gained, while there is additional computational cost associated with higher resolutions. Lowering the resolution has the advantage of reducing the influence of random PIV vector noise, as the circulation for each vortex sheet discretisation element is the area integral of the elemental vorticity. We will, however, address random errors by using a sequential averaging process, described in further detail in section 6.4. For transparency, both the directly acquired, and averaged measures of the non-circulatory vortex sheet are subsequently presented. This, along with the analysis of systematic error due to PIV vector resolution in Appendix B, completes our analysis of foreseeable errors associated with the measures of the added mass attributed vortex sheet.

5.4 Summary

This Chapter describes a methodology developed by the author, to facilitate the extraction of added mass attributed boundary-layer vorticity from PIV measurements of a real flow. To quantify this distribution of previously 'unresolvable' vorticity, using only low resolution PIV, the body is treated as a region of fluid with a velocity equal to the rigid body kinematics. Circulation is calculated using a series of closed integration contours that cross the body, and the vorticity is determined by applying

Stokes' theorem. This distribution of vorticity has two components, a non-circulatory component attributed to added mass, and a circulatory component that is generated to satisfy the no-through flow condition, due to velocities induced by the free vorticity. This component may be found from PIV measurements of free vorticity, using the conformal mapping and vortex mirror image method. Subtraction of the circulatory component from the measured boundary-layer vorticity distribution, enables the added mass component to be isolated.

By experimentally measuring the added mass attributed vorticity, and comparing it with the theoretical result, we have a direct experimental means for proving whether the added mass phenomenon is influenced by viscous effects and subsequent changes to flow topology. Added mass contributions to impulse and force may also be extracted, with an error of approximately 5% for a PIV resolution of 50 vectors per chord, and an equivalent resolution vortex sheet.

Chapter 6

Translating and Rotating Plate Experiments

In this Chapter, experiments on a flat plate wing undergoing acceleration in the direction perpendicular to the chord (surge), and impulsive rotation about the mid-chord are described. These experimental cases are illustrated in figure 6.1. The aims each case is to validate the methodology for extracting added mass quantities from PIV flow measurements, and to demonstrate the applicability of the potential flow result for a viscous and highly separated flow. This may be achieved by showing consistency between the potential flow derived added mass quantities with those obtained experimentally. The surge and rotation test cases are used, because any planar kinematics may be decomposed into a combination of such motions.

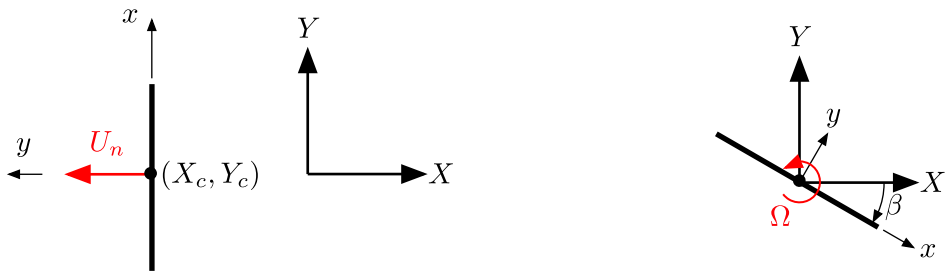

(a) Surge experiment **(b)** Rotation experiment

Fig. 6.1 Schematics of the surge and rotating flat plate experiments.

First, the kinematic motion is described in section 6.1. Qualitative analysis of the flow topology is given in section 6.2, which is followed with the quantitative measures of the added mass attributed vortex sheets, impulse, and force quantities.

6.1 Kinematics

General kinematic parameters for the surge and rotation cases are given in tables 6.1 and 6.2, respectively. For the surging profile the plate underwent nominally constant acceleration over a distance of 0.25 chord lengths, travelled at constant velocity for 1.5 chord lengths and decelerated over a distance of 0.25 chords. The total travel distance is therefore 2 chords. A Reynolds number of 10,000 is used for dye flow visualisation and PIV. For the rotation case, the plate was nominally 'impulsively' rotated in the clockwise direction from rest to a constant angular velocity ($\Omega = -d\beta/dt \approx -\pi/4$ rad s^{-1}) about an axis at the mid-chord. Based on the plate chord and edge velocity the Reynolds number is $Re = 4,600$. After rotating 180°, the plate is impulsively decelerated to rest. It is recognised that a perfectly impulsive motion is impossible due to both finite plate stiffness and torque limitations. For the calculations of pitching moment using potential theory it is assumed that the angular acceleration is constant over a time equal to the PIV sample period (0.02 s). Based on the stepping motor commanded motion, the actual acceleration period is likely shorter than 0.02 seconds, but PIV based measures of impulse are limited by the camera frame rate. The same limitation is therefore placed on the potential theory based estimate.

Table 6.1 Prescribed kinematics for the surge case.

Reynolds number	**10,000**
Acceleration distance (c)	0.25
Deceleration distance (c)	0.25
Total travel (c)	2.00
Peak velocity U_0 (m/s)	0.104

Table 6.2 Prescribed kinematics for the rotation case.

Reynolds number (edge vel.)	**4,600**
Acceleration distance (rad)	$\pi/200$
Deceleration distance (rad)	$\pi/200$
Maximum rotation angle β (rad)	π
Peak angular velocity Ω_0 (rad/s)	$-\pi/4$

6.2 Flow topology

Dye flow visualisation and PIV measurements for the surging case are shown in figures 6.2 and 6.3, while figures 6.4 and 6.5 give the corresponding measurements for the rotation case. The PIV measurements show normalised flow vorticity (red, anticlockwise positive; blue, negative) and arrows

with flow direction. For each data element, the vorticity was calculated by taking the trapezoidal closed line integral of velocity through the centroid of each adjacent element (size $2\Delta l \times 2\Delta l$, where Δl is the data point element width). This gives a circulation, which divided by the area inclosed by the integration contour ($4\Delta l^2$) gives the vorticity.

In the surge case, the following can be observed:

- At $X_c/c = -0.02$: the plate undergoes maximum acceleration but still has low velocity. The start of two vortices is visible in the flow field. PIV measurements show a (faint) region of negative vorticity at the top half of the plate and positive vorticity on the lower half.
- At $X_c/c = -1.00$: the plate is translating at constant velocity. A pair of counterrotating vortices behind the upper and lower plate edges is visible in both the dye flow and PIV measurement. Clear regions of boundary-layer vorticity are visible in the PIV measurements, but cannot be seen in the flow visualisation.
- At $X_c/c = -1.98$: the plate has decelerated to almost a complete stop. The pair of vortices has moved downstream relative to the plate, and the shear layers feeding each vortex can be seen. Discrete blobs of dye are visible in the shear layer; these are the result of the Kelvin-Helmholtz instability, and show the accumulation of vorticity from the shear layer into discrete rollers. Again there is a clear region of boundary-layer vorticity. This vorticity appears to shed off the plate edges, which is caused by flow induced in the negative X-direction by the primary vortices.

For the rotation case, the following can be observed:

- At $\beta \approx 1^\circ$: the plate has started motion and is rotating at constant angular velocity. The dye flow visualisation does not show any vortices in the flow field. The PIV measurements, however, show a strong distribution of positive vorticity at the plate edges and negative vorticity toward the centre.
- At $\beta \approx 90^\circ$: the plate is mid-way through the rotation and is moving at constant angular velocity. A positive vortex, fed by a visible shear layer, has shed at each plate edge. Again a Kelvin-Helmholtz instability is seen. There are clearly defined regions of negative boundary-layer vorticity visible in the PIV measurements which are not seen in the dye flow visualisation.
- At $\beta \approx 179^\circ$: the plate is travelling at constant angular velocity, but is about to encounter the deceleration impulse. The pair of vortices have moved further 'downstream' relative to the circumferential path of the plate edges. The Kelvin-Helmholtz instability is less coherent. This appears to be a result of secondary flow separation interacting with the primary shear layer. The

secondary separation can be seen by the thickening of the negative boundary-layer vorticity toward the plate edges. Since this secondary separation occurs at opposite edges of the plate, it results in the 'cross' shaped vorticity distribution close to the plate surface, as seen in figure 6.5c.

Both the surge and rotation test cases have shown distributions of boundary-layer vorticity during their motions. It is this vorticity that is expected to have a component attributable to the added mass effect. In the following sections this component is quantified and compared with potential theory.

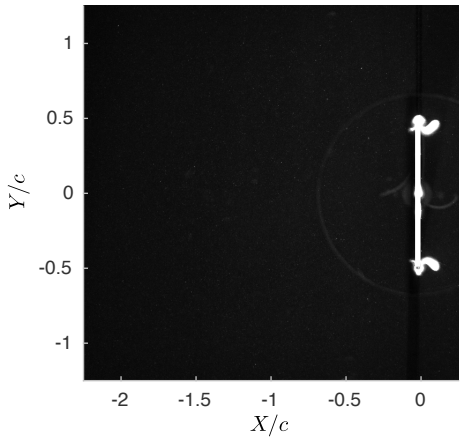

(a) $X_c/c = -0.02$

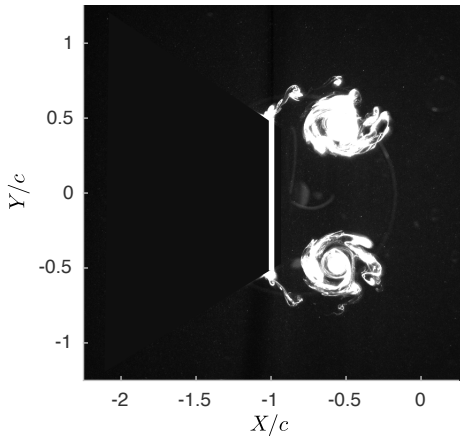

(b) $X_c/c = -1.00$

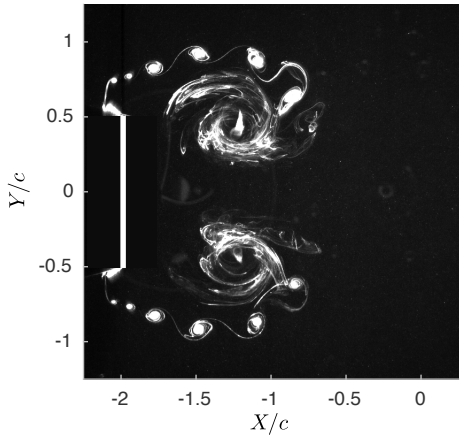

(c) $X_c/c = -1.98$

Fig. 6.2 Dye flow visualisation for the surge case.

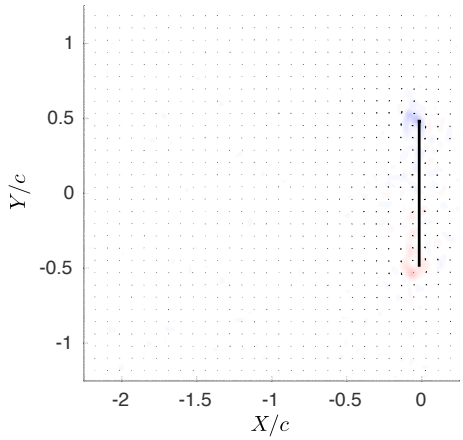

(a) $X_c/c = -0.02$

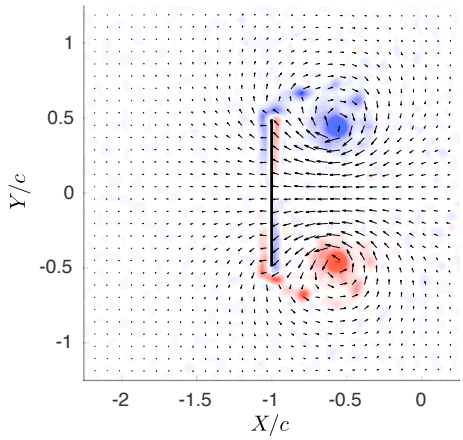

(b) $X_c/c = -1.00$

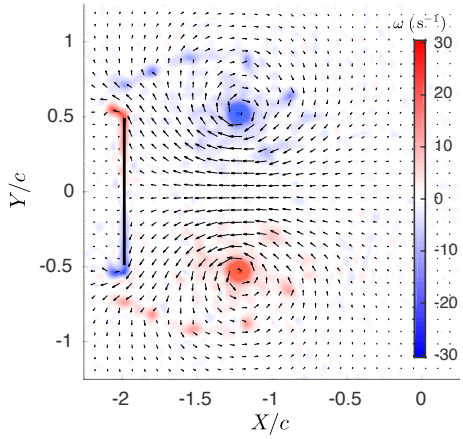

(c) $X_c/c = -1.98$

Fig. 6.3 PIV measurements for the surge case.

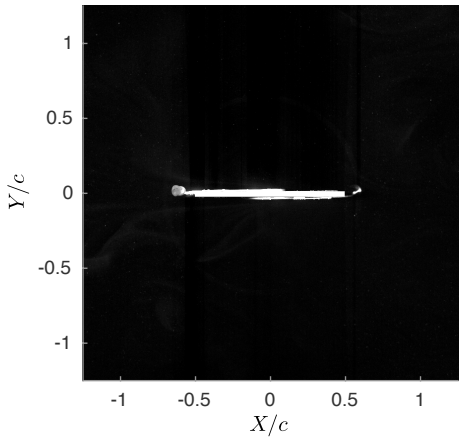

(a) $\beta \approx 1°$

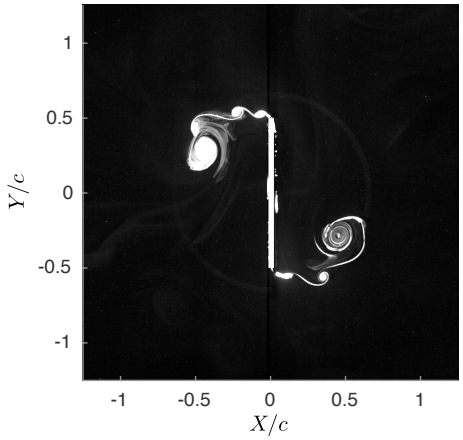

(b) $\beta \approx 90°$

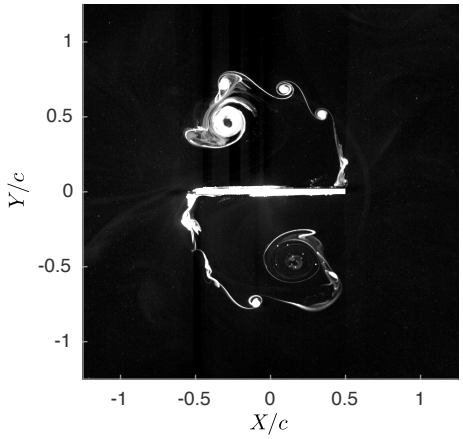

(c) $\beta \approx 179°$

Fig. 6.4 Dye visualisation for the rotation case.

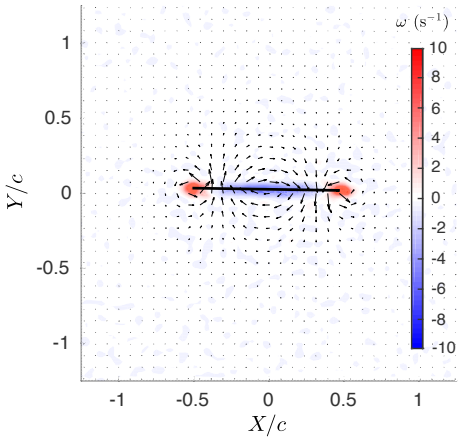

(a) $\beta \approx 1°$

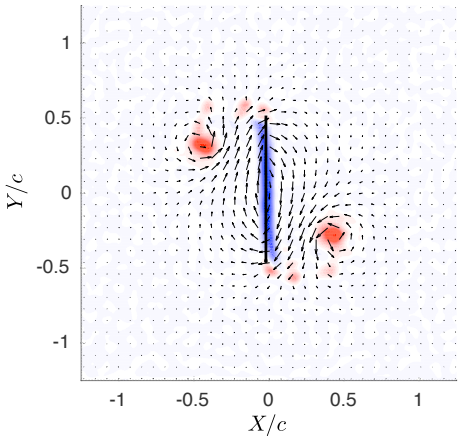

(b) $\beta \approx 90°$

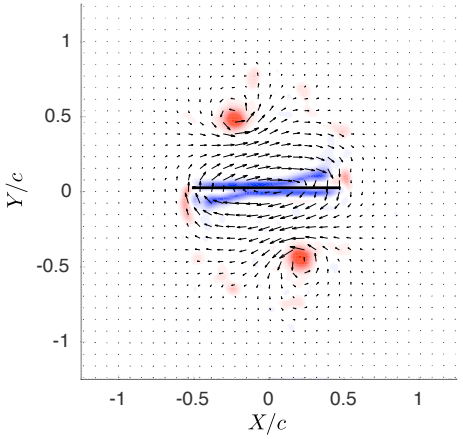

(c) $\beta \approx 179°$

Fig. 6.5 PIV for the rotation case.

6.3 Flow field circulation

Separate sums of positive and negative circulation elements are plotted in figure 6.6. The circulation elements are categorised as those that are 'attached', which means they are included in the boundary-layer areas of integration described in section 5.2; and those that are 'free', i.e. in the bulk flow field. Both test cases show zero total circulation throughout the measurement period, as expected. This suggests that no vorticity has escaped the measurement field of view, and that there are few three-dimensional effects. Note the presence of circulation discontinuities at the start and end of motion for the rotation case. This suggests that added mass attributable vorticity is captured by the PIV measurements bracketing each acceleration period. In inviscid theory, the added mass vorticity grows at a rate proportional to the acceleration of the body. An impulsive, or near infinite acceleration means the growth rate of circulation is also near infinite. This causes the circulation discontinuities. Similar added mass effects are captured for the surge case shown in figure 6.6a, but these are visible only as subtle gradient changes before and after each acceleration region.

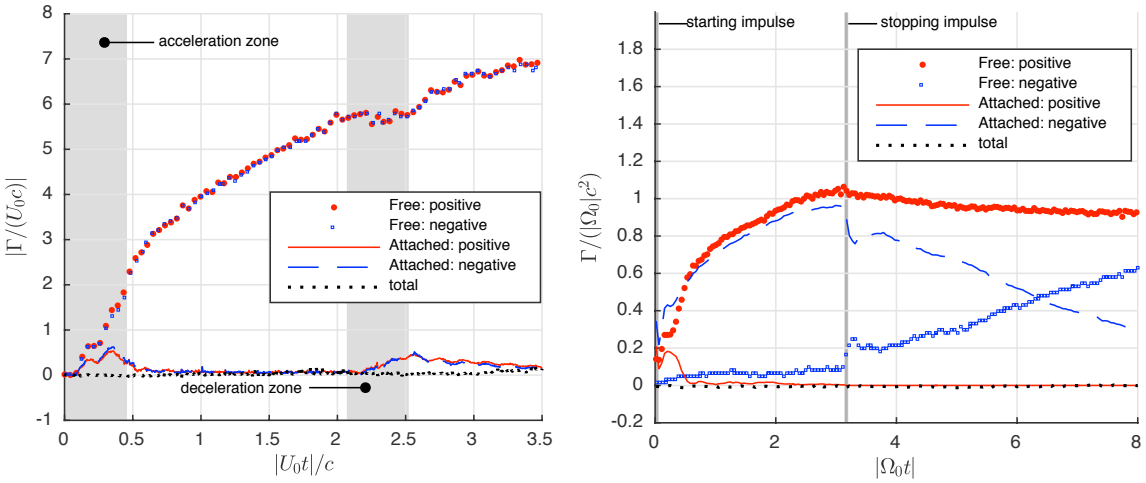

(a) Surge case **(b)** Rotation case

Fig. 6.6 Sums of the boundary-layer and bulk flow circulation elements.

In figure 6.7 the sum of the positive and negative components is shown. This gives the net attached circulation, and the net free circulation. For the surge case, given by figure 6.7a, both the attached and free circulation are approximately zero for the measured range. Equal rates of positive and negative circulation are shed at each of the plate, as shown in figure 6.3. For the rotation case, positive circulation is shed at each of the plate edges for $|\Omega_0 t| < \pi$. When rotation ceases, negative net circulation is shed into the flow field. The attached circulation follows an equal and opposite trend, as it comprises the mirror images of the free vortices. The discontinuities at the start and end of motion (at $|\Omega_0 t| \approx 0$ and $|\Omega_0 t| \approx \pi$), are believed to result from incorrectly allocated added mass generated vorticity. It was shown in Appendix B that this may be smeared past the edges of the plate

due to the discretisation of the flow field. Consequently, during acceleration motions some of the added mass attributed vorticity is incorrectly allocated as 'free'.

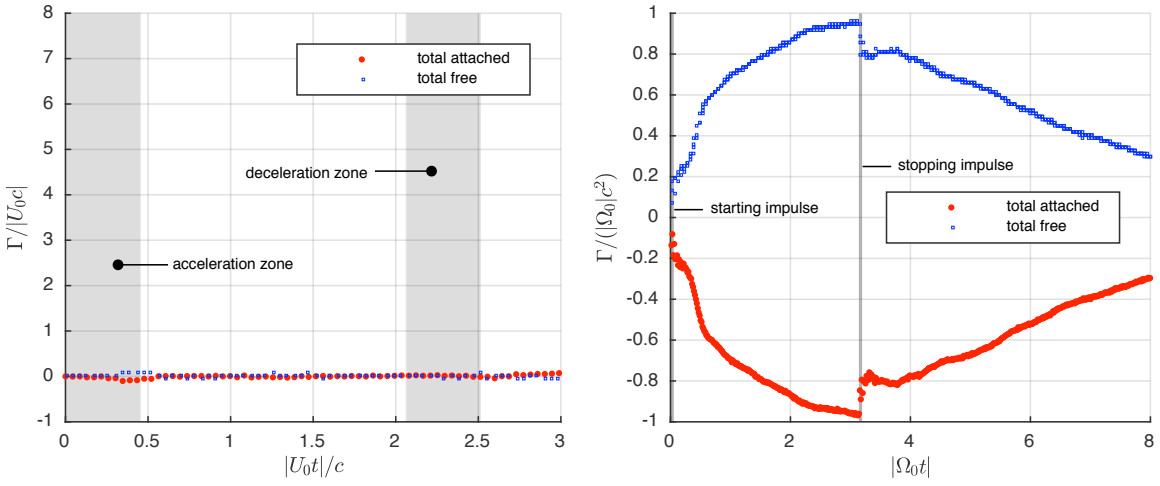

(a) Surge case **(b)** Rotation case

Fig. 6.7 Net attached and free circulation.

6.4 Non-circulatory vortex sheets

From the general measurements of flow field circulation, we now know that some added mass effects are being captured with PIV. Next we seek to isolate the added mass vortex sheet, γ^{nc}. As described in section 5.2, γ^{nc} is obtained by taking direct measurements of the boundary-layer vorticity, γ^{b} and subtracting the component attributed to free vorticity in the flow field γ^{c}. For the surge case, the instantaneous breakdown of the boundary-layer vorticity is given in figure 6.8. The line γ^{c}_{in} is the circulatory vortex sheet, attributed to free vorticity within the measurement window; γ^{c}_{out} is the sheet that compensates for net circulation outside the measurable window; and γ^{nc} is the added mass vortex sheet obtained experimentally. Since circulation was shown to be conserved within the measurement window, $\gamma^{c}_{out} \approx 0$ across the entirety of the run. Figures 6.8a to 6.8c show three instances of the acceleration zone, at $X_c/c = -0.02$, $X_c/c = -0.12$ and $X_c/c = -0.25$. Across the acceleration region, it can be seen that γ^{nc} grows in magnitude. For $X_c/c = -0.02$ and $X_c/c = -0.12$ the total boundary-layer vorticity γ^{b} is exclusively attributed to γ^{nc}. Figures 6.8d to 6.8f show three instances of the deceleration zone, at $X_c/c = -1.75$, $X_c/c = -1.88$ and $X_c/c = -1.98$. We note that for the pair of figures (a)-(f), (b)-(e) and (c)-(d) the plate has equal velocity, but different flow topologies. For each of the instance pairs the added mass attributed vortex sheet, γ^{nc}, is equivalent in magnitude. This suggests that the change in flow topology does not influence the added mass attributed vortex sheet, rather it is just scaled by velocity.

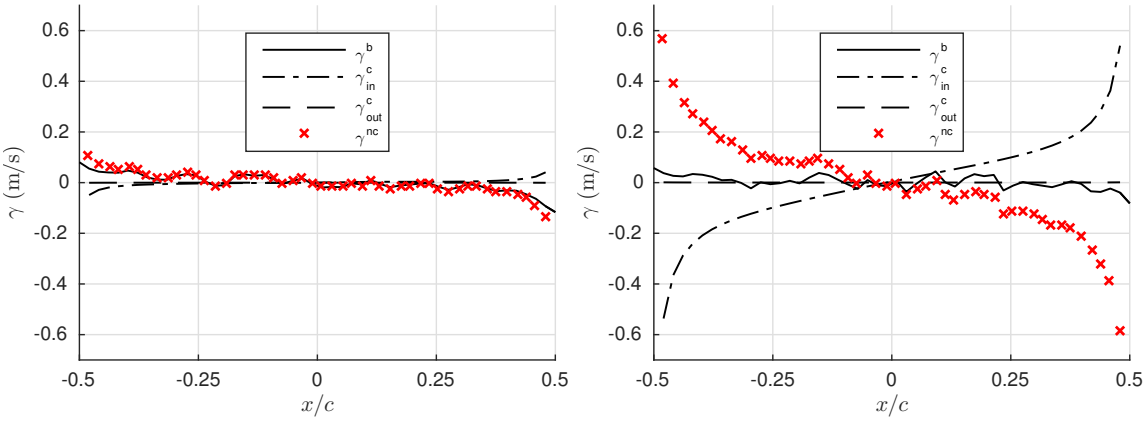

(a) $X_c/c = -0.02$

(d) $X_c/c = -1.75$

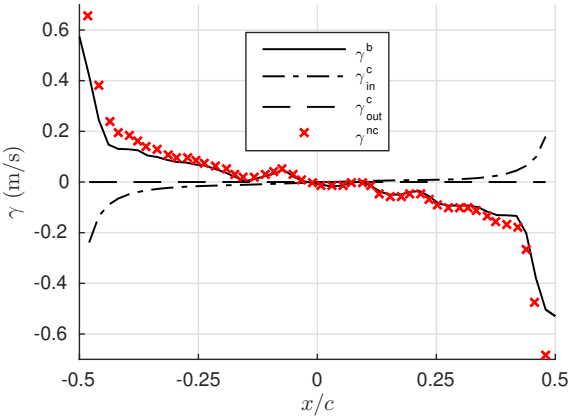

(b) $X_c/c = -0.12$

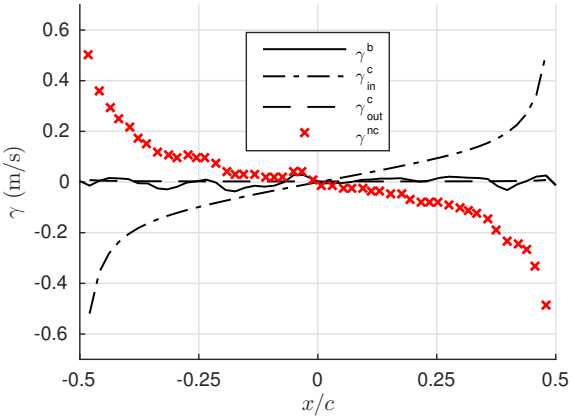

(e) $X_c/c = -1.88$

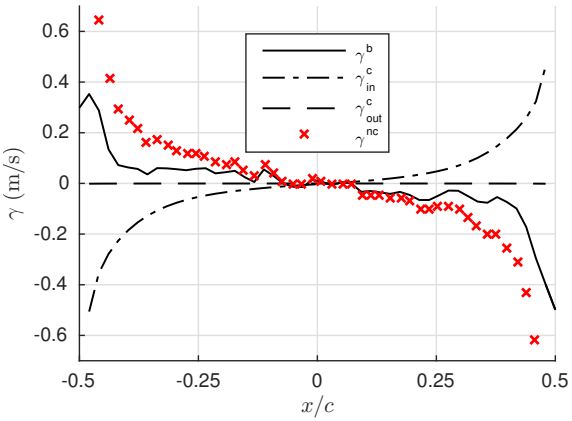

(c) $X_c/c = -0.25$

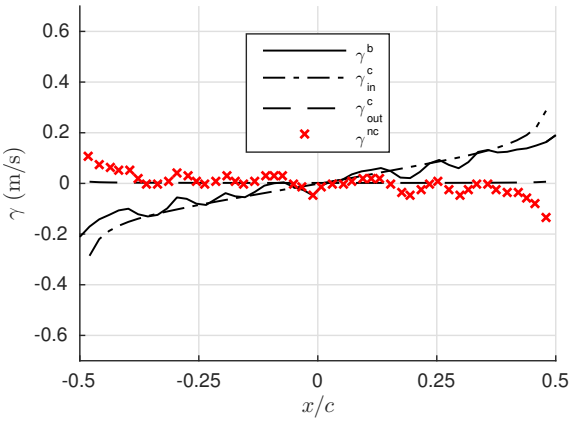

(f) $X_c/c = -1.98$

Fig. 6.8 Surge case: Instantaneous deconstruction of boundary-layer vorticity into vortex sheet constituents. The γ^c_{in} term is 'clean' because the local distribution is calculated from the free vorticity field. Measurement noise averages toward zero because many thousands of data samples are used in each calculation of γ^c_{in}. The γ^b and γ^{nc} terms are noisy as they are calculated from a few near plate velocity vectors.

For the rotation case, the instantaneous deconstruction of the boundary-layer vorticity is given by figure 6.9. At $\beta \approx 1^\circ$ almost all boundary-layer vorticity is attributed to added mass, while only a small quantity is attributed to free vorticity toward the plate edges. At $\beta \approx 90^\circ$ and $\beta \approx 179^\circ$, γ^b shows there is considerable negative attached circulation. This is attributed to γ^c_{in}. For these later times, γ^b is approximately zero at the plate edges. This is surprisingly consistent with the steady Kutta condition. Comparing all three instances, we note that the component of the attached vorticity attributed to added mass is similar in distribution and magnitude, albeit the measure is slightly noisy.

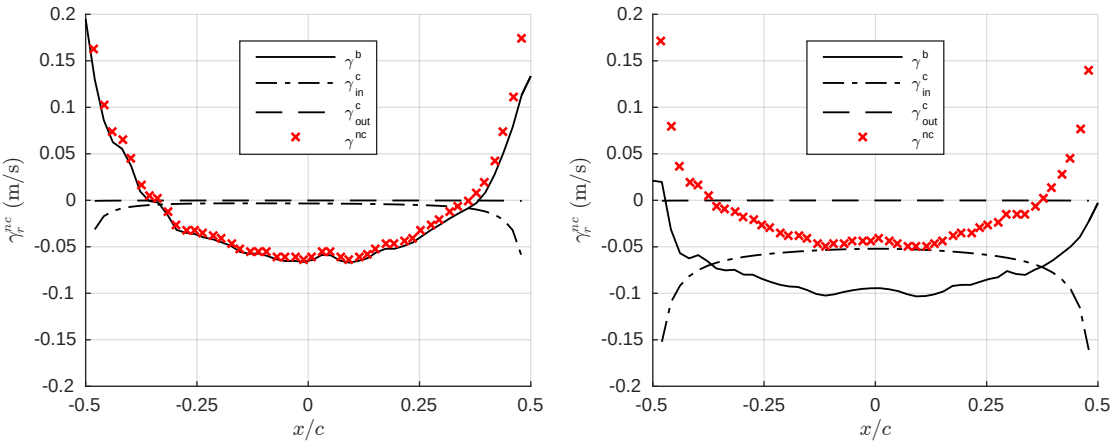

(a) $\beta \approx 1^\circ$

(b) $\beta \approx 90^\circ$

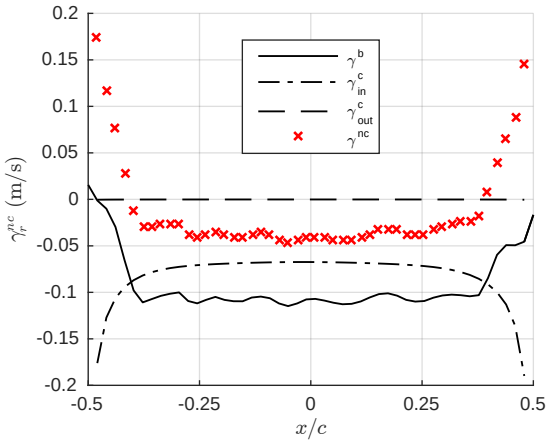

(c) $\beta \approx 179^\circ$

Fig. 6.9 Rotation: Instantaneous deconstruction of boundary-layer vorticity into vortex sheet constituents.

Before comparing the measures of the added mass vortex sheet with potential flow theory, errors attributed to the random noise need to be addressed. It was shown in section 3.2.3 that γ_t^{nc} may be scaled by U_n to give a velocity (and acceleration) independent distribution. The equivalent scaling for

γ_r^{nc} was Ωc. Here we make use of this scaling, to facilitate the reduction of experimental noise.

In figure 6.10 the theoretical, non-dimensional added mass vortex sheets given by equation (3.23) are plotted. If, as expected, the experimental measurements of the added mass vortex sheets are independent of viscous effects such as separation, then they should be equal to the theoretical distribution, albeit with additional random experimental noise. We make use of the multiple measurement sets of the scaled added mass vortex sheets, and take a sequential average of the multiple samples at each chord-wise data point to reduce the random errors. For the surge case the average of frames between $X_c/c = -0.02$ and $X_c/c = -1.98$ is taken (530 measurements). The very start ($-0.02 \leq X_c/c \leq 0.00$) and end of motion ($-2.00 \leq X_c/c \leq -1.98$) is avoided to prevent normalising the measured added mass vortex sheet by vanishingly small velocity values. For the rotating case, frames between $\beta = 1^\circ$ to $\beta = 179^\circ$ are used (approximately 100 measurements). The instantaneous and averaged experimental added mass vortex sheets are included in figure 6.10. There is striking agreement with the theoretical distribution.

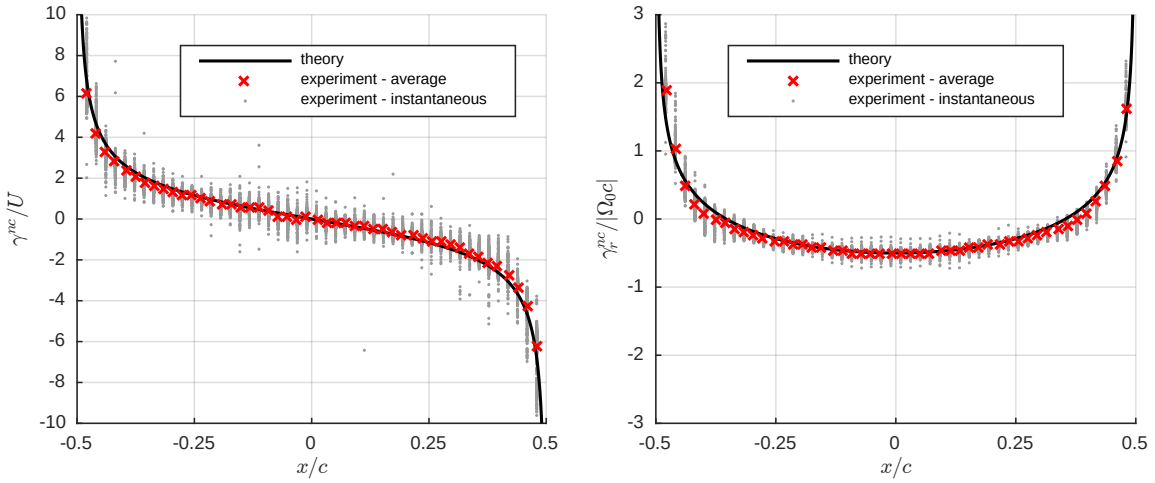

(a) Surge case **(b)** Rotation case

Fig. 6.10 Comparison of measured and potential flow vortex sheets.

The agreement between measurement and theory shows that vorticity is generated in the physical flow field when the plate is accelerated, with a distribution close (if not identical) to that predicted with inviscid theory. It can further be deduced that the distribution of this non-circulatory vortex sheet is unchanged by viscous effects and the corresponding changes to flow topology. This is because most of the measurements utilised in the averaging process were taken when the flow was in a state of severe separation. This can be shown more clearly by considering the instantaneous PIV measurements.

6.5 Instantaneous non-circulatory vortex sheet

To demonstrate further that the inviscid added mass vortex sheet is correct for a fully developed viscous flow, the rotation case flow fields are compared over the acceleration and deceleration impulses. Figure 6.11 shows (a repeat of) the flow field and added mass attributed vortex sheet at the start of motion. Here the flow is effectively a potential one, given that the bulk of the fluid is irrotational. It is perhaps unsurprising that here the experimental measure of the added mass vortex sheet matches potential theory.

Next the deceleration impulse is considered. Figure 6.12a shows the flow field before the deceleration impulse ($\beta \approx 179$) and figure 6.12b shows the flow field immediately after ($\beta = 180$). Both flow fields show significant free rotational regions, and are therefore un-potential. Why should the added mass vortex sheet match potential theory here? First we note that across the deceleration impulse the flow fields are very similar, with the strengths and position of each shed vortex practically unchanged. There is, however, a slight difference in the vorticity near the surface of the plate.

In order to satisfy the no-penetration condition, clearly there must be some change to the flow topology when the plate is suddenly brought to rest. This can be identified by taking the difference in the flow field before and after the impulse, as shown in figure 6.12c. The corresponding variation to the attached vortex sheet is shown in figure 6.12d. The change in flow field is, strikingly, equal and opposite to the starting flow shown in figure 6.11. It can therefore be concluded that, even in a highly separated viscous flow field, changes due to acceleration are equivalent to those of potential flow. The evidence thus confirms that the added mass force on the plate (or flow field), is equivalent to the potential solution for all flows, whether inviscid and attached, or viscous with significant separation.

The rotation case has also revealed an alternative method for quantifying the added mass vorticity. Taking the difference between consecutive PIV frames isolates differences in vorticity including those attributable to diffusion, advection, experimental noise and added mass effects. For bodies undergoing high rates of acceleration the latter source is dominant. The distribution of added mass attributed vorticity, generated due to a change in velocity between consecutive measurement frames, may then be quantified directly using the methodology described in section 5.2. This approach is less rigorous than the potential flow based model described in section 5.1, but is significantly simpler to implement and may be useful in situations where there are large accelerations.

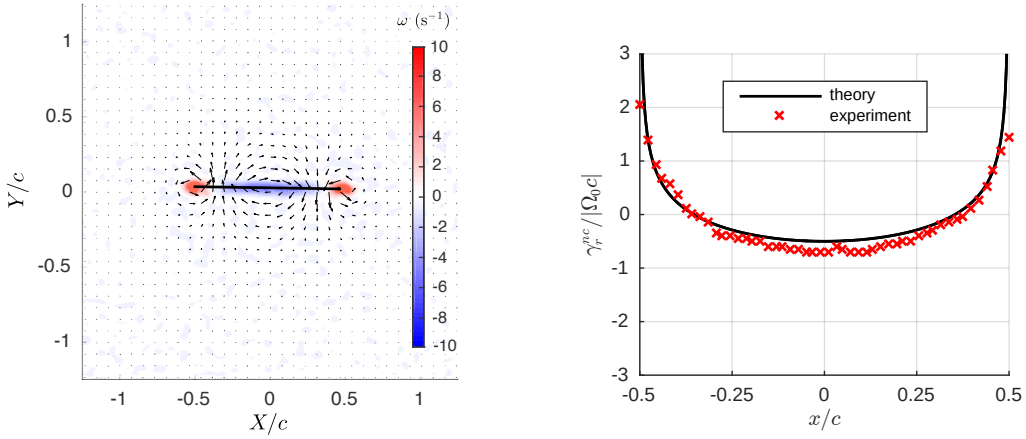

(a) Flow field at $\beta \approx 1$ **(b)** Vortex sheet

Fig. 6.11 PIV measurements over the acceleration impulse of the rotation case. $\beta \approx 1°$.

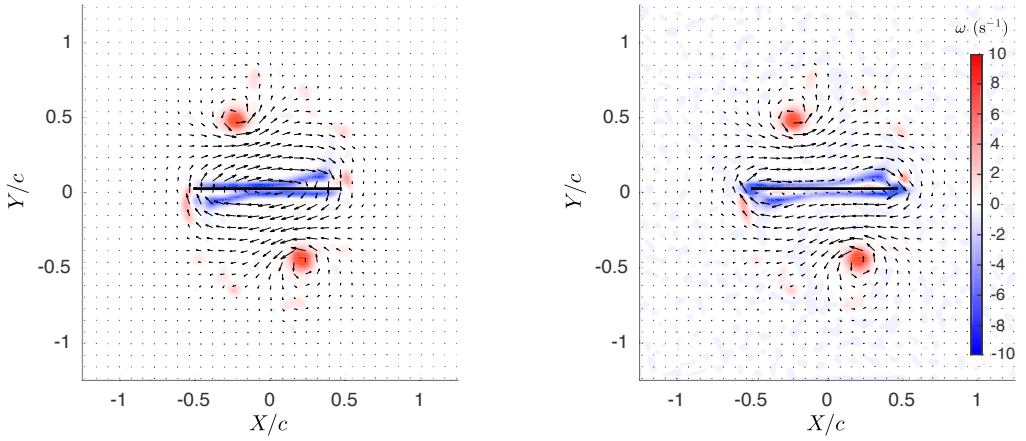

(a) Flow field at $\beta \approx 179$ **(b)** Flow field at $\beta = 180$

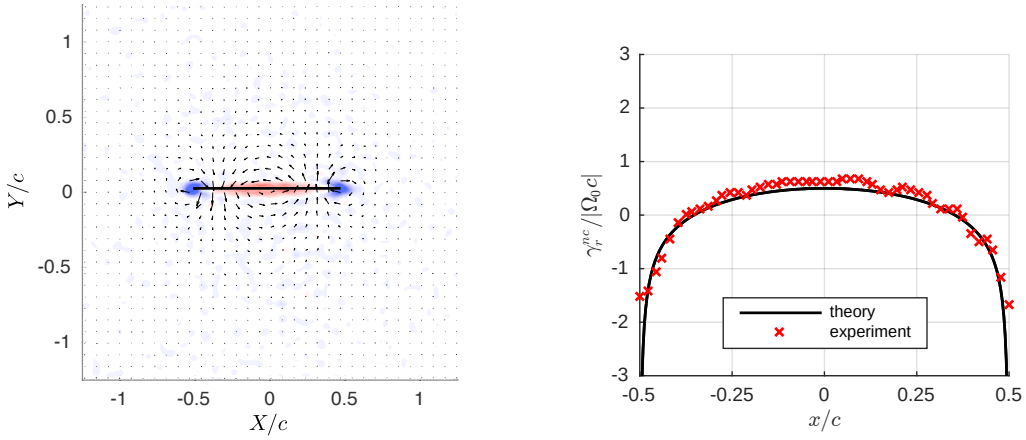

(c) Flow field difference **(d)** Vortex sheet difference

Fig. 6.12 PIV measurements over the deceleration impulse of the rotation case. $\beta \approx 180°$.

6.6 Impulse and forces from PIV

Since it is possible to extract the added mass attributable vortex sheets for each PIV measurement frame, the added mass contribution to the flow field impulse and forces can be quantified and compared with potential theory. As detailed in Appendix B, added mass impulse and force are found by first performing an analytical fit to the data to minimise discretisation errors. Impulse for the 'full' flow field, that is the sum of the contributions of attached and free vorticity, is found directly from the elemental vorticity as discretisation errors are comparatively negligible. Theoretical impulse and force values are calculated using the potential flow solution derived in section 3.2. For the surge case, the kinematics for the theoretical added mass impulse and force are based on speed sensor data. For the rotation case the kinematics are presumed to match the prescribed plate motion, as a measure of actual kinematics is unavailable.

The impulse for the surge case is shown in figure 6.13a. Here the theoretical (theory) added mass impulse is calculated from equation (3.26), all elements of vorticity in the flow field (full flow field - PIV), and the measured added mass vortex sheet (γ_t^{nc}-PIV). During the initial acceleration period $0.00 \leq -X_c/c \leq 0.20$, the impulse calculated from theory, the full flow field, and the added mass vortex sheets are almost equal. This suggests that added mass is the dominant force production mechanism. The impulse derived from the PIV data shows some oscillations. This is caused by vibration of the wing, detected by the PIV setup, but is not measured by the carriage velocity sensor. In figure 6.14, the acceleration measured using the wing-embedded accelerometer is shown. The sensor detected acceleration oscillations with the same period as that present in the PIV-derived impulse data. The corresponding flow topology, in the range $0.00 \leq -X_c/c \leq 0.50$ is shown in figure 6.15. The first frame, (figure 6.15a) is for $-X_c/c = 0.10$. It shows that little vorticity has shed into the 'free' flow field, therefore most measured vorticity is allocated as 'attached' and contributing to the added mass impulse, γ_t^{nc}-PIV. This is consistent with our previous observation in section 6.4, that during the initial acceleration range the total boundary-layer vortex sheet γ^b was almost exclusively attributed to added mass, γ_t^{nc}. For $0.20 \leq -X_c/c \leq 0.40$, a small amount of shed vorticity passes through the 'attached' flow boundary at the leeward corners, meaning it will be incorrectly attributed to the added mass vortex sheet. For $-X_c/c \geq 0.30$, shed vorticity has a significant presence, but is mostly correctly allocated as 'free'. During the constant velocity region $0.25 \leq -X_c/c \leq 1.75$, impulse determined from the PIV measurement of the non-circulatory vortex sheet (γ_t^{nc}-PIV) fits theory relatively well, albeit being slightly lower in magnitude. The cause of this discrepancy is likely attributed to the misallocation of 'attached' and 'free' vorticity. Over the deceleration region, the agreement between γ_t^{nc}-PIV and theory is reasonable. The drag force coefficient, attributed to added mass, is given in figure 6.13b. For clarity, this data set was filtered using a bi-directional windowed average (period of 0.15 seconds) to reduce noise introduced by from taking the derivative of the vibration contaminated impulse signal. There is relatively good agreement between the theoretical (given by equation 3.27), and experimental PIV extracted added mass force, across the range of the experiment. The deviation

between the PIV derived measurements and potential theory between $0.10 \leq -X_c/c \leq 0.40$, is the result of the shed vorticity passing through the region of the flow field allocated as 'attached'. This could perhaps be improved with a more sophisticated boundary definition for determining vorticity that is attached or free, but is not pursued here.

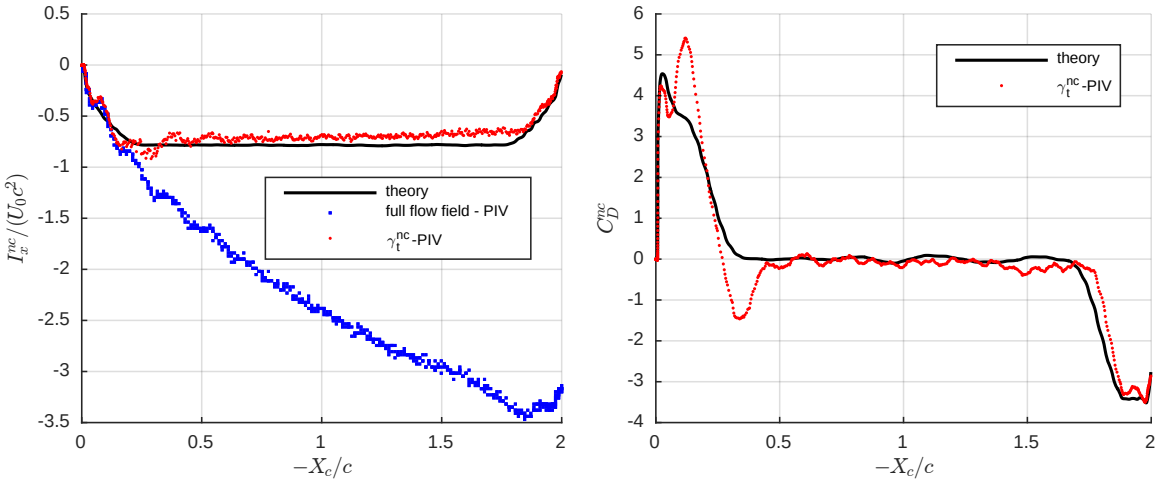

(a) Impulse **(b)** Drag coefficient

Fig. 6.13 Surge case: (*a*) Impulse compared between potential theory, the experimentally measured full flow field and the measured non-circulatory vortex sheet; (*b*) Comparison of the added mass attributed drag force coefficient between theory and the measured non-circulatory vortex sheet. For clarity, drag force coefficients are filtered using a bi-directional moving window average, with a window period of 0.15 seconds.

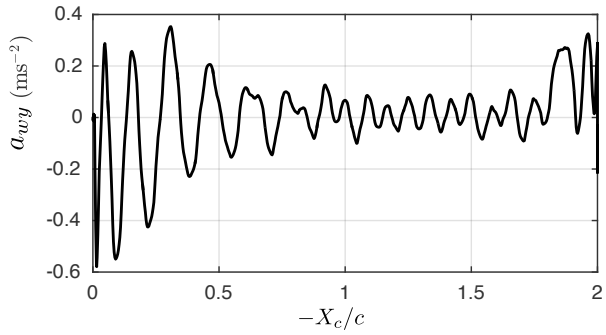

Fig. 6.14 Acceleration from the wing-embedded accelerometer.

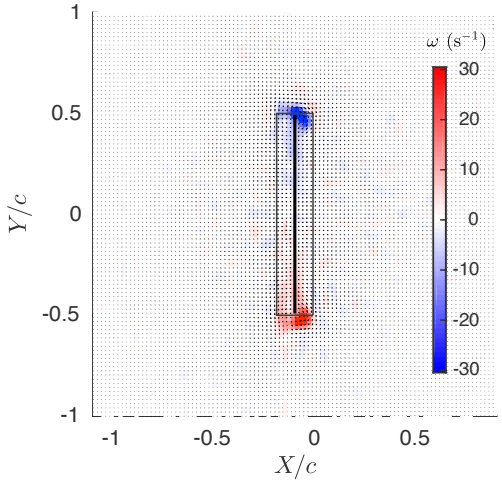

(a) $-X_c/c = 0.10$

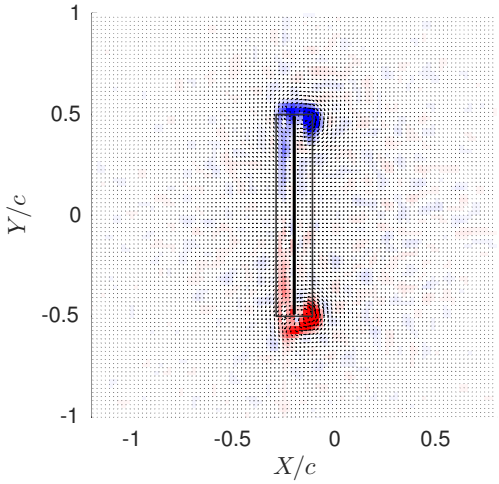

(b) $-X_c/c = 0.20$

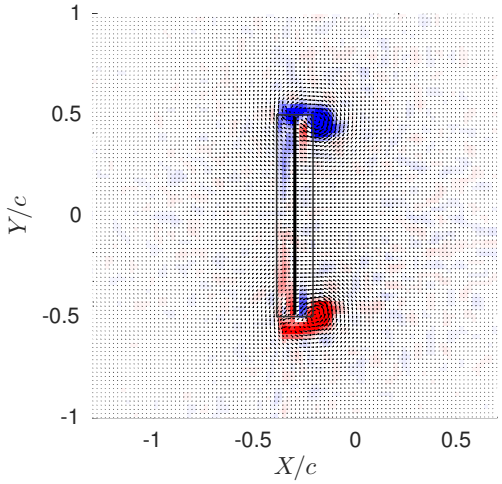

(c) $-X_c/c = 0.30$

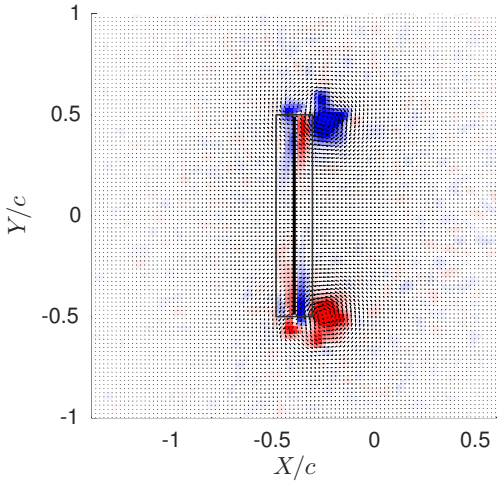

(d) $-X_c/c = 0.40$

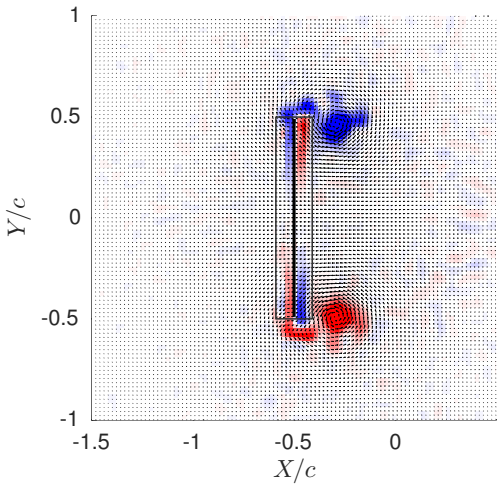

(e) $-X_c/c = 0.50$

Fig. 6.15 PIV measurements over the acceleration region of the surge case. The black rectangle divides the flow field into the 'attached' and 'free' regions. The dividing rectangle has a geometry of $0.18c \times 1.00c$.

For the rotation case, the first moment of impulse is given by figure 6.16a. Considering the full flow field, the regions of high angular acceleration at the start ($|\Omega_0 t| = 0$) and end of plate kinematic motion ($|\Omega_0 t| \approx \pi$) are clearly evident as discontinuities in the first moment of impulse. During the constant angular rotation phase, the evolution of first the moment of impulse is remarkably linear. After the plate stops ($|\Omega_0 t| > \pi$), the first moment of impulse does not immediately return back to zero. This is likely because viscous effects have resulted in the shedding of free vortices (see figure 6.5), that persist even after the plate has ceased motion. The value of the first moment of impulse would be determined by the strength of the free vortices, and γ^c. Now considering the added mass only components, there is excellent agreement between the theoretical first moment of impulse and that derived from the measure of the non-circulatory vortex sheet (γ_r^{nc}-PIV). The magnitude of the discontinuities at the start and end of kinematic motion are relatively accurately captured by the measured vortex sheet. Furthermore, γ_r^{nc}-PIV deviates little from theory over the constant angular velocity region. Further agreement between theory and experiment, for the added mass attributable pitching moment, is shown in figure 6.16b. As predicted, the measured moment (γ_r^{nc}-PIV) is approximately zero for the entirety of the motion, except during the acceleration impulses. The scattering of the pitching moment derived from PIV (γ_r^{nc}-PIV) after each acceleration impulse decays asymptotically, which suggests that it is caused by damped torsional vibration of the plate.

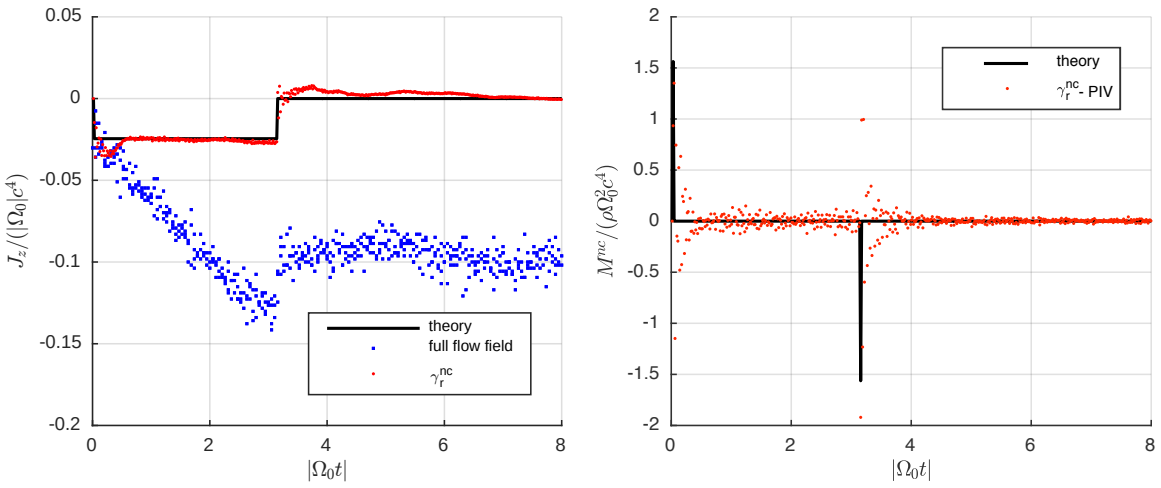

(a) First moment of impulse

(b) Moment

Fig. 6.16 Rotation case: (*a*) First moment of impulse compared between potential theory, the experimentally measured full flow field and the measured non-circulatory vortex sheet; (*b*) Comparison of the added mass attributed pitching moment between theory and the measured non-circulatory vortex sheet. No filtering is employed.

6.7 Summary of findings

Added mass is an unsteady fluid dynamic effect that has been discussed in the literature for over a century. Despite being derived for an inviscid fluid, this solution was described as being equally applicable for viscous and separated flows; a point which had never been experimentally demonstrated. This Chapter presented experiments on a flat plate wing undergoing translation in the surface normal direction and rotation about the mid-chord. The methodology described in Chapter 5 for isolating the added mass component was applied. This enabled a substantial conclusion to be made: the potential flow added mass solution is valid for a fully viscous, highly separated flow field, as suggested in the literature. We came to this conclusion because qualitative analysis of the flow showed:

- For a flat plate undergoing high angle of incidence surge and rotational motions, a distribution of attached vorticity is generated in the flow field at the start of motion.
- Subsequent motion of the body results in the shedding of vorticity at each plate edge, which coalesces into free vortices that significantly alter the flow topology compared to inviscid theory. Both the distribution of attached vorticity and surrounding flow field are altered. There is further minor secondary separation on the leeward edge of the plate for the rotating case.
- On stopping the plate, new boundary-layer vorticity is generated, with an equal and opposite distribution to that generated during the starting motion.

Meanwhile, quantitative analysis of the measurements demonstrated:

- Distributions of boundary-layer vorticity may be readily quantified from PIV measurements with a resolution incapable of directly resolving velocity gradients within the boundary-layer. The vector density for the present experiments is only 50 vectors per chord.
- The distribution of boundary-layer vorticity generated at the start of motion has similar, if not identical distribution to that of a plate in potential flow undergoing the same kinematic motion.
- For the separated flow field, the measured distribution of boundary-layer vorticity can successfully be deconstructed into components attributable to circulatory and non-circulatory components.
- The non-circulatory component has a distribution similar to the potential flow result, regardless of the state of separation.
- Flow field impulse, force and moments thereof, all derived from the non-circulatory vortex sheet, fit well with that predicted by inviscid theory.

These points indicate both the success of the methodologies used for isolating the added mass experimentally, and provides evidence pointing toward our primary conclusion. We may also conclude

(albeit somewhat lesser in importance), that the close fit between the experimental and potential theory derived added mass quantities, suggests that 3-dimensional flow effects about an (effective) aspect ratio 8 wing, undergoing rapid acceleration motions are small. The measures showing that circulation is conserved provides further evidence of this.

While the main experimental finding is a simple confirmation of existing theories, the analysis techniques developed represent an advance in our understanding of the capabilities of PIV to quantify unsteady external flows. In particular, the work shows that with careful experimental design, the added mass effect may be intentionally captured; or, equivalently, that vorticity or circulation attributable to the added mass phenomenon may be a source of 'contamination' when determining the circulation of vortices shed into a flow field. For the calculation of the circulation of a vortex close to the surface of a body using closed contours of integration, contours that cross-over, or are interpolated over the boundaries of a body will include added mass effects regardless of body-containing vector treatment. We have therefore met the 'further objectives' described in section 3.4.1, and can now progress to investigate the role of the circulatory and non-circulatory force production mechanisms for a wing-gust encounter.

Chapter 7

Gust-Encounter Results

The reader is reminded that the aims of the wing-gust encounter test cases are to develop an understanding of the underlying physics of such interactions, and investigate the applicability of Küssner's linear model through a comparison of force and flow topologies. Particular emphasis is placed on investigating the added mass phenomenon. The theoretical inviscid added mass description was shown to also apply to a viscous separated flow field in Chapter 6. However, in a wing-gust encounter neither the wing, nor the flow field undergo general acceleration, which raises a conceptual problem. We therefore seek an explanation for the cause of this discrepancy.

7.1 Gust kinematics and configurations

For each test case, the gust generation apparatus described in section 4.7 was utilised. The flow topology and forces were measured for gust ratios of 0.2, 0.5 and 1.0. In each case, only a single angle of incidence (prior to gust entry) of 0 degrees was tested. The $GR = 0.2$ case represents conditions within the expected validity of Küssner's model. The change to the angle of incidence is comparatively low (11 degrees), and the small angle assumption ($\sin\alpha \approx \alpha$) is a reasonable approximation. The $GR = 1.0$ case is the opposite extreme. Here the change in angle of incidence is 45°, therefore the Küssner model should be invalid. It is this test case that is representative of MAVs in free flight, and where flow phenomena, such as significant leading edge separation, are anticipated. Unless otherwise specified, the offset distance between the wing and the gust outlet was 100 mm, whereas the distance between the collector and outlet was 400 mm (see figure 7.17a). The effect of the spacing between the wing and outlet is discussed in section 7.6. To reduce disturbance to the surrounding flow field, the gust rig was started 60 seconds prior to each $GR = 0.2$ test run, and 30 seconds prior to each $GR = 0.5$ and $GR = 1.0$ run. This enabled sufficient time for the gust starting vortices to advect from the measurement window, and the velocity profile to settle. Dye flow visualisation was performed at a Reynolds number of 5000, while a Reynolds number of 20,000 was used for PIV and force acquisition. Reynolds number dependence is investigated in section 7.7. Finally, an attempt to extract added mass

quantities from the vorticity field is made in section 7.8.

7.2 Gust off

The flow in the wake behind the wing is briefly characterised to aid the later analysis of dye flow visualisation of the more complex gust-on cases. At zero degrees incidence the flow field should be largely symmetric. However, along the upper and lower surface of the wing, boundary layers of opposite strengths are generated. These are shed from the wing at the square trailing edge. Dye flow visualisation for this case is shown in figure 7.1. The pair of shear layers is unstable, resulting in a von Karman vortex street. The Reynolds number based on the plate thickness is $Re = 166$, thus a laminar vortex street is expected.

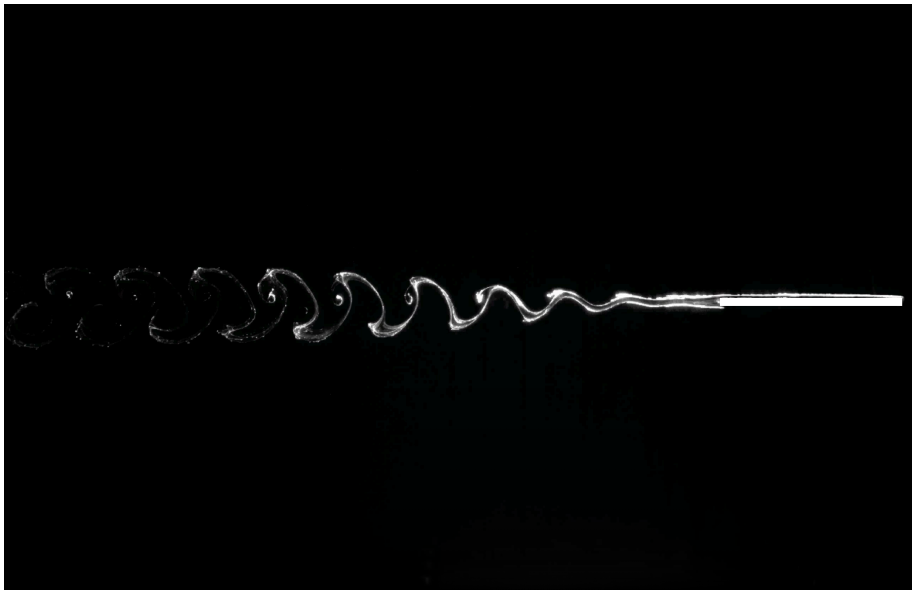

Fig. 7.1 Dye flow visualisation depicting the wake behind the plate. $Re = 5000$ (wing chord), $Re = 166$ (wing thickness). The plate is moving from left to right and is depicted by the white rectangle at the right side of the photograph.

7.3 Gust ratio 0.2

PIV measurements for a gust ratio of 0.2 are shown in figure 7.2. The first frame, figure 7.2a, shows the plate at $s/c = 0$. The leading edge has just reached the left hand shear layer of the gust, which extends over the range of $X/c = 0$ to $X/c = 2$. On the upper and lower surface of the plate, regions of positive (red) and negative (blue) vorticity, contained within the boundary-layers are visible. Spurious bands of bad measurement vectors and associated vorticity emanate downward from the leading and trailing edges. These are the result of laser light refraction from the edges of the glass wing. In the

wake, the alternating 'blobs' of positive and negative vorticity are the result of the von Karman vortex street.

On entry of the plate into the gust the following may be observed:

- Thickening of the positive vorticity on the upper surface is indicative of flow separation at the leading edge. Up until $s/c = 2.5$, the flow appears to re-attach before the trailing edge. Afterward, however, the vorticity is shed into the wake.
- From $1.5 \leq s/c \leq 2.5$, the wake appears to change from the alternate vortex shedding to discrete blobs of negative vorticity (with a little positive vorticity shed from the upper boundary-layer). The discrete blobs may be the result of a Kelvin-Helmholtz instability. Since net negative vorticity is shed at the trailing edge, the bound circulation of the plate must be non-zero.
- The wake is slightly deflected upward behind the aerofoil, but remains planar.

Dye flow visualisation of the gust shear layers is shown in figure 7.3a. At $s/c = 3.0$ it can be seen that the left hand gust shear layer, below the wing, was deflected mildly away from the gust centre. The left hand gust shear layer, above the wing, was deflected slightly inward toward the centre of the gust. For the right hand gust shear layer this process appears to occur in a reverse manner as the plate exits the gust. It appears as though the plate 'splits' each of the gust shear layers when passing through. Also visible in figure 7.3a, is slight roll up of the gust shear layers at the outlet edges. This is shown by the presence of two very small vortices at each corner of the outlet, labelled *A* and *B*. After long periods of time, ($s/c = 6.0$) as shown in figure 7.3b, the gust shear layer vortices have grown substantially.

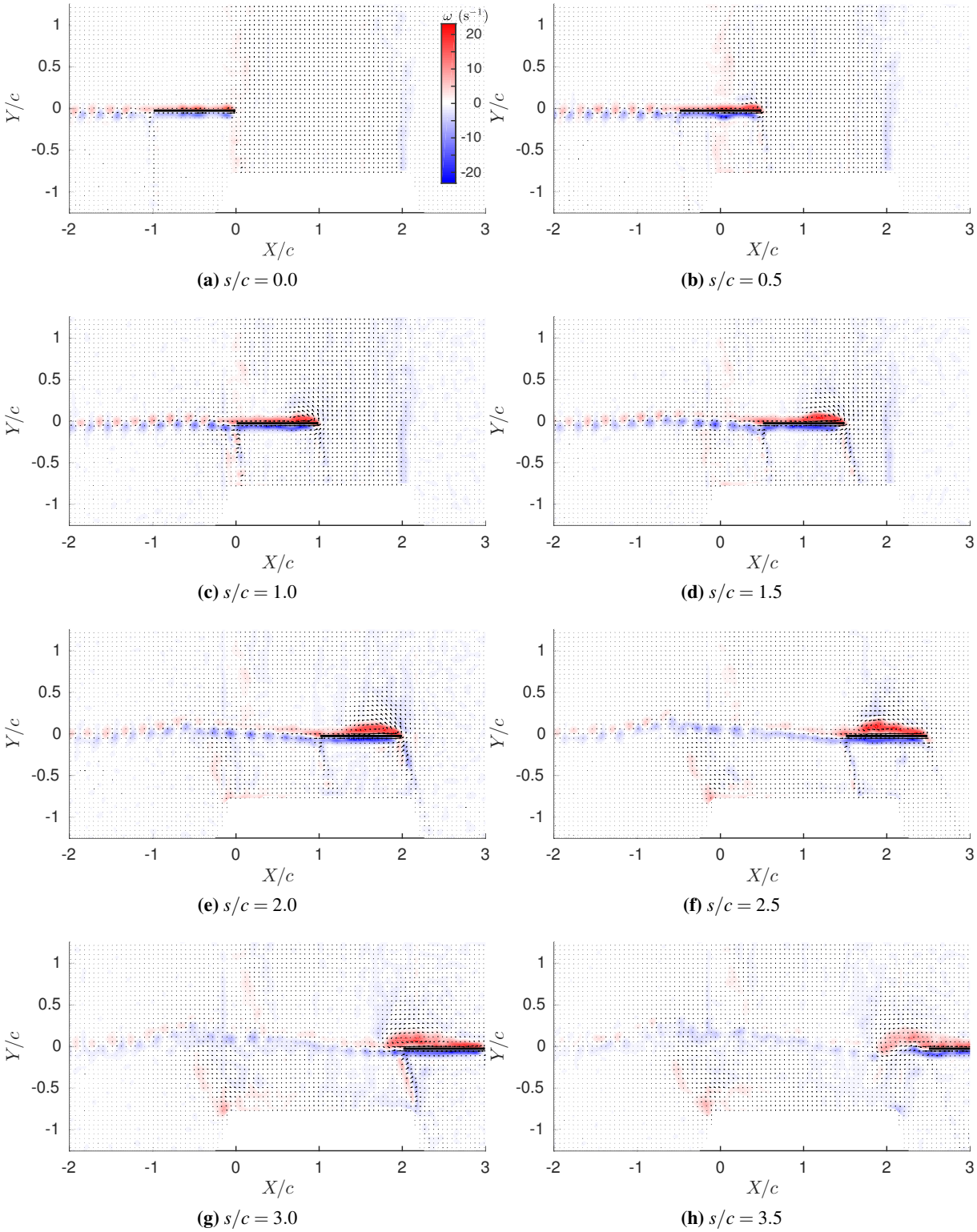

(a) $s/c = 0.0$ **(b)** $s/c = 0.5$

(c) $s/c = 1.0$ **(d)** $s/c = 1.5$

(e) $s/c = 2.0$ **(f)** $s/c = 2.5$

(g) $s/c = 3.0$ **(h)** $s/c = 3.5$

Fig. 7.2 PIV measurements of the gust entry for $GR = 0.2$. Red contours indicate positive vorticity (anticlockwise). Blue contours indicate negative vorticity (clockwise).

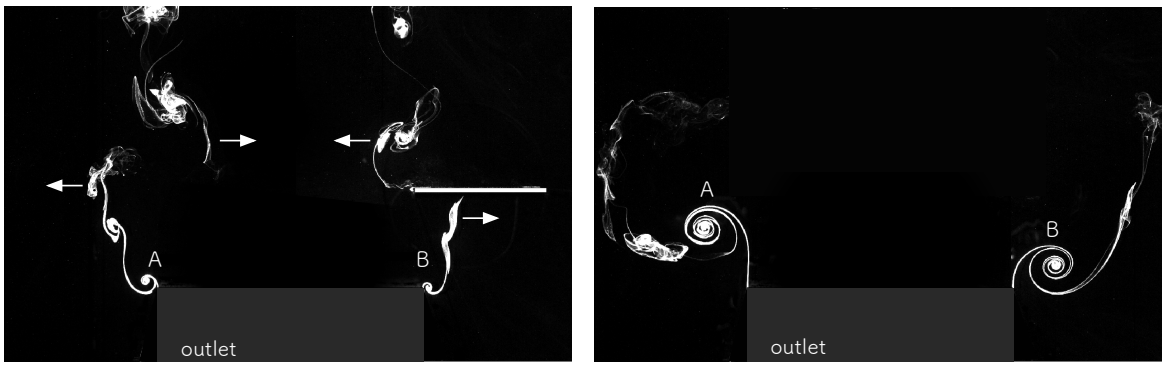

(a) $s/c = 3.0$ **(b)** $s/c = 6.0$

Fig. 7.3 Dye flow visualisation of gust shear layers. Arrows indicate the gust shear layer movement. Labels *A* and *B* show the start of roll-up and progression of the gust shear layers. $GR = 0.2$.

Now we will consider the more quantitative measures of the interaction. Separate sums of positive and negative elements of the PIV derived circulation are plotted in figure 7.4. Prior to the wing entering the measurement window, the finite positive and negative circulation is the result of vorticity contained by the gust shear layers, as well as elemental vector noise. From $-2.0 \leq s/c \leq 0.0$ the plate enters the measurement frame. This results in a rapid increase in elemental circulation due to boundary-layer and wake shed vorticity. From $s/c = 0.0$ and onward, the plate has entered the gust and there is a noticeable increase in the circulation until the plate starts to exit the gust ($s/c = 2.0$), after which the circulation begins to drop. At $s/c = 6.0$, despite the plate long having left the observation window, the circulation has not yet recovered to the pre-wing interaction state. This is likely the result of the lingering rolled up shear layer vortices. Looking at the total circulation, this is largely zero, except for some slight deviations which are likely the result of spurious error and perhaps three-dimensional effects, or an imbalance of vorticity exiting the observation window.

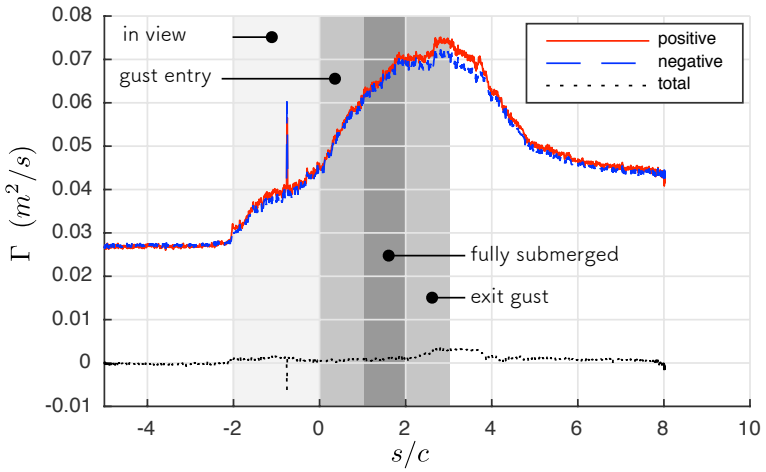

Fig. 7.4 Sum of all positive and all negative circulation 'elements' in the flow field. $GR = 0.2$.

In figure 7.5, the experimentally measured lift force coefficient is compared with that of Küssner's model. For $0 \leq s/c \leq 2$ the measured force reasonably closely fits the ideal top-hat Küssner response. On exit, from $2 \leq s/c \leq 3.5$ the measured lift coefficient overestimates the Küssner prediction. This, as illustrated schematically in figure 7.6, may be the result of increased pressure on the underside of the plate from turning gust flow, as well as a reduction in pressure on the upper surface due to ambient fluid accelerating toward the trailing edge to fill the 'void' left by the diverted gust flow.

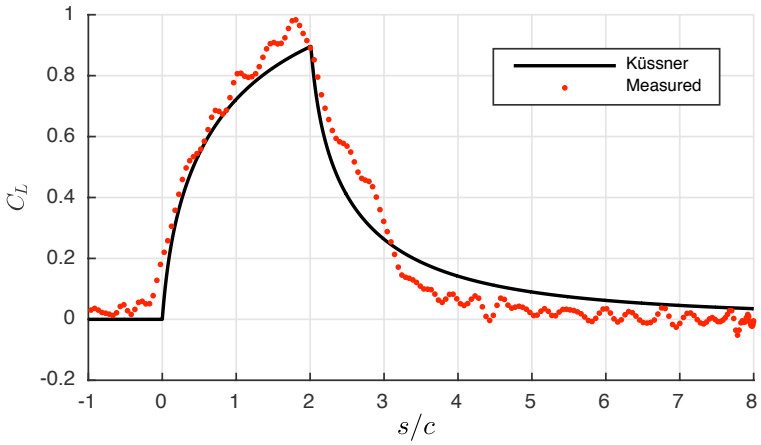

Fig. 7.5 Comparison of the measured and Küssner lift coefficient, $GR = 0.2$.

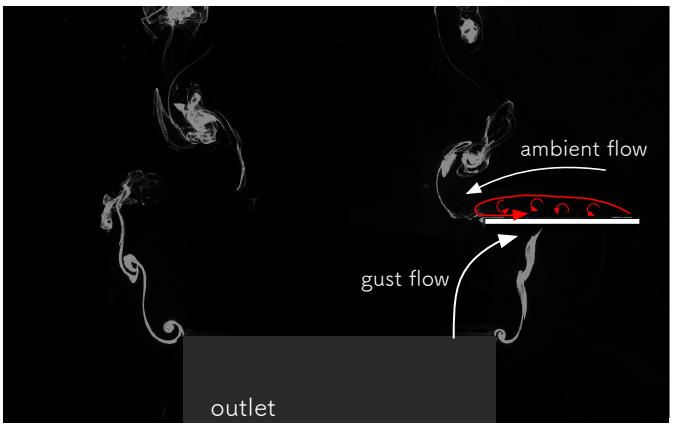

Fig. 7.6 Schematic of the flow at $s/c = 3.0$. $GR = 0.2$.

In summary, for the $GR = 0.2$ test case the wing wake, while planar, was deflected from horizontal and there was minor leading edge separation. The gust shear layers were deflected on wing entry, and subsequently rolled up into coherent vortical structures. Each of these observations represents a deviation from the idealised conditions modelled in Küssner's sharp edged gust theory. On the whole, however, the effect of each of the discrepancies appears to have only a small effect on the lift force coefficient of the wing. Küssner's model fits the measured lift history relatively well.

7.4 Gust ratio 0.5

For a gust ratio of $GR = 0.5$, the effective change in angle of incidence of the wing is 26°. Significant separation at the leading edge is expected. PIV measurements of the flow field are shown in figure 7.7.

From the measurements the following topological changes can be observed:

- At $s/c = 0.5$, some positive vorticity is shed at the leading edge. The region of vorticity is relatively localised to the leading edge and flow appears to reattach at approximately the quarter chord point. This is the beginning of a LEV. Some slight deflection of the left (positive) gust shear layer can be observed.
- From $s/c = 0.5$ to $s/c = 1.5$, the LEV grows in size due to accumulation of vorticity shed from the leading edge, and perhaps vorticity from the left gust shear layer. The centroid of the LEV appears to move toward the trailing edge. Significant deflection of the left gust shear layer is visible. Negative vorticity is shed into the wake at the trailing edge of the aerofoil. This vorticity is distributed in the wake in an approximately linear way, albeit the 'line' of vorticity is deflected from horizontal by an angle of approximately 11°.
- At $s/c = 2.0$, the leading edge of the wing has reached the original location of the back shear layer, however, it can be seen that the exit shear layer has been deflected away from the wing. The LEV is approximately the same size as the wing chord. At the mid-chord of the wing, negative vorticity in the upper surface boundary-layer appears to leave the surface. This is indicative of secondary separation.
- At $s/c = 3.0$, the wing has fully exited the gust. The leading edge vortex has moved behind the wing. A relatively small negative vortex appears to have been shed at the trailing edge of the plate. The gust shear layers have rolled up.
- At $s/c = 3.5$, the leading edge vortex and trailing edge vorticity appear to be merging and the flow field looks quite turbulent. There may be substantial three-dimensional effects.

On the whole, the flow field for the $GR = 0.5$ case appears representative of a deep dynamic stall-like process. From McCroskey et al. (1982), the dynamic stall process is characterised by an initial breakdown of the flow from steady state conditions, with the formation of a strong vortex at the leading edge. This advects downstream over the suction surface of the aerofoil, with a viscous core of order a chord length. We note, however, that the dynamics between a typical dynamic stall process, and the gust encounter will likely differ. The former is associated with a rapid pitching motion, which will have an associated production of vorticity, similar to that measured in the rotating plate experiment described in Chapter 6. There is therefore a rotational added mass effect associated with the pitching motion, which is not present in the gust case due to lack of rotational kinematic motion.

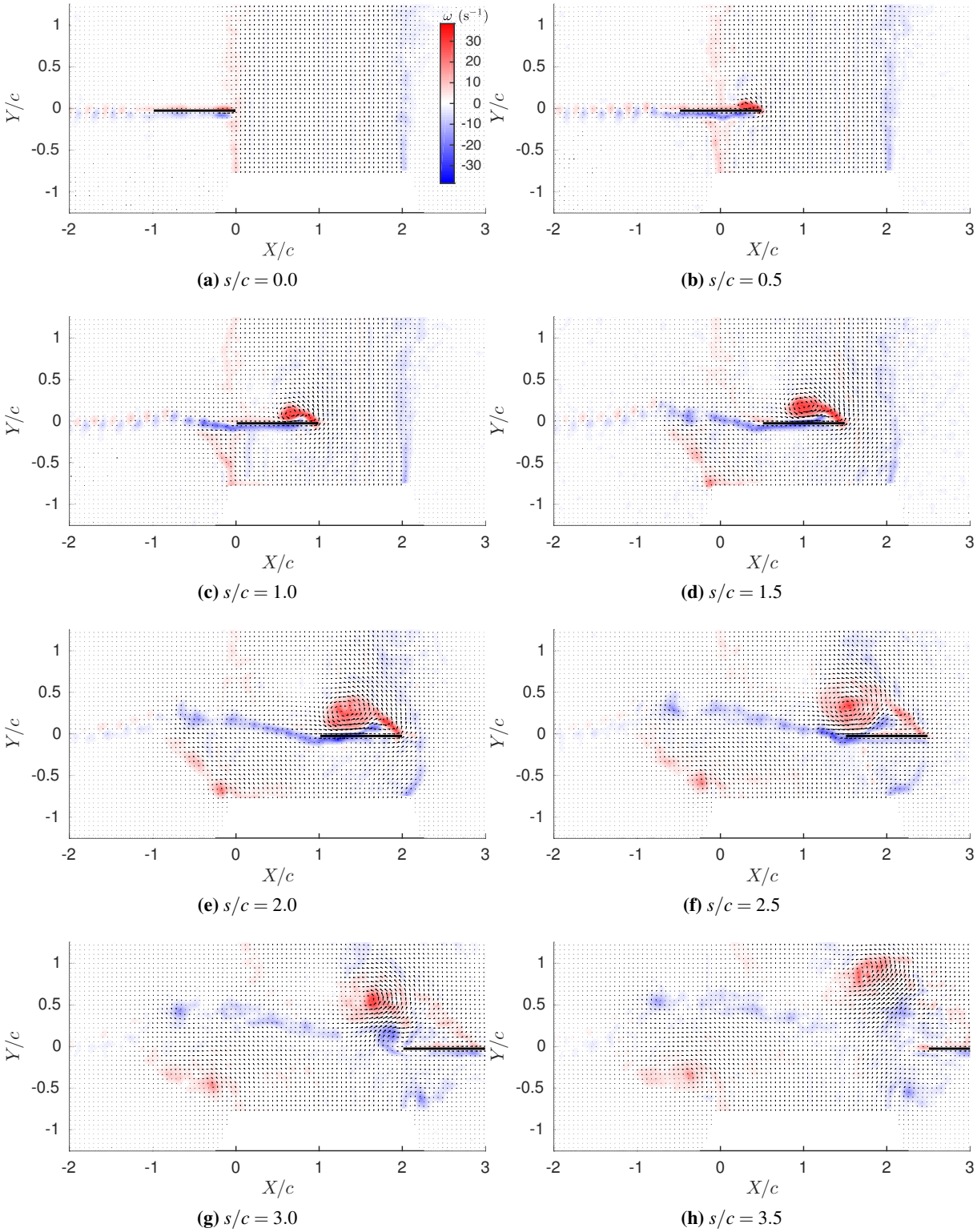

(a) $s/c = 0.0$ **(b)** $s/c = 0.5$

(c) $s/c = 1.0$ **(d)** $s/c = 1.5$

(e) $s/c = 2.0$ **(f)** $s/c = 2.5$

(g) $s/c = 3.0$ **(h)** $s/c = 3.5$

Fig. 7.7 PIV measurements of the gust entry for $GR = 0.5$. Red contours indicate positive vorticity (anticlockwise). Blue contours indicate negative vorticity (clockwise).

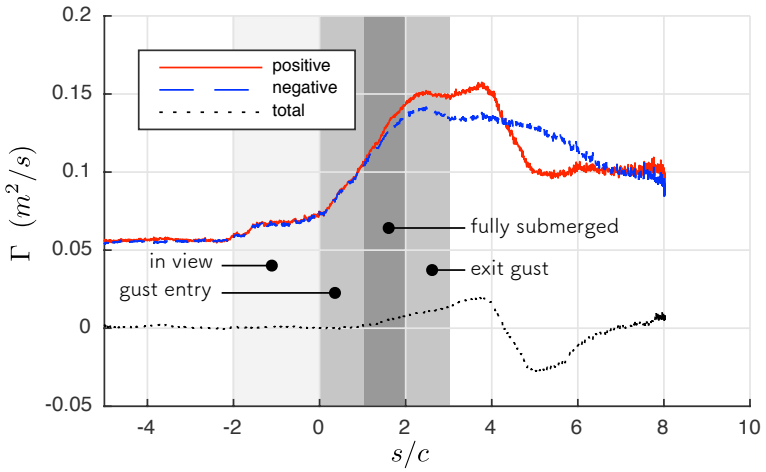

Fig. 7.8 Sum of all positive and all negative circulation 'elements' in the flow field. $GR = 0.5$.

Next we consider the separate sums of elemental circulation, as given by figure 7.8. For the gust ratio of 0.2 case it was observed that the net circulation measured in the flow field remains approximately zero throughout the entire run. This observation does not hold for the gust ratio of 0.5 case. From $s/c \approx 1$ to $s/c \approx 4$ there is an excess of positive circulation measured within the flow field. From $s/c \approx 4$ to $s/c \approx 7$ there is excess of negative circulation. Since vorticity shed by the wing largely remains within the measurement window, the variation in net circulation is likely caused by the gust shear layers. In steady state operation there is an approximately constant, equal and opposite flux of positive and negative circulation both entering the measurement window from the gust rig outlet and exiting at the top of the window. When the wing enters the gust, the positive vorticity in the left hand gust shear layer is physically blocked by the wing. This leads to an accumulation of positive gust shear layer vorticity within the measurement window. Since the right hand shear layer is initially unaffected (on the most part) by the wing, there will be an excess of positive circulation. On exit of the wing from the gust the reverse process occurs, causing the negative dip in the total circulation.

For the gust ratio of 0.5 there are significant topological differences between the measured flow field and that assumed by the linear Küssner model. In figure 7.9 the measured and predicted force coefficients are compared. During entry into the gust the measured force matches the Küssner model surprisingly well. The peak lift coefficient of $C_L \approx 2.25$ matches, albeit the the peak occurs slightly earlier than predicted by Küssner's theory. On exit of the gust between $2.0 \leq s/c \leq 2.5$ agreement is excellent, however, afterward the measured lift decays to approximately zero significantly quicker than the Küssner model. The cause of this dip will be discussed in the $GR = 1.0$ case.

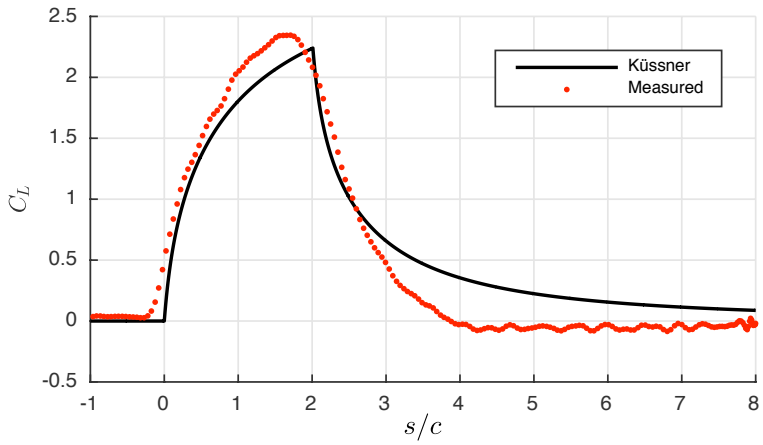

Fig. 7.9 Comparison of the measured and Küssner lift coefficient for $GR = 0.5$.

7.5 Gust ratio 1.0

For the $GR = 1.0$ case it is anticipated that the flow will deviate significantly from Küssner's model. The effective change to the angle of incidence is 45°, which will certainly compound the growth rate of the LEV compared to the $GR = 0.5$ case. Once again, we will first describe the qualitative observations of the flow field, before considering the measures of circulation and force.

PIV measurements of the gust encounter are shown in figure 7.10, while dye flow visualisation at $s/c = 1.0$ is shown in figure 7.11. In figure 7.11a, dye was injected into the flow at the leading and trailing edges of the wing, to ensure it was entrained into the shear layers feeding the leading and trailing edge vortices. In figure 7.11b dye was injected into the gust shear layers. From the measurements the following may be observed:

- At $s/c = 0.5$, a LEV has started to form above the surface of the wing. This is fed primarily by flow separating at the sharp leading edge. The LEV advects away from the surface of the plate. At $s/c = 2.0$ the LEV starts to exit the measurement window.
- The LEV appears to induce reversed flow along the upper surface of the wing, with a flow direction moving from the trailing to leading edges. At $s/c = 1.0$ and onward, secondary separation on the upper surface of the wing is visible. The secondary flow appears to be entrained into the leading edge vortex. The secondary separation can be clearly seen in the dye flow visualisation given by figure 7.11a
- Negative vorticity is shed at the trailing edge. Up to $s/c = 1.5$ the wake vorticity is oriented in a relatively linear manner, albeit at an angle deflected by approximately 20° from horizontal.
- As the wing enters the gust, the left gust shear layer below the wing is diverted away from the gust centreline. The left gust shear layer located above the wing is shifted toward the gust

centre. This can be seen from the dye flow visualisation shown in figure 7.11b. Some of the gust shear layer vorticity has additionally been entrained into the LEV.

- At $s/c = 1.5$, the right gust shear layer shows relatively significant deflection away from the leading edge of the plate.
- At $s/c = 3.5$, roll-up of both the gust shear layers can be seen. The vortex formed from the right shear layer appears directly below the trailing edge of the wing. The measure of trailing edge vorticity additionally becomes incoherent. These spurious data points suggests that three-dimensional effects are resulting in the loss of particle image pairs.

It was assumed in the Küssner model that the wing has bound circulation, the wake is planar and the position of the gust shear layers is 'rigidly' held in space. For the $GR = 1.0$ case we see that the flow field is dominated by the leading edge vortex, which indicates that the bound circulation is comparatively reduced. Vorticity shed into the wake at the trailing edge is reasonably planar, but is deflected, and both gust edges are significantly disturbed.

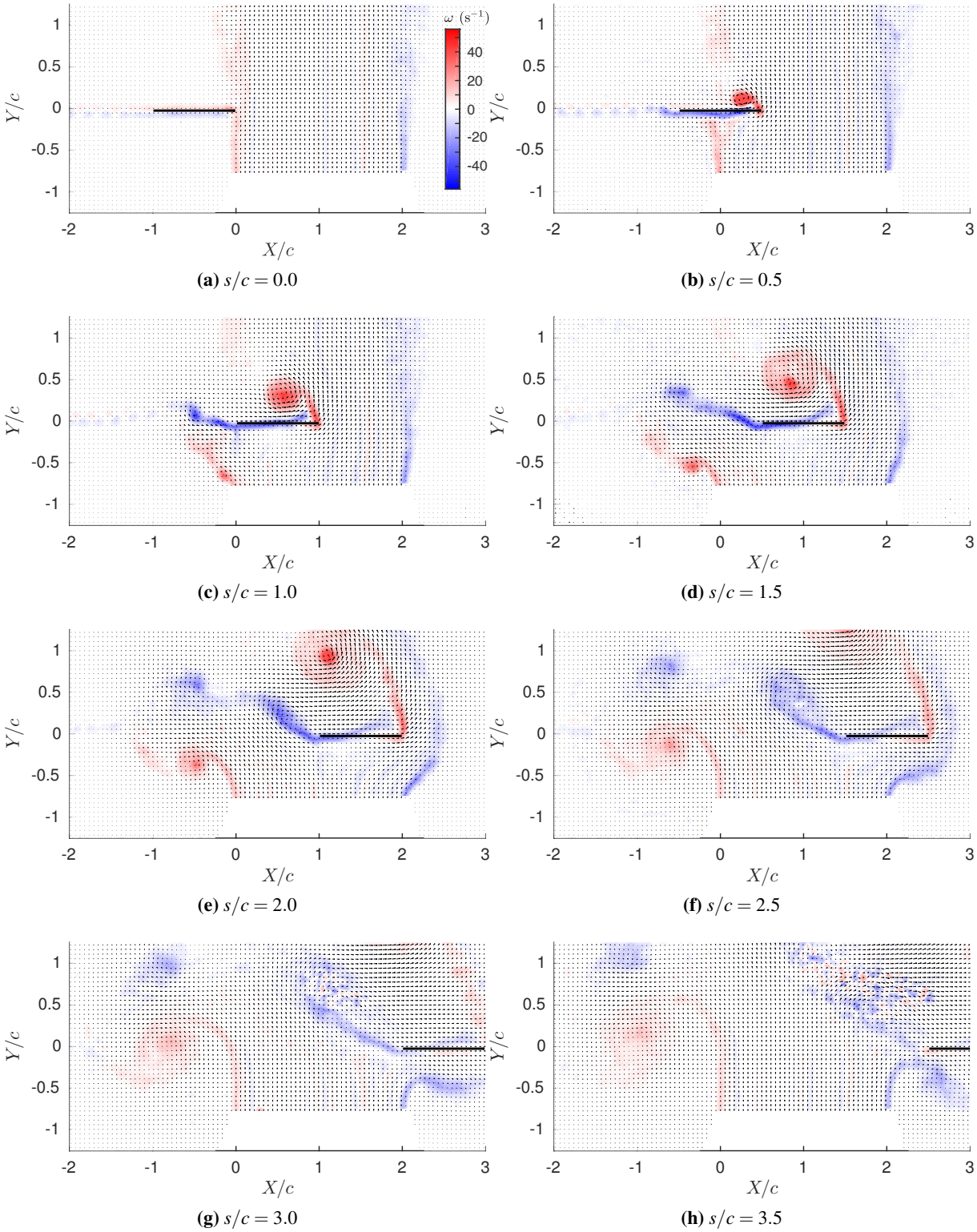

(a) $s/c = 0.0$ **(b)** $s/c = 0.5$

(c) $s/c = 1.0$ **(d)** $s/c = 1.5$

(e) $s/c = 2.0$ **(f)** $s/c = 2.5$

(g) $s/c = 3.0$ **(h)** $s/c = 3.5$

Fig. 7.10 PIV measurements of the gust entry for $GR = 1.0$. Red contours indicate positive vorticity (anticlockwise). Blue contours indicate negative vorticity (clockwise).

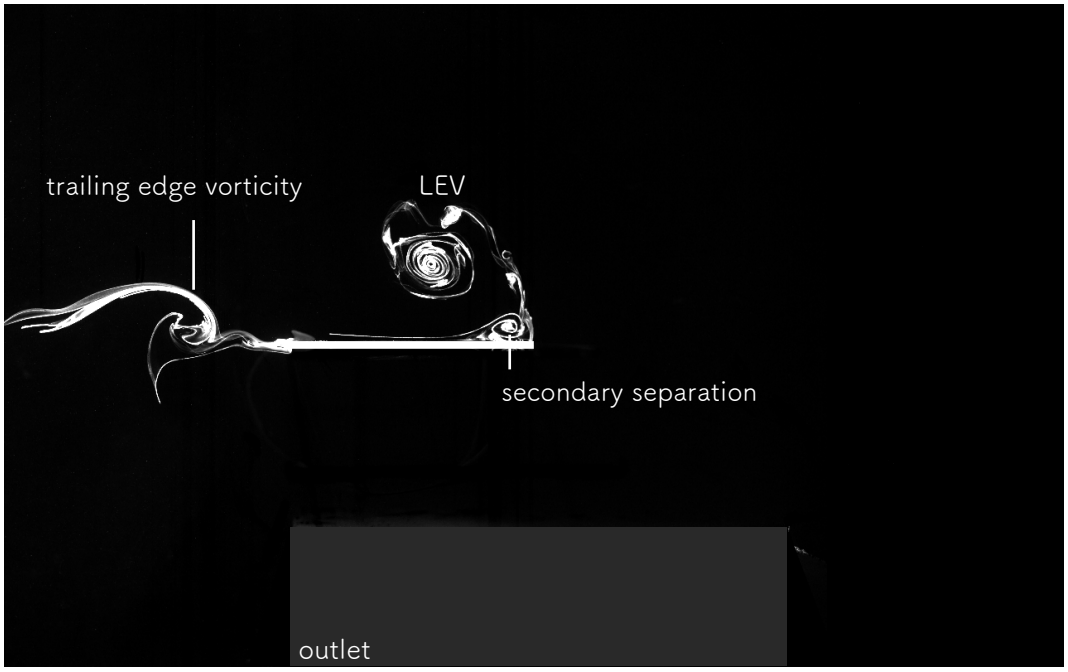

(a) Wing shed vorticity

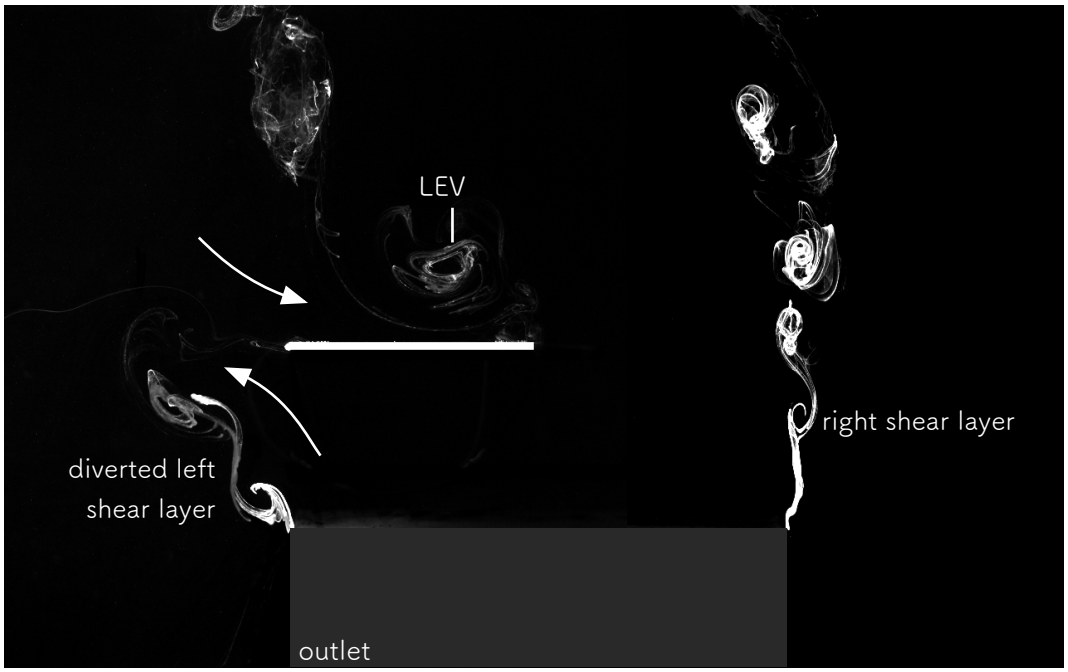

(b) Gust shear layer vorticity

Fig. 7.11 Dye flow visualisation for $GR = 1.0$, at $s/c = 1.0$. For 7.11a, the dye injection points are located at the leading and trailing wing edges. For 7.11b, dye injection points are located at the left and right edges of the gust outlet. $Re = 5000$.

Moving onto the quantitative analysis, the measured circulation is given by figure 7.12. Similar to the $GR = 0.5$ case, we see that the total positive and negative circulation measured in the flow field is zero up until $s/c = 1.0$. The initial difference is again attributed to a discrepancy in the flux of gust shear layer vorticity entering and exiting the measurement window. From $s/c = 2.0$, however, there is a very sharp drop in the total circulation. This sharp drop corresponds to the leading edge vortex exiting the measurement window, as visible in figures 7.10e to 7.10g. At approximately $s/c = 4.0$, the negative circulation also drops, and the total circulation in measured flow field recovers closer to zero. This is the result of the vorticity shed at the trailing edge leaving the measurement window.

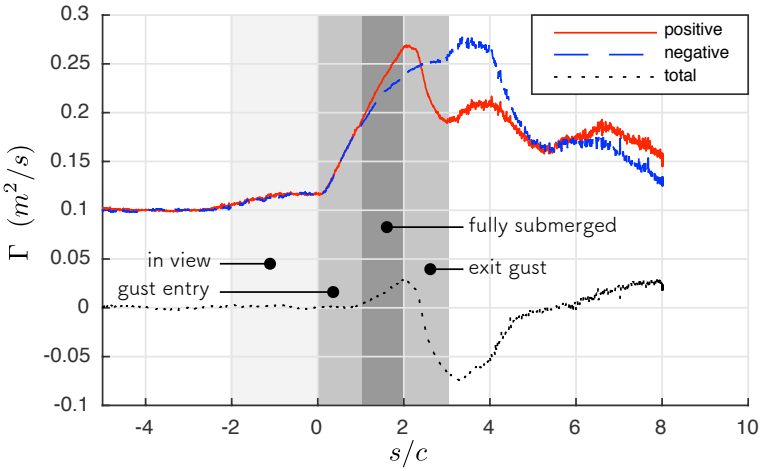

Fig. 7.12 Sum of all positive and all negative circulation 'elements' in the flow field. $GR = 1.0$.

Forces for the wing-gust interaction are given in figure 7.13. The peak lift coefficient exceeds that of the Küssner model by approximately 27% and occurs slightly earlier, at $s/c \approx 1.5$ rather than $s/c = 2.0$. Again there is good agreement between measurement and theory between $s/c = 2.0$ to $s/c = 2.5$ and a significant undershoot thereafter. Interestingly, negative lift is measured onward from $s/c \approx 3.0$, whereas Küssner's model predicts a decaying positive value. To investigate the mechanism responsible for this negative lift measurement, dye flow visualisation of the gust shear layers from $s/c = 3.0$ and onward is shown in figure 7.15. Corresponding dye flow visualisation of wing shed vorticity is shown in figure 7.16. Considering first the gust shear layers, across figures 7.15a to 7.15b, part of the highly distorted gust shear layer is 'pinched' off. This forms a coherent vortex structure initially directly underneath the wing. From 7.15c to 7.15d, the wing moves past the vortex, such that it now resides behind the trailing edge. Since a vortex has a low pressure core, when it resides directly under the wing, like in figure 7.15b, it will result in a low pressure zone on the underside of the wing and contribute toward downforce. When the vortex is behind the trailing edge, such as in figures 7.15c and 7.15d, the vortex will induce downwash back onto the wing. Furthermore, it can be seen in figures 7.16a and 7.16b that following the wing leaving the gust, there is significant residual leading and trailing edge shed vorticity located above the wing. This will further act to induce downwash

back onto the wing. Both of these mechanisms are therefore likely to cause the negative lift observed in the force history, and are summarised in the schematic given by figure 7.14.

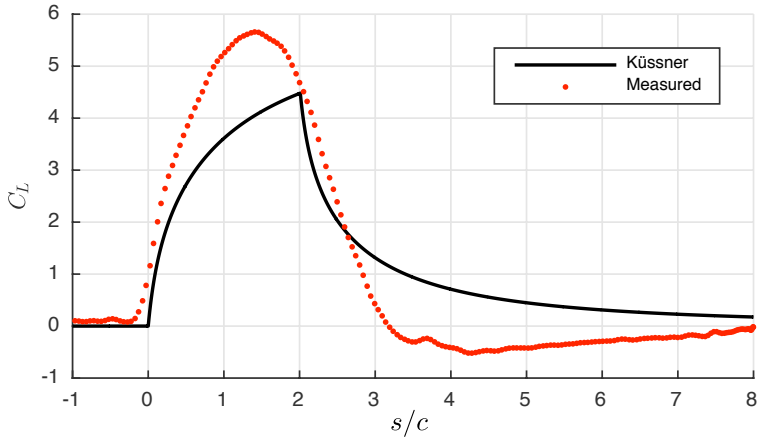

Fig. 7.13 Comparison of the measured and Küssner lift coefficient for $GR = 1.0$.

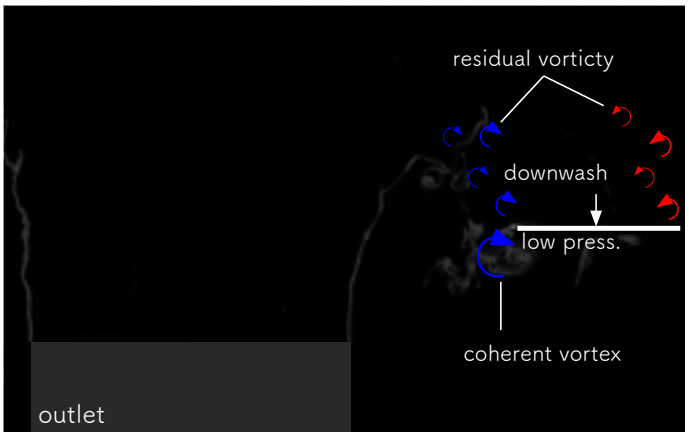

Fig. 7.14 Flow schematic: $GR = 1.0$, $s/c = 4.0$.

(a) $s/c = 3.0$

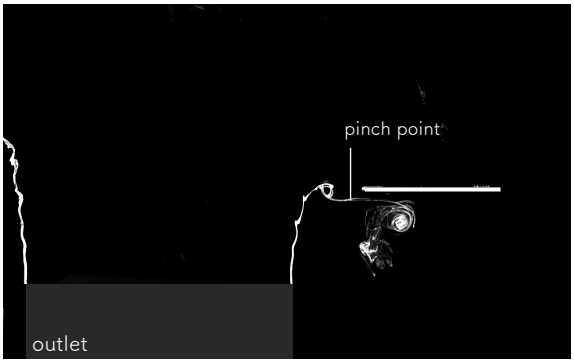

(b) $s/c = 3.5$

(c) $s/c = 4.0$

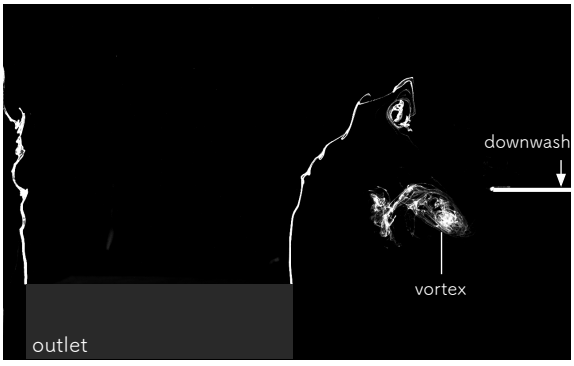

(d) $s/c = 4.5$

Fig. 7.15 Dye visualisation of the gust shear layers. $Re = 5,000$; $GR = 1.0$.

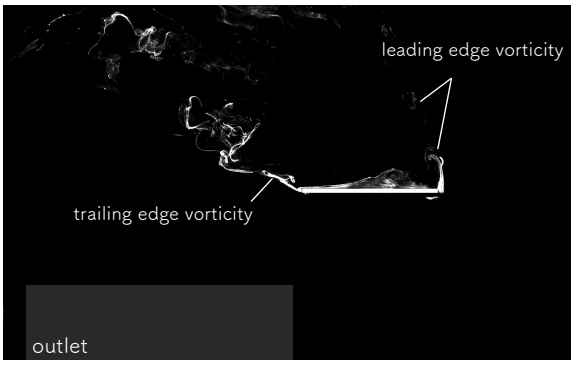

(a) $s/c = 3.0$

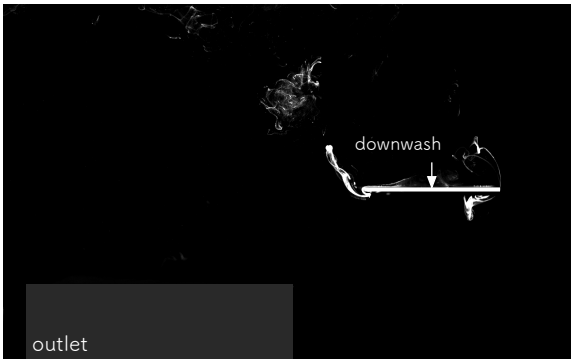

(b) $s/c = 3.5$

(c) $s/c = 4.0$

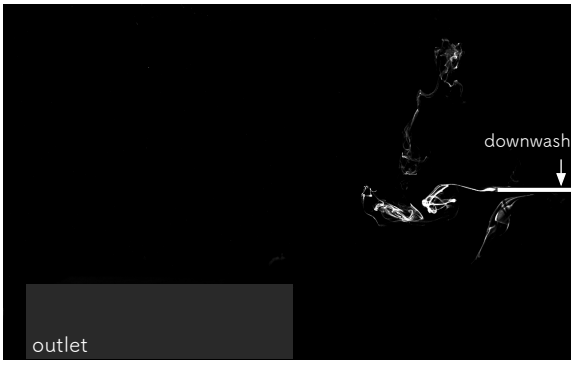

(d) $s/c = 4.5$

Fig. 7.16 Dye visualisation of wing shed vorticity. $Re = 5,000$; $GR = 1.0$.

7.6 Influence of the gust outlet position on the unsteady response

So far the flow topology and force has been considered for just a single wing to gust outlet offset distance of 100 mm, as shown in figure 7.17a. The relative proximity of the outlet and collector units may, however, change the unsteady response. Each unit imposes a no-through flow condition that would otherwise not be present in a completely free flow field. The forces arising from each force production mechanism may therefore be modified. For steady wind tunnel experiments, this phenomenon is known as *blockage* (Cooper et al., 1986; Maskell, 1965; Ramamurthy and Balachandar, 1989). Mercker and Wiedemann (1996) described interference effects relevant to open jet wind tunnels. These include:

- Expansion of the open jet.
- Deflection of the jet due to proximity of a body to the wind tunnel nozzle outlet.
- Far field interference on the flow due to the nozzle outlet and collector geometries.
- Buoyancy forces due to a static pressure gradient between the nozzle outlet and collector.

Given the highly unsteady nature of the present experimental configuration, it is doubtful that standard blockage correction factors can be applied to correct for these effects (buoyancy-like forces are, however, negligible due to the the low model volume). It is further debatable as to what the 'correct' response is. A 'natural' gust may be affected by the presence of a wing, the degree of which will depend on the circumstances (e.g. whether there are any solid surfaces nearby). In this section we therefore seek to simply quantify whether there is a non-negligible difference on the response depending on the relative gust outlet position.

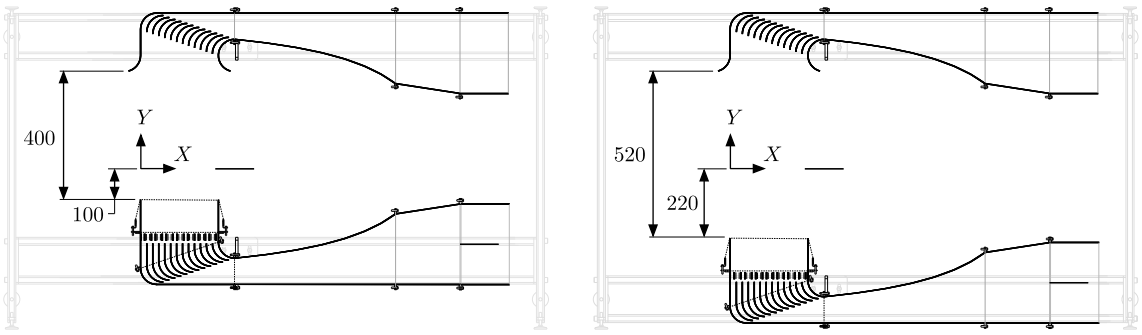

(a) Close configuration **(b)** Far configuration

Fig. 7.17 Comparison of the close and far gust outlet configurations.

The $GR = 1.0$ test case was repeated with the wing to outlet offset distance increased from 100 to 220 mm. A comparison of the flow topologies at $s/c = 2.0$ for each outlet position is shown in figure 7.18.

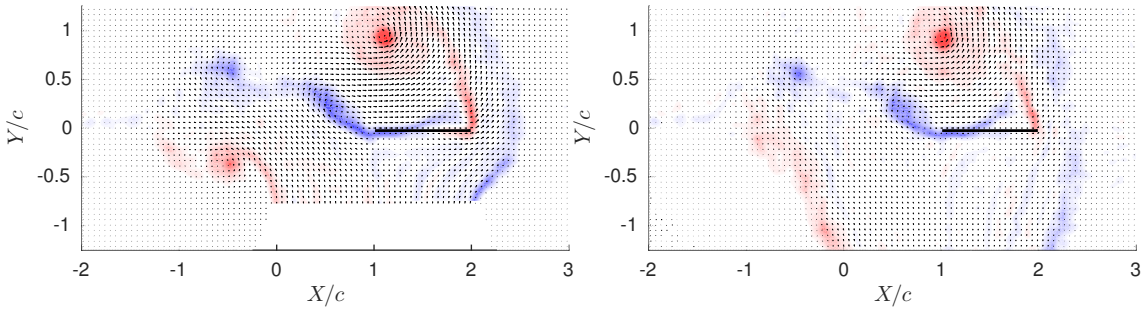

(a) Close outlet (100 mm offset) **(b)** Far outlet (220 mm offset)

Fig. 7.18 Comparison of flow topology between outlet distances of 100 and 220 mm for a gust ratio of 1.0. $s/c = 2$.

It can be seen that the leading edge vortex and trailing edge vorticity are almost identical for both test cases. The main difference is the gust shear layers. The closer outlet case shows significantly increased gust shear layer curvature and subsequent roll up, compared to the far outlet case. The increase curvature indicates a higher pressure on the underside of the plate, and thus a higher lift force. The measured forces for each outlet position are given in figure 7.19. The closer outlet position, does indeed have a higher peak lift force on gust entry, by approximately 25%. The peak lift for the far outlet case is surprisingly similar to that predicted by the Küssner model*. It may therefore be concluded that for high gust ratios the proximity of the outlet can have significant effect on both flow topology and the force response. The 'correct' response is, however, likely dependent on the application of interest. The close outlet case is most representative of a vehicle encountering, say, a gust emanating from a local topological obstruction, while the far outlet case is most representative of a gust in the free atmosphere.

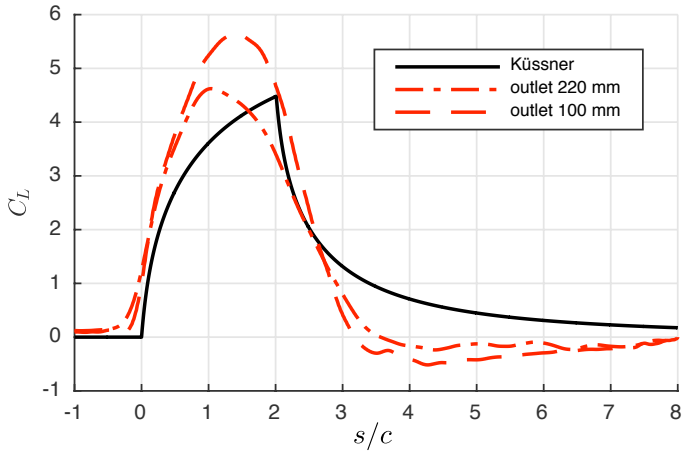

Fig. 7.19 Comparison of the lift coefficient with outlet position for a gust ratio of 1.0.

*See section 4.7.5 for evidence showing that Küssner's ideal gust is influenced only a minor amount by different gust outlet positions. Diffusion of the shear layers is not responsible for the observed force or flow topology variation.

7.7 Reynolds number effects

In the introductory section is was discussed that the performance of conventional aerofoils can be greatly dependent on Reynolds number, because it may influence the onset of flow separation. For flows about a flat plate wing at high incidence, however, the separation points are clearly defined at the leading and trailing edges. Consequently Reynolds number has only minor influence on the resulting force and flow topology (Graham et al., 2017; Ol and Babinsky, 2016; Stevens, 2013). The gust experiments appear to be no different. All the dye flow visualisation was taken at a Reynolds number of 5,000, however, the main features agreed well with the PIV taken at $Re = 20,000$. A further comparison of flow topologies between Reynolds numbers of 20,000 and 40,000 is shown in figure 7.20. In both frames the leading edge vortex appears centred at an equivalent location above the wing and is a similar size. The vorticity shed at the trailing edge is additionally deflected at approximately the same angle. There is little qualitative difference in the flow topologies, suggesting that Reynolds number effects are indeed small. Force histories for both Reynolds numbers are shown in figure 7.21. Aside from minor differences, mostly attributable to different levels of measurement noise, the forces are very similar.

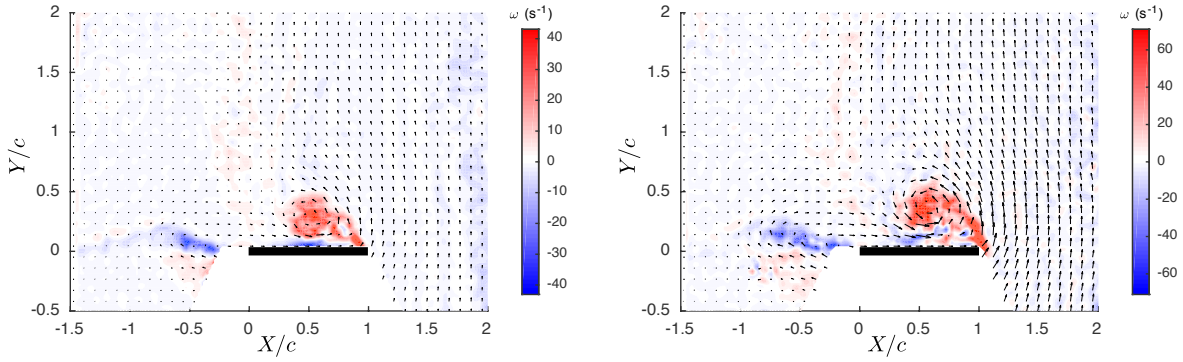

(a) $Re = 20,000$ **(b)** $Re = 40,000$

Fig. 7.20 Comparison of flow topologies between Reynolds numbers of 20,000 and 40,000; $GR = 1.0$, $s/c = 1.0$. Each image is an average of 5 test runs. Data below the wing is masked due to wing shadow.

7.8 Isolating the boundary-layer vorticity components

For each of the gust ratio cases, the force histories were surprisingly similar to Küssner's model, exceptionally so for the $GR = 0.2$ case. This result strongly suggests that the circulatory and non-circulatory force components modelled in Küssner's theory occur in a real gust encounter (see section 2.3.4.3). If not, such similarity between theory and experiment would be unlikely. The problem is that we still do not know why the non-circulatory force, attributed to added mass, does not fit with our conceptual understanding of the effect. This is because neither the wing, or the flow field, accelerates.

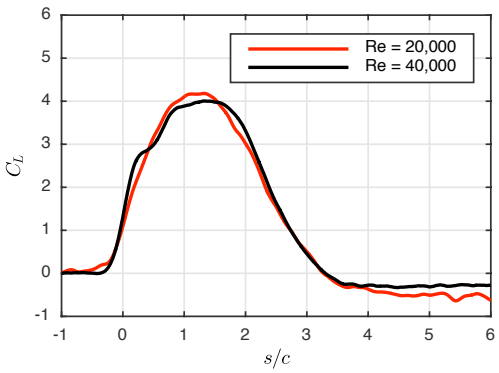

Fig. 7.21 Comparison of the lift coefficient for $GR = 1.0$, at $Re = 40,000$ and $Re = 20,000$. Outlet 220 mm.

7.8.1 Approach

In this section, the first direct steps are taken toward understanding the cause of this discrepancy. We aim first to simply prove whether there is, or is not, an added mass force by isolating the component from the vorticity field. This will be attempted using the 'added mass isolation' methodology described in Chapter 5. The technique was successfully demonstrated for the surge and rotating plate test cases in Chapter 6, and can be applied to the gust cases without modification. It is expected that the 'experimentally acquired' circulatory sheet will differ from Küssner's theory for high gust ratios. In the experiments, the flow separates at the leading edge of the wing, whereas in Küssner's theory the flow remains attached. The component attributed to added mass, however, may be similar, if not identical to Küssner's model. This is because added mass effects are independent of changes to the flow topology, as was demonstrated in Chapter 6.

In Küssner's theory, the non-circulatory vortex sheet component is described by the Fourier series given by equation (3.36), and shown in figure 3.8. This vortex sheet changes in strength during the entry zone $0.0 \leq s/c \leq 1.0$, but, for our experimental setup, theoretically has a constant strength in the zone $1.0 \leq s/c \leq 2.0$, when the plate is fully submerged in the gust. This is because there is uniform gust upwash across the chord. We will make use of this fact, as it enables multiple measurements of the same 'strength' vortex sheet, which facilitates the use of sequential averaging processes to reduce the effects of random measurement noise. This was successfully implemented for the surge and rotating plate cases in section 6.4. The result of this averaging process is a single, accurate, measure of the non-circulatory vortex sheet. While insufficient to calculate the added mass force (as the time history is required), the presence of a non-circulatory vortex sheet will indicate that the momentum of the flow field changed on entry of the plate into the gust. This change in momentum cannot be attributed to the shedding of free vortices, as they are accounted for by the circulatory terms of the analysis, and must therefore be attributed to added mass effects. We can therefore prove, or disprove whether there was an added mass force for a wing-gust encounter, simply by proving the existence of

a non-circulatory vortex sheet in fully submerged zone.

7.8.2 Vortex sheets: $GR = 1.0$

The measurements are taken for the $GR = 1.0$ case, with the outlet position at 100 mm. For this case, the attached vortex sheets have the greatest intensity, and the leading edge vortex additionally advects significantly from the surface of the plate. This enables each area of integration used for the calculation of the attached vortex sheet to primarily incorporate boundary-layer vorticity, while excluding the leading edge vortex, trailing edge vorticity, and the gust shear layers. Each integration region is shown in figure 7.22 (black dashed rectangle). All vorticity outside the rectangle is allocated as 'free vorticity', from which the circulatory component of the attached vortex sheet is computed.

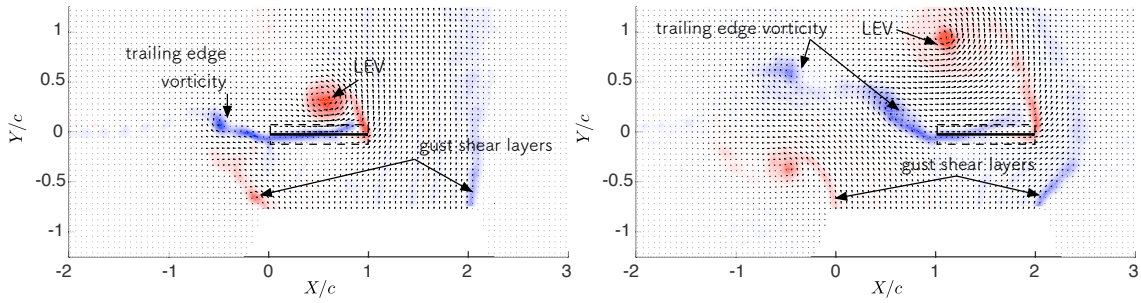

(a) $s/c = 1.0$ **(b)** $s/c = 2.0$

Fig. 7.22 Interrogation window for calculation of the non-circulatory attached vortex sheet.

In figure 7.23, the breakdown of the attached vortex sheet is given for a single frame at $s/c = 2.0$. The reader is reminded that the line, γ^b, is the attached vortex sheet as directly measured within the integration area shown in figure 7.22. The γ^c_{in} term is the circulatory vortex sheet calculated from vorticity outside the integration area, but within the observable measurement window. The γ^c_{out} term is the circulatory vortex sheet that is calculated from vorticity that we know must have drifted outside the measurement window (see section 5.1.1.2). Here, this component of the vortex sheet is significant. Large errors would arise if circulation outside the measurement window were ignored when determining the non-circulatory attached vortex sheet. As described in section 5.1.2, the non-circulatory vortex sheet is $\gamma^{nc} = \gamma^b - \gamma^c_{in} - \gamma^c_{out}$. This is given by the red crosses in figure 7.23.

Next a sequential average of the non-circulatory vortex sheet is taken over the range $1.0 \leq s/c \leq 2.0$. This gives 121 independent measurement frames. On averaging the measures of the non-circulatory vortex sheet across these frames, the standard deviation of random errors is reduced by $1/\sqrt{121} = 0.09$. Since PIV elemental vector measurement error, for an average of 5 runs, is of order 2%, random errors associated with the averaged vortex sheet are negligible. The sheet is compared with the equivalent added mass attributed sheet from Küssner's theory in figure 7.24.

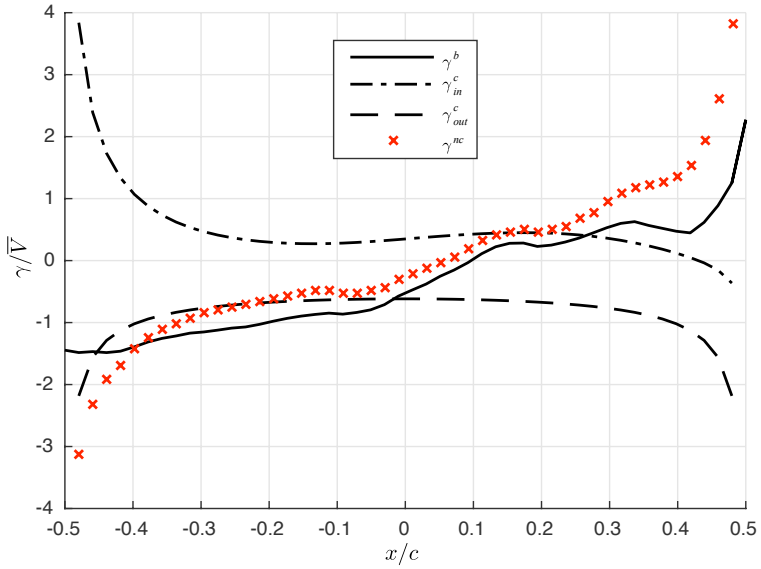

Fig. 7.23 Instantaneous breakdown of attached vorticity at $s/c = 2.0$.

Each instantaneous measurement is additionally plotted, which shows that over the 121 separate measurements the margin of error is small, except at the plate edges. The averaged non-circulatory vortex sheet is similar in 'shape' to that of Küssner's theory, however, the magnitude is incorrect by approximately 50%. This cannot be explained by measurement error. The force component von Karman and Sears (1938) attribute to added mass is described as, *"the force and moment which the airfoil would encounter in a flow without circulation, due to the reaction of the accelerated fluid masses. These contributions in both cases are called the apparent mass contribution"*. This suggests that the force is due to the formation of a non-circulatory attached vortex sheet, one that arises once the contribution of all free vorticity is accounted for. This is equivalent to our definition of added mass. The results, however, suggest otherwise.

It is therefore proposed that the discrepancies may arise because: there is vorticity outside the measurement window that is unaccounted for by the present measurements; or, the non-circulatory vortex sheet arises from an entirely different mechanism to that described by von Karman and Sears (1938). This is investigated in the following Chapter.

7.9 Summary

In this Chapter, PIV, flow visualisation and force measurements of a flat plate wing entering a transverse gust at ratios of $GR = 0.2$, 0.5 and 1.0 were presented. Each test case was conducted at an initial angle of incidence of 0°. The response at Reynolds numbers of 20,000 and 40,000 were compared and the effect of gust outlet location was investigated. The main findings are:

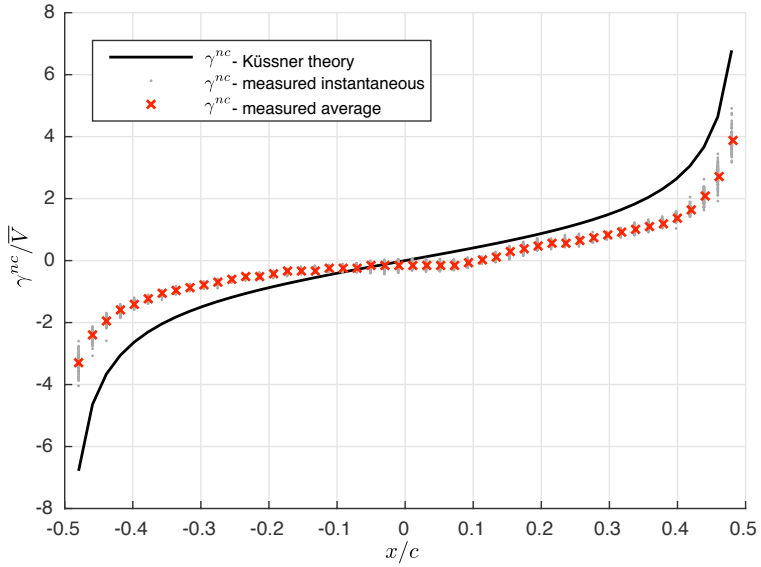

Fig. 7.24 Comparison of the average non-circulatory vortex sheet between measurement and Küssner's theory.

- For a flat plate wing-gust interaction, Reynolds number in the range from $Re = 20,000$ to $Re = 40,000$ appears to have little effect on the flow topology and force. The flow topologies at these Reynolds numbers was also consistent with the dye flow visualisation taken at $Re = 5,000$.
- For each gust ratio, deflection and subsequent roll-up of the gust shear layers was shown. This appears to result in a decrease in lift of the wing on exit from the gust due to induced downwash. The gust shear layer roll-up is influenced by the proximity of the wing to the gust outlet.
- All gust ratios demonstrated some form of leading edge separation. For $GR = 0.5$ and 1.0 the vorticity coalesced into prominent leading edge vortices.
- Vorticity shed into the wake was approximately planar for all gust ratios, albeit the plane shortly after entry was deflected up to 20 degrees for a gust ratio of 1.0.
- For each gust ratio there was relatively good agreement between the measured forces on the wing and the Küssner model. For a gust ratio of 1.0 the peak lift coefficient exceeded Küssner by approximately 27%. Increasing the distance between the gust outlet and the wing results in a change in peak lift coefficient so that it is comparable to Küssner's model, indicating that the test apparatus may introduce blockage effects for high gust ratios.
- For short period, high amplitude gusts the Küssner model therefore could be used to give a surprisingly reasonable estimate of the force response of the wing, despite significant differences between the modelled and physical flows.
- The measured non-circulatory vortex sheet is only approximately 50% that of the Küssner model, a discrepancy that cannot be explained by experimental error. The difference may be

attributed to vorticity outside the measurement window, or the non-circulatory vortex sheet arises from a different mechanism to that described by von Karman and Sears (1938).

Chapter 8

Added Mass and Wing-Gust Encounters

In the previous Chapter, reasonable agreement between forces predicted with Küssner's theory and experiment were demonstrated. However, the magnitude of the non-circulatory vortex sheet extracted from measurement was not comparable with theory. In this Chapter the causes and implications for the discrepancy are discussed.

8.1 General non-circulatory vortex flows

Inherent in the formulation of Küssner's model is the assumption that thin airfoil theory may be used to determine quantities of attached circulation. The gust flow itself is, in fact, not modelled in this theory. Rather, the change in incidence the gust causes is assumed to be comparable to that of a flat plate, that progressively and non-physically changes camber. For the real case, the wing geometry is unchanged, and the gust is enclosed by two shear layers containing vorticity. This vorticity can be measured, and its effect on the wing would therefore be included in the calculation of the circulatory vortex sheet contribution γ^c. We must therefore ask: what is the correct method for dealing with the gust shear-layer vorticity? Should gust shear layer vorticity be treated equivalently to that shed by the wing? Or, should it be excluded from calculations of attached circulation (as implemented in the Küssner model)? Here it is proposed that all vorticity must be treated equivalently*. The hypothesis is that all vorticity residing in the flow field will contribute equally to the circulatory component of the attached vortex sheet, regardless of whether it was originally shed from the wing or is present in the flow for other reasons.

To help answer how this influences our analysis of the gust results, consider an initially quiescent two-dimensional flow field of infinite extent, as illustrated in figure 8.1. To generate a velocity disturbance in the flow field (such as a gust), some force would have to be applied to an arbitrary region of the fluid. It is known from the impulse relations given by Wu (1981), that any force on a flow field may be determined uniquely from the resulting vorticity field. In other words, any force

*This includes the mechanical vorticity of a body, equal to twice the kinematic angular velocity.

applied to a flow generates a vorticity field. This may be in the form of either pairs of point vortices, vortex sheets, or distributed in a diffuse manner. Since circulation must be conserved, each element of positive circulation generated has a negative counterpart elsewhere in the flow field.

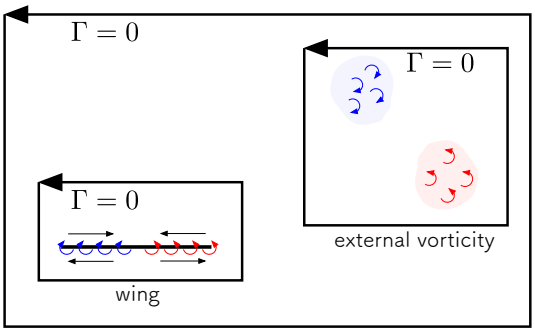

Fig. 8.1 Flow field with an arbitrary vorticity distribution generated by a mechanism external to the wing.

Now consider a flat plate wing residing somewhere in this flow field. The wing has a 'circulatory' vortex sheet constituent, with a circulation equal and opposite to all free vorticity. On creation of the external vorticity, a circulatory vortex sheet γ^c must therefore also form to satisfy the no-penetration condition. This, critically, must have zero net circulation because the total circulation of all the externally created vorticity is zero.

The circulatory component of the attached vortex sheet may therefore be broken into components depending on the origin of the free vorticity:

$$\gamma^c = \gamma^{nc}_{ext.} + \gamma^c_{wing}. \tag{8.1}$$

The $\gamma^{nc}_{ext.}$ term is the sheet arising from mechanisms external to the wing (the gust). This necessarily has zero net circulation. The γ^c_{wing} term is due to vorticity shed by the wing. This vortex sheet may have finite circulation if there is an imbalance of circulation shed by the wing, such as a starting vortex created by an impulsively started, lift generating aerofoil; equivalently it may have zero net circulation if an equal positive and negative circulation is shed by the wing, such as when a flat plate wing translates at $\alpha = 90^\circ$ incidence.

Repeating equation 5.1, the total attached circulation of the wing was equal to:

$$\gamma^b = \gamma^{nc} + \gamma^c.$$

Substituting equation (8.1) into (5.1) and re-arranging for the non-circulatory terms gives:

$$\gamma^{nc} + \gamma^{nc}_{ext.} = \gamma^b - \gamma^c_{wing}. \tag{8.2}$$

Both the terms on the left hand side are 'non-circulatory', in the sense that they form to satisfy the no-through flow condition and have zero net circulation. The difference is that γ^{nc}, the vortex sheet classically associated with the added mass effect, forms because of kinematic motion of the body in an otherwise irrotational fluid. The $\gamma^{nc}_{ext.}$ vortex sheet component forms because the net circulation of gust shear layer vorticity must necessarily be zero, but this is unrelated to the added mass effect. It is instead the result of vortices generated in the flow field by some mechanism external to the wing.

8.1.1 Force

If we know the strength and relative motion of the free vorticity, we can readily determine the force acting on a body within the flow field. The attached vortex sheet due to n external elements of vorticity (including external bodies), with circulation Γ_i, may be written as

$$\gamma^{nc}_{ext.} = \sum_{i=1}^{n} f_{1,i}(z_b, z_i)\Gamma_i, \tag{8.3}$$

where $f_{1,i}(z_b, z_i)$ is an arbitrary function that depends on the position on the surface of the body ($z_b = x_b + iy_b$) and the location of each free vortex ($z_i = x_i + iy_i$). This may be determined analytically using the complex potential method, a panel code, or some other technique. Repeating equation (3.24), the y-direction impulse due to an attached vortex sheet is

$$I_y = -\oint x\gamma dl.$$

Substituting equation (8.3) into (3.24), gives the impulse due to the free vortices

$$I_y = -\sum_{i=1}^{n} f_{2,i}\Gamma_i, \tag{8.4}$$

where

$$f_{2,i} = \oint x f_{1,i}(z_b, z_i) dl. \tag{8.5}$$

The force on the plate is

$$\begin{aligned} F_y &= -\rho \frac{dI_y}{dt}, \\ &= \sum_{i=1}^{n} \Big(\underbrace{\frac{df_{2,i}}{dt}\Gamma_i}_{\text{advection}} + \underbrace{f_{2,i}\frac{d\Gamma_i}{dt}}_{\text{growth}} \Big). \end{aligned} \tag{8.6}$$

From equation (8.6), it can be seen that there is a non-circulatory vortex force on the body when the free vortices either advect relative to the body ($\frac{df_{2,i}}{dt} \neq 0$), or when the free vorticity is stationary

relative to the body, but changes in strength ($\frac{d\Gamma_i}{dt} \neq 0$). In the following section, we investigate how this might apply to Küssner's model and the wing-gust encounter experiments.

8.2 On the role of gust shear layer vorticity for a wing-gust encounter

8.2.1 Küssner's model

If we try to apply the concept of a non-circulatory vortex force to interpret Küssner's model, we immediately encounter a problem. As illustrated in figure 8.2a, in Küssner's idealised gust there is only a single sharp rising gust edge, or shear layer, of some very large (infinite) length, i.e. the gust shear layer extends from $Y = -\infty$ to $Y = \infty$. This shear layer therefore approaches infinite circulation, which means the wing would have infinite negative circulation, if the overall flow field circulation were to add up to zero. Clearly this is not the case. If a large contour is taken about the wing and gust shear layer, we know that prior to the wing entering the gust region, circulation of the wing is zero, therefore, circulation in the full flow field would not be conserved. It is therefore reasoned that the flow field described by Küssner's model is only a partial representation of a much larger field. In Küssner's model there must actually be two shear layers, as illustrated in figure 8.2b. The first is the rising velocity edge that the travelling wing enters, and the second is a falling gust edge located some arbitrarily large distance from the first. After including the falling gust edge, the total contribution to the circulation of γ^b from the gust shear layers is now zero. As preluded in section 8.1, the two gust shear layers arise because at some stage a force has been applied to an otherwise stationary flow field to 'create' the gust in the first place.

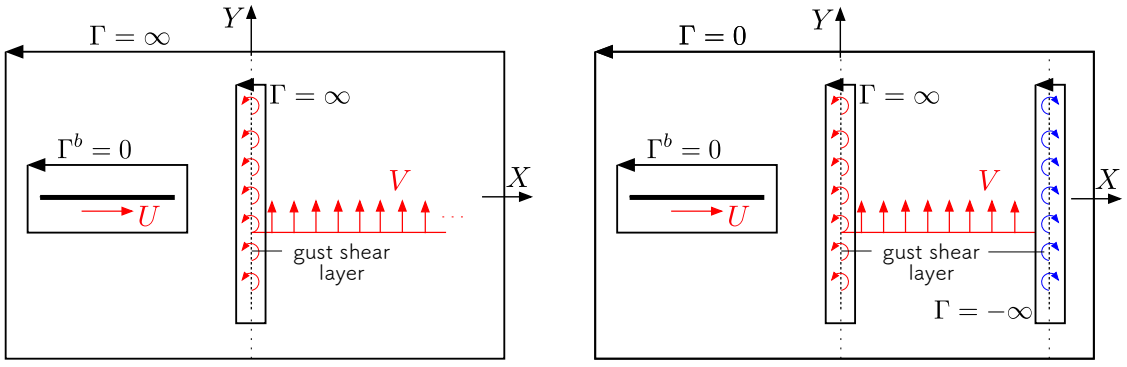

(a) Original Küssner model

(b) Modified Küssner model

Fig. 8.2 Schematics comparing the original Küssner model, which has a single rising gust edge, with the proposed modification that has both a rising and falling gust edges. The falling gust edge is required to conserve circulation in the flow field.

8.2.1.1 Isolation of $\gamma^{nc}_{ext.}$

Given that there should be a gust shear layer vortex sheet component $\gamma^{nc}_{ext.}$, it is suspected that this may be responsible for the force von Karman and Sears (1938) have attributed to the added mass effect. We therefore test whether $\gamma^{nc}_{ext.}$ is equivalent to the non-circulatory vortex sheet described in the Küssner model. As shown in figure 8.3, an artificial flow field replicating Küssner's model was generated by defining two shear layers of length h, and separated by the distance w. Each shear layer is specified a strength $\gamma_{gust} = V$. Both the gust shear layers and plate were discretised with a spatial resolution of 200 vortex elements per chord. The simulated gust shear layers were used to calculate the attached vortex sheet γ^c for the wing, using the methodology given in section 5.2. This is compared with Küssner's non-circulatory vortex sheet in figure 8.4b for gust lengths of $h/c = 1$, 10, and 1000. The latter is representative of gust shear layers that are of infinite length. The corresponding flow field for the $h/c = 1000$ case is shown in figure 8.4a. It can be seen that with increasing gust shear layer length, the non-circulatory, gust shear layer attributed vortex sheet $\gamma^{nc}_{ext.}$ converges to Küssner's theoretical distribution.

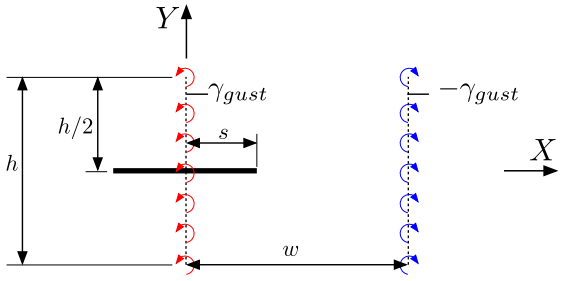

Fig. 8.3 Schematic showing the dimensions of the artificial shear layers. The variable s is the distance from the leading edge of the wing to the left gust shear layer (at $X = 0$).

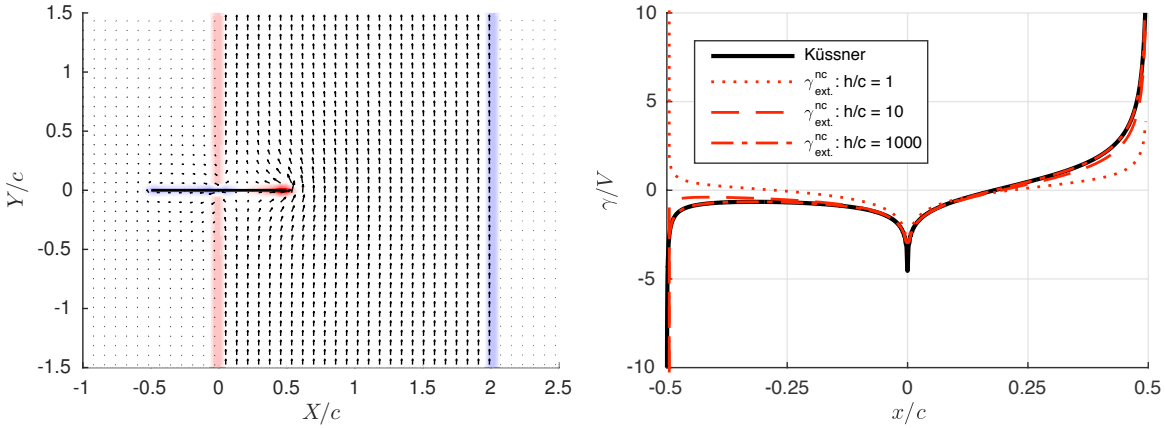

(a) Modelled flow field with $h/c = 1000$

(b) Attached vortex sheets

Fig. 8.4 Change to the flow field for a flat plate wing entering a gust with rigid shear layers and no flow separation. $s/c = 0.5$, and $w/c = 2$.

In Küssner's model, von Karman and Sears (1938) excluded all gust shear layer vorticity from the calculation of the circulatory component of the wing's attached vortex sheet (γ^c). This, in effect, forces the $\gamma^{nc}_{ext.}$ term in equation 8.2 to be zero. Consequently the authors attributed the non-circulatory vortex sheet to γ^{nc}, that responsible for the added mass effect of an accelerating body. The above analysis shows this to be incorrect. The vortex sheet, and associated forces, may be directly attributed to the relative advection of the gust shear layer vortices.

Next, the effect of the proximity of the downstream gust shear layer is considered. In figure 8.6, the velocity induced onto the plate by the gust shear layers is plotted for gust widths varying from $w/c = 2$, 5 and 10, and gust shear layer lengths of $h/c = 10$ and $h/c = 1000$ respectively. For $h/c = 10$, the net velocity induced by the gust shear layers onto the wing varys considerably with the position of the back gust shear layer, while for $h/c = 1000$ the variation is comparatively negligible.

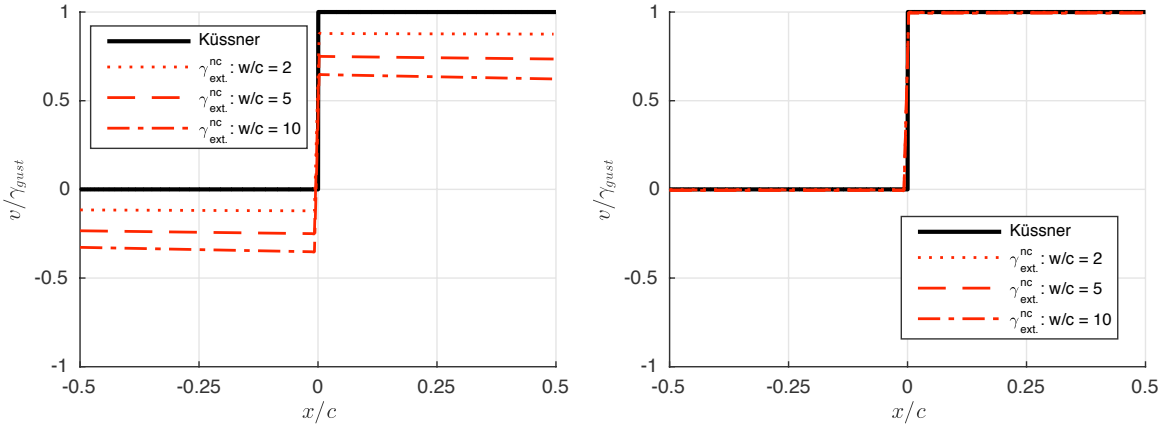

(a) $h/c = 10$ **(b)** $h/c = 1000$

Fig. 8.5 Velocity induced onto the plate, located at $s/c = 0.5$, by gust shear layer vorticity of lengths $h/c = 10$ and $h/c = 1000$, with varying shear layer spacing of $w/c = 2, 5$ and 10.

The effect that the varying induced velocities has on the resulting vortex sheet distributions is shown in figure 8.6a. It can be seen that for $h/c = 10$, with increasing distance between the gust shear layers, the non-circulatory vortex sheet deviates from the Küssner distribution. For $h/c = 1000$, however, no such variation from Küssner's theory can be observed. This is because the variation in velocity induced by the shear layers onto the plate is largely independent of the shear layer spacing. Provided the downstream gust shear layer does not intersect the wing, for a gust of infinite height, uniform velocity is induced onto the plate regardless of the position of the downstream shear layer. The vortex sheet will therefore be unchanged.

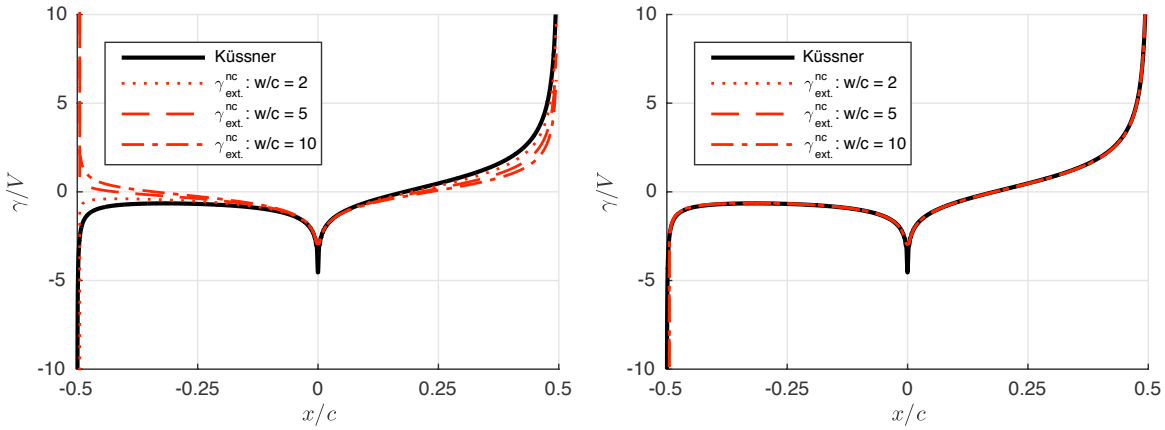

(a) $h/c = 10$ **(b)** $h/c = 1000$

Fig. 8.6 Vortex sheets at varying gust shear layer spacing (w/c). $s/c = 0.5$.

While it seems counterintuitive that the actual position of the downstream gust shear layer has no effect, this is true as long as the gust stretches to infinity in the vertical (Y) direction. If the wing is on either side, or fully within the gust shear layers, the relative position of both shear layers do not matter. The vortex sheet $\gamma_{ext.}^{nc}$ will only change when the plate crosses through a gust shear layer.

8.2.2 Experimental wing-gust encounter

With the improved understanding of the origin of the non-circulatory vortex sheet, the experimental measurements of the wing-gust interaction may be reprocessed. The aims are to further demonstrate experimentally that the non-circulatory vortex sheet originates from the gust shear layer vorticity, and to isolate the force associated with this component. For the real gust case, the rigid gust shear layer assumption inherent in Küssner's model is not correct, because the experiments have shown that the gust edges are considerably affected by the presence of the wing. As a consequence, the experimental formation of $\gamma_{ext.}^{nc}$, and therefore the force on the wing may differ from theory.

With the PIV measurements of a wing-gust interaction presented in Chapter 7, it is not possible to directly extract the gust shear layer component of the circulatory attached vortex ($\gamma_{ext.}^{nc}$) in the same manner as demonstrated using the artificial flow field. To calculate $\gamma_{ext.}^{nc}$ using the mirror image method described in section 5.1.1.1, the position and strength of each element of gust shear layer vorticity within the flow field must be known. The PIV measurements, however, encompass only the flow field within a few chord lengths either side of the wing. The method for correcting for circulation outside the field of view described in section 5.1.1.2, will not correct for the gust shear layer vorticity outside the measurement window, because it will typically have zero net circulation. The following section describes a workaround for the problem.

8.2.2.1 Extracting $\gamma^{nc}_{ext.}$ using a finite measurement window

A schematic of the 'missing' quantity of externally generated vorticity is shown in figure 8.7. To find the contribution of this vorticity, we utilise equation (8.2). The sum of the non-circulatory added mass vortex sheet (γ^{nc}), and the quantity we are interested in ($\gamma^{nc}_{ext.}$), is equal to the difference between the directly measured attached vortex sheet γ^b, less the component attributed to vorticity the wing shed into the flow field.

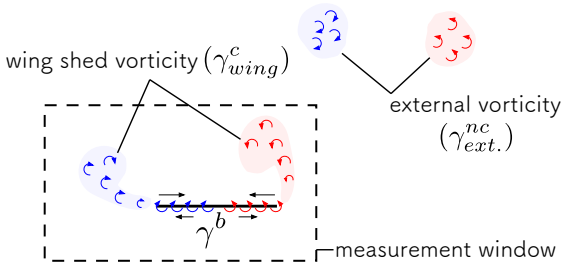

Fig. 8.7 Schematic of missing gust vorticity.

For the wing-gust interaction cases, the plate has no velocity component normal to the chord, therefore $\gamma^{nc} = 0$ (see equation 3.23). The non-circulatory vortex sheet for the gust case, given by equation (8.2) is therefore

$$\gamma^{nc}_{ext.} = \gamma^b - \gamma^c_{wing}. \tag{8.7}$$

Since γ^b and γ^c_{wing} are both quantities which can quantified from data within the measurement window, we can calculate $\gamma^{nc}_{ext.}$, itself attributed to externally generated vorticity both inside, and outside the measurement window. The limitation is that from the measured vorticity field, we must isolate wing shed vorticity from externally generated vorticity.

To isolate the wing shed and gust shear layer vorticity, the $GR = 1.0$ PIV measurements, described initially in section 7.5 were reprocessed using a manual vector mask. Regions of the flow field containing only gust shear layer vorticity were removed, and as shown in figure 8.8, the remaining flow field contains (mostly) only vorticity shed by the wing. We may therefore calculate γ^c_{wing}, and γ^b from the masked flow field, and therefore $\gamma^{nc}_{ext.}$ can be calculated from equation (8.7).

Since the gust shear layers have zero total circulation, the circulation in the masked flow field should add up to zero. Separate sums of post-masking elemental circulation are given in figure 8.9. There is a slight imbalance of circulation between $0 \leq s/c \leq 1$. This is likely due to some of the left, positive gust shear layer entering the unmasked zone of the flow field. Recall the dye flow visualisation of the encounter, given by figure 7.11. Gust shear layer vorticity was shown to be entrained into the leading edge vortex, therefore an imbalance of the total circulation within the unmasked region of the flow field is unavoidable. The 'lost circulation' method described in section 5.1.1.2 is used to correct

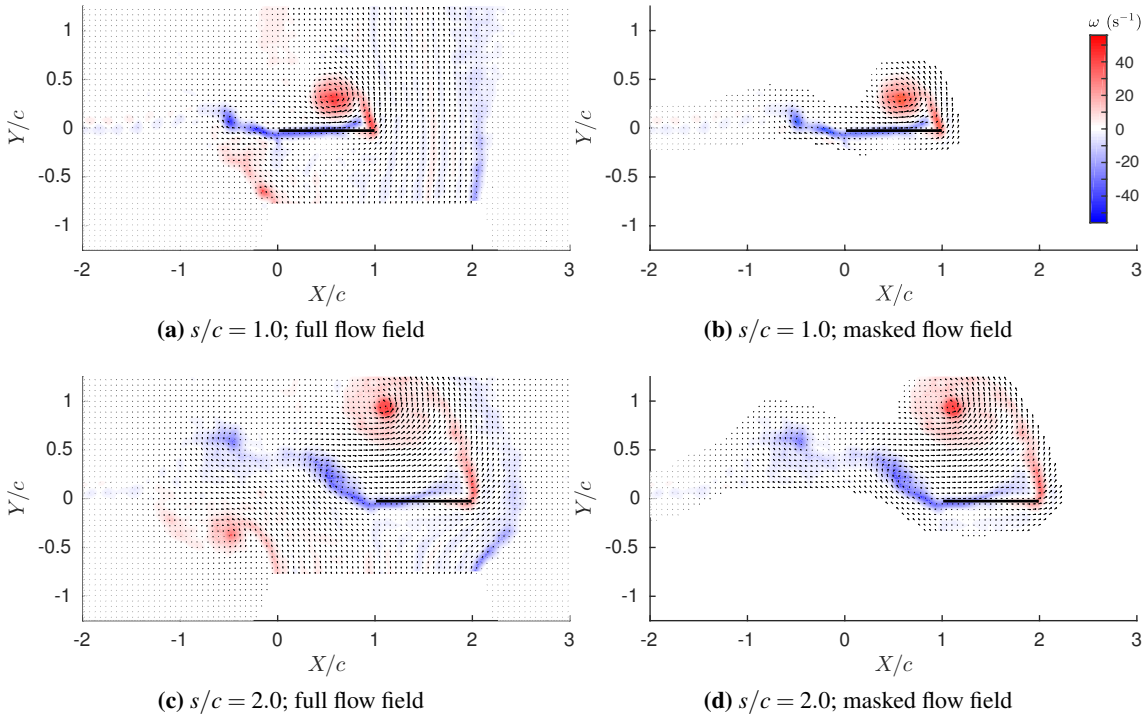

(a) $s/c = 1.0$; full flow field

(b) $s/c = 1.0$; masked flow field

(c) $s/c = 2.0$; full flow field

(d) $s/c = 2.0$; masked flow field

Fig. 8.8 Masking of the gust shear layers used to isolate vorticity shed by the plate. $GR = 1.0$.

for this. For $s/c > 2$, there is a significant circulation imbalance. This, as described in section 7.5, is caused by the LEV leaving the PIV camera field of view (see figure 8.8d). PIV derived quantities of force will therefore be truncated after $s/c = 2$.

8.2.2.2 Measurements of $\gamma^{nc}_{ext.}$: $GR = 1.0$

With a means of accounting for vorticity that is outside the measurement field of view, the vortex sheet attributed to the gust shear layers was extracted for the gust ratio of 1.0 case. The non-circulatory attached vortex sheet as given by Küssner's theory (equation 3.36) is shown in figure 8.10. Once again, this is for the region where the wing is fully submerged in the gust ($1.0 \leq s/c \leq 2.0$) and the vortex sheet distribution is independent of wing position relative to the gust. To calculate γ^{b}, the height of the integration contours (black rectangle on figure 8.11) that defines the regions of the flow that are considered 'attached' and 'free' is set to 0.15c. The required height of this contour is relatively ambiguous, but it is set such that it approximately extends just beyond the boundary-layer. This is to try and avoid the misallocation of LEV vorticity. In figure 8.10, Küssner's non-circulatory vorticity distribution is compared with $\gamma^{nc}_{ext.}$, calculated from the masked flow field and equation (8.7). The scatter across the 121 instantaneous measurements between the range of ($1.0 \leq s/c \leq 2.0$) is extremely small. The average of $\gamma^{nc}_{ext.}$ is close to Küssner's added mass attributed vortex sheet γ^{nc}.

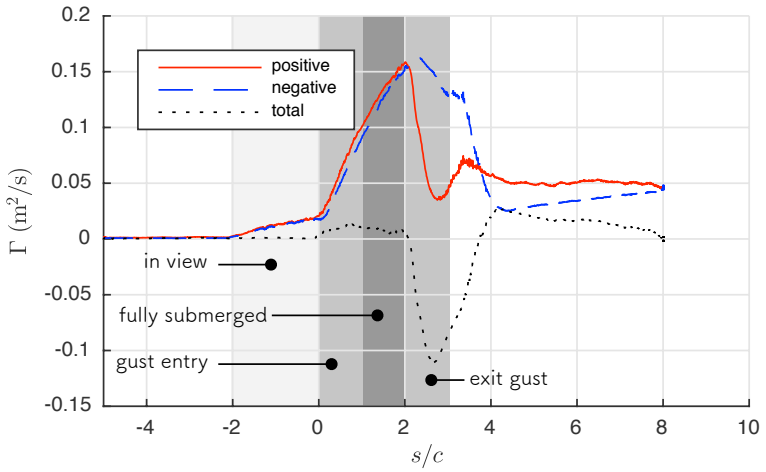

Fig. 8.9 Sum of all positive and all negative circulation 'elements' in the masked flow field. $GR = 1.0$. Shaded regions indicate the position of the wing within the measurement window.

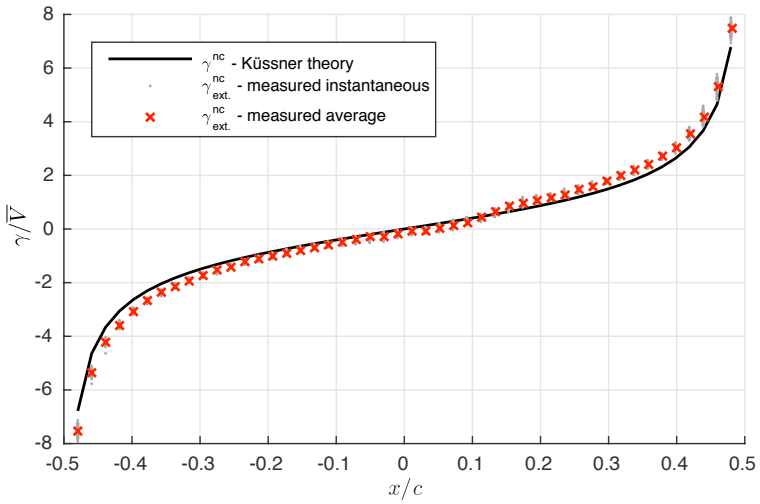

Fig. 8.10 Comparison of the theoretical and measured non-circulatory vortex sheet for $1.0 \leq s/c \leq 2.0$.

This tells us:

- It is certain that the added mass attributed force in the Küssner model is instead a non-circulatory vortex force resulting from the presence of the shear layers bordering the gust velocity field.
- Despite the different physical force production mechanism, the change in momentum attributed to the non-circulatory vortex force, and therefore the lift impulse over the entry region for the $GR = 1.0$ case is very close to the added mass attributed component predicted by Küssner's model. Since the $GR = 1.0$ case is an extreme deviation from the small angle assumption inherent in Küssner's model, this finding is likely valid in the entire range from $0.0 \leq GR \leq 1.0$, and perhaps higher gust ratios still.

- The distortion of the gust shear layers appears to have only minor effect on the formation of the non-circulatory vortex sheet.

8.2.2.3 Force breakdown: $GR = 1.0$

As a further check of the hypothesis that Küssner's added mass force is in fact the result of the gust shear layers, we now attempt isolate the force associated with the formation of $\gamma^{nc}_{ext.}$ and compare this with Küssner's model. To extract the force a measure of the time history of $\gamma^{nc}_{ext.}$ is required, such that the impulse methods described in section 2.3.1.7 may be applied. As shown in figure 8.11, early in the gust encounter (from $0 \leq s/c \leq 0.75$), some LEV vorticity is included in the 'attached' region of the flow field, and will therefore be misallocated as the vortex sheet γ^{b}, instead of γ^{c}_{wing}. Keeping this in mind, we will still proceed and calculate the force history from the PIV measurements.

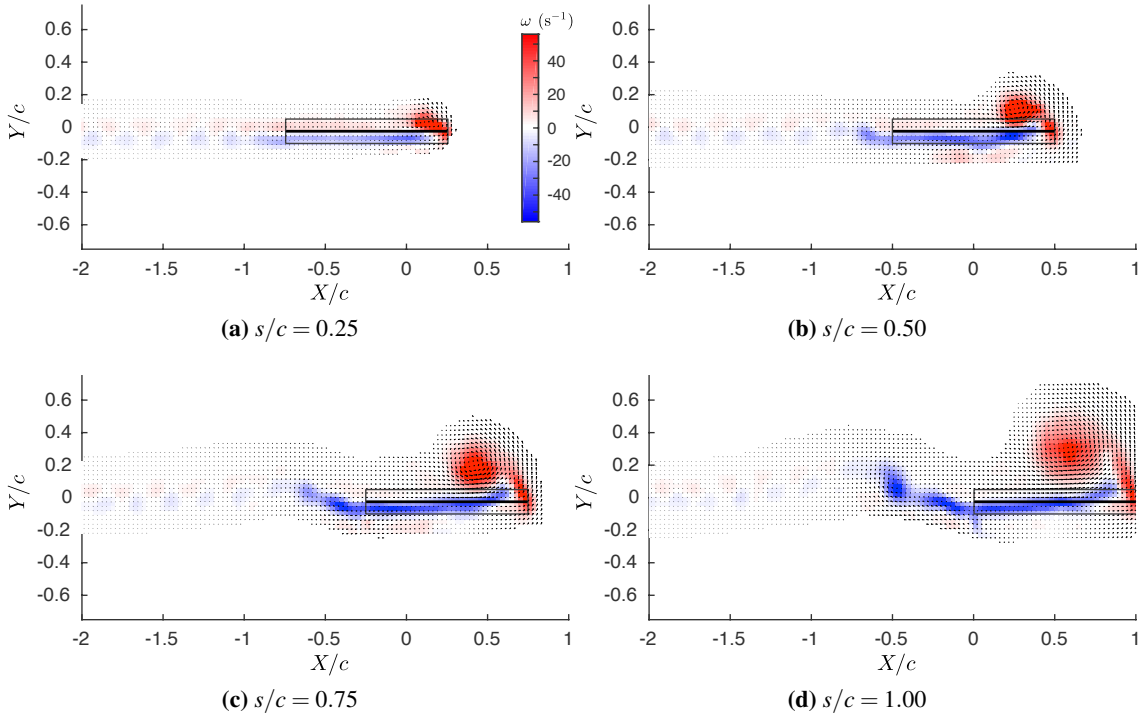

(a) $s/c = 0.25$ **(b)** $s/c = 0.50$

(c) $s/c = 0.75$ **(d)** $s/c = 1.00$

Fig. 8.11 Detailed view of the masking used for the gust entry zone, GR = 1.0. The black rectangle indicates the boundary between flow regions considered attached and free.

In figure 8.12 the forces as predicted by Küssner's model, measured by the force balance, and calculated from PIV vorticity are compared. The force calculated from PIV vorticity across the 'full' flow only includes vorticity that is within the unmasked zone (the gust shear layers are excluded). This component shows relatively good agreement with the direct force balance lift measurement. The magnitude of the PIV derived force does, however, slightly exceed the force balance values. This may be attributed to the miscounting of the gust shear layer vorticity (that was entrained into the LEV), or perhaps finite wing aspect ratio effects. It can be seen that during the gust entry region, there

is clearly a component of the PIV derived force attributed to the formation of the non-circulatory vortex sheet (labelled PIV - $\gamma^{nc}_{ext.}$)[†]. This roughly has a magnitude and distribution similar to Küssner's non-circulatory component. The initial force transients are clearly attributed to $\gamma^{nc}_{ext.}$, while the non-circulatory force drops toward zero as the wing approaches $s/c = 1.0$.

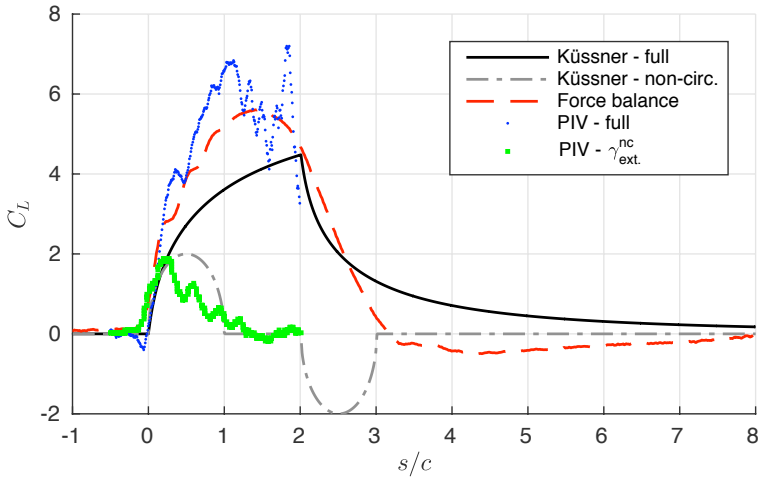

Fig. 8.12 Comparison of the measured and Küssner lift coefficient for $GR = 1.0$. PIV derived forces have are filtered with a bi-directional moving average with a window size of 0.06 seconds, or 12 data points.

The resemblance of the non-circulatory force between PIV and Küssner is surprisingly good considering the ambiguity between vorticity that is considered as 'attached' or 'free', the non-rigidity of the gust shear layers, approximate masking of the gust, and noise attributed to differentiation of the flow field impulse. The gust shear layer attributed vortex sheet $\gamma^{nc}_{ext.}$, and Küssner's non-circulatory vortex sheet (equation 3.36), were additionally shown in section 8.2.2.2 to be equivalent in magnitude for the $GR = 1.0$ case. This indicates that the force impulse over the gust entry is equivalent. The evidence therefore suggests that the non-circulatory force predicted by Küssner's theory, despite being incorrectly attributed to added mass, is relatively accurate for even large amplitude wing-gust encounters.

[†]The force derived from $\gamma^{nc}_{ext.}$ has been corrected by a factor of 1/0.875 to account for the discretisation error, as described in Appendix B.

8.2.3 The non-circulatory vortex growth force

In section 8.1 it was shown that there are two inviscid force contributions on a body that may be attributed to vorticity generated by 'external' methods in the flow field. Both of these force contributions are 'circulatory', in the sense that they are caused by free vorticity, but where the sum of the strengths of the external vortex elements is zero. The wing-gust encounters were shown to arise from the 'advection' term in equation (8.6). Here we investigate the 'growth' term. In particular, we seek to show that this particular force exists, and furthermore, is attributable to the added mass and buoyancy like force components present when a flow field is accelerated uniformly past a stationary body.

In the review of the literature it was explained that for accelerating flows the added mass term is said to be equivalent to that of an accelerating body in quiescent flow. The buoyancy force arises because to accelerate an inviscid flow field there must be a pressure gradient, giving rise to a net force on the body. Here it is argued that this explanation of the mechanism responsible for the presence of these force components is not strictly correct.

We argue that it is not possible to uniformly accelerate a flow field of infinite extent, as to do so would require both infinite force and power. We are instead constrained and may only apply a finite force over a finite area of fluid. As described in section 8.1 the application of any force on an initially quiescent flow will result in the production of vorticity, but with zero net circulation. This vorticity would be located some arbitrarily large distance from a body within this flow field. The added mass and buoyancy like force components experienced when a flow field is accelerated relative to a body, may therefore be directly attributed to this free and distant vorticity.

For the proof, we will once again return to the flow about a circular cylinder, given that we derived the accelerating flow field forces in section 3.1.2. To generate a uniform velocity on the cylinder, two infinite vortex sheets, such as that shown in section 8.2.1.1 may be used. For simplicity, however, we assume here that each vortex sheet may be represented by a single 'free stream' point vortex. As shown in figure 8.13 these are labelled Γ_1 and Γ_2, are located at $z_1 = 0 + iy_p$ and $z_2 = 0 - iy_p$, and have a circulation of magnitude Γ.

By application of the Biot-Savart law, the u-component of velocity induced by the two external vortices, along the y-axis is

$$U(y) = \frac{\Gamma}{\pi}\left(\frac{y_p}{y_p^2 - y^2}\right). \tag{8.8}$$

Two mirror vortices are placed at the positions $z_{m1} = a^2 z_1/|z_1|^2$ and $z_{m2} = a^2 z_2/|z_2|^2$. These mirror vortices have a circulation equal and opposite to the external vortices, and make the surface of the cylinder (with radius a) a streamline. The complex potentials for the external and mirror vortices

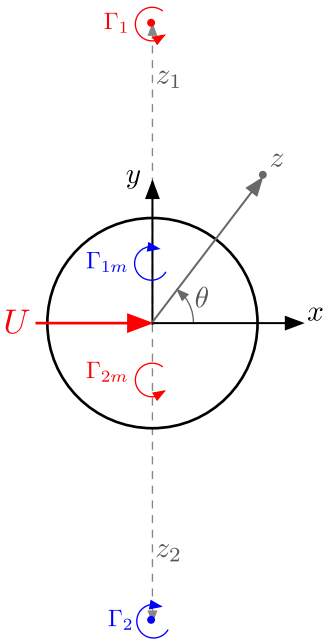

Fig. 8.13 Schematic of the four point vortex model.

are:

$$F_1(z) = -i\frac{\Gamma}{2\pi}\ln(z - iy_p) \tag{8.9}$$

$$F_{m1}(z) = i\frac{\Gamma}{2\pi}\ln(z - i\frac{a^2}{y_p}) \tag{8.10}$$

$$F_2(z) = i\frac{\Gamma}{2\pi}\ln(z + iy_p) \tag{8.11}$$

$$F_{m2}(z) = -i\frac{\Gamma}{2\pi}\ln(z + i\frac{a^2}{y_p}). \tag{8.12}$$

The total complex potential for the flow is the sum of each point vortex,

$$\begin{aligned} F_t(z) &= F_1 + F_{m1} + F_2 + F_{2m} \\ &= -i\frac{\Gamma}{2\pi}\ln\left(\frac{(z - iy_p)(zy_p + ia^2)}{(z + iy_p)(zy_p - ia^2)}\right). \end{aligned} \tag{8.13}$$

The potential (Φ_t) and stream functions (Ψ_t) for the flow field are given by the real and imaginary terms of equation (8.13), ($F_t = \Phi_t + i\Psi_t$).

To model a 'uniform' incident flow onto the cylinder, we will 'move' the two vortices to an infinite distance from the origin. From equation (8.8), the circulation required to induce a velocity of U at $y = 0$ is

$$\Gamma = \pi y_p U. \tag{8.14}$$

Substituting equation (8.14) into (8.13) gives the complex potential

$$F_t(z) = -iU\frac{y_p}{2}\ln\left(\frac{(z-iy_p)(zy_p+ia^2)}{(z+iy_p)(zy_p-ia^2)}\right). \tag{8.15}$$

Taking the limit of equation (8.13) as $y_p \to \infty$, returns an infinite result because the magnitude of the circulation of each of the free stream point vortices tends toward infinity. While the magnitude of the complex potential is infinite, there is a finite change to the complex potential around the surface of the cylinder. We are interested only in local gradients of the complex potential, as this determines the fluid velocity. A reference, or complex potential 'zero' point at $z = a$ is therefore defined. Here the complex potential is

$$F_{ref} = -iU\frac{y_p}{2}\ln\left(\frac{(a-iy_p)(ay_p+ia^2)}{(a+iy_p)(ay_p-ia^2)}\right). \tag{8.16}$$

Taking the difference between equations (8.13) and (8.16) gives the new complex potential, which is zero at $z = a$

$$\begin{aligned} F(z) &= F_t - F_{ref} \\ &= -iU\frac{y_p}{2}\ln\left(\frac{(z-iy_p)(zy_p+ia^2)}{(z+iy_p)(zy_p-ia^2)}\right) + iU\frac{y_p}{2}\ln\left(\frac{(a-iy_p)(ay_p+ia^2)}{(a+iy_p)(ay_p-ia^2)}\right) \\ &= -iU\frac{y_p}{2}\ln\left(\frac{(z-iy_p)(zy_p+ia^2)(a+iy_p)(ay_p-ia^2)}{(z+iy_p)(zy_p-ia^2)(a-iy_p)(ay_p+ia^2)}\right). \end{aligned} \tag{8.17}$$

Taking the limit as $y_p \to \infty$, equation (8.17) eventually reduces to

$$\lim_{y_p\to\infty} F(z) = U\frac{a^2}{z} + Uz - 2a. \tag{8.18}$$

Dropping the constant $(-2a)$, gives the result

$$F(z) = U\frac{a^2}{z} + Uz. \tag{8.19}$$

The first term on the right hand side is the complex potential resulting from the mirror vortex doublet, while the second term is the flow induced by the external vortex pair. The stream and potential functions are plotted in figure 8.14.

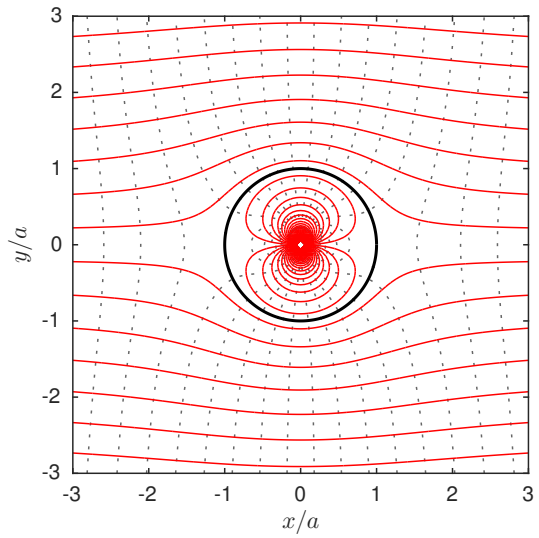

Fig. 8.14 Contour lines of the stream (−) and potential (..) functions for a pair of equal and opposite vortices at $y = \pm\infty$, and the corresponding mirror images at $y = 0^+$ and $y = 0^-$.

From equation (8.19) and figure 8.14 it is clear that the flow about a cylinder due to vorticity a very large distance away is equivalent to that of a cylinder in a uniform free stream. The equivalent flow field, given in section 2.3.4.1, was derived using a source-sink doublet in a free stream. The forces are also identical. From equation (8.19), the potential function and time rate of change on the surface of the cylinder are

$$\Phi = 2Ua\cos\theta, \tag{8.20}$$

$$\frac{\partial\Phi}{\partial t} = 2\frac{\partial U}{\partial t}a\cos\theta. \tag{8.21}$$

In section 2.3.4.1, the net force in the x-direction was shown to be

$$F_x = \rho a\int_0^{2\pi}\frac{\partial\Phi_t}{\partial t}\cos\theta d\theta. \tag{8.22}$$

Substituting equation (8.21) into (8.22), and evaluating the integral gives

$$F_x = 2\rho\pi a^2\frac{\partial U}{\partial t}. \tag{8.23}$$

We have just shown that the flow about a cylinder, subjected to an accelerating flow induced by a pair of vortices at a sufficiently far distance from the body, is identical to that of a uniform accelerating free stream. The pressure force is equivalent in magnitude also. The cause of these forces, however, is not the same. An added mass force arises due to surface pressures on an accelerating body. It is independent of vorticity in the bulk flow field. A hydrostatic buoyancy force arises due to a pressure gradient, created to react a body force on the fluid. It too is independent of vorticity in the bulk flow field. Here it is shown that, for a body immersed in an accelerating flow, both of

these force components can be attributed to the production of vorticity elsewhere in the flow field. They are therefore both non-circulatory vortex forces and not added mass or buoyancy effects. The non-circulatory vortex forces can be quantified by measurement of the free vortices which were necessary to create the accelerating flow, while added mass and hydrostatic buoyancy forces cannot.

8.2.4 Application to unsteady wind and water tunnels

In the previous section it was shown that in cases where a flow field is accelerated relative to a body, the forces on the body are directly attributable to free vortices. This finding has a direct application to unsteady wind (or water) tunnels. For such devices, a force is applied to a flow field by a fan and the wind tunnel walls. A pressure gradient through the tunnel results in the acceleration of the fluid, which simultaneously creates boundary-layers along each surface. This is illustrated in figure 8.15a. If the fluid were inviscid, the boundary-layers would be in the form of infinitely thin vortex sheets, each rigidly constrained to the wind tunnel walls. At the fan face there is effectively a discontinuous pressure change where work is being done to the fluid.

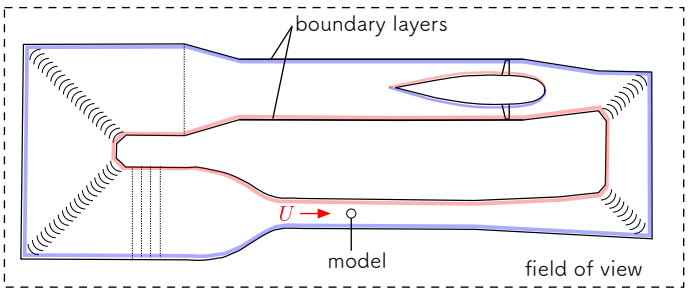

(a) Wide field of view

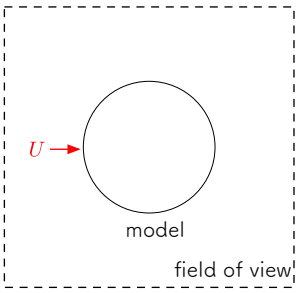

(b) Narrow field of view

Fig. 8.15 Schematic of a model in a wind tunnel. Geometry adapted from Mehta and Bradshaw (1979).

Now consider a model fixed within this wind tunnel and subjected to the inviscid, time dependent free stream velocity. If we constrained our 'field of view' to that only immediately about the model

and forgot that the wind tunnel existed, then one would assume that the flow outside the field of view is without circulation. This is illustrated in figure 8.15b. In absence of further information the forces on the model look identical to the classical added mass and hydrostatic buoyancy components. However, this conclusion is only drawn because of the assumption that the flow outside the field of view has no circulation. Upon increasing our field of view such that it encompasses the walls of the wind tunnel (figure 8.15a), we would note that as the flow is accelerated, the increase in velocity will result in the growth in the strength of wall boundary-layer vorticity, and therefore circulation. With this growing circulation, from equation (8.6) there is a non-circulatory vortex force that exactly accounts for the unsteady forces.

It may be argued that the origin of the unsteady forces is inconsequential for most practical purposes. If one were interested only in measuring the unsteady forces on a body then this may be true. With, however, the more sophisticated measurement techniques such as PIV, as well as CFD modelling, more in depth analysis linking forces on a model to flow structures can be in error if free and wall boundary-layer vorticity is dealt with incorrectly. Furthermore, for gust interaction studies, real gust velocity perturbations are inherently coupled with free vorticity fields which cannot always be decoupled from vorticity shed by a body. As we saw, the incorrect treatment of the gust shear layer vorticity can lead to the misallocation of forces. This will impact any subsequent models based on empirical data of such flows.

8.3 Summary

In this Chapter we investigated the origin of the non-circulatory vortex sheet within the Küssner model. The formation of this sheet was attributed to added mass by von Karman and Sears (1938). Here it is argued that the component is instead a ‘non-circulatory vortex force’, and that in Küssner’s model there must be a second shear layer an infinite distance from the first. This is necessary to ensure that the net circulation contained by the gust shear layers is zero. The mechanism whereby this force arises is due to the relative advection of free vortices; it therefore fundamentally differs to the classical added mass result for an accelerating body in potential flow. The existence of such force production mechanism was demonstrated using both a simple potential flow model, and the experimental gust measurements. For a gust encounter with a gust ratio equal to one, the measured magnitude of the non-circulatory vortex force is remarkably consistent with the added mass force predicted using Küssner’s model.

It was additionally argued that the mechanisms attributed to the generation of unsteady forces for body acceleration and flow field acceleration cases in potential (and non-potential) flows, fundamentally differ. The former gives rise to the classical added mass force, whereas the latter is conventionally attributed to an added mass and buoyancy term. Here it is argued that it is not possible to uniformly accelerate a flow field of infinite extent, only a finite portion. In doing so, free external vortices

are created. This gives rise to another non-circulatory vortex force, that is exactly equivalent to the buoyancy and added mass terms derived for a body in a uniformly accelerating free stream. This was confirmed using a simple potential flow calculation of a cylinder, subjected to flow induced by free vortices. The finding has direct application toward explaining the mechanisms which forces arise for unsteady wind and water tunnel experiments. For such experiments the external vortices are contained within the boundary-layers over the tunnel and fan surfaces.

In the broader context, this work was motivated by a desire to develop predictive low-order models for large wind gusts, as well as surging and rotating wings. Any vorticity generated by a mechanism external to the wing will create a non-circulatory distribution of attached vorticity. The non-circulatory vortex advection and growth forces can be found relatively simply. They are inviscid force production mechanisms, but differ to added mass. Added mass effects arise only when a body accelerates, changes shape, or rotates relative to the free stream. Each of these motions can create a non-circulatory distribution of attached vorticity, that cannot be attributed to other free vortices in the flow field. The advantage of this definition, is that it can prevent the accidental double- or miscounting of force components in complex scenarios, such as wing-gusts encounters. Each of the force components, be that the non-circulatory vortex forces, added mass, and conventional circulatory terms due to self shed vorticity may find their place in a new model describing unsteady aerodynamic flows.

Chapter 9

Conclusions and Future Work

9.1 General comments

This thesis was a fundamental study into the mechanisms which contribute toward force production in unsteady aerodynamic flows. The review of the literature revealed that little is known about the flow physics of large amplitude transverse wing-gust encounters. This is where the assumptions of classical linear theories, in particular Küssner's model, start to breakdown. While motivated toward improving the gust performance of Micro Air Vehicles, the main findings of this thesis, which clarify the role of vorticity and added mass toward force production, have application in any unsteady case.

9.2 Isolating added mass effects with PIV

The added mass phenomenon can result in large transient changes in force, in flows that have high accelerations. This was therefore expected to play an important role in a wing-gust encounter. The review of the literature revealed that the added mass result, derived for a potential flow, had not been shown experimentally to be applicable to a viscous, non-potential, flow. Furthermore, there was no known experimental method for doing so with direct flow field measurements such as PIV. In Chapter 3, it was shown that the classical added mass force may be described by the formation of a non-circulatory vortex sheet. By assuming a body in a flow field may be represented by a region of fluid, with a velocity equal to the rigid body motion, we proposed in Chapter 5 a methodology to measure, and isolate, the added mass attributed vorticity from PIV derived flow data, about any arbitrary two-dimensional body. The technique was applied to a flat plate wing, undergoing translation and rotation accelerations in Chapter 6. From the experiments we drew the following primary conclusions:

- The potential added mass result is applicable to a non-potential flow.
- The proposed methodology for quantifying added mass attributed vorticity within the boundary-layer, using low resolution PIV was successful.

It was possible to draw these main conclusions because:

- Prescribing PIV vector elements contained within a body, a velocity equal to the local rigid body kinematics, forces the circulation of wall bound vector elements to incorporate boundary-layer vorticity. This results from the application of Stokes' theorem about a single PIV vector element. This allows the measurement of the vortex sheet attached to an object in a flow. This vortex sheet has two components, one being 'circulatory', and the other 'non-circulatory'.
- The 'circulatory' part of the attached vortex sheet is attributed to velocities induced by free vorticity in the flow field. For a flat plate, it may be quantified by measurement of the free vorticity and the conformal mapping and mirror vortex method described by Graham et al. (2017), or panel method codes.
- The 'non-circulatory' component is attributed to the kinematic motion of the body, and is the distribution of vorticity attributed to the added mass effect. Subtracting the circulatory component from the total measured vortex sheet on the surface of a body, isolates the non-circulatory vortex sheet. This was shown to be equivalent to the theoretical added mass vortex sheet, even for viscous, separated flows. The added mass attributed distribution of attached vorticity was therefore quantified from PIV measurements.

9.3 Gust encounters

Having proven the validity of the potential flow added mass results to viscous flows, and validated the methodology for isolating the circulatory and non-circulatory vortex sheet components, we sought to analyse a wing-gust encounter in a similar manner, to meet the primary aims of this thesis. Once again, the aims were to characterise and understand of the underlying physics of large amplitude wing-gust encounters, and investigate the applicability of Küssner's linear model. In Chapter 7, PIV, force and dye flow visualisation measurements of wing-gust encounters were described. The gust ratios tested were $GR = 0.2$, 0.5 and 1.0. Initial experiments were conducted with a gust outlet offset distance of $0.83c$ from the plate. These measurements were compared to the Küssner model for a gust of 2 chords, which was calculated by application of Duhamel's integral. The primary conclusion from this Chapter, was:

- The non-circulatory vorticity distribution, attributed to added mass within Küssner's model, must arise from a different phenomenon to added mass.

We drew this conclusion from the attempt to isolate the non-circulatory vortex sheet for the $GR = 1.0$ test case. To minimise random errors, an average of this vortex sheet was taken over the range $1.0 \leq s/c \leq 2.0$, where it is theoretically constant. The measured non-circulatory vortex sheet had a magnitude approximately half that predicted by Küssner's theory. The difference was not due to

experimental uncertainty.

Meanwhile, characterisation of the flow field and forces for the encounter showed:

- For the $GR = 0.2$ encounter, the flow topology reasonably followed the approximations of the Küssner model. Flow separated at the leading edge but appeared to re-attach. The wake remained planar. There was some deflection of each gust shear layer during the immediate entry and exit of the wing. The force measurements relatively closely followed Küssner's model, but deviated mildly from $s/c = 2$.
- For the $GR = 0.5$ encounter, there was significant leading edge separation, and the shedding of vorticity at the trailing edge of the wing. The trailing edge vorticity remained relatively planar, but was deflected by approximately 11°. There was still relatively good agreement between the measured force and Küssner's model up to $s/c = 2.5$. For $s/c \geq 2.5$, the lift force dropped to zero significantly faster than that predicted by Küssner's model. This was partly attributed to a vortex formed from gust shear layer vorticity, inducing downwash onto the wing.
- For the $GR = 1.0$ encounter, there was significant leading edge separation, shedding of vorticity at the trailing edge, and deflection of gust shear layers. The measured peak lift force exceeded Küssner's theory by 27%, and generated negative lift for $s/c \geq 3$. This was also caused by a vortex formed from gust shear layer vorticity, inducing downwash onto the wing. Force and flow topologies were influenced by the offset distance between the wing and gust outlet. Increasing the distance between the wing and outlet to $1.83c$ reduced the peak lift force, such that it was closer to Küssner's prediction. Reynolds number, in the range of 20,000 to 40,000, had little effect on the flow topology and force for a gust ratio of 1.0.

9.4 Subsequent discussion on added mass and wing-gust encounters

Chapter 8 was a discussion on added mass, and its role (or lack thereof) in wing-gust encounters. The reason behind, and implications of, the discrepancy between the measured non-circulatory vortex sheet in the gust experiments, and Küssner's model, was explored. From this work the following can be concluded:

- An inviscid force may act on a body if externally generated vortices grow, or advect relative to a body. These vortices must have zero net circulation. The forces are therefore called 'non-circulatory' vortex forces.
- Added mass forces are attributed to the growth of a non-circulatory vortex sheet, attached to the surface. This is determined only by the body kinematics. This differs to the non-circulatory vortex force, which may be attributed to free vorticity in the flow field.

- The advective non-circulatory vortex force is responsible for the added mass-like force in Küssner's model.
- For a gust ratio of 1.0, the force impulse attributable to the formation of the non-circulatory vortex sheet is close, if not equivalent, to Küssner's added mass force (despite arising from a different mechanism). The finding implies that this force component is accurate for all gust amplitudes.
- The non-circulatory vortex growth force is responsible for the buoyancy and added mass-like forces experienced by any object immersed in flows with an accelerating free stream.

9.5 Recommendations and future work

With the availability of complete PIV velocity field information of unsteady aerodynamic experiments, such as that described in this work, it is suggested that velocity vectors within a body in the flow field be prescribed a velocity equal to the rigid body kinematics instead of simple masking. Vorticity subsequently calculated will include a distribution attributable to the added mass mechanism. Measures of integral quantities such as impulse and force derived from the flow field vorticity will therefore incorporate added mass effects, and have surprisingly little error for reasonable PIV vector resolutions. For many PIV measurements there is incomplete or spurious velocity field information near a body due to shadow effects and surface reflections. Since added mass is an effect that may be quantified by attached vorticity, the masking of vectors close to a body will remove such vorticity and thus the impulse and forces subsequently derived. Often added mass forces are added analytically without this near wall vorticity masking. This study suggests the approach is incorrect and that added mass effects will be duplicated.

There are a number of suggested avenues for further work. Many of the fundamental ideas discussed in this thesis can start to be incorporated into a low-order model. The non-circulatory vortex forces can be calculated based on vortex location, strength, Helmholtz laws of vortex motion and the body kinematics. However, the vortex kinematics will likely be influenced by vorticity shed into the flow field by a body. This is particularly relevant for flat plate geometries due to the sharp leading and trailing edges. Unfortunately this is quite difficult to calculate, and is a continuing topic of research (see Pullin and Wang (2004); Ramesh et al. (2014, 2018); Wang and Eldredge (2012); Xia and Mohseni (2016)). To create a fully predictive model, the rate at which vorticity is shed and its subsequent motion must be determinable.

Secondly, a much larger gust-encounter parametric study would be useful for the validation of any low-order model. Parametric variations, including angle of incidence, aspect and gust ratios would be a good start. Further development of the towing tank based gust generator are also required. In the methodology section it was discussed that some of the variations in the gust velocity profile may be

caused by either flow separation of the vanes, or thickening of the boundary-layers. A more detailed investigation into the cause of this variation, and perhaps a redesign of the vanes may significantly improve the flow quality.

Finally, much of the early inspiration for this work came from surging and pitching wing experiments as similar flow features were expected. As discussed in the review of the literature, a low-order model was derived by Babinsky et al. (2016), and Stevens and Babinsky (2017) for the surge and pitch cases. This was based on a combination of force components including added mass, vortex growth, advection and a Magnus or virtual camber term. This thesis has shown that vorticity attributable to added mass can be quantified with PIV, thus is a potential source of contamination when determining the growth rate of vortices during starting motion. It is additionally believed that the Magnus term is incorrect, given that any change in attached circulation will result in the shedding of net vorticity into the flow. This would be incorporated in measures of the trailing edge vortex. The low-order model should therefore be revisited.

Appendix A

Duhamel's Integral

The Wagner and Küssner functions were derived for an impulsively started wing, and sharp edge gust, respectively. Duhamel superposition allows the response to an arbitrary acceleration, or gust profile to be constructed (Anderson, 2011). If $b(s)$ is the principle response to a unit step of a forcing function $e(s)$, then by linear superposition, the response to an arbitrary forcing function at any position s can be found by summing the response of incremental elements in the history (each occurring at position σ). The Duhamel integral is thus a means of computing and applying the effect of past changes of the forcing function. For a continuous system the effective response function $b_e(s)$ is:

$$b_e(s) = e(0)b(s) + \int_0^s \frac{de}{ds} b(s-\sigma)d\sigma. \tag{A.1}$$

In discretised form, equation (A.1) may be written as:

$$b_e = e_0 b(s) + \delta e_1 b(s-\sigma_1) + \delta e_2 b(s-\sigma_2) + ... + \delta e_i b(s-\sigma_i). \tag{A.2}$$

Here δe_i is the incremental change to the forcing function between two consecutive time steps, $\delta e_i = e_i - e_{i-1}$.

Appendix B

Extracting added mass with PIV - validation with an artificial flow field

PIV measurements are a discretised representation of a continuous flow field. Consequently, the discretisation can be a source of error when it comes to extracting distributions of bound vorticity, impulse and force quantities. Here this error is quantified by generating an artificial flow field, from which the non-circulatory bound vortex sheet γ^{nc} is 'measured' using the methods described in Chapter 5. Separate flow fields were generated for both the translation and rotation flat plate motions using the potential flow solution given in section 3.2. As shown in figure B.1, velocity vectors were calculated at points given by a high resolution structured mesh with approximately 600 vectors per chord ($c/\Delta l$, where Δl is the distance between adjacent vector elements). Secondary variable resolution vector grids were used to represent PIV measurements. These had vector densities of $c/\Delta l = 25$, 50 and 100 vectors per chord. For each secondary grid point, the velocity was found by averaging the velocities at the high resolution grid points over an area of $2\Delta l \times 2\Delta l$, thereby replicating the spatial average which arises during the calculation of PIV vectors using a cross-correlation of particle images*. For the calculation of bound circulation the plate was divided into 50 integration contours, with a height of 0.25 chord lengths.

The flow field for the 25 element case is shown in figure B.2a. The red boxes are the first and last contours used for the calculation of bound circulation, whereas the shaded background indicates vorticity calculated from the discretised curl of the secondary (low resolution) vector field. The averaging process spreads vorticity past the left and right boundaries of the integration contours; thus some of the vorticity will be allocated as 'free' in the flow field. Measurements of the non-circulatory bound vortex sheet, γ_r^{nc}, for each grid resolution are given in figure B.2b. Each measure of the bound vortex sheet approximately follows the theoretical value, albeit the lower resolutions show significant

*The PIV measurements were processed with a 50% interrogation window overlap, thus the cross-correlation area is four times that with no overlap.

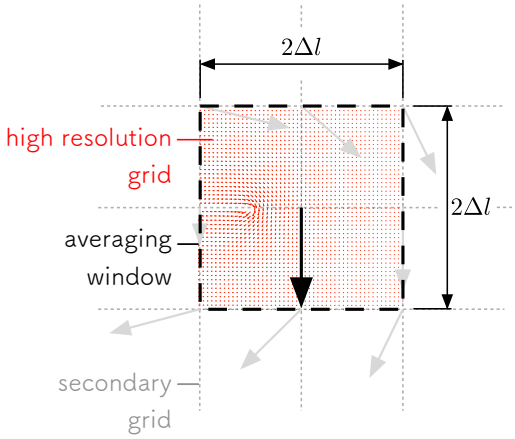

Fig. B.1 Schematic of the spatial averaging window for replicating a PIV interrogation area.

deviation from theory at the plate edges where there are large gradients in vorticity.

The first moment of impulse, J_z, was calculated in three ways. One method uses all of the vorticity in the flow field, as determined from the secondary vector field. In discretised form, the second moment of vorticity, given by equation (2.24) is

$$\upsilon_z = \sum_{k=1}^{n} (x_k^2 + y_k^2)\omega_{z,k}(\Delta l)^2, \tag{B.1}$$

where the subscript k is the index for each vortex element in the discretised flow field. With equation (2.25), J_z can therefore be found from the measured vorticity elements. This is the line identified by blue square markers shown in figure B.2c, scaled by the theoretical potential flow value given by equation (2.25). Despite the significant smoothing of vorticity around the plate surface, the resolution of the secondary grid has negligible effect on the first moment of impulse. Given reasonable vector resolution, the result suggests that, if vector elements contained by an arbitrary body are prescribed velocities equal to the rigid body kinematics, subsequent calculation of vorticity from the velocity field will result in surface vortex sheets being represented in a spatially averaged form in the discretised vector field. Impulse and force quantities derived from such a discretised flow field will therefore include added mass effects.

The problem with directly calculating impulse (and moments thereof) from flow field vorticity is that the added mass contribution is superimposed with other vorticity sources. To isolate the added mass component, impulse is calculated from the measure of γ^{nc} acquired from the procedure outlined in section 5.1.2. For the rotation case, this is given by the line identified by black triangles in figure B.2c. The significant error may in part be attributed to relatively high measurement error at the plate edges.

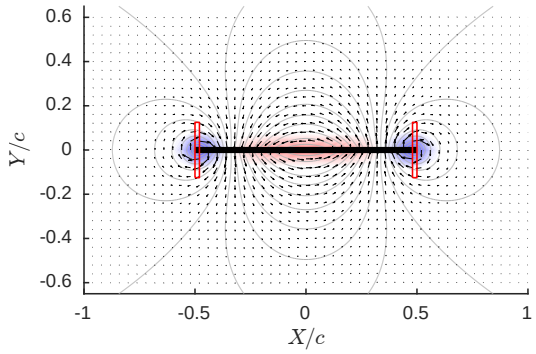

(a) Artificial flow field for $c/\Delta l = 25$

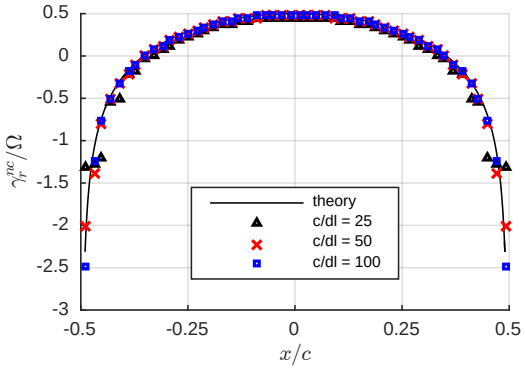

(b) Measured non-circulatory vortex sheet, compared with potential theory

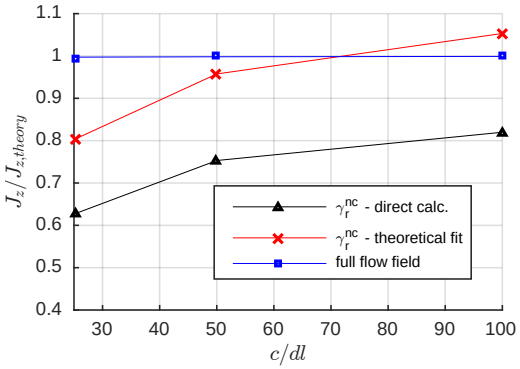

(c) Ratio of the measured to theoretical first moment of impulse

Fig. B.2 Quantification of discretisation errors using an artificially generated flow field for the rotating plate case. In the case of (c): blue squares - first moment of impulse calculated from vorticity in the full flow field. Black triangles - non-circulatory vortex sheet as directly measured. Red crosses - analytical function fit to the measured non-circulatory vortex sheet.

For the purpose of extracting the portion of impulse (and moments thereof) attributed to the non-circulatory vortex sheet, it is proposed that some of the discretisation error may be corrected by fitting the analytical non-circulatory vortex sheet function given by equation (3.23) to the measurements. For each kinematic case, rotation or translation, the analytical function is a geometrical 'mode shape' that is scaled by the instantaneous velocity. Provided the measures of the non-circulatory vortex sheet follow the geometric shape (this was demonstrated in section 6.4), a measure of the plate kinematics U_n or Ω may be obtained by using a least squares fit or similar. Then impulse and forces may be directly calculated from the analytical solutions given in Chapter 3. This is the line identified by red-cross markers in figure B.2c. For the lowest vector resolution case the error is halved to 20%, whereas it is within $\pm 5\%$ for $c/\Delta l = 50$ and 100. Each of the impulse measures for the translation case are given in figure B.3. Once again errors are negligible when impulse is calculated using all elemental vorticity. The error is approximately half that of the rotation case for impulse calculated

from the measured non-circulatory vortex sheet, and is comparable to the rotation case for the fitted vortex sheet.

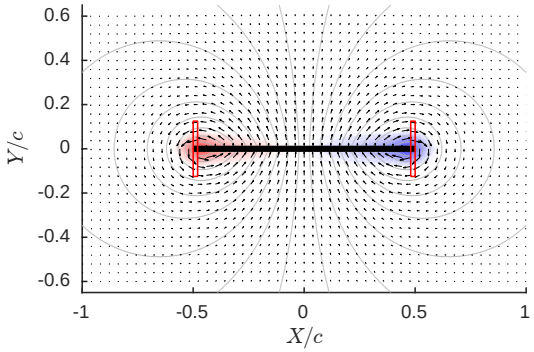

(a) Artificial flow field for $c/\Delta l = 25$

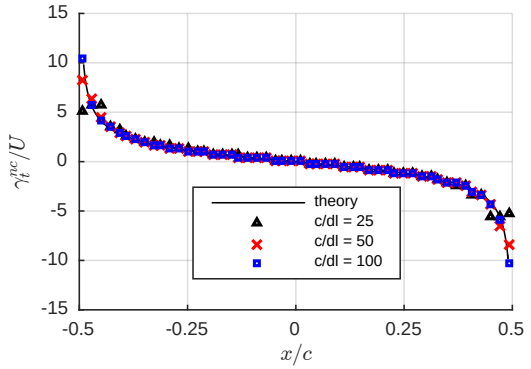

(b) Measured non-circulatory vortex sheet, compared with potential theory

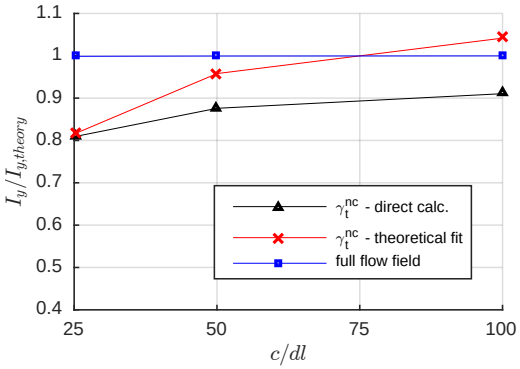

(c) Ratio of the measured to theoretical impulse

Fig. B.3 Quantification of discretisation errors using an artificially generated flow field for the translating plate case. In the case of (c): blue squares - impulse calculated from vorticity in the full flow field. Black triangles - non-circulatory vortex sheet as directly measured. Red crosses - analytical function fit to the measured non-circulatory vortex sheet.

References

Adrian, R. J. and Westerweel, J. (2011). *Particle image velocimetry*. Cambridge University Press.

Anderson, J. D. (1997). *A history of aerodynamics and its impact on flying machines*. Cambridge University Press.

Anderson, J. D. (2011). *Fundamentals of aerodynamics*. McGraw-Hill, London.

Babinsky, H., Stevens, P. R. R. J., Jones, A. R., Bernal, L. P., and Ol, M. V. (2016). Low order modelling of lift forces for unsteady pitching and surging wings. *54th AIAA Aerospace Sciences Meeting*, pages 1–12.

Beckwith, R. M. H. and Babinsky, H. (2009). Impulsively started flat plate flow. *Journal of Aircraft*, 46(6):2186–2189.

Beem, H. R., Rival, D. E., and Triantafyllou, M. S. (2012). On the stabilization of leading-edge vortices with spanwise flow. *Experiments in Fluids*, 52(2):511–517.

Bejan, A. (2005). The constructal law of organization in nature: tree-shaped flows and body size. *The Journal of Experimental Biology*, 208(Pt 9):1677–86.

Benjamin, T. B. (1986). Note on added mass and drift. *Journal of Fluid Mechanics*, 169:251–256.

Bisplinghoff, R. L., Ashley, H., and Halfman, R. L. (1955). *Aeroelasticity*. Addison-Wesley series in mechanics. Addison-Wesley, Cambridge, MA.

Brennen, C. E. (1982). A review of added mass and fluid inertial forces. Technical Report CR 82.010, Naval Civil Engineering Laboratory.

Brion, V., Lepage, A., Amosse, Y., Soulevant, D., Senecat, P., Abart, J. C., and Paillart, P. (2015). Generation of vertical gusts in a transonic wind tunnel. *Experiments in Fluids*, 56(145):1–16.

Buchner, A. J., Buchmann, N., Kilany, K., Atkinson, C., and Soria, J. (2012). Stereoscopic and tomographic PIV of a pitching plate. *Experiments in Fluids*, 52(2):299–314.

Cengel, Y. A., Turner, R. H., and Cimbala, J. M. (2008). *Fundamentals of thermal fluid sciences*, volume 3. McGraw-Hill, New York.

Chen, K. K., Colonius, T., and Taira, K. (2010). The leading-edge vortex and quasisteady vortex shedding on an accelerating plate. *Physics of Fluids*, 22(3):033601.

Choi, J., Colonius, T., and Williams, D. R. (2015). Surging and plunging oscillations of an airfoil at low Reynolds number. *Journal of Fluid Mechanics*, 763:237–253.

Clayton, B. R. and Massey, B. S. (1967). Flow visualization in water: a review of techniques. *Journal of Scientific Instruments*, 44(1):2–11.

Cooper, K. R., Gerhardt, H. J., Whitbread, R., Garry, K. P., and Carr, G. W. (1986). A comparison of aerodynamic drag measurements on model trucks in closed-jet and open-jet wind tunnels. *Journal of Wind Engineering and Industrial Aerodynamics*, 22(2-3):299–316.

Darwin, C. (1953). Note on hydrodynamics. *Mathematical Proceedings of the Cambridge Philosophical Society*, 49(2):342–354.

Davies, F., Middleton, D. R., and Bozier, K. E. (2007). Urban air pollution modelling and measurements of boundary layer height. *Atmospheric Environment*, 41:4040–4049.

Davis, W. R. J., Kosicki, B. B., Boroson, D. M., and Kostishack, D. F. (1996). Micro air vehicles for optical surveillance. *The Lincoln Laboratory Journal*, 9(2):197–214.

Donely, P. (1950). Summary of information relating to gust loads on airplanes. Technical Report 997, National Advisory Committee for Aeronautics.

Drischler, J. A. and Diederich, F. W. (1957). Lift and moment responses to penetration of sharp-edged traveling gusts, with application to penetration of weak blast waves. Technical Report TN-3956, National Advisory Committee for Aeronautics.

Durand, W. F. (1935). *A general review of progress*. Aerodynamic theory, Volume II. Julius Springer, Berlin.

Eldredge, J. D. (2010). A reconciliation of viscous and inviscid approaches to computing locomotion of deforming bodies. *Experimental Mechanics*, 50(9):1349–1353.

Eldredge, J. D. and Wang, C. (2010). High-fidelity simulations and low-order modeling of a rapidly pitching plate. *AIAA Paper*, (July):1–19.

Ellington, C. P., van den Berg, C., Willmott, A. P., and Thomas, A. L. R. (1996). Leading-edge vortices in insect flight. *Nature*, 384(6610):626–630.

Evans, S., KC, A., Bradney, D. R., Urmee, T. P., Whale, J., and Clausen, P. D. (2017). The suitability of the IEC 61400-2 wind model for small wind turbines operating in the built environment. *Renewable Energy and Environmental Sustainability*, 2:31.

Federal Aviation Administration (2014). Dynamic Gust loads. Technical Report 14 CFR 25.341, U.S. Department of Transportation.

Flomenhoft, H. I. (1994). Brief history of gust models for aircraft design. *Journal of Aircraft*, 31(5):1225–1227.

Fowles, G. R. (1989). *Introduction to modern optics*. Dover Publications INC., New York, 2nd edition.

Francis, R. H. and Cohen, J. (1933). The flow near a wing which starts suddenly from rest and then stalls. Technical Report 1561, Aeronautical Research Committee.

Friedman, D. and Westphal, W. R. (1952). Experimental investigation of a 90 degree cascade diffusing bend with an area ratio of 1.45:1 and with several inlet boundary layers. Technical Report TN 2668, National Advisory Committee for Aeronautics.

Frost, W. and Turner, R. E. (1982). A discrete gust model for use in the design of wind energy conversion systems. *Journal of Applied Meteorology*, 21(6):770 – 776.

Garrick, I. E. (1938). On some reciprocal relations in the theory of nonstationary flows. Technical Report 629, National Advisory Committee for Aeronautics.

Graham, W. R., Pitt Ford, C. W., and Babinsky, H. (2017). An impulse-based approach to estimating forces in unsteady flow. *Journal of Fluid Mechanics*, 815:60–76.

Granlund, K., Monnier, B., Ol, M., and Williams, D. (2014). Airfoil longitudinal gust response in separated vs. attached flows. *Physics of Fluids*, 26(2):14.

Granlund, K., Ol, M., and Bernal, L. (2011). Experiments on pitching plates: force and flowfield measurements at low Reynolds Numbers. In *49th AIAA Aerospace Sciences Meeting*.

Granlund, K. O., Ol, M. V., and Bernal, L. P. (2013). Unsteady pitching flat plates. *Journal of Fluid Mechanics*, 733:R5.

Grasmeyer, J. and Keennon, M. (2001). Development of the black widow micro air vehicle. In *39th Aerospace Sciences Meeting and Exhibit*, pages 519–535, Reston, Virigina. American Institute of Aeronautics and Astronautics.

Gursul, I. and Cleaver, D. (2018). Plunging oscillations of airfoils and wings: progress, opportunities, and challenges. *AIAA Journal*, Article in:1–18.

Ham, N. D., Bauer, P. H., and Lawrence, T. L. (1974). Wind tunnel generation of sinusoidal lateral and longitudinal gusts by circulation of twin parallel airfoils. Technical Report CR-137547, NASA.

Hartloper, C., Kinzel, M., and Rival, D. E. (2013). On the competition between leading-edge and tip-vortex growth for a pitching plate. *Experiments in Fluids*, 54(1):1447.

Homer, M. B., Saliveros, E., Kokkalis, A., and Galbraith, R. A. M. (1993). Results from a set of low speed blade-vortex interaction experiments. *Experiments in Fluids: Experimental Methods and their Applications to Fluid Flow*, 14(5):341–352.

Humphreys, N. D. (1995). *High cross wind gust loads on ground from moving model experiments*. PhD thesis, University of Nottingham.

Jones, A. R. and Babinsky, H. (2010). Unsteady lift generation on rotating wings at low Reynolds numbers. *Journal of Aircraft*, 47(3):1013–1021.

Jones, A. R. and Babinsky, H. (2011). Reynolds number effects on leading edge vortex development on a waving wing. *Experiments in Fluids*, 51(1):197–210.

Jones, M. A. (2003). The separated flow of an inviscid fluid around a moving flat plate. *Journal of Fluid Mechanics*, 496:405–441.

Jones, R. T. (1940). The unsteady lift of a wing of finite aspect ratio. Technical Report 681, National Advisory Committee for Aeronautics.

Keennon, M., Klingebiel, K., and Won, H. (2012). Development of the nano hummingbird: A tailless flapping wing micro air vehicle. *50th AIAA Aerospace Sciences Meeting including the New Horizons Forum and Aerospace Exposition*, (January):1–24.

Kelvin, W. T. (1869). *On vortex motion*. Royal Society of Edinburgh, Edinburgh.

Küssner, H. G. (1930). Untersuchung der bewegung einer platte beim eintrill in eine strahlgrenze. *Luftfahrtforschung*, page 425.

Kussner, H. G. (1932). Stresses produced in airplane wings by gusts. Technical report, National Advisory Committee for Aeronautics.

Lamb, H. (1895). *Hydrodynamics*. Cambridge University Press, Cambridge.

Leahy, F. B. (2008). Discrete gust model for launch vehicle assessments. In *13th Conference on Aviation, Range and Aerospace Meteorology*. American Meteorology Society.

Leishman, J. G. (1996). Subsonic unsteady aerodynamics caused by gusts using the indicial method. *Journal of Aircraft*, 33(5):869–879.

Leishman, J. G. (1997). Unsteady aerodynamics of airfoils encountering traveling gusts and vortices. *Journal of Aircraft*, 34(6):719–729.

Leishman, J. G. (2000). *Principles of helicopter aerodynamics*, volume 18 of *Cambridge Aerospace Series*. Cambridge University Press, Cambridge, 2nd edition.

Lentink, D. and Dickinson, M. H. (2009). Rotational accelerations stabilize leading edge vortices on revolving fly wings. *Journal of Experimental Biology*, 212(16):2705–2719.

Leonard, A. and Roshko, A. (2001). Aspects of flow-induced vibration. *Journal of Fluids and Structures*, 15(3-4):415–425.

Li, J. and Wu, Z. N. (2016). A vortex force study for a flat plate at high angle of attack. *Journal of Fluid Mechanics*, 801:222–249.

Lighthill, M. J. (1986). *An informal introduction to theoretical fluid meschanics*. Clarendon, Oxford.

Lissaman, P. B. S. (1983). Low-Reynolds-number airfoils. *Annual Review of Fluid Mechanics*, 15:223–239.

Mai, H., Neumann, J., and Hennings, H. (2011). Gust response: a validation experiment and preliminary numerical simulations. *15th International Forum on Aeroelasticity and Structural Dynamics*, pages 1–20.

Manar, F., Mancini, P., Mayo, D., and Jones, A. R. (2016). Comparison of rotating and translating wings: force production and vortex characteristics. *AIAA Journal*, 54(2):519–530.

Manar, F. H. and Jones, A. R. (2017). Vorticity production at the leading edge of flat plates at high incidence. In *55th AIAA Aerospace Sciences Meeting*, number January, pages 1–11, Reston, Virginia. American Institute of Aeronautics and Astronautics.

Maskell, E. C. (1965). A theory of blockage effects on bluff bodies and stalled wings in a closed wind tunnel. Technical Report 3400, Aeronautical Research Council.

Maxworthy, T. (2007). The formation and maintenance of a leading-edge vortex during the forward motion of an animal wing. *Journal of Fluid Mechanics*, 587:471–475.

McCroskey, W. J., McAlister, K. W., and Carr, L. W. (1982). An experimental study of dynamic stall on advanced airfoil sections. Technical Report 84245, NASA.

McGowan, G. Z., Granlund, K., Ol, M. V., Gopalarathnam, A., and Edwards, J. R. (2011). Investigations of lift-based pitch-plunge equivalence for airfoils at low Reynolds numbers. *AIAA Journal*, 49(7):1511–1524.

Mehta, R. D. (1985). Turbulent boundary layer perturbed by a screen. *AIAA Journal*, 23(9):1335–1342.

Mehta, R. D. and Bradshaw, P. (1979). Design rules for small low speed wind tunnels. *The Aeronautical Journal of the Royal Aeronautical Society*, pages 443–449.

Mercker, E. and Wiedemann, J. (1996). On the correction of interference effects in open jet wind tunnels. In *International Congress & Exposition*. SAE International.

Miles, J. W. (1956). The aerodynamic force on an airfoil in a moving gust. *Journal of Aeronautical Sciences*, 23:1044–1050.

Milne-Thomson, L. M. (1986). *Theoretical hydrodynamics*. Macmillan, 5th edition.

Minotti, F. O. (2011). Determination of the instantaneous forces on flapping wings from a localized fluid velocity field. *Physics of Fluids*, 23:111902.

Mohamed, A., Abdulrahim, M., Watkins, S., and Clothier, R. (2015). Development and flight testing of a turbulence mitigation system for micro air vehicles. *Journal of Field Robotics*, 33(5):639–660.

Mohamed, A., Massey, K., Watkins, S., and Clothier, R. (2014). The attitude control of fixed-wing MAVS in turbulent environments. *Progress in Aerospace Sciences*, 66:37–48.

Nakata, T. and Liu, H. (2012). Aerodynamic performance of a hovering hawkmoth with flexible wings: a computational approach. *Proceedings of the Royal Society B: Biological Sciences*, 279(1729):722–731.

Nobach, H. and Bodenschatz, E. (2009). Limitations of accuracy in PIV due to individual variations of particle image intensities. *Experiments in Fluids*, 47(1):27–38.

Noback, R. (1986). Comparison of discrete and continuous gust methods for airplane design loads determination. *Journal of Aircraft*, 23(3):226 – 231.

Ol, M. and Babinsky, H. (2016). Extensions of fundamental flow physics to practical MAV aerodynamics. Technical Report TR-AVT-202, North Atlantic Treaty Organization.

Ol, M., Parker, G., Abate, G., and Evers, J. (2008). Flight controls and performance challenges for MAVs in complex environments. In *AIAA Guidance, Navigation and Control Conference and Exhibit*. American Institute of Aeronautics and Astronautics.

Ol, M. V. (2009). The high-frequency, high-amplitude pitch problem: Airfoils , plates and wings. In *39th AIAA Fluid Dynamics Conference*, number June, pages 1–14, San Antonio, Texas. American Institute of Aeronautics and Astronautics.

Ol, M. V., Bernal, L., Kang, C. K., and Shyy, W. (2010). Shallow and deep dynamic stall for flapping low Reynolds number airfoils. *Animal Locomotion*, pages 321–339.

Parameswaran, V. (1995). *Concepts for the reduction of blade vortex inteaction noise and the use of CFD to determine indicial and gust responses of an airfoil in compressible flow*. PhD thesis, University of Maryland.

Parameswaran, V. and Baeder, J. (1997). Indicial aerodynamics in compressible flow-direct computational fluid dynamic calculations. *Journal of Aircraft*, 34(1):131–133.

Patel, M. H. (1982). Aerodynamic forces on finite wings in oblique gusts. *Journal of Aircraft*, 19(1):71–75.

Patel, M. H. and Hancock, G. J. (1977). A gust tunnel facility. Technical Report 3802, Aeronautical Research Council.

Peng, D. and Gregory, J. W. (2015). Vortex dynamics during blade-vortex interactions. *Physics of Fluids*, 27(5):1–23.

Perrotta, G. and Jones, A. R. (2017). Unsteady forcing on a flat-plate wing in large transverse gusts. *Experiments in Fluids*, 58(8):1–11.

Petricca, L., Ohlckers, P., and Grinde, C. (2011). Micro- and nano-air vehicles: state of the art. *International Journal of Aerospace Engineering*, 2011:1–17.

Pitt Ford, C. W. (2013). *Unsteady aerodynamic forces on accelerating wings at low Reynolds numbers*. PhD thesis, The University of Cambridge.

Pitt Ford, C. W. and Babinsky, H. (2013). Lift and the leading-edge vortex. *Journal of Fluid Mechanics*, 720:280–313.

Poelma, C., Dickson, W. B., and Dickinson, M. H. (2006). Time-resolved reconstruction of the full velocity field around a dynamically-scaled flapping wing. *Experiments in Fluids*, 41(2):213–225.

Polet, D. T., Rival, D. E., and Weymouth, G. D. (2015). Unsteady dynamics of rapid perching manoeuvres. *Journal of Fluid Mechanics*, 767:323–341.

Poling, D. R. and Telionis, D. P. (1986). The response of airfoils to periodic disturbances - the unsteady kutta condition. *AIAA Journal*, 24(2):193–199.

Pope, S. B. (2000). *Turbulent flows*. Cambridge University Press.

Pratt, K. G. (1953). A revised formula for the calculation of gust loads. Technical Report 2964, National Advisory Committee for Aeronautics.

Pullin, D. I. (1978). The large-scale structure of unsteady self-similar rolled-up vortex sheets. *Journal of Fluid Mechanics*, 88(03):401–430.

Pullin, D. I. and Wang, Z. J. (2004). Unsteady forces on an accelerating plate and application to hovering insect flight. *Journal of Fluid Mechanics*, 509:1–21.

Raffel, M., Willert, C. E., Wereley, S. T., and Kompenhans, J. (2007). *Particle image velocimetry: a practical guide*. Springer.

Ramamurthy, R. S. and Balachandar, R. (1989). Blockage correction for sharp-edged bluff bodies. *Journal of Engineering Mechanics*, 115(7):1569–1576.

Ramesh, K., Gopalarathnam, A., Granlund, K., Ol, M. V., and Edwards, J. R. (2014). Discrete-vortex method with novel shedding criterion for unsteady aerofoil flows with intermittent leading-edge vortex shedding. *Journal of Fluid Mechanics*, 751:500–538.

Ramesh, K., Granlund, K., Ol, M. V., Gopalarathnam, A., and Edwards, J. R. (2018). Leading-edge flow criticality as a governing factor in leading-edge vortex initiation in unsteady airfoil flows. *Theoretical and Computational Fluid Dynamics*, 32(2):109–136.

Raveh, D. E. (2007). CFD-based models of aerodynamic gust response. *Journal of Aircraft*, 44(3):888–897.

Rhode, R. V. and Lundquist, E. E. (1931). Preliminary study of applied load factors in bumpy air. Technical Report 374, National Advisory Committee for Aeronautics.

Ringuette, M. J., Milano, M., and Gharib, M. (2007). Role of the tip vortex in the force generation of low-aspect-ratio normal flat plates. *Journal of Fluid Mechanics*, 581:453–468.

Rival, D., Manejev, R., and Tropea, C. (2010). Measurement of parallel blade-vortex interaction at low Reynolds numbers. *Experiments in Fluids*, 49(1):89–99.

Rival, D. E., Prangemeier, T., and Tropea, C. (2009). The influence of airfoil kinematics on the formation of leading-edge vortices in bio-inspired flight. *Experiments in Fluids*, 46(5):823–833.

Ryan, A. and Dominy, R. G. (2000). Wake surveys behind a passenger car subjected to a transient cross-wind gust. Technical Report 2000-01-0874, SAE International.

Saddington, A., Finnis, M., and Knowles, K. (2014). The characterisation of a gust generator for aerodynamic testing. *Proceedings of the Institution of Mechanical Engineers, Part G: Journal of Aerospace Engineering*, 229(7):1214–1225.

Saffman, P. G. (1992). *Vortex dynamics*. Cambridge University Press.

Shukla, R. K. and Eldredge, J. D. (2007). An inviscid model for vortex shedding from a deforming body. *Theoretical and Computational Fluid Dynamics*, 21(5):343–368.

Simpson, C. E., Babinsky, H., Harvey, J. K., and Corkery, S. (2018). Detecting vortices within unsteady flows when using single-shot PIV. *Experiments in Fluids*, 59(8):125.

Son, O., Cetiner, O., Stevens, P. R. R. J., Babinsky, H., Manar, F., Mancini, P., Jones, A. R., Ol, M. V., and Gozukara, A. C. (2016). Parametric variations in aspect ratio, leading edge and planform shapes for the rectilinear pitch cases of AVT-202. In *54th AIAA Aerospace Sciences Meeting*, pages 1–17.

Spedding, G. R. and Lissaman, P. B. S. (1998). Technical aspects of microscale flight systems. *Journal of Avian Biology*, 29(4):458–468.

Stevens, P. R. R. J. (2013). *Unsteady low Reynolds number aerodynamic forces*. PhD thesis, The University of Cambridge.

Stevens, P. R. R. J. and Babinsky, H. (2017). Experiments to investigate lift production mechanisms on pitching flat plates. *Experiments in Fluids*, 58(1):7.

Tang, D. and Dowell, E. H. (2002). Experimental and theoretical study of gust response for high-aspect-ratio wing. *AIAA Journal*, 40(3):419–429.

Tang, D. and Dowell, E. H. (2010). Aeroelastic airfoil with free play at angle of attack with gust excitation. *AIAA Journal*, 48(2):427–442.

Tang, D. M., Cizmas, P. G. A., and Dowell, E. H. (1996). Experiments and analysis for a gust generator in a wind tunnel. *Journal of Aircraft*, 33(1):139–148.

Turner, E. W. (1977). An exposition on aircraft response to atmospheric turbulence using power spectral density analysis techniques. Technical Report AFFDL-TR-76-162, Air Force Flight Dynamics Laboratory.

Volpe, R., Da Silva, A., Ferrand, V., and Le Moyne, L. (2013). Experimental and numerical validation of a wind gust facility. *Journal of Fluids Engineering*, 135(1):9.

von Karman, T. and Sears, W. R. (1938). Airfoil theory for non-uniform motion. *Journal of the Aeronautical Sciences*, 5(10):379–390.

Wagner, H. A. (1925). Über die entstehung des dynamischen auftriebes von tragflügeln. *Zeitschrift für angewandte Mathematik und Mechanik*, 5(1):17–35.

Walker, P. (1931). Experiments on the growth of circulation about a wing. Technical Report 1402, Aeronautical Research Committee.

Walker, P. B. (1932). Experiments of the growth of circulation about a wing with a description of an apparatus for measuring fluid motion. *The Aircraft Engineer*, page 16.

Walshe, D. E. J. (1972). *Wind-excited oscillation of structures*. H.M. Stationery Office.

Wang, C. and Eldredge, J. D. (2012). Low-order phenomenological modeling of leading-edge vortex formation. *Theoretical and Computational Fluid Dynamics*, 27(5):577–598.

Watkins, S., Milbank, J., Loxton, B. J., and Melbourne, W. H. (2006). Atmospheric winds and their implications for microair vehicles. *AIAA Journal*, 44(11):2591–2600.

Watkins, S., Thompson, M., Loxton, B., and Abdulrahim, M. (2010). On low altitude flight through the atmospheric boundary layer. *International Journal of Micro Air Vehicles*, 2(2):55–68.

Westerweel, J. (1999). Fundamentals of digital particle image velocimetry. *Measurement Science and Technology*, 8(12):1379–1392.

White, C., Lim, E., Watkins, S., Mohamed, A., and Thompson, M. (2012). A feasibility study of micro air vehicles soaring tall buildings. *Journal of Wind Engineering and Industrial Aerodynamics*, 103:41–49.

Wong, N. P. (1988). *Fundamentals of dairy chemistry*. Springer, 3rd edition.

Wu, J. C. (1981). Theory for aerodynamic force and moment in viscous flows. *AIAA Journal*, 19(4):432–441.

Wu, J. C. (2018). *Elements of vorticity aerodynamics*. Springer.

Xia, X. and Mohseni, K. (2013). Lift evaluation of a two-dimensional pitching flat plate. *Physics of Fluids*, 25(9):6.

Xia, X. and Mohseni, K. (2016). Unsteady aerodynamics and vortex-sheet formation of a two-dimensional airfoil. *Journal of Fluid Mechanics*, 830:439–478.

Zaide, A. and Raveh, D. E. (2006). Numerical simulation and reduced-order modeling of airfoil gust response. *AIAA Journal*, 44(8):1826–1834.